Fundamental Limitations of Rotating Magnetic Field Thrusters

by

Tate M. Gill

A dissertation submitted in partial fulfillment
of the requirements for the degree of
Doctor of Philosophy
(Aerospace Engineering)
in the University of Michigan
2024

Doctoral Committee:

Professor Benjamin A. Jorns, Chair
Professor John E. Foster
Professor Alec D. Gallimore, Duke University
Professor Justin M. Little, University of Washington
Dr. Kurt A. Polzin, NASA—George C. Marshall Space Flight Center

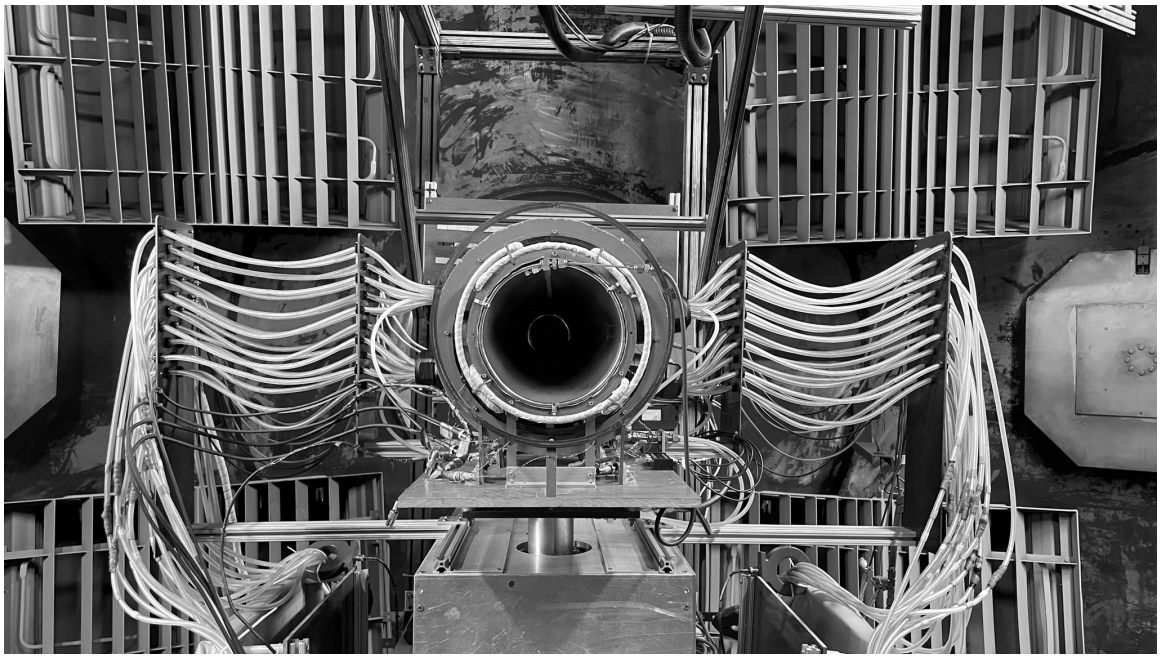

Tate M. Gill
tategill@umich.edu
ORCID iD: 0000-0002-5585-4869

To my dad
—Water off a duck's back

ACKNOWLEDGEMENTS

I am profoundly grateful to all those who have helped me towards the completion of this thesis. Their support, guidance, and encouragement have been invaluable throughout this journey.

First and foremost, I need to express my deep appreciation to Foss Miller who offered me guidance and support when I truly needed it. Without you, my life could look very different. I would not have started this degree let alone completed it. Thank you for believing in me.

To my advisor, Ben: my first phone call with you lasted eight minutes. You may not remember it, but I remember clearly that it did not go well. It took me moving to Michigan and several months of persistent pestering before you agreed to take me on as a student. We've come along way from that call six years ago, and now I feel honored to have you as a mentor. You've certainly made me a better writer and academic (committee opinions forthcoming). I am immensely grateful for your ability to plainly show me where the standard of excellence is, and for your ability to instruct and guide me towards it.

To my closest colleague, Chris: without your teamwork this project would not have been possible. I've not met nor heard of anyone else who could build a plasma thruster with nothing more than a jigsaw and a dream. It has been a gift to find someone that I disagree with so productively, and I have undoubtedly become a stronger scientist working alongside you. It will be an honor to call you a colleague and a friend for many years to come.

To my labmates at PEPL: you're probably pretty sick of my bad jokes at this point, but I feel so lucky to come to work next to all of you every day. While I only understand five percent of what most of you do (particularly if you evoke the legendary Bayes' rule), I know I'm surrounded by super smart people who motivate me to back up my ideas with science. Thanks for your support.

To my mom: from letting me buy that motorcycle at age 16 to going across the country for college—you've always believed in me enough to let me spread my wings. Although I've made my share poor decisions, that potentially unfounded faith has led to so many self discoveries about who I am and who I want to become. Your confidence in yourself and your willingness to pursue your goals is admirable. Thanks for teaching me to follow my dreams.

To my older brother, Thane: I remember always looking up to you and your projects from marble runs, to broken bicycles, to trebuchets. I think you're probably the reason I

wanted to be an engineer. You're absolutely the smartest person I know, and while my eyes absolutely glaze over when you explain your work to me, you might be the only person I know outside of my committee that will even attempt to read this document. Thanks for not only being my brother but being my friend.

To my wife, Victoria: many years ago, I told you the part I loved about you the most was your brain; I'm not sure my brain will ever match yours, but at least now I will have one more degree on the wall than you. One dream down. Many to go. Can't wait to enjoy the ride with you.

To my dog, Maisie: thanks for being a true companion throughout this entire process. You kept me on track and showed me when it was time to work and when it was time to play. Thanks for being a great office mate.

I would also like to acknowledge NASA's Space Technology Graduate Research Opportunities program for their financial support, which made this research possible. Funding was provided under NSTGRO grant number 80NSSC20K1168.

Thank you all for being a crucial part of this significant chapter in my life.

TABLE OF CONTENTS

LIST OF FIGURES

FIGURE

LIST OF TABLES

TABLE

ABSTRACT

This dissertation investigates the challenges in achieving high efficiency for rotating magnetic field (RMF) thrusters. These thrusters are a novel form of in-space electric propulsion aimed towards high power applications (>100 kW) and operation on non-traditional propellants such as air, water, or carbon dioxide. These capabilities could enable missions such as air-breathing satellites in very low earth orbit, cargo transportation to Mars, or rapid repositioning in cis lunar space. RMF thrusters may be well suited to these applications; however, the efficiency of research prototypes remains low at around 1%, whereas state-of-the-art electric thrusters reach upwards of 60%.

This work showcases the development of several RMF thruster prototypes with the aim of characterizing their performance and improving their efficiency. Analysis of the overall propulsive efficiency of the initial RMF thruster prototype was conducted using plasma diagnostic probes. This analysis revealed that the RMF thruster is severely limited in its ability to convert power coupled into the propellant into an energetic beam, and the majority of the power is lost through visible light.

Because of this result, an updated thruster was constructed to operate continuously, instead of the typical discrete pulsed operation. This operational regime was found to raise propulsive efficiency by a factor of over 400%; however, the overall thruster efficiency still only reached a maximum of just under 3%. To further explain the performance of these thrusters, an analytical performance model was development to predict performance in the continuous mode. This model agrees with the present experimental results and predicts RMF thruster efficiency of up to 65% through critical design changes to the device.

This effort marks the first comprehensive diagnostic evaluation of RMF thrusters, the first operation of an RMF thruster in the continuous mode, and an updated inferred maximum theoretical efficiency for this technology.

CHAPTER 1

Introduction

1.1 The Traditional Role of Electric Propulsion in Spaceflight

Although electric propulsion is not a new concept—in fact concepts for it date back to the earliest days of rocketry—it represents a significant departure from the much more familiar chemical rockets seen on Saturn V, the Space Shuttle, Delta IV, the Falcon 9 and a slew of other impressive and photogenic displays of rocketry. The key reasoning for this departure is the main limitation of chemical rockets and also the reason they are so impressive, their size.

Chemical rockets need to be large, as they need to carry an enormous mass of fuel. This is a direct requirement of the notorious rocket equation.

$$M_i = M_f \exp\left(\frac{\Delta v}{I_{sp} g_0}\right). \tag{1.1}$$

This expression describes how heavy a rocket must initially be, M_i, to deliver a final payload mass, M_f, as a function of the change in velocity Δv required for the mission and the specific impulse of the rocket, I_{sp}.

The I_{sp} of a propulsion system is defined as the change in momentum that the system can achieve per unit weight of propellant. This metric is typically measured in seconds but can also be thought of in terms of the effective exhaust velocity of the propellant,

$$u_{ex} = I_{sp} g_0, \tag{1.2}$$

where g_0 is the gravitational acceleration at Earth's surface. Due to the exponential scaling in the rocket equation, the specific impulse has a pronounced effect on the amount of fuel required and the maximum velocity change or Δv that a spacecraft can achieve.

The theoretical maximum specific impulse for a chemical rocket is 450 s, using a hydrogen-oxygen reaction. However, many spacecraft use less optimum bi- and mono-propellants for simplicity and storability. This means that for a one-way trip from low earth orbit to the moon—$\Delta v \sim 1$ km/s, assuming an initial transfer orbit kick from the launch vehicle—, roughly 50 % of the initial spacecraft mass must consist of propellant [52]. Due to the relatively low specific impulse of chemical rockets, missions destined for high Δv targets, or missions that need to operate for long periods of time while performing station-keeping maneuvers, are required to carry a propellant load that is much more massive than the actual payload. This directly translates into dramatically higher launch costs due to the extra mass or—because launch vehicles are limited in the amount of mass they can carry into orbit—a propulsion system with a low I_{sp} constrains its payload to certain Δv missions even given an unlimited budget. Ultimately, chemical rockets can provide high thrust, but their low specific impulse translates to poor use of propellant mass for in-space propulsion.

Electric propulsion (EP) stands as a viable solution to the substantial propellant consumption inherent in chemical rockets. EP boasts exhaust velocities orders of magnitude higher than what is theoretically achievable for chemical systems, correlating with significantly higher I_{sp} [45]. The crux of this capability lies in the separation of propellant and power source. Unlike chemical systems that rely on the making and breaking of molecular bonds, EP supplies energy to the ionized propellant in the form of electrical energy from an external source (e.g. solar panels). This approach theoretically allows an uncapped amount of energy to be provided to each mass unit of propellant.

The commonly used analogy to illustrate the disparity between chemical and electric propulsion is the distinction between gas and electric vehicles. It suggests that chemical rockets are comparable to heavy diesel trucks—capable of carrying substantial loads and generating considerable power, but unfortunately lacking fuel efficiency. In contrast, electric propulsion systems are likened to small electric cars—swift and more "fuel" efficient. However, in my opinion, this analogy does not fully capture the essence of the distinction between chemical and electrical propulsion given that gasoline boasts a higher energy storage density than batteries, and electric cars often exhibit higher instantaneous power than their gas counterparts.

I find a better analogy is the difference between a fire truck and a drip irrigation system. Imagine a fire hose connected to a standalone fire engine. When the pump is activated, the fire hose unleashes a powerful continuous stream of water, projecting it with significant force. However, the water supply on the truck is finite and once the reservoir is depleted, the fire hose is useless unless the truck is refilled or connected to an additional water reservoir. The fire engine is capable of quickly providing this jet of water, which is exactly what is necessary

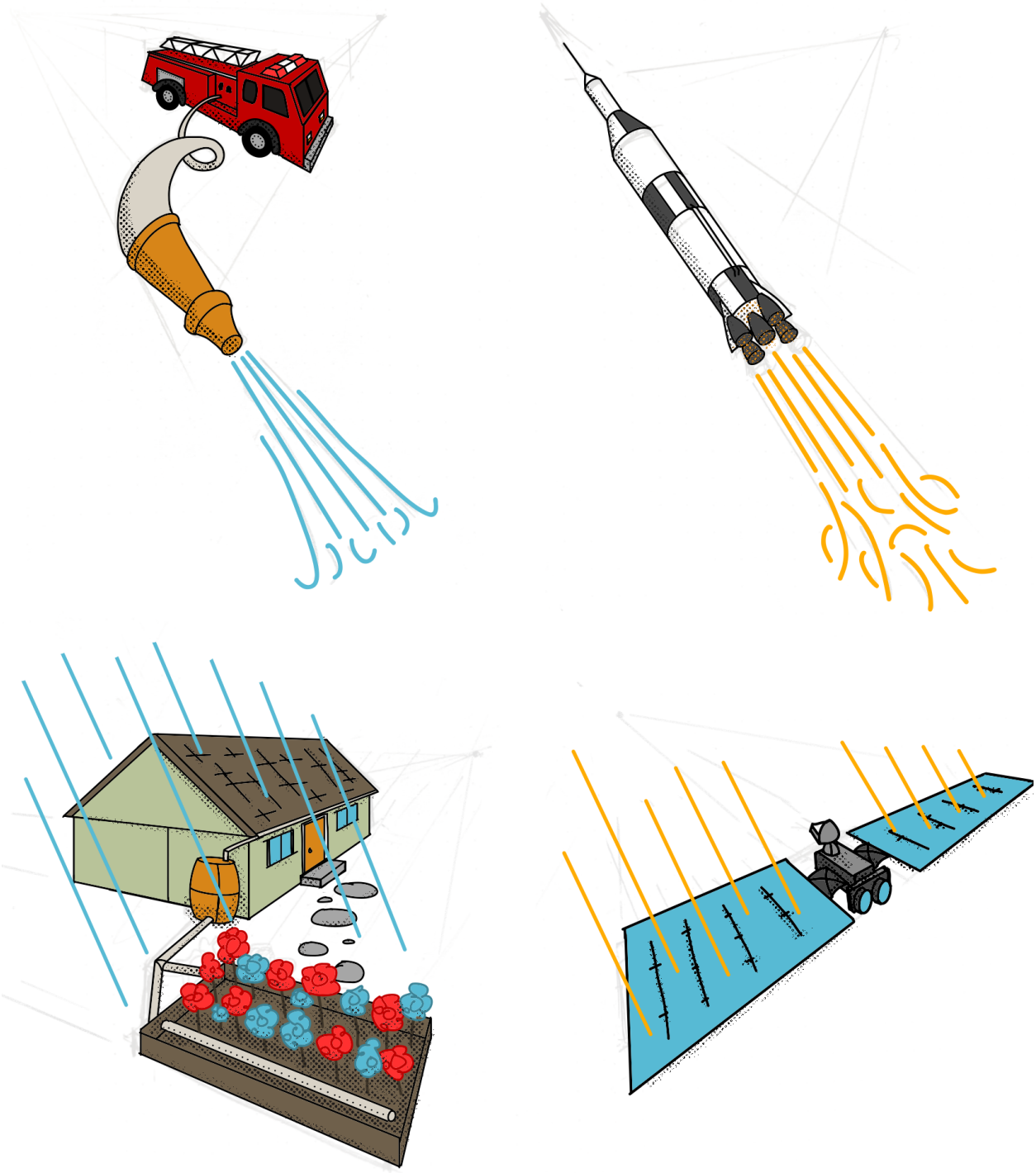

Figure 1.1: A hydrodynamic analogy for electric propulsion.

for certain jobs, such as putting out structural fires. Similarly, chemical rockets are the exact right tool for launching spacecraft into orbit, where high-power thrust is required for several minutes.

However, other jobs are not suitable for fire trucks. If one was, for instance, attempting to water their garden with a firetruck, they may run into some challenges. They would certainly accomplish their task quickly, however, they would consume a large volume of water and most would end up as runoff or evaporating into the air. For a task that is repeated or sustained, such as watering (or station keeping and orbit raising), we seek a more efficient system that is better suited to that task.

Now imagine a drip irrigation system strategically placed throughout the garden connected to a rain collection basin. Each drip emitter provides a slow and steady flow of water to nourish the plants consistently. The system operates continuously without the need for frequent refills and is able to efficiently use the available water. This is the niche of electric propulsion where efficient use of available resources over an extended period of time is necessary.

However, the material efficiency of electric propulsion is directly traded for low thrust and low power, just as it would be difficult to extinguish a house fire with a drip sprinkler. In this manner, the thrust-to-power ratio of a rocket is inversely proportional to the specific impulse

$$T/P = \frac{2\eta}{I_{sp} g_0}, \tag{1.3}$$

where T/P is the thrust-to-power ratio and η is the rocket efficiency. This expression directly shows that high thrust from an electric propulsion system requires increased power in addition to efficiency if high specific impulse is maintained.

For chemical rockets, the maximum specific impulse, the thrust, and the propulsive power are given by

$$I_{sp} = \frac{1}{g_0}\sqrt{2\eta\epsilon}, \tag{1.4}$$

$$T = \dot{m}\sqrt{2\eta\epsilon}, \tag{1.5}$$

$$P = \dot{m}\eta\epsilon, \tag{1.6}$$

where ϵ is the energy density of the chemical reaction in J / kg, $\eta \in [0, 1]$ is the efficiency of the reaction into directed jet power, and $\dot{m}$ is the propellant mass flow rate. These scaling relations show that an increase in thrust or power of a chemical system requires increasing

the mass flow rate. For reference, the Space Shuttle main engine, the RS-25, used hydrogen and oxygen as fuel and oxidizer ($\epsilon \sim 10$ MJ/kg) and had a flow rate of approximately 500 kg/s [74, 6]. Therefore, the power of this system is equivalent to roughly 5 GW, and this is the power required for an EP system to match that thrust at the same specific impulse. Generally speaking, this is far too much electrical power to generate on board a spacecraft, even for proposed near-term nuclear electric propulsion systems [60, 65]. Therefore, EP is restricted to significantly lower thrust levels than chemical systems. A consequence of this is that the reduced thrust typically increases travel times. This puts dramatically longer lifetime requirements on electric propulsion systems that often must operate continuously for tens of thousands of hours, as opposed to chemical rockets that operate for minutes with burn times equivalent to their specific impulses in seconds.

1.1.1 Scaling of Electric Propulsion Systems

The most well-characterized EP technologies are gridded ion thrusters (GITs), Hall thrusters (HTs), and resistojets and arcjets. These latter two systems operate electrothermally and exhibit lower specific impulses, while the former two systems operate electromagnetically and exhibit higher specific impulses [32]. As a result, GITs and HTs have been the prevailing EP technologies of study in recent years. Both these systems ionize their propellant gas to form a plasma, an electrically conductive state of matter that consists primarily of singly or multiply ionized nuclei surrounded by free dissociated electrons. Plasmas are characterized as being quasi-neutral in that their electron and ion density is regionally balanced by internal electric forces, and their motion is governed by long-range electromagnetic forces as opposed to local hydrodynamic forces such that the particle collision frequency is much slower than characteristic electromagnetic oscillations [12]. GITs and HTs both share the same electrostatic thrust mechanism[1] where ions are accelerated by an electric field. I show a sketch of a GIT in Fig. 1.2 to help explain the operation of these devices. The thrust of a GIT is produced by ions passing through the accelerating grids that are biased to a high voltage.

This voltage is then tied to specific impulse, thrust, and power through these scaling relations:

[1]Note, there is ongoing debate over the acceleration mechanism of Hall thrusters. Some researchers claim that they are electrostatic; others claim they are electromagnetic. I would say that they are magnetostatic, but this debate is largely semantics

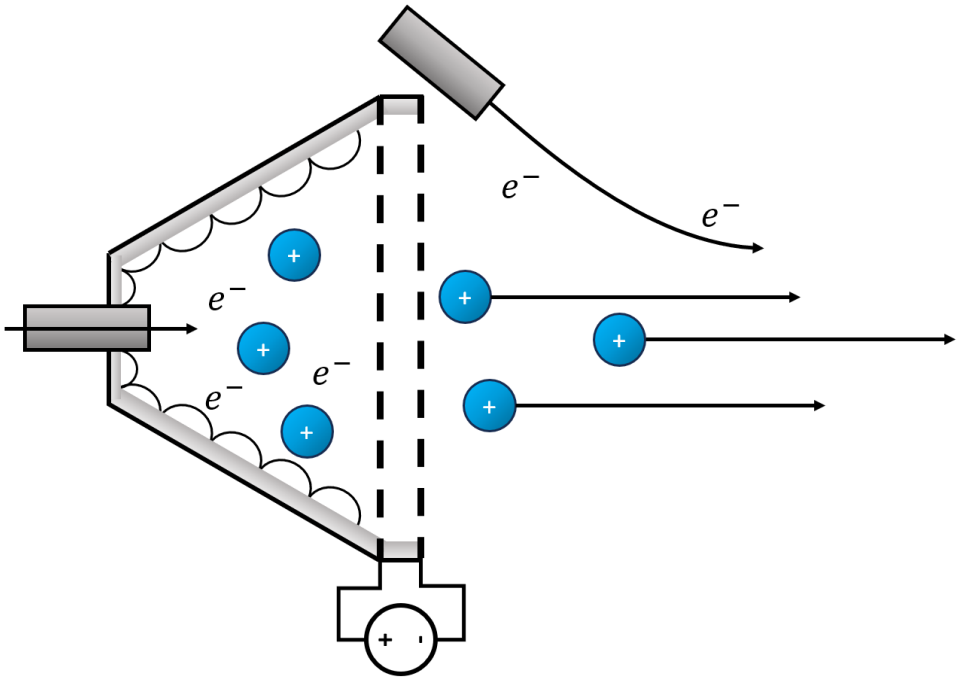

Figure 1.2: Illustration of a gridded ion thruster. Adapted from Ref. [27]

$$I_{sp}g_0 = u_{ex} \propto \sqrt{2qV/m}, \tag{1.7}$$

$$T \propto I\sqrt{2Vm/q}, \tag{1.8}$$

$$P = IV, \tag{1.9}$$

$$\eta = \frac{Tu_{ex}}{2P}, \tag{1.10}$$

where V is the applied voltage, q is the ion charge, m is the ion mass, and I is the ion current. Compared to Eqs. 1.4 - 1.6, this shows that the specific impulse now scales with the voltage and the thrust scales with the amount of current that is available for a given overall thruster power. In particular, Eq. 1.7 provides great flexibility in the choice of specific impulse to the point of becoming nearly unbounded. However, as shown by Eq. 1.3 this comes at a direct cost to thrust-to-power ratio, and indeed this limits thrust density as it is only feasible to operate EP systems up to certain power and thrust densities (based on thruster area).

The most straightforward example of this is the current density limit for gridded ion thrusters. Because these systems have a single positive ion charge species between their grids, they are susceptible to space-charge-limitations where the density of positive charges

shields the applied voltage and thus limit the maximum ion current, I, for a given grid voltage, V. This is dictated by the Child-Langmuir law

$$I = \frac{4}{9}\epsilon_0 \sqrt{\frac{2e}{m_i}} \frac{V^{3/2}}{d^2}, \tag{1.11}$$

where ϵ_0 is vacuum permittivity and d is the distance between the grids. Note, this space-charge limitation does not generally apply to all EP devices. However, there are similar, yet softer, limitations for power and thrust density for other technologies such as for Hall thrusters; however, many of these limits involve ongoing research.

1.1.2 Example Missions

Electric propulsion has showcased its versatility in various space applications, exemplified by missions such as NASA's Dawn spacecraft and the Lunar Gateway project, highlighting its effectiveness. The Dawn spacecraft utilized an gridded ion propulsion system during its mission to explore the proto-planets Vesta and Ceres in the asteroid belt. This innovative use of electric propulsion allowed Dawn to achieve an extended mission duration and, for the first time, enabled the exploration of multiple celestial bodies within a single mission [9].

In the context of future lunar exploration, the Gateway project, a key component of NASA's Artemis program, relies on electric propulsion for efficient and reliable transportation in lunar orbit. The seven Hall thrusters contained within Gateway's power and propulsion element represent the highest-power electric propulsion system on a spacecraft at 48 kW. The Gateway project underscores the crucial role of electric propulsion in supporting sustained human presence beyond Earth [39].

Furthermore, NASA's Psyche mission, aimed at exploring a metallic asteroid, represents another noteworthy application of electric propulsion. The spacecraft employs a solar electric propulsion system based on Hall thrusters for its deep space journey, enabling efficient orbital maneuvers and precise positioning around the target asteroid. Electric propulsion enhances the mission's overall flexibility and maneuverability in the complex environment of deep space [66].

Beyond planetary exploration, electric propulsion has been instrumental in the Starlink project, where SpaceX utilizes it to efficiently position and maintain a vast constellation of communication satellites in very low earth orbit (VLEO). This constellation marks a dramatic increase in the number of electric thrusters in space, signaling a shift toward Hall thrusters as the dominant electric propulsion device [99].

1.2 The Need to Expand the Operating Envelope

In light of these missions, it is evident that gridded ion and Hall thrusters have emerged as the workhorse plasma propulsion device, offering specific impulses on the order of 2000 s or higher with efficiencies exceeding 60% [32]. However, despite their proven track record, these devices have certain limitations, such as thrust and power density, throttleability, and reliance on rare noble gases as propellant. Overall, addressing these open needs will necessitate substantial changes in present electric propulsion systems and encourages the development of novel EP architectures.

1.2.1 High Power Density

High-power electric propulsion systems are crucial for ambitious missions beyond Earth, especially for Mars cargo, where efficiently transporting significant payloads is paramount. Most Hall thrusters have only been demonstrated up to power levels of tens of kilowatts, and current efforts are underway to scale them up to as much as 100 kW [35]. However, even this may not be suitable for electric propulsion for Mars missions, where thrusters operating in the multi-megawatt range running off miniature nuclear reactors may be required [60, 65].

Indeed, current squared thrust scaling may be critical for the development of high-power EP devices in the super-100 kW class, as thrusters that exhibit these traits can be significantly smaller than other EP systems for a given plasma current density [72]. HTs and GITs both exhibit linear thrust scaling with plasma currents, however GITs are more restricted based on space-charge-limits. I plot in Fig. 1.3 notional curves of the thruster jet power as a function of the diameter of the thruster for several technologies and current densities.

1.2.2 Alternative Propellants

In situ resource utilization (ISRU) missions pose a challenge for conventional EP systems from a material compatibility standpoint. For these missions propellants are extracted from the environment, such as from Earth's atmosphere in VLEO, lunar regolith, or the Martian atmosphere. These mission require compatibility with a variety of possible propellants for maximum mission flexibility. And indeed, the use of ISRU fuels can significantly enhance the scope of a given mission by allowing spacecraft to refuel mid mission with propellants found at their destination [31].

Furthermore, the use of shared fuel resources with chemical propulsion systems in dual-mode architectures [76] is also desirable. This reduces the fixed mass of the spacecraft by eliminating the need for extra tankage and flow systems. This integrated approach not

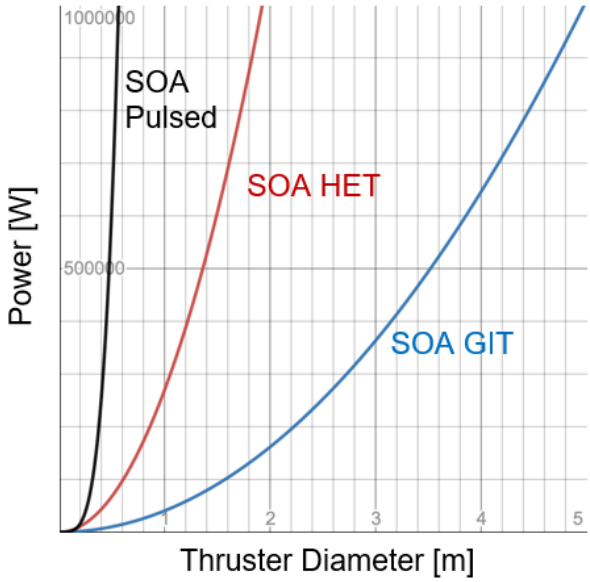

Figure 1.3: Power density scaling for various technologies.

only enhances mission adaptability but also contributes to overall spacecraft efficiency and resource utilization. Dual-mode systems allow for a spacecraft to posses the high thrust of a chemical system and the high specific impulse of an electric propulsion system while keeping system complexity and size at a minimum.

Accounting for both ISRU and dual-mode architectures, the propellants that EP systems are likely required to ingest in the future may include H2O, N2, O2, CO2, NH3, or hydrazine [72]. However these gases typically pose challenges in conventional electric propulsion thrusters and typically result in system failures after only minutes of operation.

The primary limitation for conventional EP systems often lies in the thermionic cathode (electron source) needed to neutralize the ion beam in GITs and HTs. These electrodes are highly susceptible to corrosion from the plasma, leading these systems to predominantly use inert noble gases as propellants. Noble gases, such as xenon, commonly used in electric propulsion, have low storage density and have become increasingly expensive, surpassing 200 $/L in 2022 [19].

To produce the large electron currents required (1-100 A), the cathode surfaces must reach temperatures around 2000 K. Even for robust thermionic emitters, the presence of reactive gases (beyond trace impurities) at these temperatures quickly causes deterioration of the surface and the emission current [25]. Recent work on radio-frequency plasma cathodes has shown moderate success in addressing the challenges posed by reactive propellants [26]. However, their current efficiency in terms of amps per watt remains impractical for high-current cathodes [20].

1.2.3 Throttling without Consequence

Hall and gridded ion thrusters are often constrained to narrow operating set-points to ensure efficient operation. This results in mission planing limitations as the thrust and specific impulse of the propulsion system may not be able to suitably address the needs of a given mission as they change.

These constraints can be significant for interplanetary satellites, where solar energy availability can vary significantly. A system with a highly throttleable thrust permits the spacecraft to take advantage of all available power at any given time without compromising efficiency. In Earth orbit, high throttleability proves crucial for satellites, too, as the thruster can operate in a high-thrust burst for quasi-impulsive maneuvers to avoid orbital debris or in a low-power mode for station keeping and orbit raising.

While achieving this flexibility is possible with two separate propulsion systems—one chemical for impulsive maneuvers and one electric for routine station keeping—the inclusion of multiple thruster types increases mission complexity and associated risks. The implementation of a single propulsion system capable of both high and low thrust modes offers greater versatility and simplifies mission planning and execution.

1.3 The Need for a New Technology

Inductive pulsed plasma thrusters (IPPTs) are an advanced EP concept that aims to address some of the unaddressed problems for future electric propulsion systems. Importantly, they offer several distinct advantages over other conventional electric propulsion architectures. These key traits are their high power scaling feasibility, their tolerance to reactive propellants, and their suitability for multi-mode propulsion concepts.

Generally speaking, IPPTs operate via Faraday's law of induction:

$$\mathcal{E} = -\frac{d\Phi}{dt}, \tag{1.12}$$

where $\mathcal{E}$ is the electromotive force (EMF), $d\Phi/dt$ is the time rate of change of the magnetic flux. IPPTs leverage this expression to produce an EMF in a plasma by discharging large primary coil currents, thus producing a transient magnetic flux from the coil. The EMF in the plasma drives electron "mirror" currents that oppose the flux of the primary coil. In this way, an IPPT acts akin to an isolation transformer where power is transferred "wirelessly" and the thruster is galvanically isolated from the plasma.

The electron mirror current is then accelerated by magnetic repulsion to the primary coil or optionally through an additional applied-field Lorentz force. The accelerated electrons

then accelerate the heavy momentum-carrying ion species as internal electric fields work to maintain qausi neutrality in the plasma. This process produces a discrete plasma impulse, and can be repeated (often 100's to 1000's of times per second) to produce a steady thrust.

This magnetic acceleration mechanism allows the thrust in IPPTs to scale with the square of the coil current. This is because the coil and the plasma act as two opposing magnets where the force is dependent on the square of the magnetic field

$$F \propto \frac{B^2}{2\mu_0}, \tag{1.13}$$

where the B is the magnetic field, μ_0 is the magnetic vacuum permeability, and the proportionality depends on the geometry of the system [2]. The magnetic field is produced by currents both in the coil and in the plasma, and since the current in the plasma is directly influenced by the coil current, this implies that the force (thrust) for an IPPT scales with the square of the coil current.

This relationship implies that IPPTs share a scaling law with self-field magnetoplasmadynamic thrusters (MPDTs) [14] and pulsed plasma thrusters (PPTs). However, in these latter two systems, the discharge current runs partially through the plasma and partially through the thruster; in IPPTs these current loops are isolated.

This I^2 scaling relation, means that IPPTs are potentially capable of achieving very high power densities. Additionally, because IPPTs exhibit no fundamental limits on plasma current density, this allows for up to MW-level powers in devices 10's of cm in diameter [87], this can yield potential specific powers as low as 0.05 kg/kW as compared to Hall thrusters at approximately 2 kg/kW [46].

Furthermore, because IPPTs do not necessitate the use of plasma wetted electrodes they avoid the problem of alternative propellants and provide increased propellant versatility over other electric propulsion concepts.

The final major advantage of inductive thrusters is their operation in a pulsed mode, allowing for easy throttling of thrust and total power by adjusting only the pulse repetition rate. This feature facilitates variable performance, enabling a seamless transition between high and low thrust while maintaining a constant efficiency optimized for a single pulse.

In light of these advantages, IPPTs are a uniquely attractive emerging high-power electric propulsion concept. These traits indicate that they are a promising improvement over current state-of-the-art electric thrusters to address the future needs of EP systems.

1.4 Summary

In conclusion, this examination of propulsion systems highlights the inherent challenges of traditional chemical rockets, primarily rooted in their substantial propellant mass requirements, as evidenced by the constraints posed by the rocket equation. A shift towards electric propulsion emerges as a pragmatic solution, emphasizing the fuel efficiency gained through the separation of propellant and power source. In this way, chemical rockets are the tool of choice for launch vehicles; however, electric thrusters align with missions that demand consistent and targeted use of resources. Specific electric propulsion technologies, exemplified by gridded ion thrusters and Hall thrusters in notable space missions, showcase the practicality and success of EP in diverse applications. However, there are notable challenges for future of EP technology. I introduce inductive pulsed plasma thrusters which are suited to address many of these issues. Particularly, IPPTs exhibit high-power scaling feasibility, tolerance to reactive propellants, and high throttleability. This commentary should serve as a preface to the field of electric propulsion, delineate the use cases between chemical rockets and electric thrusters, and introduce the advantages of IPPTs. In the following chapter I elaborate further on IPPTs and give examples of the traits of specific thruster systems.

CHAPTER 2

Background

2.1 Introduction

This chapter presents the historical development of inductive pulsed plasma thrusters (IPPTs), providing a foundational understanding of their evolution and limitations. The overview places IPPTs within the context of electric propulsion and describes the operation of different thruster architectures within the IPPT family. This information is important for understanding the subsequent sections of this work. Additionally, the chapter outlines the milestones and challenges encountered during the development of IPPTs. These challenges highlight the need for innovation to overcome inherent limitations of conventional IPPTs and have led to a detailed exploration of the rotating magnetic field (RMF) thruster. RMF thrusters, while existing within the IPPT family, demonstrate differing scaling relations to conventional IPPTs. As a result, RMF thrusters have the potential to overcome these constraints and are a promising option for next-generation electric propulsion systems, making them the central focus of this dissertation. To conclude the chapter, a comprehensive account of the history of RMF plasma devices, with a specific emphasis on RMF thrusters, is provided. Through this examination, the rationale behind the development of the RMF thruster is explained, while also highlighting current gaps in scientific understanding and how these questions will be addressed in the following chapters.

2.2 IPPT Thruster Method of Operation

In this section, I will discuss different types of IPPTs and explain how they operate. Polzin et al. provide a extensive review of IPPT systems in Ref. [72], but what follows here are abridged descriptions of several propulsion concepts to motivate the development of the RMF thruster.

To start, I will simplify things by focusing on pulsed plasma thrusters (PPTs) and remove

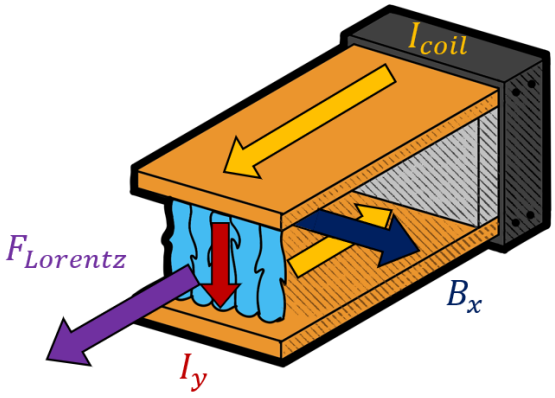

Figure 2.1: Notional illustration of a pulsed plasma thruster.

the "inductive" aspect. Figure 2.1 shows an illustration of a PPT, which will help explain the underlying principles. A PPT generates thrust by passing a large current through a plasma along a pair of conducting rails. The plasma is usually either ablated from a solid propellant block, such as PTFE, located at the back of the device from an initial current arc [15], or ignited from a gaseous propellant [100]. As the current flows through the newly formed plasma, it creates an internal magnetic field that is perpendicular to the device's axis. This magnetic field interacts with the current in the plasma, resulting in a Lorentz force that propels the plasma forward along the rails and out of the device, similar to a solid-mass rail gun. The force can be expressed as

$$F = I(\vec{l} \times \vec{B}). \tag{2.1}$$

Here, I represents the conducted current, $\vec{l}$ is the vector length of conduction along the plasma, and $\vec{B}$ is the magnetic field vector along the plasma. Since the magnetic field $\vec{B}$ is generated by the current in the loop, the force is proportional to the square of the driven current. Therefore, it is beneficial to pass the highest current possible. However, achieving these high currents often requires pulsing to maintain low average system power. In fact, PPTs are commonly used for propulsion in small low-power satellites.

The method of force transfer in self-field magnetoplasmadyanic thrusters (MPDTs) is the same as in pulsed plasma thrusters (PPTs). However, there are some key distinctions. MPDTs utilize gaseous propellants, have a cylindrical shape, and are specifically designed for high-power operation (>100 kW). Furthermore, MPDTs can be fired continuously because

they do not need to vaporize propellant in discrete bursts. However, the fundamental design principles and scaling relationships for MPDTs are mostly similar to those for PPTs.

Both thruster types, PPTs and MPDTs, are closely related to IPPTs. The reason for including "induction" is due to the fact that these thrusters require high current (>100 A) electrodes, which can limit their lifespan [15, 67, 58]. The negative cathode, in particular, is susceptible to erosion and material sputtering caused by the bombardment of positive ions over time[1]. In order to overcome this issue, IPPTs utilize induction to generate high currents in the plasma without any physical contact between the thruster conductors and the plasma. Thus, the possibility of electrode wear is eliminated. As explained in the previous chapter, IPPTs still exhibit a thrust scaling proportional to the square of the current (I^2). However, in IPPTs, this coupling occurs through the mutual inductance between the plasma and the conductors in the thruster. This characteristic sets IPPTs apart from PPTs and MPDTs because it addresses a limitation in their operation. Because of this aspect, IPPTs are considered a promising option for next-generation high-power electric propulsion. In terms of background, various types of inductive thrusters have been studied, with extensive research conducted on theta pinch thrusters, pulsed inductive thrusters, and rotating magnetic field thrusters.

2.2.1 Theta Pinch Thrusters

Theta pinch thrusters operate similarly to the fusion devices that bear the same name. In the fusion device, a circular coil that surrounds a plasma is rapidly energized to create an axial magnetic field. Consequently, the plasma generates a current to counteract the coil field in accordance with Lenz's law. The opposing currents repel each other, causing the plasma to compress radially inward. Theta pinch thrusters deviate from the symmetry of fusion devices by employing a conical primary coil instead of a cylindrical or toroidal one. This coil configuration produces a radial magnetic field component that exerts an axial force on the plasma current. This setup can also be understood as the asymmetric compression of the plasma, effectively expelling it from the open end of the thruster. Figure 2.2 depicts an illustration of the operation of a theta pinch thruster and a representative picture of a physical device.

Notable experimentation with these devices demonstrated specific impulses of approximately 2500 s [49], and later work achieved 1 mN-s impulse at 3 % efficiency [71].

[1]To this point, vacuum arc thrusters are an off-shoot technology that relies on the ablated electrode material to serve as the propellant.

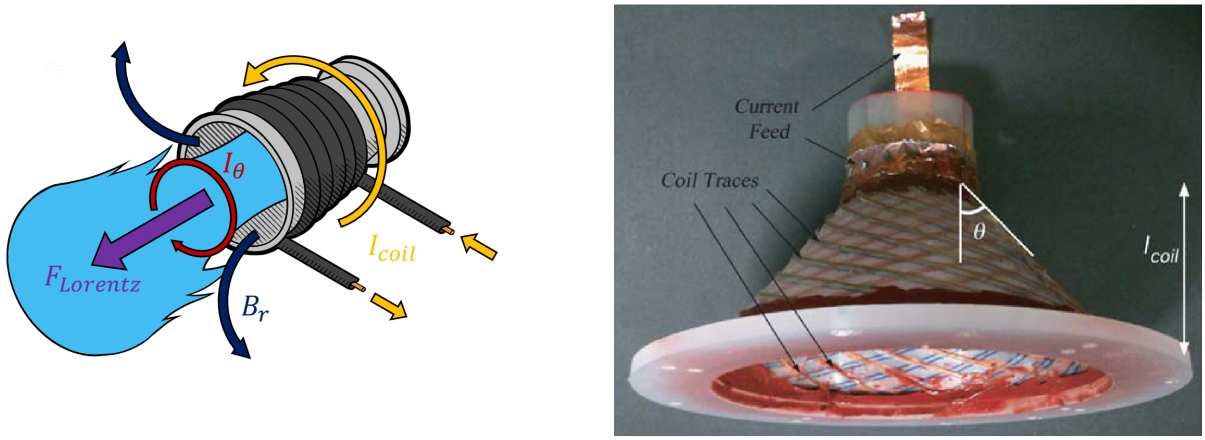

(a) Illustration of theta pinch thruster.

(b) CTP thruster from Ref. [71].

Figure 2.2: Overview of theta pinch thrusters.

2.2.2 Pulsed Inductive Thrusters

Pulsed inductive thrusters (PITs) and theta pinch thrusters are related in terms of coil angle. The coil angle is an important parameter for theta pinch thrusters as it determines the compression-to-axial-acceleration ratio. PIT thrusters incorporate a flat spiral coil with a 90-degree angle, which maximizes plasma acceleration without compression. As a result, these thrusters are typically more efficient. In PITs, the plasma current sheet is accelerated directly away from the flat primary coil, acting as two opposing magnets. However, a drawback of this configuration is decreased mass utilization[2]. Because PITs do not have walls, some propellant can be wasted from the sides. To address this issue, many PIT iterations incorporate downstream propellant injectors to carefully distribute neutral gas across the flat coil. I show in Fig. 2.3 an illustration of the PIT configuration and two representative thruster systems.

Extensive testing has been conducted on PITs and, to the best of my knowledge, they have demonstrated the highest performance among IPPTs to date. These thrusters achieved an optimum performance of 7000 s specific impulse with an efficiency of 50% [62, 68, 72]. Notably, ammonia gas (NH_3) was chosen as the propellant for this experiment. Ammonia is an uncommon choice for electric propulsion, but it outperformed more commonly used propellants such as hydrogen, helium, and argon in PIT testing. This is attributed to a reduction in collisional excitation radiation in ammonia, which is a significant loss mechanism for high density pulsed thrusters [68]. Instead, it is likely that electron-ion collisions in

[2]Note, conical theta pinch thrusters might also suffer from low mass utilization due to centerline gas density becoming inaccessible to the azimuthal electron current as a result of the field-reversed configuration FRC plasmas that form in these devices (See Sec. 3.2.2 for more explanation of FRCs).

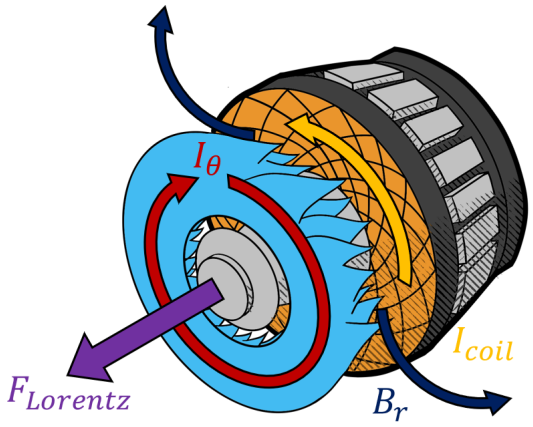

(a) Illustration of pulsed inductive thruster

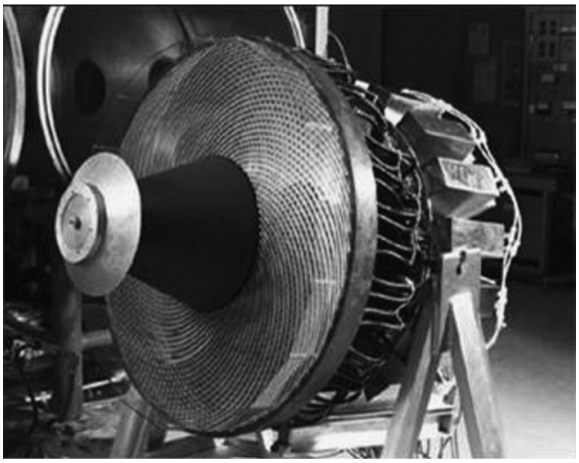

(b) PIT mkV from Ref. [68].

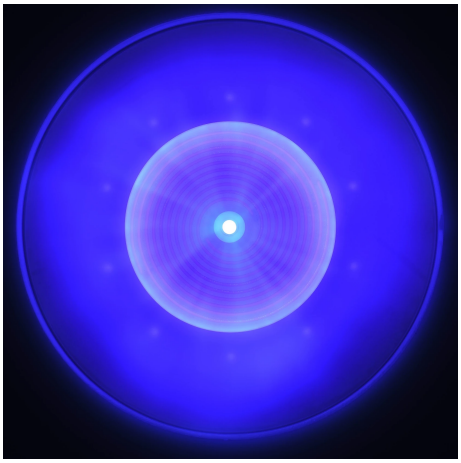

(c) HiPeR-PIT from Ref. [73].

Figure 2.3: Overview of pulsed inductive thrusters.

ammonia result in increased rotational and vibrational states or dissociation, which may be less energetically costly than excitation radiation. Despite the demonstrated performance and existing body of work on PITs, there are still some issues with their operation. One major issue is the high voltages (30-60 kV) required for efficient operation. This can be seen through the current drive scaling relation for PITs

$$I_\theta(t) = -\frac{\int_0^t V_{\text{coil}} d\tau}{\mu_0 \kappa_g}, \tag{2.2}$$

where t is time, τ is a constant of integration, V_{coil} is the primary coil voltage, μ_0 is vacuum permeability, and κ_g is a geometric factor. For PITs to drive the large azimuthal currents for Lorentz force thrust, they directly require large coil voltages. Because of these high voltage

pulses, PITs also experience difficulty in timing the onset and rise of coil currents to match the injected gas which often necessities precise pulsed gas injection valves. Ultimately, these two factors have limited the adoption of PITs for flight applications.

2.2.3 Rotating Magnetic Field Thrusters

The Rotating Magnetic Field (RMF) thruster is a promising advancement from the conventional IPPTs mentioned above. Unlike conventional IPPTs, the RMF scheme reduces the demands on drive circuitry. This is because the induced currents in the plasma are proportional to the frequency of a rotating field rather than its magnitude. This unique feature allows RMF thrusters to operate without the historically required high voltages of PITs. By reducing the stress on the driving circuit, RMF thrusters can achieve higher duty cycles or even operate continuously at 100 % duty cycle. In this mode, the plasma currents are constantly driven, resulting in steady thrust. And importantly, the need for critical timings of pulsed currents and puffed gas valves is eliminated, and thus may lead to higher mass utilization efficiency [72].

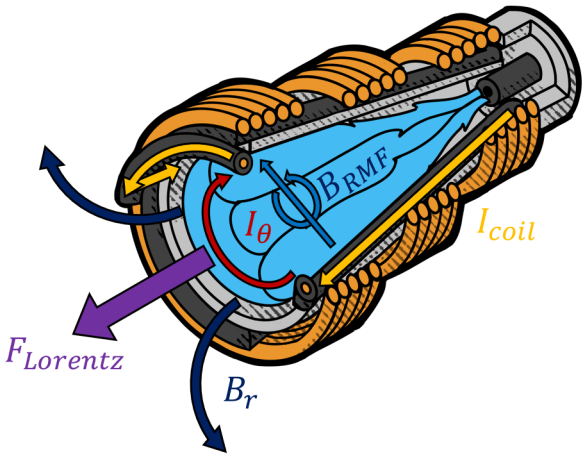

Figure 2.4: Illustration of RMF thruster principles of operation.

Fig. 2.4 illustrates the standard configuration and operating principle of an RMF thruster. In this device, a plasma with a low ionization fraction is introduced into the thruster from a seed cathode or pre-ionizer. The resulting ionized particles are confined by a mainly longitudinal magnetic field created by a series of concentric bias magnets. The RMF antennas are then activated in a controlled sequence to generate an approximately uniform transverse

magnetic field that rotates around the primary axis of the thruster, which is referred to as the rotating magnetic field (RMF). The RMF is triggered at a frequency that is sufficiently high, surpassing the ion gyrotron frequency, to selectively capture the electrons in the seed plasma. These captured electrons move at the frequency of the RMF, causing further ionization of the propellant and the formation of an cohesive azimuthal current in relation to the background ions. When the amplitude of the RMF is strong enough, the azimuthal current is independent of the magnitude of the primary coil current [47]:

$$I_\theta = \frac{eN_e\omega}{2\pi}, \tag{2.3}$$

where N_e is the total number of electrons and ω is the RMF frequency. As this scaling shows, in principle, the current driven in RMF thrusters is only a function of the total number of free electrons and the frequency of the RMF. This is in contrast to conventional IPPTs where the induced current is based on the rapid discharge of high-amplitude voltages as shown in Eq. 2.2. The reduction in the required voltages for the RMF significantly reduces the stress on the driving circuitry which better favors scaling to higher powers and duty cycles.

The Lorentz force, generated by the interaction between the applied bias field and the time-varying magnetic fields induced by the azimuthal electron current, accelerates the ring of induced azimuthal electron current in the thruster [81]. This force is counterbalanced by the ambipolar electric field, which is created by the charge separation with the ions. The ions are subsequently accelerated, determining the thrust and exhaust velocity of the device. This process results in a thrust

$$T \propto f_{rep} \int_0^{1/f_{rep}} I_\theta \langle B_r \rangle dt, \tag{2.4}$$

where f_{rep} is the pulse repetition rate, and $\langle B_r \rangle$ is a spatially averaged magnetic field arising from both the applied field and the self-field. The generation of impulse shots can be repeated in a pulsed manner, or the RMF can be continuously active to deliver steady-state thrust.

The orientation of the coils in RMF thrusters distinguishes them from other IPPTs. Theta pinch thrusters and PITs have a single primary coil aligned with the thrust axis, allowing direct coupling of the plasma for thrust generation. On the other hand, RMF thrusters have coils oriented perpendicular to the thrust axis, resulting in indirect plasma propulsion. This change in orientation effectively separates the RMF coil currents from the plasma currents, enabling thrust to scale with frequency rather than coil current or voltage. However, this decoupling limits the effectiveness of I^2 thrust scaling. Conventional IPPTs exert a thrust force on the plasma,

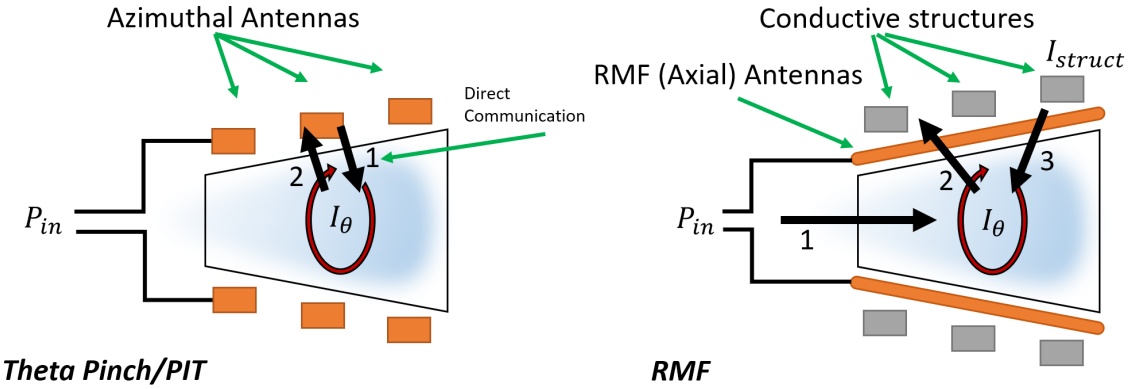

Figure 2.5: Power flow for I^2 thrust scaling in PIT/Theta pinch and RMF thrusters.

$$T = kI^2 \frac{\partial}{\partial z} M, \tag{2.5}$$

where I is the coil current, k is a coupling coefficient, and M denotes the mutual inductance between the coil and the plasma [70] The mutual inductance depends on the inductances of the coil and the plasma, as well as the coupling coefficient $0 \leq k \leq 1$. The sub-unity coupling factor makes I^2 scaling slightly less effective for IPPTs compared to PPTs. In contrast, RMF thrusters lack this mutual inductance and coupling between the primary coils and the plasma due to the orientation change. Instead, magnetic coupling occurs between the plasma and surrounding conductive structures, often called flux conservers [95]. To achieve "squared" acceleration of the plasma, the RMF must first induce an azimuthal current in the plasma, which then generates tertiary currents in the flux conservers to produce a repulsive force. Figure 2.5 illustrates this conceptual difference in the energy flow for RMF thrusters. This approach is even less efficient in terms of I^2 thrust scaling than other IPPTs due to resistive losses in both the primary antennas and the conductive flux conservers [80]. Consequently, RMF thrusters often rely on the applied bias field to drive most of the Lorentz force interaction. In this way, RMF thrusters resemble an inductive version of applied field magnetoplasmadynamic thrusters (AF-MPDT).

2.3 Timeline of RMF Research

The unique plasma current drive mechanism of the RMF has motivated investigation by several research groups over the past several decades. In this section, I provide an overview of these endeavors and highlight the progress made in advancing this technology. I show

images of several of these thruster in Fig. 2.6.

RMF plasma technology, like theta pinch thrusters, was initially considered as a potential option for controlled fusion technology. This is because an RMF has the ability to generate stable and compact plasmoids that are magnetically confined. In fact, this concept is the basis for at least one modern commercial fusion project [86]. The first papers on this concept were published by Blevin and Thonemann in the 1960's. They developed a significant part of the theoretical framework for RMF current drive in a plasma and experimentally verified their theories using a benchtop RMF system [7]. In the early 1980's, Hugass and Jones published a series of papers further improving the theory behind this concept. They also performed numerical simulations to study the transient response of the plasma to the RMF.

Work on RMF thrusters began in the late 2000's, with Mathematical Sciences Northwest (MSNW) and the University of Washington generating some of the first thruster performance metrics. With the Electrodeless Lorentz Force (ELF) thruster, they demonstrated distinct plasmoid ejection and inferred specific impulses from 450 to 6000 s on nitrogen. This resulted in impulses per shot of 1.0 mN-s at a maximum efficiency of 8 % [87, 95]. With the Electromagnetic Plasmoid Thruster (EMPT) they showed steady operation at 1 kW and high pulse repetition rates at frequencies up to 2800 Hz for 50 pulses [48, 93].

More recently, a group at the Tokyo University of Agriculture and Technology (TUAT) has developed a fully RF discharge thruster and measured current densities induced by their RMF on the order of 10 mA/cm^2 [21, 22]. TUAT ran their RMF test article semi-continuously at 1 kW on argon and achieved an inferred efficiency of 1 %.

Several other groups have also explored RMF thrusters in recent years. Shinohara et al, constructed an RMF thruster model as an acceleration stage for a helicon source [85]. Following this, Sun et al. conducted an RMF experiment demonstrating high-density plasma generation from an RMF [90]. Additionally, Liu et al. tested an RMF thruster on argon, nitrogen, and xenon, measured the density of the ion plume, and reported a generous efficiency estimate of 10 % [56]. These works do not provide sufficient results to evaluate the performance of these devices; however, they indicate ongoing interest in the technology.

Despite variations in how these systems were built and their size, the thrust performance of RMF was found to be quite poor, with efficiencies of approximately 1%. The highest reported efficiency so far was 8%, achieved by MSNW. However, this value might be an overestimate since it did not take into account the typical losses caused by divergence or antenna coupling. These findings highlight the early stage of development of this technology, considering that the maximum predicted efficiency of RMF thrusters can reach as high as 85% with optimal RMF current drive, as suggested by Slough [87]. It is worth noting that the demonstrated performance of RMF thrusters still falls significantly short of the performance

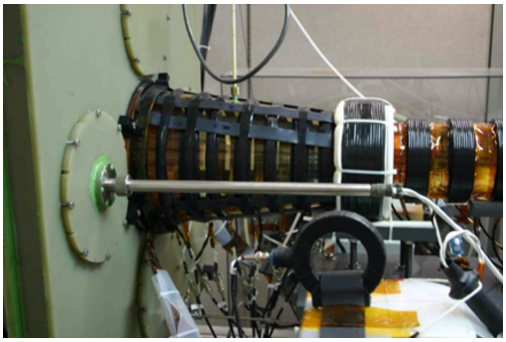

(a) ELF thruster from Ref. [95].

(b) EPEP thruster from Ref. [56].

Figure 2.6: Representative RMF thruster experiments.

metrics achieved by PITs.

The cause of the difference between the expected and observed performance of RMF thrusters is still unknown, and various theories have been proposed to explain it. According to Polzin et al. [72] and Weber et al. [95], the high densities in these devices could result in significant radiative losses, which would consume a substantial amount of energy. Brackbill et al. [8] suggest, based on their computational modeling work, that RMF thrusters are limited by a low ionization fraction. Furthermore, Koo et al. [50] demonstrated that plasma instabilities can easily develop and impede performance by increasing resistivity. Despite these theories, there has been no direct experimental investigation into these losses. Most test articles have not been operated in a sufficiently representative space environment, and in many cases, only limited measurements of the plume have been conducted. Given these unanswered questions and the lack of experimental data, it is necessary to identify and characterize the relevant physical phenomena that contribute to the low efficiency and overall performance of RMF thrusters. Furthermore, there are aspects of their operation that are not well understood, such as their performance in representative environments and how they might scale to higher power levels. Addressing these questions, among others, is crucial for improving and demonstrating the full capabilities of RMF thrusters.

2.4 Research Questions

The aim of this thesis is to address several unanswered questions regarding the operation, performance, scaling, and efficiency of RMF thrusters. To achieve this, I will comprehensively evaluate the performance of representative state-of-the-art RMF thruster prototypes, aiming to identify the limiting physical mechanisms while distinguishing them from engineering suboptimalities and implementations. To accomplish this, I will utilize conventional

phenomenological efficiency models as a framework [53, 41, 54], which will be informed by measurements obtained through both near and far-field plasma diagnostics. By directly measuring the contributions of various efficiency losses in RMF thrusters, I will seek to answer the following specific questions throughout the subsequent chapters:

1. What are the main drivers of the efficiency loss in RMF thrusters?
2. Can we use physical insights to guide designs for improved thruster performance?
3. Can we combine experimental measurements and first-principles analysis to explain the efficiency losses and infer the maximum theoretical performance?

To address these questions, the remaining chapters of the thesis are structured as follows: Chapter 3: A basic theory of the current drive of RMF thrusters will be presented and the phenomenological efficiency model referenced throughout the thesis will be derived and explained. Chapter 4: I describe the construction and implementation of three RMF thruster prototypes built at the University of Michigan. Additionally, an overview of their performance characteristics, including thrust, specific impulse, and efficiency scaling, will be provided. Chapter 5: I describe the experimental diagnostics and methods used to inform the efficiency model and obtain detailed plasma characteristics. Chapter 6: The results of the RMFv2 thruster experiments, which characterized its performance and efficiency losses, will be presented. Chapter 7: The results of the RMFv3 experiment, in which performance changes between pulsed and continuous wave modes for RMF thrusters are analyzed, will be presented. Chapter 8: A performance model for RMF thrusters, informed by the experimental work, will be derived to make predictions for RMF thruster efficiency and identify key parameters to improve their performance. Chapter 9: The thesis will conclude with closing thoughts on avenues for additional research and the future of RMF thruster technology.

CHAPTER 3

Rotating Magnetic Field Thruster Theory

3.1 Introduction

The force transfer mechanism of the rotating magnetic field (RMF) thruster is unconventional compared to other electro- and magneto-static accelerators like Hall and gridded ion thrusters. Even among inductive thrusters, the RMF thruster stands out with its unique mechanism for inducing electron currents within the plasma. This current drive mechanism sets RMF thrusters apart from other EP technologies and makes them an intriguing subject for ongoing research.

In this chapter, I provide an overview of the operating principles of the RMF thruster as a necessary foundation for the experiments discussed later. I explain how the azimuthal electron currents in the thruster are formed according to Faraday's law. While a simplified theoretical model suggests a specific current pattern, practical considerations introduce complexities that require a more comprehensive understanding of the required RMF field strength. This section draws heavily on Sercel's work from Ref. [78] on RMF thruster current drive; however, I present an alternative interpretation based on different underlying assumptions that better highlight the physics I aim to emphasize in this study.

With this understanding of RMF thruster operation, I introduce an efficiency model for these thrusters. This model offers a framework for evaluating thruster performance from the perspective of several distinct physically relevant modes. Using this model, I can analyze the mass, momentum, and energy exchange within the RMF thruster and assess the main factors contributing to the low efficiency typically observed in these devices.

3.2 RMF Thruster Principle of Operation

As mentioned in the preceding chapter, the total force generated by an RMF thruster is primarily influenced by the azimuthal current generated by the electrons that are entrained

to the spokes of the RMF. In this section, I will present a descriptive model to explain the mechanism through which the RMF drives the azimuthal electron drifts, how this current interacts with the radial magnetic field to produce thrust, and how perfromance is expected to scale for RMF thrusters.

3.2.1 RMF Current Drive

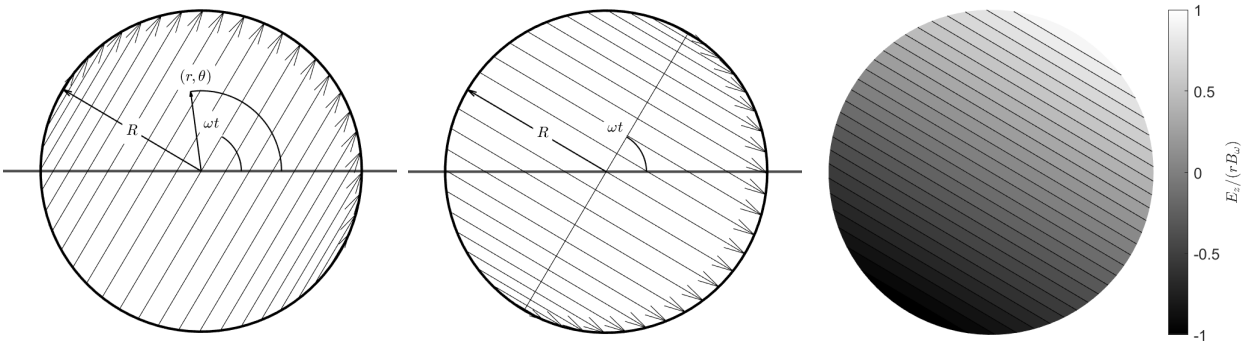

(a) $\vec{B}_\omega$ (b) $-\partial\vec{B}/\partial t$ (c) E_z

Figure 3.1: Coordinate system and fields for RMF current drive. (a) RMF vector field, (b) curl of electric field, (c) distribution of axial electric field for an infinitely long cylinder.

In general, the total magnetic field applied to the thruster has the form

$$\vec{B} = \{B_\omega \cos(\omega t - \theta) + B_{r,0}\}\hat{r} + B_\omega \sin(\omega t - \theta)\hat{\theta} + B_{z,0}\hat{z}, \tag{3.1}$$

where the RMF is produced in the radial and azimuthal directions and rotates at an angular frequency ω. B_ω is the amplitude of the RMF, and $B_{r,0}$ and $B_{z,0}$ are the static components of the radial and axial magnetic fields respectively. In this context, "static" refers to changes that occur slowly on the time scale of the RMF (1-2 μs). However, it is important to note that these fields can undergo significant changes over longer time scales on the order of pulse durations (100-1000 μs). Figure 3.1a illustrates the shape of a uniform RMF—without static radial or axial fields—for reference. Faraday's law of induction explains the generation of electric fields by time-varying magnetic fields. This can be expressed in derivative form for the applied RMF, as shown in Equation 3.1 as:

$$\nabla \times \vec{E} = -\frac{\partial \vec{B}}{\partial t} = \omega B_\omega \sin(\omega t - \theta)\hat{r} - \omega B_\omega \cos(\omega t - \theta)\hat{\theta}. \tag{3.2}$$

I show in 3.1b the shape of the curl of the electric field which is identical to the shape of RMF field with a phase lag of $\pi/2$. The curl of electric field in cylindrical coordinates is

$$\nabla \times \vec{E} = \left(\frac{1}{r}\frac{\partial E_z}{\partial \theta} - \frac{\partial E_\theta}{\partial z}\right)\hat{r} + \left(\frac{\partial E_r}{\partial z} - \frac{\partial E_z}{\partial r}\right)\hat{\theta} + \frac{1}{r}\left(\frac{\partial\left(rE_\theta\right)}{\partial r} - \frac{\partial E_r}{\partial \theta}\right)\hat{\mathbf{z}} \tag{3.3}$$

If I make the assumption that axial gradients are much weaker than radial or azimuthal gradients (essentially assuming the geometry is infinitely long), I can reduce this equation into a pair of expressions:

$$\frac{1}{r}\frac{\partial E_z}{\partial \theta} = \omega B_\omega \sin(\omega t - \theta), \tag{3.4}$$

$$\frac{\partial E_z}{\partial r} = \omega B_\omega \cos(\omega t - \theta). \tag{3.5}$$

These equations permit the evaluation of the axial electric field produced by the RMF,

$$E_z = \omega r B_\omega cos(\omega t - \theta), \tag{3.6}$$

and I show in Fig. 3.1c its distribution. The derivation presented here demonstrates that the RMF generates an oscillating electric field inside the thruster. This oscillating field drives corresponding axial electron currents which have a dual effect of heating the plasma and interacting with the radial component of the RMF to generate an azimuthal Lorentz force. This phenomenon can be understood by considering a generalized ohm's law for the electrons

$$0 = -en_e\left(\vec{E} + \vec{u} \times \vec{B}\right) - \nabla p_e - m_e n_e \nu_{ei}(\vec{u} - \vec{u_i}), \tag{3.7}$$

where e is he elementary electron charge, n_e is the electron density, $\vec{u}$ is the electron velocity, p_e is the electron thermal pressure, m_e is the electron mass, ν_{ei} is the electron ion collision frequency, and $\vec{u_i}$ is the ion velocity. Moving forward, I will make the following simplifying assumptions:

1. Pressure forces will be neglected: while thermal pressure is important to explain the operation of contemporary RMF thrusters, its significance is undesirable for their operation. Therefore I will disregard it in this idealized descriptive model.

2. Ion motion will be neglected: ion motion in the azimuthal direction is solely influenced by electron-ion collisions. However, at the energies and densities that are relevant, these collisions are unable to significantly affect the momentum of the ions in these directions.

3. Neutral collisions will be neglected: this assumes complete ionization which is justified by the experimental measurements of high mass utilization in these thrusters (Chapters 6 and 7). However, in general neutral collisions would introduce an additional drag term to this equation.

Applying these two assumptions leaves us with

$$0 = \left(\vec{E} + \vec{u} \times \vec{B}\right) + \zeta \vec{u}, \tag{3.8}$$

where I have replaced $(m_e \nu_{ei})/e = \zeta$ as a collisional drag factor for simplicity. To determine the steady azimuthal current that arises from the application of the RMF induced electric field (Eq. 3.6), I can right-cross-multiply Eq. 3.8 with $\vec{B_{r,z}}$—being only the radial and axial components of magnetic field—this results in

$$\vec{E} \times \vec{B_{r,z}} + \zeta \vec{u} \times \vec{B_{r,z}} = -\left(\vec{u} \times \vec{B}\right) \times \vec{B_{r,z}}. \tag{3.9}$$

The right hand side is expanded as

$$\begin{aligned} -\left(\vec{u} \times \vec{B}\right) \times \vec{B_{r,z}} &= \left(\vec{B_{r,z}} \cdot \vec{B}\right) \vec{u} - \left(\vec{B_{r,z}} \cdot \vec{u}\right) \vec{B} \\ &= (B_r^2 + B_z^2)\vec{u} - (B_r u_r + B_z u_z)\vec{B}. \end{aligned} \tag{3.10}$$

Combining Eqs. 3.10 and 3.9 and looking at only the azimuthal direction gives

$$E_z B_r + \zeta(u_z B_r - u_r B_z) = (B_r^2 + B_z^2)u_\theta - (B_r u_r + B_z u_z)B_\theta, \tag{3.11}$$

Where I have neglected the contribution of E_r which is informed from our analysis of Faraday's law for the RMF. I can further invoke the azimuthal component of Eq. 3.8 multiplied by ζ,

$$\zeta\left(u_z B_r - u_r B_z\right) = -\zeta^2 u_\theta. \tag{3.12}$$

Using this in Eq. 3.11 and combining terms gives an expression for azimuthal electron velocity

$$u_\theta = \frac{E_z B_r + (B_r u_r + B_z u_z)B_\theta}{B_r^2 + B_z^2 + \zeta^2}. \tag{3.13}$$

This expression generally varies in time and space, that is to say $u_\theta(t, \theta)$. This aligns with the understanding presented by Hugrass [42] that the presence of the RMF leads to the generation of high order spatial harmonics. With this finding, it becomes possible to determine the

average electron drift velocity by expanding the terms in Eq. 3.13. Through this process Eq. 3.13 becomes

$$u_\theta = \frac{\omega r B_\omega \cos(\omega t - \theta)[B_\omega \cos(\omega t - \theta) + B_{r,0}] + \{[B_\omega \cos(\omega t - \theta) + B_{r,0}]u_r + B_z u_z\} B_\theta}{[B_\omega \cos(\omega t - \theta) + B_{r,0}]^2 + B_z^2 + \zeta^2}. \tag{3.14}$$

To take the average of this expression over the thruster azimuth I note the following

1. $\cos^2$ terms average to 1/2
2. Linear cos and sin terms average to zero
3. B_θ terms all average to zero, as $\cos \cdot \sin$ terms have zero average and u_z to the lowest order has been shown to be in-phase with $\cos(\omega t - \theta)$ as a result of the axial electric field also exhibiting this phase relation [42].

As a result of averaging, what remains from Eq. 3.14 is,

$$\bar{u_\theta} = \frac{\omega r}{1 + 2\left(B_0^2 + \zeta^2\right)/B_\omega^2}, \tag{3.15}$$

where I have replaced $B_{r,0}^2 + B_{z,0}^2 = B_0^2$ as the magnitude of the static magnetic field. This expression is consistent with that of Sercel [78] under the assumption of no pressure forces with the notable change that the azimuthal component of the RMF does not appear in denominator of Eq. 3.15. This is owing to a more careful consideration of the forces that lead to this cross-field drift, u_θ, which makes intuitive sense as the azimuthal component of the RMF should have little impact on bulk electron motion along itself.

I outlined in chapter 2 that the ideal current drive produced by an RMF is $j_\theta = e n_e \omega r$ and is independent of RMF field strength. In practice there are deleterious effects to retard the electron motion that do put requirements on the magnetic field strength. One such requirement is provided by Eq. 3.15. which shows us that effective RMF current drive is only achieved for

$$B_\omega^2 \gg B_0^2 + \zeta^2. \tag{3.16}$$

The physical intuition behind this is that both the static field and heavy particle collisions provide an effective drag to the desired synchronous electron motion with the RMF. Furthermore, notably in the derivation of Eq. 3.15, I have implicitly neglected the effect of plasma currents altering the imposed magnetic field. While this expression can account for the static field produced by low order plasma current, j_θ, it does not taken into account the high

frequency field produced by the oscillating axial electron currents j_z. The inclusion of this effect requires solving Ampere's law within the plasma ($\nabla \times \vec{B} = \mu_0 \vec{j}$) and in general is not analytically tractable. However, a perturbation analysis performed by Jones and Hugrass in Ref. [47] to include this effects shows that it can justifiably be ignored provided that

$$\left(\frac{\zeta}{B_\omega}\right)^2 \left(\frac{R}{\delta}\right)^2 \ll 1, \tag{3.17}$$

where, R is the radius of the device, and $\delta = \sqrt{2\eta/\mu_0\omega}$ is the classical skin depth. If this inequality is satisfied, the existence of the axial "screening" currents in the plasma is minimal, allowing the RMF field to completely penetrate the plasma column and induce azimuthal current which is required for effective thruster operation. Despite most practical RMF thrusters exhibiting a ratio of device radius to classical skin depth significantly greater than one, penetration of the RMF into the plasma is usually achieved by means of the first parenthetical term in Eq. 3.17. Increasing the magnetization to the RMF via this term produces an electron current that increasingly rotates synchronously with the RMF. This synchronous azimuthal electron motion does not experience any electric field from Faraday's law and as a result becomes transparent to the RMF. This effect has been shown to permit RMFs to penetrate much further into dense plasmas than would be expected by classical skin depth effects, and is leveraged in the design of RMF thrusters to achieve full RMF penetration.

3.2.2 Thrust Production

Leveraging this derivation of azimuthal electron drift, I can now write the current density as

$$j_\theta = n_e u_\theta = \frac{e n_e \omega r}{1 + 2\left(B_0^2 + \zeta^2\right)/B_\omega^2}, \tag{3.18}$$

where n_e is the electron density. The electron density in the above expression is primarily influenced by the thruster mass flow rate in addition to the ionization fraction. The total density (neutrals and ions) in the thruster can be related to the mass flow rate via mass continuity as

$$n = \frac{\dot{m}}{m_i A \bar{v}}, \tag{3.19}$$

where $\dot{m}$ is the mass flow rate, m_i, is the ion mass, A is the thruster cross sectional area, and $\bar{v}$ is the average particle speed. This equation directly shows that increasing mass flow rate—to first order—linearly increases density and increasing particle velocity decreases density.

Although, the density is predominantly controlled by Eq. 3.19, it can be affected by the RMF through the static self-field produced by the azimuthal current. This coupled interaction can generate a structure known as a field reversed configuration (FRC) plasmoid [7]. This structure forms when the driven current produces an axial flux that opposes and reverses the original applied field along centerline. In this scenario the applied field is compressed towards the outer wall and a magnetic separatrix forms between the two field directions. The plasma density dynamically responds to this via a radial pressure balance, and as a result the plasma density is largest in between the zones of high magnetic pressure occurring along centerline and near the wall. I show in Fig. 3.2 a diagram to illustrate the structure of an FRC plasmoid.

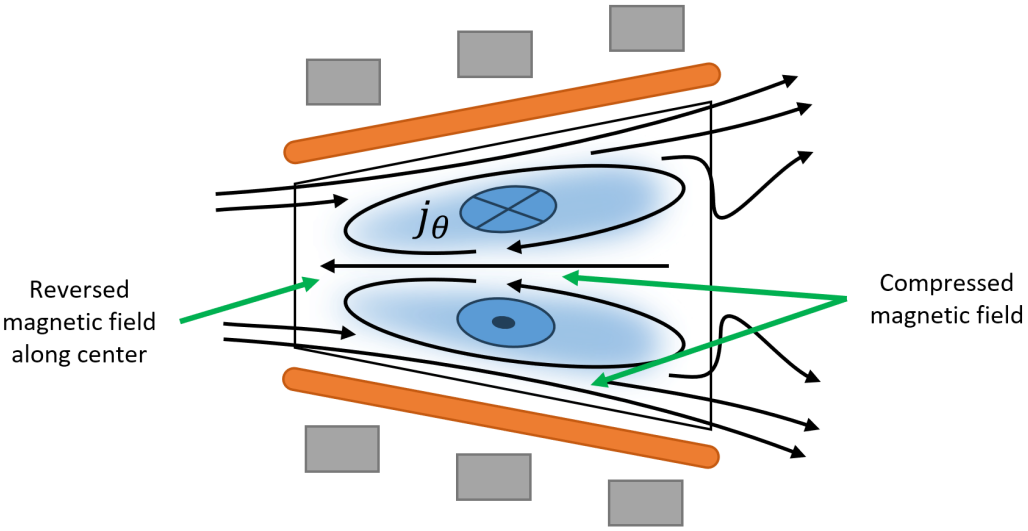

Figure 3.2: Diagram of field reversed configuration in RMF thruster.

FRC plasmas have shown potential as a nuclear fusion concept [24, 86] because of their ability to confine and compress the plasma. These characteristics have also been seen as advantageous for electric propulsion applications. Previous authors in the field (See Refs. [95, 40]) claim that FRC formation has two distinct advantages. First, isolating the plasma from the wall to reduce losses, and second, assisting in magnetic detachment from the thruster field to decrease beam divergence. To this first point, in propulsion scenarios, the main goal is to expel propellant at high speeds, such that the exhaust velocity likely dominates over the diffusion rate to the walls. Here, enhanced confinement from the walls is not as crucial as for fusion. This is evident in Hall thrusters that do not exhibit magnetic shielding [61], where the plasma is in direct contact with the thruster walls, yet they still achieve efficiencies above 50% [5]. Furthermore, to the second point, as an FRC plasmoid exits the thruster, its internal

magnetic pressure will force radial expansion and may indeed lead to increased divergence losses. This effect is further discussed in Sec. 7.4.3 along side experimental results. In my opinion, this implies that FRC formation is largely a byproduct of RMF thruster operation and not required or necessarily sought behavior.

Using the current density from Eq. 3.18 the overall thrust force produced is

$$T = f_{rep} \int_0^{1/f_{rep}} \left(\int_V j_\theta B_r dV \right) dt \tag{3.20}$$

where f_{rep} is the pulse repetition frequency, and B_r is the total radial magnetic field. In the above expression the inner integral is performed over the thruster internal volume, V, and the outer integral is performed over the pulse period, f_{rep}^{-1}. B_r in Eq. 3.20 refers to the combined radial component of the applied, structure, and self magnetic fields. However note that the self-field in general cannot self accelerate the center-of-mass of the plasma and provides no net thrust. Furthermore, Eq. 3.20 only takes into account the Lorentz force thrust and similar to our treatment of the azimuthal drift neglects pressure effects. Pressure gradients in the thruster will also drive a diamagnetic drift contributing to j_θ as well and contribute directly to the thrust through an axial pressure gradient. Again, these effects are not the intended method of operation for an RMF thruster and so are not expressly written here.

3.2.3 Performance Scaling

To understand the performance scaling of RMF thrusters and IPPT thrusters in general, I introduce the concept of specific energy:

$$\epsilon^* = P_{in}/\dot{m} \tag{3.21}$$

where P_{in} is the input power, and $\dot{m}$ is the neutral mass flow rate. This metric, typically reported in J/mg, is represented in the literature of pulsed thruster systems [72, 68, 30]. Using this metric allows for a comparison of performance parameters across thruster operating conditions, and by identifying trends relative to specific energy, I can evaluate the scaling relations of RMF thrusters.

For instance, A Hall thruster has a specific energy that scales as

$$\epsilon^* \propto \frac{IV}{\dot{m}} = \frac{qV}{m_i}, \tag{3.22}$$

where I and V are the discharge current and voltage respectively, and I have made use of the definition $I = q\dot{m}/m_i$, where q is the ion charge, and m_i is the ion mass. Similarly, Hall

thruster specific impulse, and thrust scale as

$$I_{sp} \propto \sqrt{\frac{2qV}{m_i}}, \tag{3.23}$$

$$T \propto \dot{m}\sqrt{\frac{2qV}{m_i}}. \tag{3.24}$$

$$\tag{3.25}$$

Using these scaling arguments, I would expect a performance plot for Hall thrusters to exhibit square root scaling for both thrust and specific impulse and have a roughly constant efficiency when plotted over specific energy.

However, for thrusters that exhibit I^2 thrust scaling such as pulsed inductive thrusters, or self-field MPDs [70, 14] (see Chapter 1 Eq. 1.13), the specific energy should scale as

$$\epsilon^* \propto I^2/m_i, \tag{3.26}$$

and the thrust and specific impulse should scale as

$$T \propto I^2, \tag{3.27}$$

$$I_{sp} \propto I^2/m_i. \tag{3.28}$$

$$\tag{3.29}$$

A distinct change for these systems, compared to electrostatic/magnetostatic accelerators, is that some sort of linear trend should be resolvable with both thrust and specific impulse when plotted against specific energy. In Chapter 4, I refer back to these definitions to compare and evaluate the performance scaling of the RMF thruster systems tested in this work.

3.3 Derivation of the Efficiency Model

In the preceding section, I developed a model to represent the thrust generated by an RMF thruster as a function of the applied field and plasma resistivity. Now, in this section, I present a different model that establishes a connection between the thrust produced and the propulsive efficiency of the device. I analyze the efficiency of the thruster by categorizing it into distinct phenomenological efficiency modes, allowing for a comprehensive examination of the mass, momentum, and energy transfer within the device. Figure 3.3 illustrates the

terms of these four modes that are referenced in this derivation. To begin, I define overall thrust efficiency as

$$\eta = \frac{T^2}{2\dot{m}P_{in}}, \tag{3.30}$$

where, $\dot{m}$ is the mass flow rate of propellant, P_{in} is the input electrical power, and T is the thrust. This performance parameter is critical for all electric propulsion devices and is effectively written as the ratio of jet power to input electrical power. For RMF thrusters, in particular, I seek to breakdown the total efficiency in discrete terms with physical significance. These terms are meant to shed light on the various loss mechanisms inherent to RMF devices and provide a basis for the optimization of their operation.

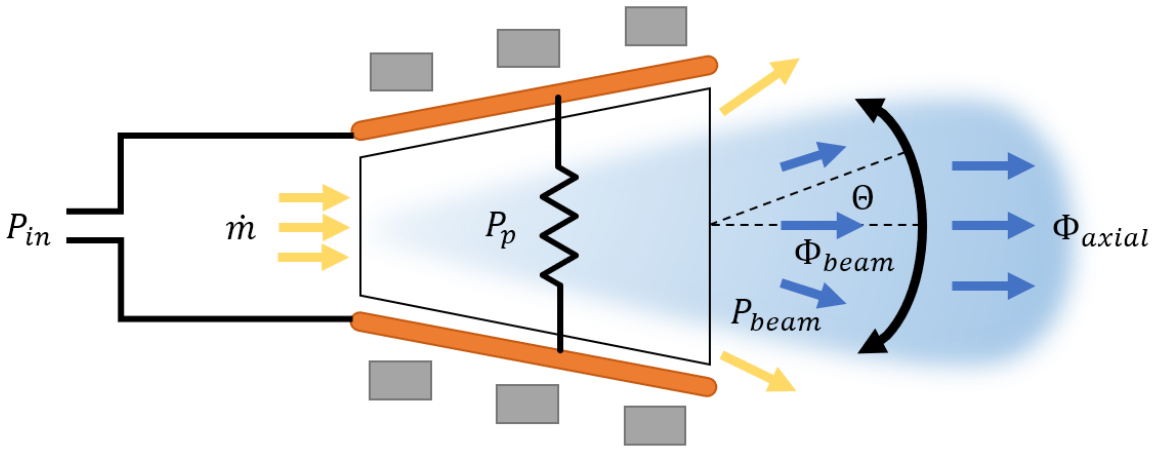

Figure 3.3: Efficiency model illustrative diagram.

Addressing the thruster plume and treating the thruster as a "black box", thrust can be expressed as

$$T = \dot{m}_i \, u_{ex} \cos\Theta, \tag{1}$$

where $\dot{m}_i$ is the ion mass flow rate that contributes to thrust, u_{ex} is the axially directed exhaust velocity, and Θ is the characteristic divergence angle of the exhaust plume. This characteristic angle represents the relative contribution of momentum directed in the axial direction and is written as

$$\Theta = \cos^{-1}\left(\frac{\Phi_{\text{axial}}}{\Phi_{\text{beam}}}\right) \tag{3.31}$$

where Φ_{axial} is the component of momentum flux in the axial direction, and Φ_{beam} is the total momentum flux of the beam. I also define a beam power as

$$P_{\text{beam}} = \frac{1}{2}\dot{m}_i u_{ex}^2, \tag{3.32}$$

where this beam power represents the momentum-carrying component of kinetic energy in the beam. This is in contrast to the total energy flux of the beam which is necessarily larger due to the thermal energy (aka. polydispersivity) of the beam.

This definition allows me to recast the thrust efficiency efficiency from Eq. 3.30 as

$$\eta = \left(\frac{\Phi_{\text{axial}}}{\Phi_{\text{beam}}}\right)^2 \left(\frac{\dot{m}_i}{\dot{m}}\right) \left(\frac{P_{\text{p}}}{P_{\text{in}}}\right) \left(\frac{P_{\text{beam}}}{P_{\text{p}}}\right), \tag{3.33}$$

where I have added the term P_{p} as representing the energy inductively coupled into the plasma by the RMF. In this form I can write the efficiency as the product of four modes

$$\eta = \eta_d \eta_m \eta_c \eta_p, \tag{3.34}$$

where η_d is the divergence efficiency, η_m is the mass utilization efficiency, η_c is the coupling efficiency, and η_p is the plasma efficiency. Using this phenomenological efficiency model, I have a framework to evaluate and explain the overall efficiency of the RMF thrusters employed for this research effort. What follows is a description and physical interpretation of each mode along with its definition.

3.3.1 Divergence Efficiency

Divergence efficiency characterizes the ability of the thruster to collimate the accelerated plasma ions into a narrow beam, reducing losses due to radially directed momentum which symmetrically cancels. Divergence efficiency is defined as

$$\eta_d = \left(\frac{\Phi_a}{\Phi_{beam}}\right)^2, \tag{3.35}$$

where Φ_a and Φ_{beam} are the axial and total momentum flux from the thruster.

3.3.2 Mass Utilization Efficiency

Mass utilization efficiency quantifies how effectively the propellant mass is ionized and therefore able to be acted upon by the electromagnetic forces produced by the thruster. This mode is particularly important for electric propulsion, as any unionized propellant will contribute

a substantial penalty to the specific impulse of the rocket. Mass utilization efficiency is defined as

$$\eta_m = \frac{\dot{m}_i}{\dot{m}}, \tag{3.36}$$

where $\dot{m}_i$ is the mass flow rate of ions in the beam and $\dot{m}$ is the mass flow rate of neutrals to the thruster.

3.3.3 Coupling Efficiency

Coupling efficiency quantifies the effectiveness of the energy transfer from the RMF power system to the plasma. This mode is a measure of parasitic losses in the formation of the RMF relative to the effective load of the plasma. It implicitly takes into account losses due to power that is resistively dissipated in the antenna circuit, consumed by switching losses in the power supply, coupled into other structures, or radiated away as electromagnetic waves.

Coupling efficiency is defined as:

$$\eta_c = \frac{P_p}{P_{in}}, \tag{3.37}$$

where P_p is the power into the plasma, and P_{in} is the power into the RMF power processing unit.

3.3.4 Plasma Efficiency

Plasma efficiency represents the ratio of the total beam power of the accelerated ions to the power coupled to the plasma by the RMF. It accounts for the overall energy conversion efficiency of the thruster. Plasma efficiency is defined as:

$$\eta_p = \frac{P_{\text{beam}}}{P_p}, \tag{3.38}$$

where again the beam power is written as $P_{\text{beam}} = \frac{1}{2}\dot{m}_i u_{ex}^2$. In conjunction with this definition, the plasma efficiency can also be thought of in terms of constituent internal loss modes. In this way, I can write the plasma power as a sum of energy channels

$$P_p = P_{beam} + P_{th} + P_{iz} + P_{wall} + P_{rad}, \tag{3.39}$$

where P_{th} is the thermal power carried by the ions in the beam—this includes the effect of polydispersion due to varying charge states and acceleration mechanisms—, P_{iz} is the

power consumed by ionization reactions, P_{wall} is the power transferred to the thruster wall via diffusion, and P_{rad} is the power lost optically through excitation reactions.

3.4 Internal Loss Processes

It is crucial to characterize the plasma efficiency by considering internal loss modes, as these losses are caused by different physical phenomena and may necessitate different mitigation strategies. To provide a comprehensive understanding of the internal loss processes, it is essential to explore the mechanisms and reactions that occur within the system. This section aims to shed light on the various factors that contribute to the dissipation of energy within the RMF thruster from Eq. 3.39. By examining these processes, we can gain valuable insights into the overall efficiency and performance of the system.

Due to the additive nature of these power channels, it is not possible to express these effects as the product of disparate efficiency modes, as I have done above in Eq.3.34. However, I can rewrite Eq. 3.39 in terms of power relative to the beam power:

$$\eta_p = \left(1 + \rho_{th} + \rho_{iz} + \rho_{wall} + \rho_{rad}\right)^{-1}, \tag{3.40}$$

where $\rho_{th} = P_{th}/P_{beam}$ is the relative thermal power, $\rho_{iz} = P_{iz}/P_{beam}$ is the relative ionization power, $\rho_{wall} = P_{wall}/P_{beam}$ is the relative wall power, and $\rho_{rad} = P_{rad}/P_{beam}$ is the relative radiative power. These definitions of relative powers provide a framework for comparing the relative importance of these loss mechanisms across operating conditions and experiments.

I show in Fig. 3.4 a representation of how I treat the energy and mass flow within the RMF thruster. Note I restrict this analysis to a xenon plasma as that represents the majority of the experimental result presented in the following chapters. More complex propellants may exhibit additional losses from rotational and vibrational excitation in addition to chemical reactions including discossication.

This image displays four islands, one for each of the component species—electrons, ions, and neutrals—and one for the thruster wall. I represent the relevant reactions that occur in the system as arrows that track how mass and energy enter and leave the system and how they are exchanged between these islands.

Starting with mass flow as a clarifying example, all of the mass enters the system as neutral particles (I will ignore the small ionized fraction of propellant from a seed plasma source). From this we can write two relevant reactions, collisional ionization recombination and radiative ionization recombination. [34]

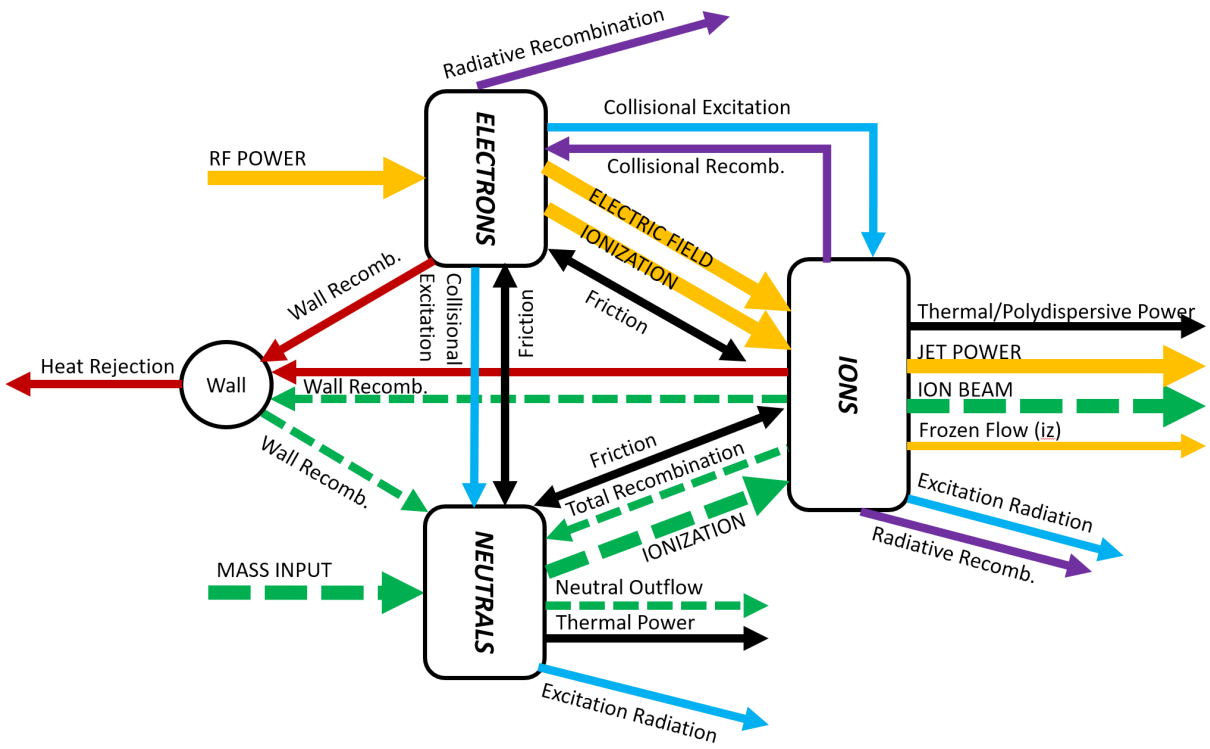

Figure 3.4: Visualization of energy and mass flow within the RMF thruster.
This includes the effects of elastic and inelastic collisions as well as the energy transfer from the electromagnetic fields. Solid arrows represent energy flow, and dashed green arrows represent mass flow. Arrows point in the direction of energy and mass flow for the given reaction or effect.

$$e^- + \mathrm{Xe} \rightleftharpoons e^- + \mathrm{Xe}^+ + e^- \qquad \text{(Collisional Ion./Recomb.)} \tag{3.41}$$

$$h\nu + \mathrm{Xe} \rightleftharpoons \mathrm{Xe}^+ + e^- \qquad \text{(Radiative Ion./Recomb.)} \tag{3.42}$$

In the forward reaction (ionization) in both these cases the mass transfers form the neutral species to the ion species, where I neglect the small contribution of electron mass. These effects are represented as the "IONIZATION" arrow in Fig. 3.4. Practically in electric propulsion systems, the rate of radiative ionization is exceedingly small and is typically neglected. These two reactions can also take place in the reverse direction (recombination), where the mass is transferred from the ions to the neutrals. This is shown as the "Total Recombination" arrow. The final mass reaction is plasma recombination at the thruster wall. Since the thruster walls are electrically floating, the flux of ions and electrons are necessarily equivalent. When an ion strikes the wall it is neutralized by electrons on the material surface and returns as a flux of neutrals back to the system. This can be written as

$$\Gamma_{i,wall} = \Gamma_{n,wall}, \tag{3.43}$$

where $\Gamma_{i,wall}$ is the mass flux of ions to the wall, and $\Gamma_{n,wall}$ is the mass flux of ions from the wall. This effect is shown as the "Wall Recomb." arrows. Lastly, mass can exit the system through the ion beam flux ("ION BEAM"), and any remaining neutral flux ("Neutral Outflow").

For the energy flow within this system representation, all the energy enters via radio frequency (RF) power deposited in the electrons. This absorption can be in the form of randomized motion resulting in electron heating or into directed drifts such as the desired j_θ current. Energy can leave the electron species through a variety of mechanisms. Most importantly the j_θ electron current produces an electric field which accelerates the ions, transferring energy and producing the jet power of the thruster. This is shown as the "ELECTRIC FIELD" and "JET POWER" arrows, respectively.

Additionally, the electrons can transfer energy to the heavy species via collisions. Collisional ionization (listed in Eq. 3.41) removes energy from the incident electron and leaves the resulting ion with a remnant amount of ionization energy. This ionization energy leaves the system as a frozen flow loss carried by the ions and is unavoidable. The power sunk into ionization can be written as

$$P_{iz} = \int_V n_n n_e \langle \sigma_{iz} v_e \rangle \varepsilon_{iz} dV, \tag{3.44}$$

where n_e is the local plasma density, n_n is the local neutral density, and V is the total volume in the cone. Additionally, $\langle \sigma_{iz} v_e \rangle$ is the reaction rate of ionization averaged over an assumed Maxwellian electron distribution. Empirical data for this reaction is tabulated in Ref. [32]. I assume for this analysis that all the ions are singly charged and that each ionization event requires an energy input of $\varepsilon_{iz} = 12.13$ eV, the first ionization energy of Xe.

Radiative recombination removes the ionization energy from the ions as well as a small amount from the captured low-energy electron and emits it from the system optically as radiative power. However, for low temperature plasmas, as are commonly found in EP systems, collisional recombination rates are insignificant when compared to wall diffusion recombination and are therefore neglected in this analysis but are mentioned for completeness.

However, the primary radiative energy transfer mechanism is a result of collisional excitation reactions. Free elections can collide with ions and neutrals to cause bound electrons to transfer into excited electronic states. These reactions are of the form:

$$e^- + \mathrm{Xe} \rightarrow \mathrm{Xe}^* + e^- \rightarrow \mathrm{Xe} + e^- + h\nu \qquad \text{(Neutral Excitation)} \tag{3.45}$$

$$e^- + \mathrm{Xe}^+ \rightarrow \mathrm{Xe}^{+*} + e^- \rightarrow \mathrm{Xe}^+ + e^- + h\nu \qquad \text{(Ion Excitation)} \tag{3.46}$$

where I have denoted excited states as (*), and followed these excitation reactions with spontaneous emission of photons. The photon energy released exits the system and contributes to the radiative power, P_{rad}. These reactions are simplified as there are many xenon excited states and multiple excitation and de-excitation pathways including radiative excitation and collisional de-excitation. However, the unidirectional reactions written above are typically the most significant for the low temperature and optically thin plasma that exist in EP applications. The excitation radiation power can be written as

$$P_{rad} = \int_V n_n n_e \langle \sigma_{ex,n} v_e \rangle \varepsilon_{ex,n} + n_e^2 \langle \sigma_{ex,i} v_e \rangle \varepsilon_{ex,i} dV. \tag{3.47}$$

This equation is essentially a low-fidelity coronal model for radiation, where I assume that there is no persistent excited population and that all energy put into the excited states spontaneously radiates out to the environment without re-absorption into the plasma. In this way, I have represented all the excitation processes with an effective total excitation rate and energy per excitation. For the neutral collisions, I adopt the approach from Ref. [32], which is informed by Ref [38], in using $\langle \sigma_{ex,n} v_e \rangle$ as the total neutral excitation reaction rate and $\varepsilon_{ex,n} = 8.32$ eV as the average energy per excitation collision. For electron-ion collisions, I have defined $\langle \sigma_{ex,i} v_e \rangle$ as the total ion excitation rate summing for all possible transitions from the ground state, 5p5, to the 6p state. These are the dominant transitions in terms of relative intensity and cross-section [94]. The average energy of these transitions is $\varepsilon_{ex,i} = 14.8$ eV. I have plotted these effective reaction rates for neutral and ion excitation averaged over a Maxwellian electron population in Fig. 3.5.

Frictional drag also plays a role between the species through elastic scattering collisions. These collisions largely serve to remove energy from the electrons and contribute to randomized motion (heating) of the heavy species, and this thermal energy can leave the system through the neutral and ion flux out of the device. Practically, this can be calculated for the ion population as

$$P_{th} = P_{KE} - P_{ME}, \tag{3.48}$$

where P_{KE} is the total kinetic energy flux in the beam and P_{ME} is the momentum carrying part of that energy. Written out the kinetic energy flux is

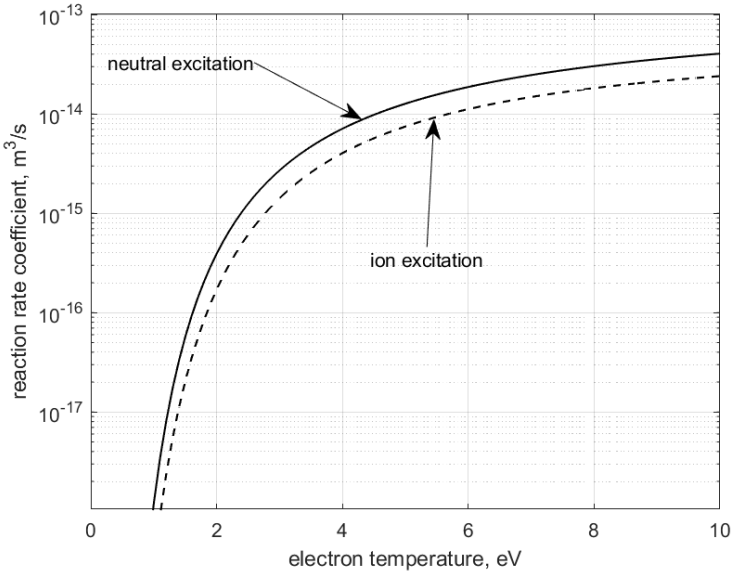

Figure 3.5: Excitation reaction rates averaged over a Maxwellian electron distribution for neutrals and ions. Neutral excitation rates reproduced from fit from Ref. [32]. Ion excitation rates from sum of ground state to 6p transitions from Ref. [94].

$$P_{KE} = 2\pi r^2 \int_0^{\pi/2} \int_0^{\infty} \left[\frac{1}{2} m_i n_i(\theta) v(\theta)^2\right] v(\theta) f(v) dv \sin\theta \, d\theta, \tag{3.49}$$

where r the the radial distance from the thruster where properties are measured, m_i is the ion mass $n_i(\theta)$ is the ion density as a function of the angle θ about the thruster, v is the ion velocity, and $f(v)$ is the ion velocity distribution function. The momentum energy is then

$$P_{ME} = \frac{\left\{\int_0^{\pi/2} \int_0^{\infty} \left[m_i n_i(\theta) v(\theta)\right] v(\theta) f(v) dv \sin\theta \, d\theta\right\}^2}{2 \int_0^{\pi/2} \int_0^{\infty} \left[m_i n_i(\theta)\right] v(\theta) f(v) dv \sin\theta \, d\theta}, \tag{3.50}$$

where the numerator represents the square of the momentum flux, and the denominator represents twice the mass flux. In this way, this equation is directly related to the definition of jet power, $P_{jet} = T^2/(2\dot{m})$.

Lastly, through wall recombination the flux of ions and electron to the thruster wall removes energy from the plasma. This energy primarily leaves through the electron flux which carries an average loss of the electron temperature as well as the decelerating potential of the wall sheath. This results in a power to the wall that must be rejected by the thruster of

$$P_{wall} = \frac{1}{4} e n_e \sqrt{\frac{8T_{eV}}{\pi m_e}} \left(2T_{eV} + \phi\right) \exp\left(\frac{-\phi}{T_{eV}}\right) f_c \tag{3.51}$$

where, n_e is the electron temperature, T_{eV} is the electron temperature in eV, ϕ is the sheath potential, and $0 < f_c \leq 1$ denotes the degree of magnetic confinement of the electrons [32]. In this expression, $\sqrt{eT_{eV}/m_i}$ is the Bohm speed and $(5/2T_{eV} + 2\Phi)$ is the energy lost from the plasma per electron/ion pair.

3.5 Summary

In this chapter, I provide a comprehensive overview of the physics of RMF thrusters, an innovative inductive accelerator that produces an azimuthal Lorentz force within the plasma using a distinctive current drive scheme. This discussion serves as a foundational understanding for the subsequent experiments explored in this study.

Drawing on Sercel's work on RMF thruster current drive [78], I presented a descriptive model to explain how the RMF couples to the electrons in the plasma to drive the azimuthal electron current. In this, I acknowledge physical complexities which drive practical requirements on the magnitude of the RMF. From this, I discuss the force transfer mechanism for RMF thrusters and how thrust is produced, including a discussion on field reversed configuration (FRC) physics.

The end of this chapter includes the derivation of an efficiency model tailored for RMF thrusters. This model offers a structured framework for evaluating performance in various physically relevant modes. Using this model, I analyze mass, momentum, and energy exchange within the RMF thruster, shedding light on the key factors contributing to the observed low efficiency in these devices.

CHAPTER 4

Description of RMF Thruster Hardware

4.1 Introduction

In this chapter, I present a chronology of RMF thruster development at the University of Michigan's Plasmadynamics and Electric Propulsion Laboratory (PEPL). Over the time period of this dissertation, we have developed three rotating magnetic field thruster prototypes, and I provide a description of their design and implementation. In particular, I describe the details of the various RMF power systems employed for each prototype, as this was found to have a profound effect on their propulsive performance.

Our first prototype, designated RMFv1, was constructed leveraging design heritage from MSNW's ELF thruster. This thruster was built to replicate some of MSNW's findings as well as to probe the propulsive capabilities of the technology using direct thrust measurement. The chapter delves into the specific components comprising RMFv1 and explains the choices made in material selection, coil configuration, and power supply. Furthermore, it highlights the challenges encountered with this thruster design which ultimately led to an unresolvably small thrust for this device.

Building upon the lessons learned from RMFv1, the subsequent prototype, RMFv2, was developed with a refined design aimed at improving overall performance, such that it could serve as an experimental test bed. This section of the chapter provides an in-depth examination of the improvements incorporated into RMFv2, including an updated RMF power system, a modified gas injection scheme, and material choices.

The third and latest prototype, RMFv3, represents the present status of the University of Michigan's research efforts in rotating magnetic field thruster development. This section details the state-of-the-art features of RMFv3, including further advancements to power system design, pre-ionization location, and thruster geometry. Ultimately, these changes led to notable improved performance metrics compared to its predecessors.

At the end of each thruster description, I provide a selection of performance results

including thrust, specific impulse, and efficiency—specifically for the v2 and v3 thrusters. This is presented here as part of the description of these devices as a baseline knowledge that motivates the studies presented in in the latter half of this dissertation. The detailed accounting of the overall performance trends of these thrusters has been presented elsewhere by my collaborators [78, 96] and represents a substantial part of their contributions to the field. The section of performance results in this chapter is intended to set the stage for Chapters 6 and 7 of this work, where I investigate more thoroughly a subset of the most effective operating conditions for the v2 and v3 thruster prototypes to explain the losses of these thrusters using the phenomenological efficiency model presented in Chapter 3.

4.2 RMFv1 Thruster (2019-2020)

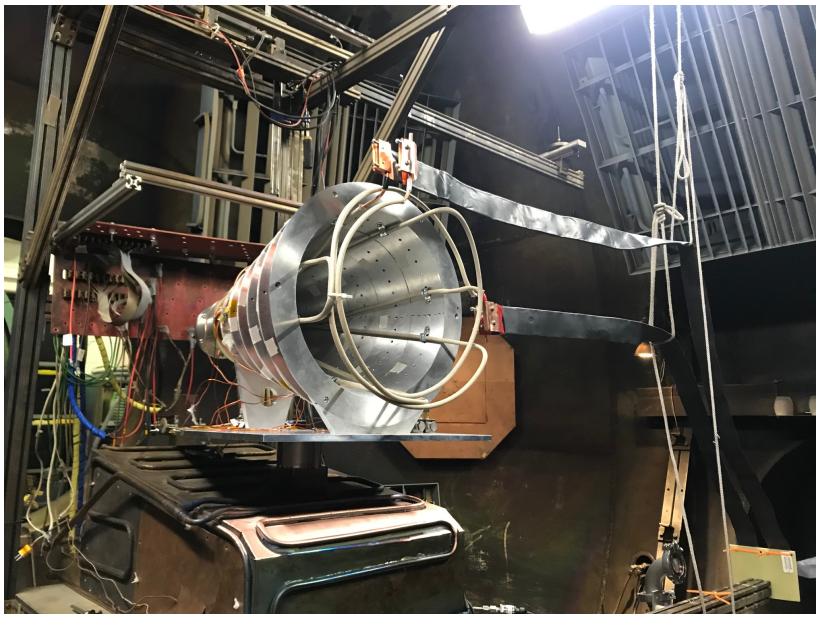

Figure 4.1: PEPL RMFv1 thruster installed for initial electrical checkouts in the Large Vacuum Test Facility at UM.

The first iteration of the lineage of RMF thrusters fabricated at the University of Michigan was the PEPL RMFv1 thruster. This thruster was, in many ways, designed to mimic the implementation of the Electrodeless Lorentz Force Thruster (ELF) from MSNW [95]. Further details on this design can be found in Refs. [98, 97, 84]. I show in Fig 4.1 an image of the RMFv1 installed in the Alec Gallimore Large Vacuum Test Facility at the University of Michigan, and I show in Fig. 4.2 a side-on cross-section of a computer render of the device.

4.2.1 Thruster Design

As seen in Fig. 4.2, the primary structure of the version one thruster is comprised of six aluminum magnet bobbins. When energized, the copper coils surrounding these bobbins form the DC bias magnetic field. The current through each bias coil is controlled to ensure that the magnetic field aligns approximately tangentially to the conical wall. Additionally, the aluminum bobbins serve a dual purpose in this design as magnetic flux conserving rings. The purpose of the flux conservers is to maintain the total magnetic flux inside the thruster cone. In principle, the spin-up of the azimuthal plasma current will reject magnetic flux along the centerline of the device. If total flux is conserved, this will compress the magnetic field external to the plasma. This compression aids in plasma confinement and provides an additional contribution to the Lorentz force proportional to the square of the driven plasma current. The bobbins are electrically isolated to shorten the path length of eddy currents which form in response to the primary currents in the RMF antennas, reducing the power inductively coupled into the thruster body.

The two RMF antennas can be seen situated inside the device in Fig.4.1. These antennas consisted of 6.35 mm soft copper tubing that was bent to form two series Helmholtz-like pairs. These coils are oriented horizontally and vertically in Fig.4.1. Water was supplied to the interior of the antennas to provide additional cooling under vacuum conditions. The antennas shown in the image are wrapped in fiberglass sleeving and were subsequently wrapped in PVC heat shrink to provide high voltage isolation. Additionally, not shown in the figure is a conical mica sheet which acts as a plasma bounding surface. The conical shape of these antennas means that the strength of the RMF varies throughout the thruster. As a point of reference, Woods [96] measured the antenna field factor using a DC gaussmeter to be approximately 0.0625 G/A at the axial center of the thruster.

At the rear of the thruster is a LaB6 hollow cathode, identical to those used in modern Hall thrusters. This cathode acts as the pre-ionizer for the RMF thruster providing the requisite seed plasma for RMF ignition. Surrounding the cathode is an anode and neutral injector assembly. The anode sustains the cathode discharge current (typically 18 A), and the neutral injector supplies xenon propellant in addition to the flow through the cathode. Xenon is readily compatible with existing cathode hardware available at PEPL and is used as the propellant exclusively in this work. This choice is further influenced by xenon's large ionization cross section and low ionization energy which make it a suitable choice for attaining high efficiencies.

I designed and constructed a power processing unit (PPU) for the RMFv1 thruster. This PPU consisted of two capacitor charge/discharge boxes in addition to a second-order low-pass filter to ease the pulse transients on the DC power supply. Each capacitor charge/discharge

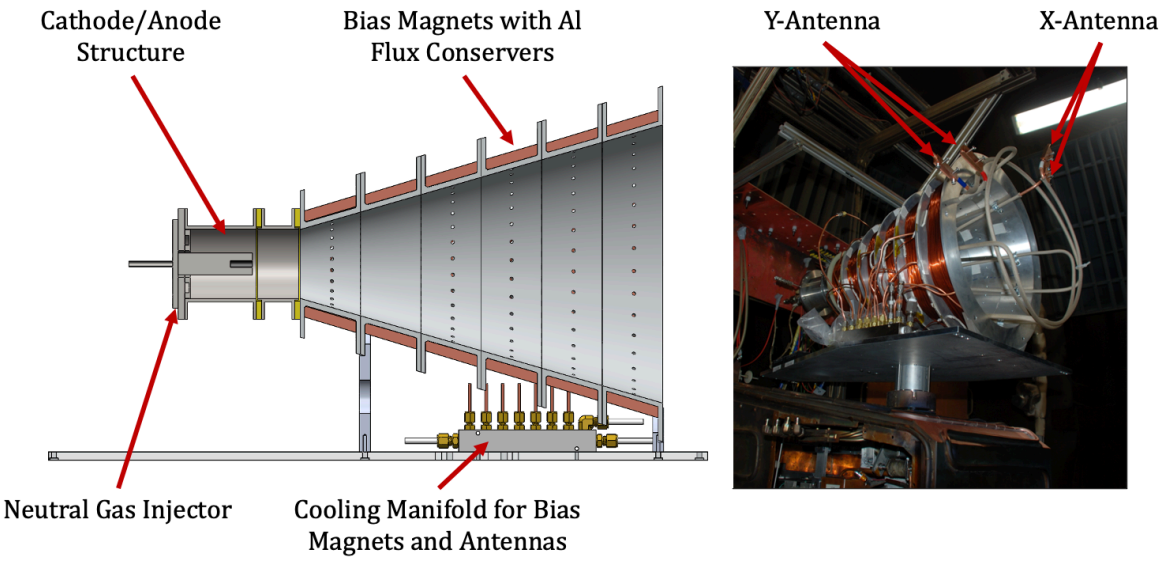

Figure 4.2: Cross sectional view of PEPL RMFv1 thruster computer model with main components labeled.

box contains a high-power insulated gate bipolar transistor (IGBT) which acts as a single-pole double-throw switch to either charge the main capacitor bank from a high voltage DC source or discharge it through the RMF antenna. The capacitance of the main bank is chosen such that the LC constant of the circuit is at the desired RMF frequency. In this thruster, two capacitor banks were used, which correspond to two RMF frequencies, 20 kHz, and 125 kHz. For triggering, an external microcontroller fires each capacitor charge/discharge box with a 90-degree phase delay between them to activate the RMF. The schematic of the RMFv1 PPU is shown in figure 4.3a, and a render of the physical unit is shown in Fig. 4.3b.

4.2.2 Performance

Ultimately, the implementation of the version one thruster was found to be sub-optimal. The primary faults were excessive gas density along the thruster axis, low RMF frequency, low output PPU power, and substantial coupling to the aluminum flux conserving body.

The rear neutral gas injector did not adequately disperse the propellant radially, leaving the majority of the propellant along the centerline of the thruster. At this location, the RMF exhibits little ability to couple energy to the plasma because the rotating field has very little changing magnetic field along centerline. As a result, the inwardly radial plasma experiences only a small inductive force.

The low RMF frequency (20-125 kHz) and the resistivity of the circuit also meant that

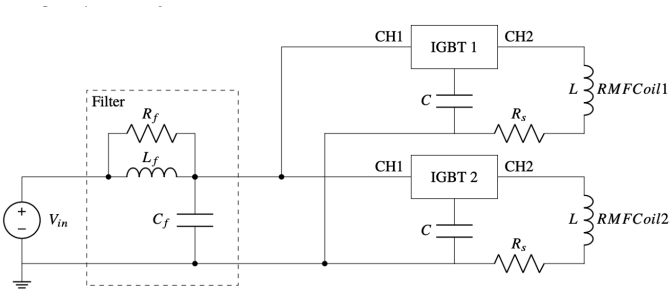

(a) Circuit schematic.

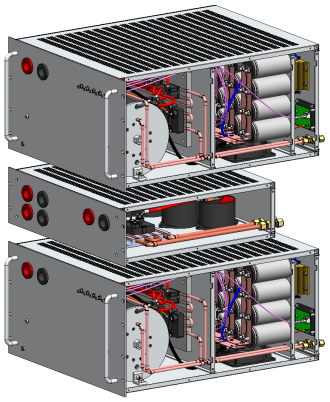

(b) CAD render of switching units.

Figure 4.3: RMFv1 power system.

during an RMF ring-down there were only a few periods where the currents in the antenna were at relevant magnitudes to couple energy into the plasma. The proximity of the near-monolithic conductive body of the thruster worsened this effect by enhancing the resistance of the RMF circuit by parasitic coupling. Figure 4.4 shows the RMF current amplitudes during vacuum and a plasma-loaded RMF pulse at 125 kHz frequency. While the current initially reaches a peak of nearly 400 A, corresponding to an RMF strength of 25 G, it decays to half of that value after only four periods (which is 25% of the initial energy).

These characteristics led to low overall performance for the RMFv1 thruster. We were only able to measure a maximum coupling efficiency of 5%—seen characteristically as the negligible difference between the vacuum and plasma waveforms in Fig.4.4—and were unable to resolve meaningful thrust. We did, however, see trends that indicate that coupling increased with higher gas density, which corresponds to higher electron density being present near the RMF antenna to absorb energy [97].

4.3 RMFv2 Thruster (2021-2022)

Following the unsatisfactory performance of the RMFv1 thruster, we constructed a second RMF thruster version, the PEPL RMFv2, to address the shortcomings of the first iteration. These shortcomings, in summary, were

1. Excessively large flux conservers, addressed in v2 with increased use of dielectric materials

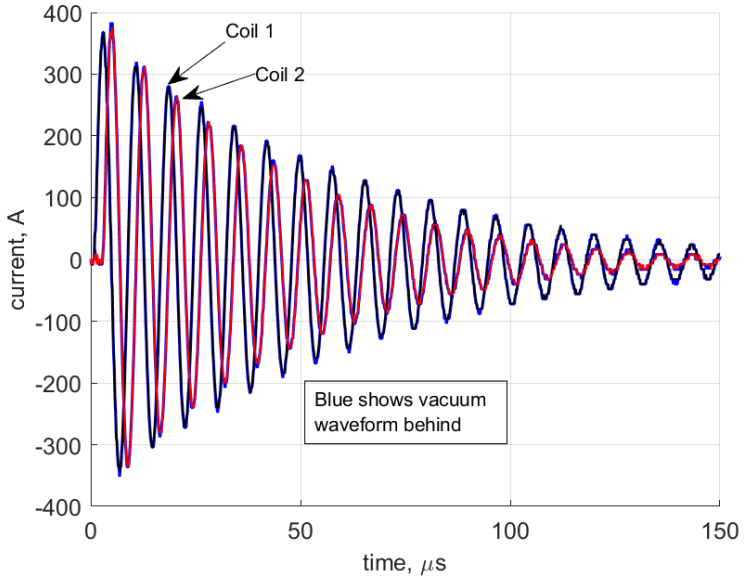

Figure 4.4: RMFv1 waveform for 125 kHz operation. Note, blue waveforms represent vacuum operation and show negligible coupling.

2. Concentration of propellant along centerline, addressed in v2 with a new neutral injector

3. Rate of resistive decay of RMF amplitude and low RMF frequency, addressed in v2 with new RMF power system architecture.

In the remainder of this section, I explain these changes between the version 1 and version 2 thrusters, and present some performance results for the improved system.

4.3.1 Thruster Design

I show in Fig 4.5 an image of the RMFv2 thruster with some of the major components labeled. This new thruster shares a similar conical shape as the RMFv1; however, it is roughly 2/3rds the internal volume of the first. This was done in order to match the magnetic energy of the internal azimuthal electron current to available pulse electrical energy [83]. The conical thruster body is characterized by a cone with a half angle of 14°, a 20 cm exit diameter, and a length of 33 cm, where again a mica sheet serves as the plasma bounding surface. The majority of the remaining thruster structure, however, is constructed from dielectric FR4 and G10 fiberglass to minimize coupling losses to the thruster structure [83]. This includes the bobbins for the (now) three DC bias magnets, which again are designed to shape the field lines along the walls of the cone. These magnets are capable of generating magnetic

fields up to 240 G on thruster centerline. Sercel et al. provides a detailed analysis of the design considerations that went into the sizing of the v2 thruster in Ref. [80].

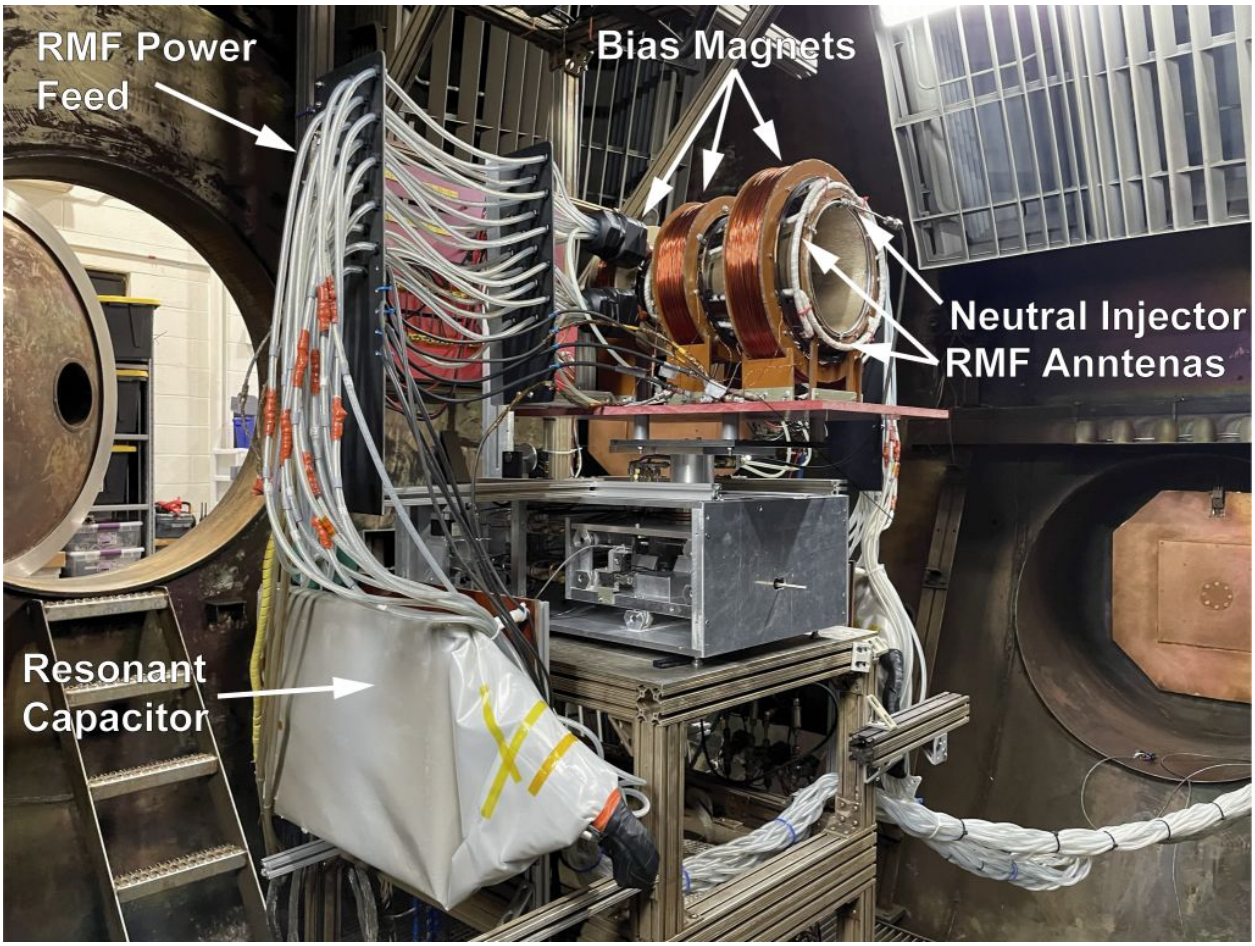

Figure 4.5: RMFv2 experimental setup and components.

While the significant adoption of dielectric materials may at first glance seem to forgo the flux conservers of both the v1 thruster and ELF, transient measurements of the currents through the bias magnets during plasma pulsed reveals that the plasma can induce on the order of 100 amp-turns on the bias magnet windings, thus allowing them to serve the role of flux conservers without introducing excessive conductive material for the RMF to inadvertently couple energy to.

We repurposed the same anode-cathode structure for the v2 thruster, and we again use a LaB6 hollow cathode to act as our pre-ionization source. For the v2 thruster, we again typically operate the cathode at 18 A discharge current to the anode and provide a small (15 sccm) amount of neutral xenon through the cathode bore. However, instead of using the rear injector from the v1 thruster, we incorporate a new upstream-facing annular neutral injector at the thruster exit plane to source the majority of the neutral propellant flow. This injector

serves two purposes: first, to increase the residence time of the neutrals to increase ionization, and second to increase gas density along the thruster walls near the RMF antennas for improved coupling. Injecting propellant along the coils has also been investigated previously in theta pinch thrusters by Hallock et al. and may have also contributed to improving their performance [36].

The RMF antennas are again constructed from 6.35 mm water-cooled copper tubing that is bent to form a set of two single-turn Helmholtz pairs that are oriented orthogonally to one another. The v2 thruster also employed improved voltage isolation techniques for the antennas. The antennas themselves are wrapped in a double layer of high voltage EPDM self-fusing tape followed with a layer of fiberglass tape. The RMF and water cooling lines are passed through submersion rated cable glands and are connected to the RMF antennas inside an acetal plastic shell that is subsequently potted with silicone sealant. RMF antennas are necessarily subject to high voltage to drive the high-frequency currents, and these connections are often a pain point for operating the thruster successfully. The antennas offer a similar coil constant to the v1 thruster antennas, providing $\sim$0.0625 G/A.

The largest change, however, to the RMFv2 thruster was the power processing unit. In the v2 thruster, the RMF is generated by a power processing unit developed by Eagle Harbor Technologies (EHT) [63]. This PPU employs a resonant sine inverter, where each of the two RMF antennas is connected in series to a 40 nF resonant capacitor bank located next to the thruster. This forms an LC circuit which is driven at its resonant frequency with a full bridge solid-state switching unit to produce kiloamp-level currents through the antennas. I show a schematic of the EHT PPU in Fig. 4.6.

This system was typically operated with a current amplitude of up to 1 kA, generating a weaker peak RMF than the v1 thruster at 20 kHz (approximately 50 gauss). However, a notable advantage of this system lies in its ability to sustain high-amplitude RMF application. The switching units can repeatedly pump energy into the LC tanks, allowing significantly higher RMF frequencies (up to 420 kHz for this unit). This is possible as the capacitance of the circuit is now independent of the input power. The elevated RMF frequency benefits both plasma heating, leading to enhanced ionization, and facilitates faster azimuthal electron velocities, thereby increasing the Lorentz force. In Fig. 4.7, a representative RMF current waveform for the v2 thruster under vacuum and plasma-loaded conditions is presented. This figure illustrates markedly different behavior than that shown in Fig. 4.4: the RMF currents are sustained for many (approximately 100) cycles, allowing the RMF to more effectively drive electron current. The visual contrast in height between the vacuum and plasma waveforms indicates successful energy coupling into the plasma.

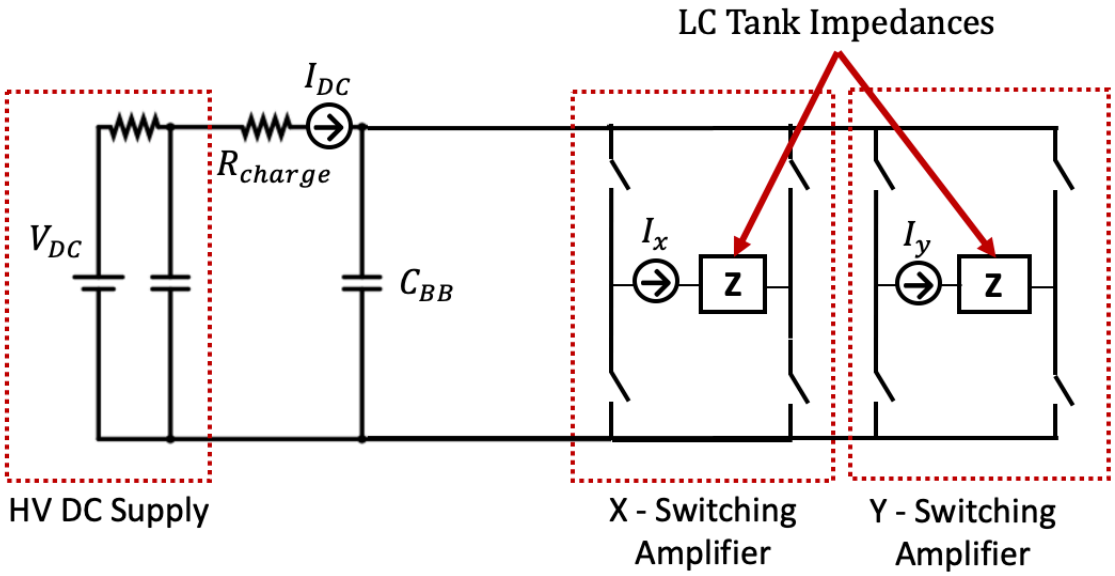

Figure 4.6: RMFv2 power processing unit circuit schematic.

4.3.2 Performance

I present in Fig. 4.8 plots of the main thruster performance criteria: thrust, specific impulse, and efficiency for the RMFv2 thruster as a function of specific energy (see Sec. 3.2.3). These plots include data from 67 distinct operating conditions where flow rate, RMF amplitude, bias magnetic field strength, pulse length, and pulse repetition rate were varied.

In these plots, particularly for specific impulse and efficiency, an interesting trend emerges. For low specific energy, we can identify a reasonably linear slope; however, for increasingly higher specific energy, this trend breaks, and we observe notably lower specific impulse and efficiency. I believe that this is the result of too little propellant for the RMF to deposit energy into at these high energies and low mass flow rates. Sercel performed a scaling analysis for the v2 thruster to identify optimum thruster volumes and propellant density for the available energy of the RMF [80], and this theory agrees with his interpretation. Ultimately, this effect led to an optimum propellant flow rate for this thruster of 4.0 mg/s (45 sccm) xenon to maximize overall propulsive efficiency. Albeit, all the performance metrics are very low with the highest performance of the RMFv3 thruster being 11.6 mN of thrust at 292 s specific impulse and 4 kW input power, resulting in an efficiency of 0.41 %.

The development and evolution from the RMFv1 to the RMFv2 thruster reflect a dedicated effort to address and overcome limitations encountered in the initial v1 iteration. The RMFv2 thruster introduces significant design enhancements and innovative features, resulting in improved performance and increased efficiency compared to its predecessor. This

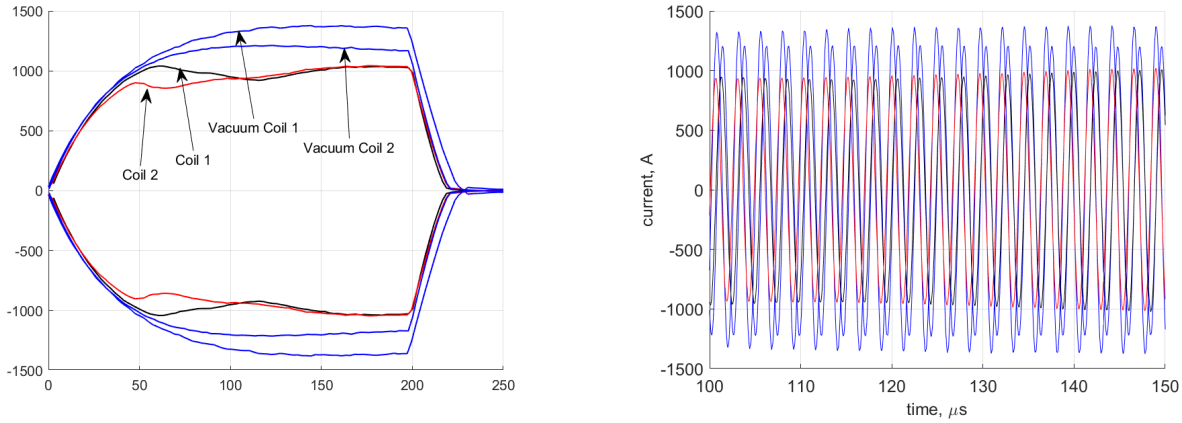

(a) Waveform envelopes

(b) Waveforms between 100 and 150 μs

Figure 4.7: RMFv2 waveform envelopes for typical 200 μs pulse. Blue curves show amplitude of equivalent vacuum waveform.

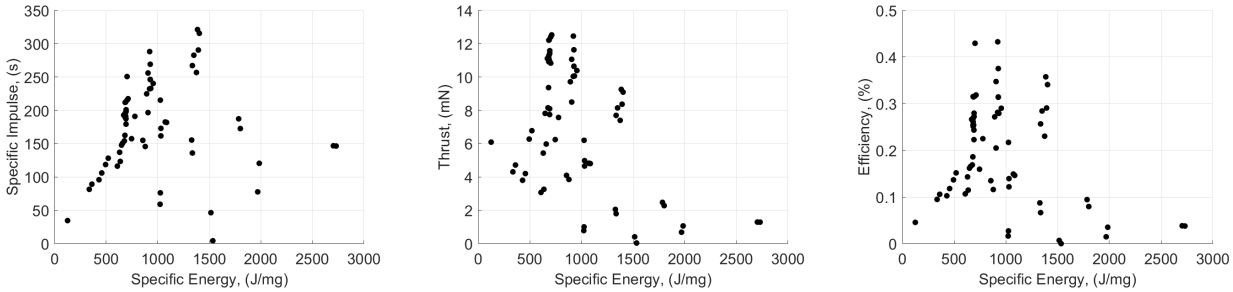

(a) I_{sp}

(b) Thrust

(c) Efficiency

Figure 4.8: RMFv2 performance parameters as a function of specific energy.

enhanced performance provided us with the opportunity to conduct a comprehensive set of experiments with this thruster. Our work included a wide range of performance measurements under various operating conditions, along with detailed plasma diagnostic probing, as discussed in Chapter 6. The development of the RMFv2 thruster represents a crucial step in advancing our understanding and capabilities of RMF propulsion systems.

Building upon the successes and limitations of its predecessors, this progress has been channeled into the latest iteration, the RMFv3 thruster. This thruster was designed to address the low performance of the v2 thrust and was primarily designed to operate in continuous wave (CW) mode to reduce the internal losses exhibited in the v2 thruster. The rationale for this is explained further in Sec. 7.2.

4.4 RMFv3 Thruster (2023-)

In this section, I will guide you through the design and construction details of the PEPL RMFv3 thruster, representing the latest advancement in our ongoing RMF thruster research. Similar to its predecessor, the v3 design is built upon insights gleaned from past experiments. In summary, the shortcomings of the RMFv2 thruster were

1. Low RMF uniformity, addressed in v3 with a three phase RMF system
2. Excessive thruster length, addressed in v3 with a shorter thruster body
3. Small static magnetic field in the radial direction, addressed in v3 with increase cone angle and magnetic field shape
4. Dispersion of seed electrons, addressed in v3 with off-center cathode source
5. Low RMF antenna coil constant, addressed in v3 with multi-turn antennas
6. Pulsed mode operation leading to high densities, addressed in v3 with RMF power system capable of continuous wave operation.

I explain these adjustments to the thruster's geometry, material composition, gas injection methodologies, RMF antennas, and power system in the remainder of this section. This begins with an examination of the thruster head, highlighting the modifications listed above from the v2 thruster. Following that, I will provide a thorough account of the design and development of the v3 power system.

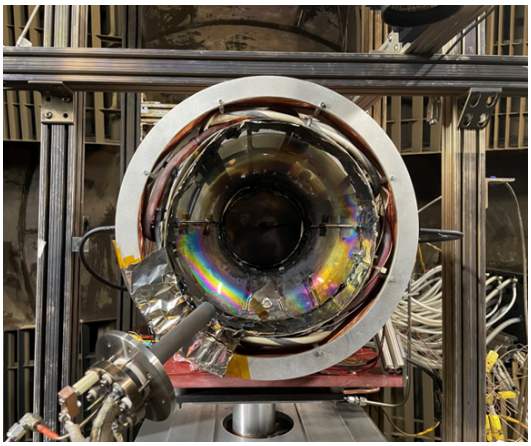

(a) End on view after experiments.

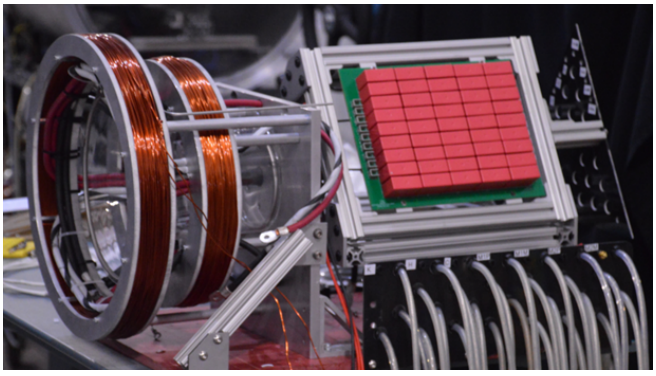

(b) Side on view during thruster assembly.

Figure 4.9: RMFv3 thruster installed for testing.

4.4.1 Thruster Design

4.4.1.1 Thruster Body

In Fig. 4.9, images of the PEPL RMFv3 thruster test article are presented, both after the completion of our experimental work and during construction. The v3 thruster body comprises a blown glass nozzle following the shape of a single air-core solenoid magnet. With a 14 cm initial diameter, a 25 cm exit diameter, and a length of approximately 15 cm, the thruster is now half as long, with twice the average radius, and exhibits more divergence compared to the v2 thruster. These modifications serve three purposes: first, the increased diameter promotes larger Lorentz force acceleration through a larger tangential velocity resulting from the larger radius (See Eq.3.18); second, the increased divergence angle enhances the radial component of the bias field along the wall, aiding in the applied field Lorentz force; and lastly, the reduced thruster length minimizes wall contact area with the plasma, reducing diffusion losses. This adjustment was informed by inductive probing measurements which indicated minimal azimuthal current drive near the upstream end of the RMFv2 thruster [82].

4.4.1.2 Bias Magnets

The steady magnetic field is primary produced by the main bias electromagnet located at the thruster's throat (the rightmost electromagnet in Fig.4.9b). An additional trim magnet downstream at the thruster exit shapes the magnetic field to contour the curved thruster wall. The bobbins of these magnets are constructed from aluminum, similar to the v1 thruster. However, they do not cover the same relative area as the v1 bobbins, resulting in reduced stray coupling losses. Despite this, the conductive bobbin rings enhance flux conservation over the v2 design. A standard map of the field produced by these magnets is presented in Fig.4.10. In the figure, the white boxes show the locations of the magnetic coils and the black line represents the curved thruster wall.

4.4.1.3 Neutral Injectors

The thruster incorporates two neutral injectors fed from independent mass flow controllers. The first annular injector is positioned at the thruster's throat, facing downstream, and the second is a pair of injectors located at 3 and 9 o'clock along the thruster wall, producing flow tangentially opposing the motion of the RMF. These wall injectors aim to disperse gas near the RMF antennas, providing benefits similar to the downstream injector in the v2 thruster.

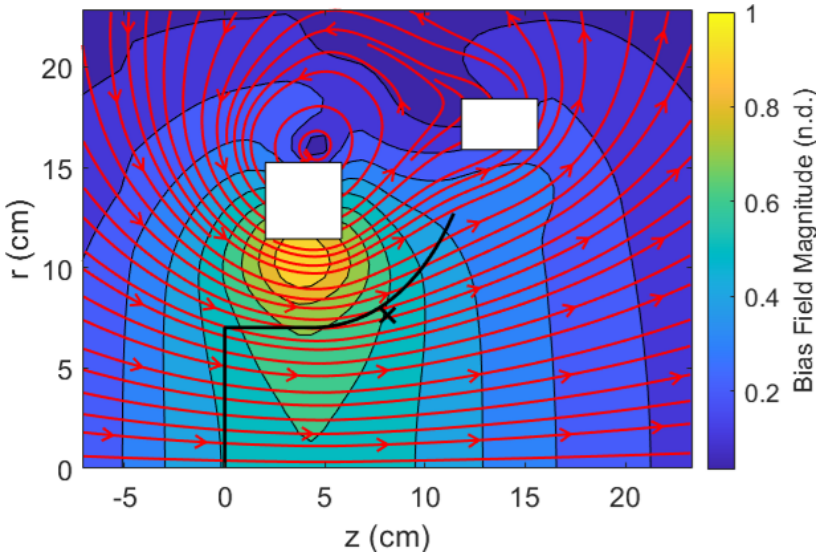

Figure 4.10: Typical bias field map for the RMFv3 Thruster.

4.4.1.4 Cathode

Similar to the first two RMF thrusters, the v3 thruster is equipped with a LaB6 hollow cathode serving as a seed ionizer. However, the cathode now departs from the thruster centerline, pointing into the thruster along the bias field off-axis (Fig.4.9b). This configuration promotes the coupling of seed electrons to the RMF by supplying them close to the antennas, akin to the neutral injectors. The cathode for the v3 thruster operates at a steady 3 A keeper current at 15 sccm xenon, without discharging to an anode. As demonstrated in Chapter 7, this current is unrelated to the thruster's beam current and could theoretically be replaced by an inductively-coupled radio-frequency or helicon source.

4.4.1.5 RMF Antennas

A significant change in the v3 thruster is the adoption of a three-phase RMF system. Unlike previous works employing two Helmholtz pairs for a two-phase RMF, we opt for a three-phase system to mitigate the effects of spatial harmonics in the rotating field. Hugrass (1986) [44] argued that odd-order harmonics induced by a finite number of antennas counteract the effects of the fundamental field, reducing performance, and a three-phase Helmholtz pair antenna can nearly eliminate these effects. Each v3 antenna consists of a double-turn Helmholtz pair constructed from stranded 4 AWG EPDM insulated copper cable. This construction has severe skin depth effects at the operating frequency of the system (400-420 kHz). As such, the skin depth at 420 kHz is 0.1 mm, resulting in an effective cross-sectional area for the 4 AWG wire of 3.23 mm^2 which is commensurate of the conductivity at DC of a

12 AWG wire. While braided litz wire would be a preferred solution to overcome skin depth effects, its availability in large cross-sectional areas with high voltage insulation is limited. Each antenna phase can be identified in Fig. 4.9a by the runs of black, red, and white-black striped cable and Fig.4.11 provides a computer render of one antenna phase wrapped on its mounting structure.

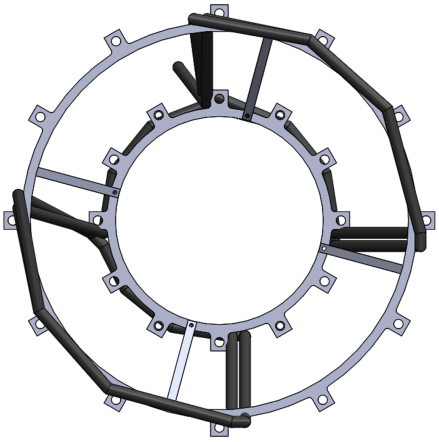

Figure 4.11: Render of single RMFv3 antenna coil.

In addition to enhanced RMF uniformity, the three-phase system offers other advantages. With the RMF phases no longer completely orthogonal, their overlap allows the fields of all antennas to superimpose, strengthening the field of an individual antenna. The total magnitude of the field is given by

$$|B| = \frac{1}{2} N_\phi B_i, \tag{4.1}$$

where, N_ϕ is the number of phases, and B_i is the magnetic field produced by a single antenna. Thus, our three-phase system is 1.5 times stronger than an equivalent two-phase system for the same currents. This, combined with the double-turn antennas, results in a v3 thruster coil factor of 0.13 G/A. I show in Fig. 4.12 the field produced by each of the RMF coils individually.

Furthermore, the three-phase power system exhibits a significant advantage in power delivery, as commonly observed in grid-level power distribution. Each antenna line serves as the current return path for the other two, reducing the overall conductor cross-section to deliver the same power. This is evident in the comparison between Fig.4.9 and Fig.4.5. Note the large number of transmission lines for the RMF coming off both sides of the v2 thruster relative to the smaller number coming off only the left side of the v3 thruster. This is further evidenced by the v3 thruster operating at over three times the maximum power level as

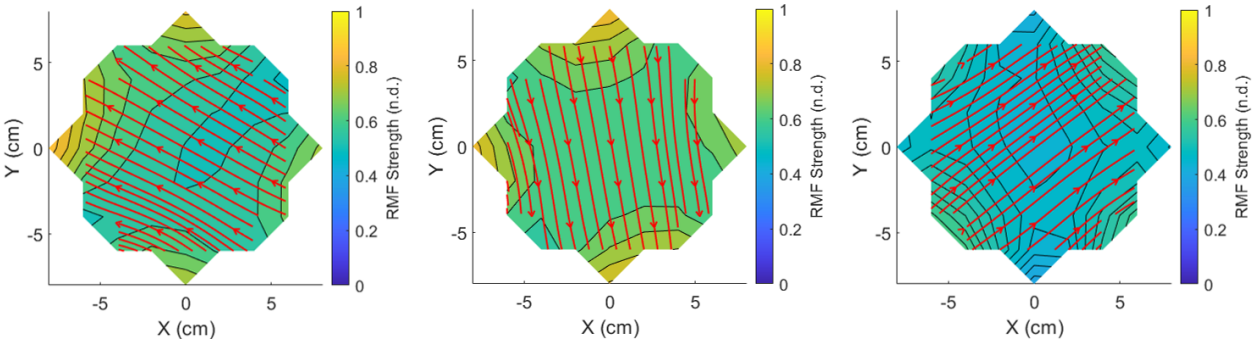

(a) Phase A (b) Phase B (c) Phase C

Figure 4.12: Field maps from each antenna phase of RMFv3.

the v2 thruster. The reduction of total transmission line size serves a practical purpose of reducing the thermal drift for thrust stand measurements, as there is less material heating up which can apply unintended forces to the thrust stand.

4.4.2 RMFv3 PPU Design and Development

RMF thruster power systems exhibit greater complexity compared to other electric propulsion systems, necessitating custom power processing units tailored to their unique demands. Custom power supplies are required to manage large currents at high frequencies (100-1000 A at 0.1 - 1 MHz) with precision phase control, a critical factor for thruster performance. High-power induction motor systems are not designed for operation at these high frequencies, and while induction heating systems operate at the correct frequency and power, to my knowledge, they never implement more than a single phase. Due to these limitations of off-the-shelf power systems, there is a need to design and characterize bespoke PPUs for use with RMF thrusters.

In this section, I describe the design and construction of the power processing unit central to the PEPL RMFv3 thruster. For the experiment presented in chapter 7, we have chosen to explore the thruster's operation in both the typical pulsed mode for inductive thrusters and a continuous wave mode, where the RMF is applied at a 100% duty cycle. This significant change, in addition to the adoption of a three-phase RMF power system, has prompted the development of this third RMF power processing unit.

I show in Fig. 4.13 a schematic of the primary circuit configuration for the UM three-phase RMF PPU. This system works by exciting a resonant capacitor bank in series with each RMF antenna with a voltage square-wave to drive high amplitude currents through the antennas. The capacitance of each bank is selected such that, along with the inductance

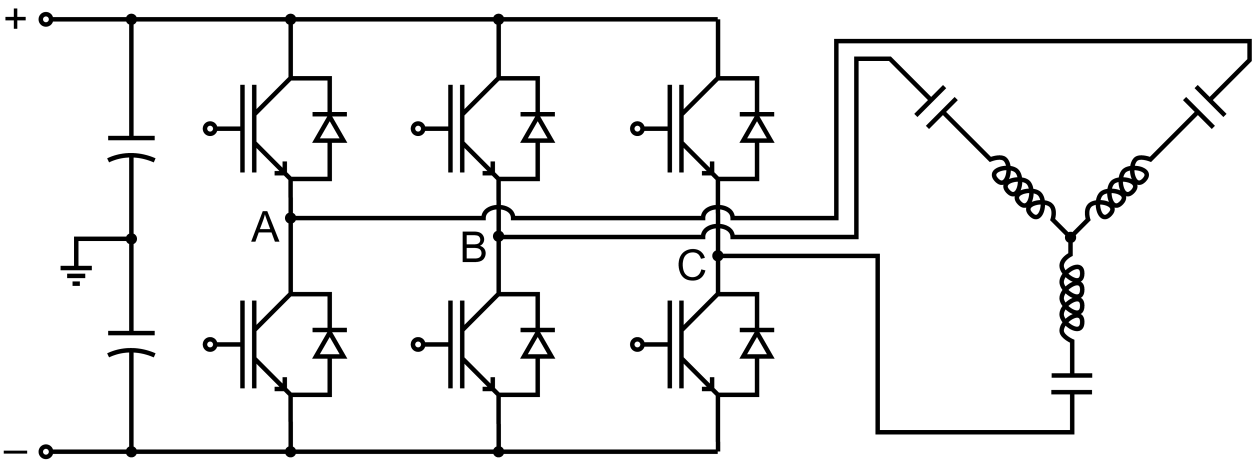

Figure 4.13: RMFv3 power processing unit circuit schematic.

of the antenna, it forms an LC resonator at the desired RMF frequency. As a result, when the LC resonant tanks are driven at their resonant frequency the current is only limited by the real resistance of the circuit. This resistance is typically small on the order of 100's of mΩ, therefore large currents can be generated with relatively low voltages. The excitation voltage is produced by the three half-bridge IGBT units, labeled in accordance with their phase, A, B, and C, in Fig. 4.13. This excitation signal is produced by periodically switching connections to the positive or negative terminal of a DC voltage supply. Take phase A for instance. During the first half cycle of phase A the high side (top) switch of channel A is closed, and the low side (bottom) switch is open. This connects the the phase A resonant capacitor to the positive DC rail. During the second half cycle the high side switch opens, and the low side switch closes. This connecting the resonant capacitor to the negative voltage rail. This produces a voltage square wave on the capacitor bank with an amplitude of half the DC supply voltage at the RMF frequency. This is often several hundred volts and can produce kiloampere level currents in the antennas.

In power electronics literature, the configuration described above would be known as a series-loaded resonant sine inverter, with a primary advantage being low voltage constraints on the driving silicon switches, which only see the several hundred volts square wave [64]. In contrast, the resonant capacitors and antenna will experience tens of kilovolts to drive antenna currents in the kiloampere range. Additionally, the three LC tanks in this system are arranged in a balanced wye configuration. This means that the current return path for each phase is through the other two, and practically in a balanced three-phase system no charge builds up on the neutral connection point. The wye configuration was adopted to maximize the antenna current for the available current capacity of the switching units. This

is desirable as we aim to maximize the RMF strength.

4.4.2.1 Experimental Data

I show in Fig. 4.14 the waveforms for the RMFv3 PPU in vacuum and under plasma loaded conditions for a 200 μs pulse length. Similar to the RMFv2 waveforms in Fig. 4.7, this plot shows noticeable coupling between the plasma-loaded and vacuum conditions as seen by the difference in height between the vacuum (blue) curves and plasma-loaded (black, red, and gray) curves. The noticeable difference between these v2 and v3 is the additional coil phase in the v3 system.

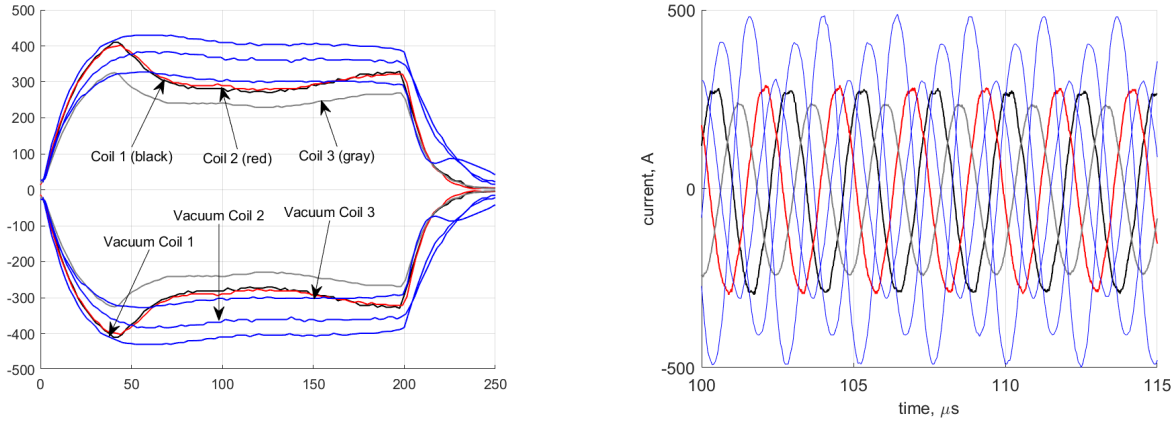

(a) Waveform envelopes

(b) Waveforms between 100 and 115 μs

Figure 4.14: RMFv3 waveform envelopes for typical 200 μs pulse. Blue curves show amplitude of equivalent vacuum waveform.

4.4.2.2 DC Supply

The system is fed by a high-voltage Magna-Power MT Series 1000V 150A DC source. The DC power is directed into a set of large filter capacitors that provide a positive and negative voltage rail with respect to facility ground for the inverter. These are shown as the polarized capacitors on the left side of Fig. 4.13. In practice, these capacitors primarily serve as energy storage for pulsed mode operation of the thruster. The DC capacitors are two Sprague Powerlytic 36D 2500 μF 350 V, and this bank is capable of storing 300 J combined at a maximum of 700 V.

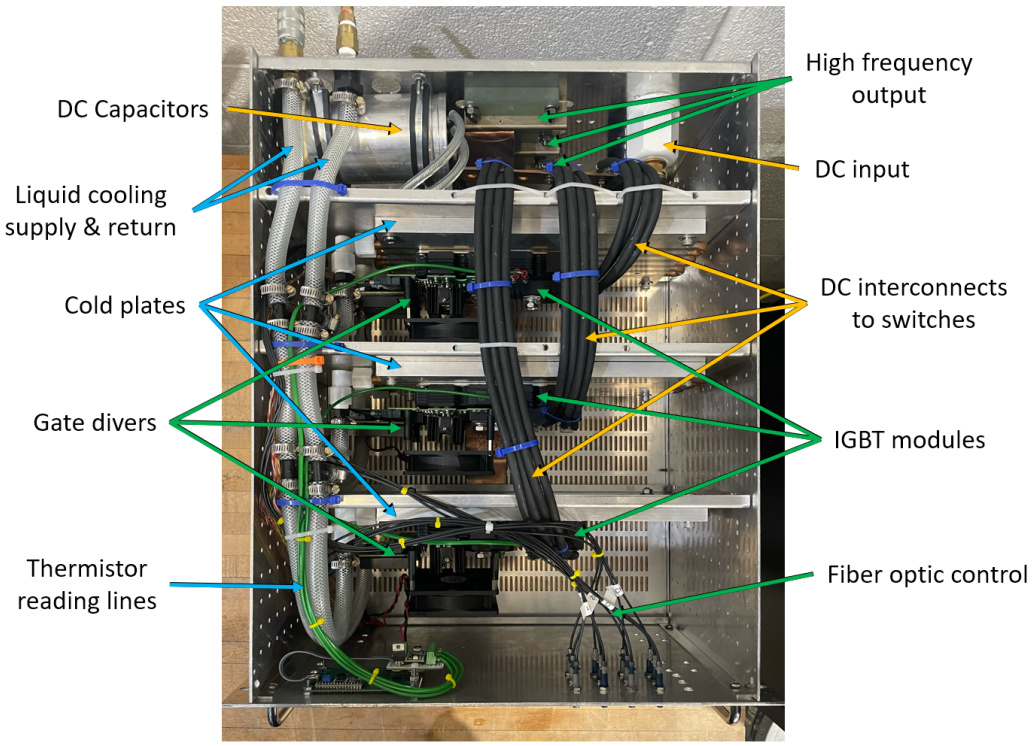

Figure 4.15: RMFv3 power processing unit with primary components labeled.

4.4.2.3 IGBT Switches

At the core of the circuit are six independent IGBT switches, each driven by an isolated gate driver. The selected switches are three Infineon FF450R12IE4 1200 V 450 A dual IGBT modules. These IGBTs are mounted on Aavid 416201U00000G 17.8 cm by 30.5 cm aluminum cold plates using silicone thermal paste for efficient heat dissipation. Cooling is facilitated by a 5 kW recirculating liquid chiller, operating with a 1:1 water-glycol mixture. The cooling lines are depicted on the left side of Fig. 4.15.

For this application, solid state switches with high current capacity with minimal gate charge are critical, enabling the system to operate at high frequency and high RMF strength. The operating frequency, given a fixed driver power, is determined by the expression:

$$\omega = \frac{2\pi P_{\text{driver}}}{\Delta V Q_{\text{gate}}}, \tag{4.2}$$

where P_{driver} represents the driver power, ΔV is the gate voltage, and Q_{gate} is the gate charge [4]. For the RMF, it is desirable to maximize both the current and frequency (See Eq. 3.18), leading to a figure of merit for switches that we aim to minimize:

$$\tau_s = \frac{Q_{\text{gate}}}{I_{\text{max}}}, \tag{4.3}$$

where I_{max} is the maximum rated device current. In principle, τ_s physically scales with the minimum switching time for a semiconductor. Fig. 4.16 illustrates τ_s for a selection of IGBT discretes and modules from Infineon, a major high-power semiconductor manufacturer [91].

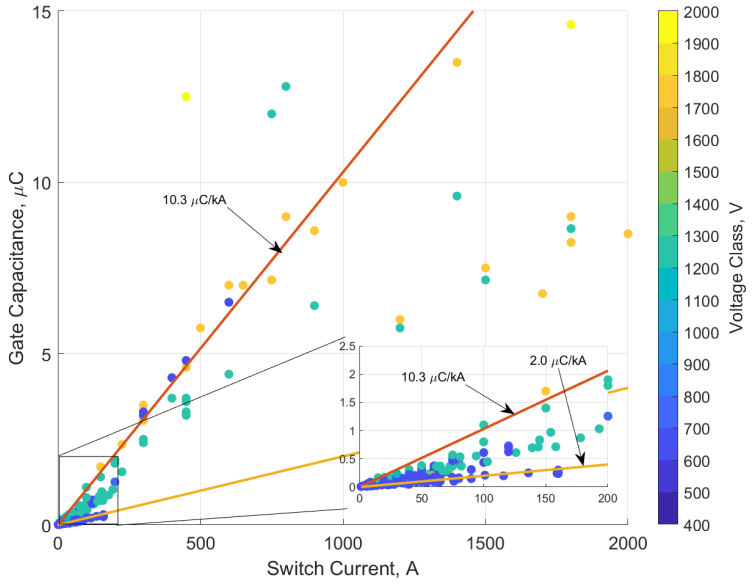

Figure 4.16: IGBT gate capacitance scaling with rated current.

The figure reveals generally two populations of constant τ_s corresponding to the discretes (single semiconducting unit per package with low current and voltage ratings) and modules (multiple semiconducting units per package with high current and voltage ratings). On average, for the modules, $\tau_s \approx 10.3\,\mu$C/kA, although some outperform this average. For the discretes, $\tau_s \approx 2.0\,\mu$C/kA on average, representing roughly the minimum possible value. Concerning our IGBT modules, with a gate charge of 3.2 μC, we achieve $\tau_s = 7.1\,\mu$C/kA—a comparatively low value for high current modules. A similar analysis for a selection of MOSFET semiconductors [91] indicates that τ_s can be as low as $0.2\,\mu$C/kA, which is expected given the high frequency at which these devices operate. However, if the search is restricted to products with a voltage rating above 500 V—a reasonable requirement for high-power applications—the recovered $\tau_s \approx 2.0\,\mu$C/kA is identical to that of small IGBTs.

Applying Eq. 4.2 for our selected IGBT modules and operational frequency (420 kHz) gives a required driver power of roughly 33 W per switch (200 W total). For the v3 system, I modified commercial-off-the-shelf Power Integrations 2SP0320V2A0-12 dual gate driver

modules capable of producing 3 W gate drive power per switch. I increased the output power capability by over an order of magnitude with several modifications. I bypassed the stock DC/DC isolation circuitry, replacing it with two CUI inc. PQAE50-D24-S24-D DC/DC 50 W isolation converters per board. I also replaced the manufacturer-recommended Vishay 2 W gate resistors with a parallel combination of two Ohmite AP8511RF 50 W 1 Ω power resistors for gate turn-on (resulting in 0.5 Ω turn-on gate resistance) and a parallel combination of two Ohmite TCH35P3R30JE 35 W 3.3 Ω power resistors for gate turn-off (resulting in 1.65 Ω turn-off gate resistance). These resistor pairs were mounted back-to-back on Aavid 531002B00000G finned heatsinks with silicone thermal paste. Additionally, I attached Cooling Source CS9461010BM 10x10x10mm finned heatsinks to each of the Power Integrations driver cores with fast-cure epoxy. Above each board, I mounted a 92x92mm 12 V PC fan directed downward to enhance cooling to the heatsinks.

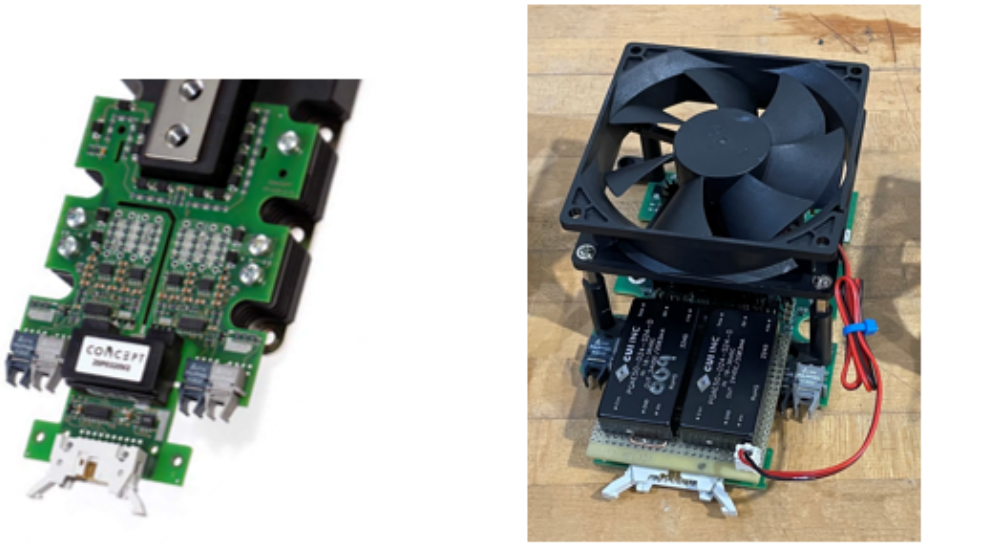

Figure 4.17: Upgraded gate driver boards for RMFv3 power processing unit.

Power was provided to the IGBT gate drivers from a 36 V 15 A DC power supply, maintained at a constant 18 V. The drivers are controlled with fiber optic signals from an Eagle Harbor Technologies FT4x4 fiber optic transmitter, along with two additional Eagle Harbor Technologies FT-1 fiber optic transmitters, providing a total of six channels of fiber optic command. The transmitters are regulated through TTL signals from a BNC 525 six-channel delay/pulse generator operating at the switching frequency. The channels are divided into three pairs, A, B, and C, corresponding to the three RMF phases and are commanded

120 degrees out of phase. Phase B and C are consistently commanded with a phase delay of 1/3 and 2/3 of the RMF period, $2\pi/(\omega)$ relative to phase A. For pulsed mode operation of the thruster, the pulser's output is gated by an external signal generator with a square wave at the desired thruster duty cycle and pulse repetition frequency. This setup is shown in Fig. 4.18

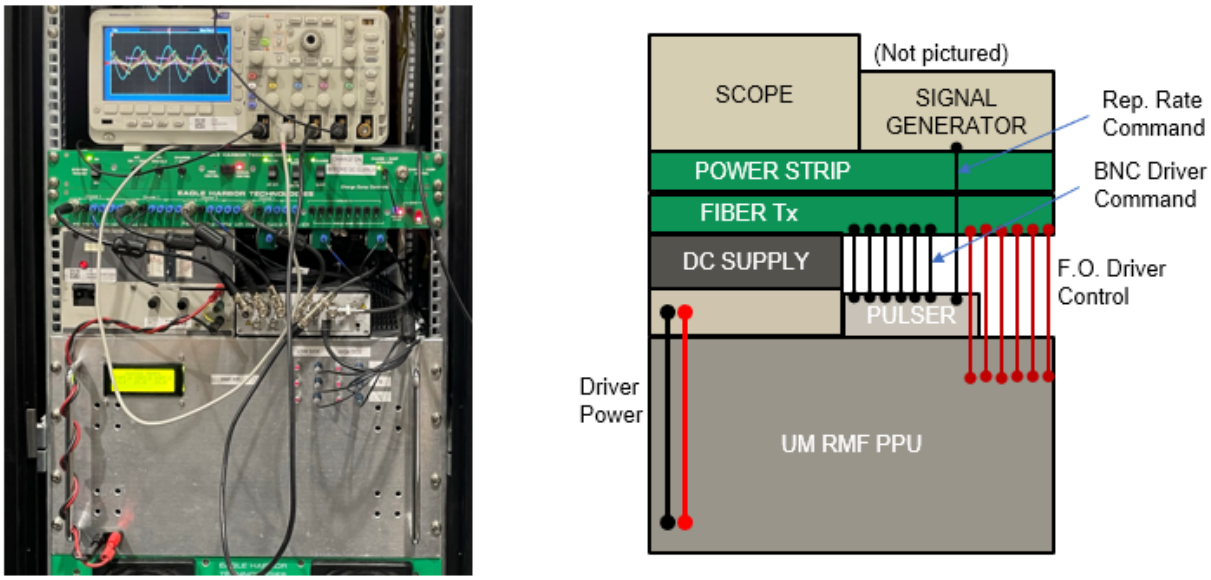

Figure 4.18: RMFv3 power processing unit control overview.

The BNC 525 pulser needs to be operated in a particular manner to achieve the desired switching for the three phase system. The BNC 525 sets the pulse frequency through a global system clock rate. Each of the six independent output channels has essentially two settings that dictate the output based on this clock rate, a delay time after the clock pulse is acknowledged, and a pulse width to turn the output on for. A quirk of this system, is that the output channels cannot acknowledge a clock signal if they are in the "on" state during the pulse width. This becomes a problem for the offset phases B and C that require long delay times of 120 and 240 degrees relative to phase A, and as a result they will not be able to "see" every other clock signal and will drop pulses.

To avoid this effect, the clock period of the BNC pulser is set to half the desired RMF period $T_0 = \pi/\omega$. This provides extra clock signals such that phases B and C can read them in between their respective on cycles. In this scheme, phase A is commanded to "wait" and do nothing for these extra signals. This scheme for the commands sent by the BNC 525 pulser is illustrated in Fig. 4.19 which facilitates the required delay settings for 120-degree offsets without switching interruption.

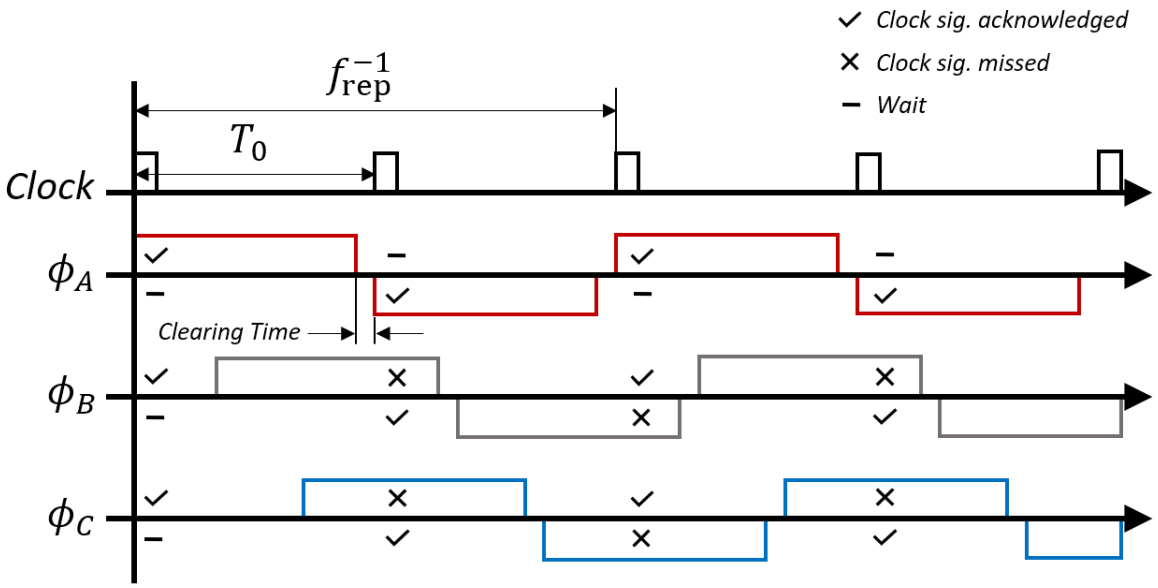

Figure 4.19: RMFv3 power processing unit switch command scheme.

A clearing interval is established for each phase between high and low cycle commands from the pulser. This "dead time" is necessary to prevent shoot-through between the two PPU voltage rails when both switch sides (high and low) are partially conducting. A constant clearing interval of 250 ns is used for our testing, found to be optimal for reducing unloaded PPU power consumption when switching at representative frequencies. Fig. 4.20 displays the normalized power consumption for a single phase as a function of clearing interval time.

4.4.2.4 Resonant Capacitor Banks

Each of the three RMF antennas is connected in series with a resonant capacitor bank positioned directly behind the thruster body inside the vacuum chamber. The capacitance of the banks is designed such that the resonant frequency of each series LC tank equals the desired RMF frequency. The resonant capacitor banks are mounted on a triangular frame close to the thruster to balance and minimize stray inductance as shown in Fig. 4.9b.

Each capacitor bank is constructed from a series-parallel array of smaller capacitors. This strategy allows for a somewhat unbounded maximum current and voltage ratings at the expense of array size/weight. However, the design of the capacitor array is subject to several constraints. Firstly, the target capacitance must be the appropriate value for the thruster antenna inductance and operating frequency, given by

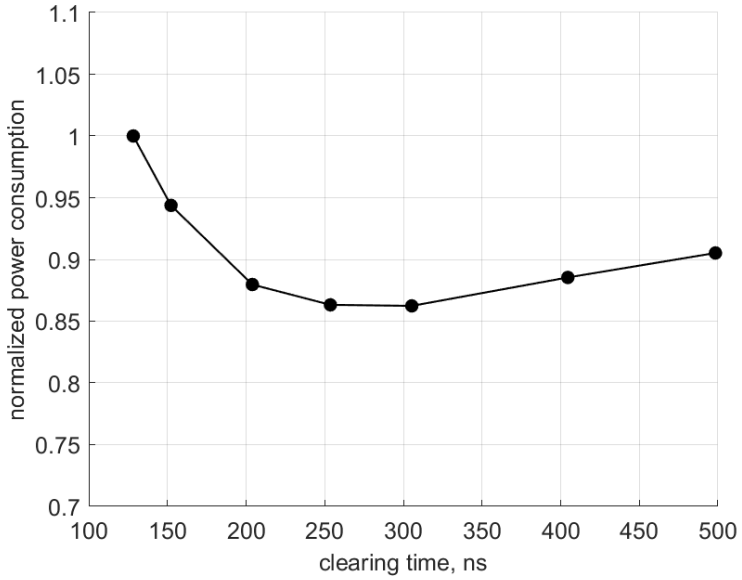

Figure 4.20: Normalized unloaded PPU power as a function of switch clearing time.

$$C = \frac{1}{L\omega^2}, \tag{4.4}$$

where L is the antenna inductance, and ω is the RMF frequency in rad/s. Second, a unit capacitor in the array must have a capacitance

$$C_i = C\frac{N_s}{N_p}, \tag{4.5}$$

where N_s is the number of series capacitors, and N_p is the number of parallel capacitors. Square arrays, $N_s/N_p \approx 1$, are desirable as they are often the most compact. The above equation shows that for a square array, the unit capacitance should be close to the capacitance of the full array.

Lastly, the most restrictive constraint is typically the AC voltage rating of the capacitors, as the large high-frequency currents in the antennas necessitate large AC voltages. The required voltage magnitude is

$$V_\omega = \omega L I_\omega. \tag{4.6}$$

Both the DC and AC voltage ratings of the capacitor bank must be larger than this voltage by some safety margin. Exceeding the DC voltage rating will result in dielectric breakdown, and exceeding the AC voltage rating will result in overheating of the capacitors. In practice, the DC rating almost always exceeds the AC rating, so the more restrictive AC

rating is used to guide the design.

For an array, the AC voltage rating of a capacitor unit is governed by

$$V_{i,AC} > \frac{\omega L I_\omega}{N_s}, \tag{4.7}$$

where the total array voltage is split between each series element, N_s. This is a direct result of the governing impedance relation for ideal capacitors. I can also turn this expression into a constraint for the parallel number of elements. Using Eq. 4.4 and 4.5 in the above expression I can write:

$$V_{i,AC} C_i > \frac{I_\omega}{N_p \omega}. \tag{4.8}$$

I can combine these two expressions and rearrange to give a requirement on the total number of capacitors in our array:

$$N_p N_s > \frac{L I_\omega^2}{C_i V_{i,AC}^2}. \tag{4.9}$$

This equation implies that for a small array the maximum peak energy storage of a unit capacitor, $C_i V_{i,AC}^2$, should be as large as possible. By similar reasoning, I can also state that the total volume and weight of the capacitor bank is driven by the energy storage density of the chosen unit capacitor.

We these constraints in mind, I provide the following guidance on unit capacitor selection:

1. Choose a capacitor candidate with high energy density within the same order of magnitude as the required array capacitance.

2. Apply Eq. 4.5 to identify the correct ratio of series and parallel elements N_s/N_p.

3. Apply Eq. 4.9 to calculate a total number of array elements with some safety factor, typically 2-4x.

4. The dimensions of the array are as follows: $N_s = \sqrt{(N_s N_p)(N_s/N_p)}$ and $N_p = \sqrt{(N_s N_p)(N_s/N_p)^{-1}}$.

Note: In applying this algorithm, it is critical to realize that for film capacitors, $V_{i,AC}$ is typically de-rated proportionally as frequency increases into the RF range. Film capacitors are desirable for this application as they exhibit high power density at the proper capacitances. However, high-performing ceramic capacitors may also be a suitable choice, especially if lower capacitances are required as the target frequency is increased.

Following this guidance, the v3 thruster capacitor banks consist of a five series by nine parallel array of WIMA FKP1X022207E00JSSD 22 nF polypropylene film capacitors. This array has a total capacitance of 39.6 nF and a continuous working current of 90 A peak. The capacitors are soldered to a 1.57mm thick FR4 printed circuit board, with 140 μm deep x 160 mm wide copper traces. The capacitor arrays are then potted with clear epoxy resin for in-vacuum high-voltage insulation. I show a picture of one resonant capacitor bank installed behind the thruster for testing in Fig. 4.21.

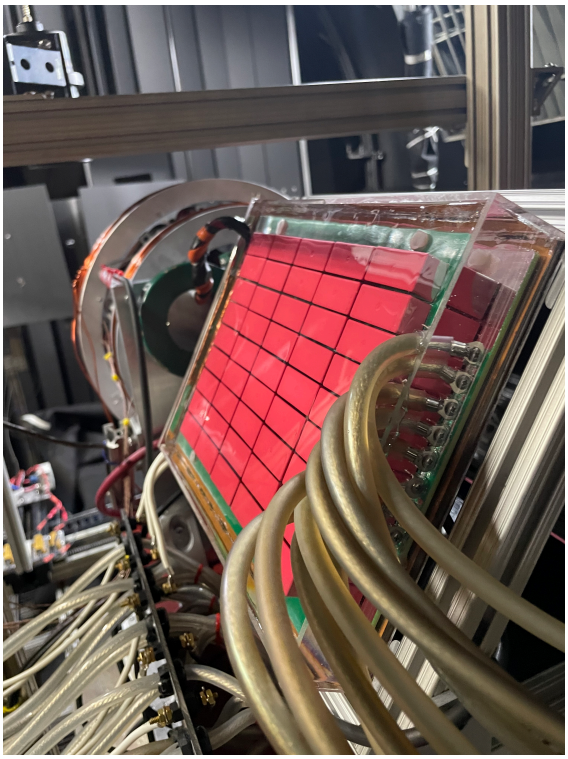

Figure 4.21: Image of RMFv3 thruster resonant capacitor bank.

4.4.2.5 Transmission Lines

The thrusters are tested under high vacuum conditions (see Sec. 5.1), and as such the RMF PPU need to feeds power to the thruster via a set of transmission lines. These lines are necessary as the cooling requirements of the PPU make it infeasible to put it under vacuum conditions. The transmission lines are constructed as braided triplets with one conductor per phase. This was done to reduce stray inductance in the line which can alter the resonant frequency of the thruster and diminish the antenna current amplitude. The total transmission line is a set of 10 parallel triplets (30 total conductors). Each conductor is a flexible 12 AWG silicone-insulated wire with a DC voltage rating of 42 kV and an outer diameter of

0.30 in.

I can estimate the complex impedance for this transmission line (following Ref. [88]) by assuming each twisted triplet is equilaterally spaced, and the parallel bundles have no cross-talk. Under these assumptions the phase inductance per length of each triplet is:

$$L' = \frac{\mu_0}{2\pi}\left(\frac{1}{4} + \ln\left(\frac{D}{a}\right)\right), \tag{4.10}$$

where D is the distance between conductor centers and a is the conductor radius. The total inductance per phase is then

$$L = L'\frac{l_{\text{line}}}{N_{\text{line}}}, \tag{4.11}$$

where l_{line} is the transmission line length, and N_{line} is the number of parallel triplets. Similarly, a phase-to-neutral capacitance per length is

$$C' = \frac{2\pi\varepsilon_0}{\ln(D/a)}, \tag{4.12}$$

where ε_0 is the vacuum permittivity. The total capacitance to neutral per phase is then

$$C = C' l_{\text{line}} N_{\text{line}}. \tag{4.13}$$

Lastly, the resistance of each phase in each triplet per unit length is

$$R' = \frac{\rho}{\pi(a^2 - (r-\delta)^2)}, \tag{4.14}$$

where ρ is the conductor resistivity, and $\delta = \sqrt{2\rho/(\omega\mu_0)}$ is the skin depth in the conductor. The total resistance per phase is

$$R = R'\frac{l_{\text{line}}}{N_{\text{line}}}. \tag{4.15}$$

The total length of these transmission lines is 7 m. This is a result of the vacuum chamber size. Using the above equations, the characteristic impedances for our transmission line are an inductance of 660 nH, a capacitance of 3.3 nF, and a resistance of 40 mΩ.

Two custom high-voltage vacuum feedthroughs were used to seal around the 21 conductors. Each feedthrough consists of a central nylon core that seals to the vacuum chamber with a rubber O-ring. The cable ends are brazed to an epoxy-potted central copper stud. On either side of the feedthrough surrounding the copper stud is a PPE sleeve that extends 4 cm past the copper joint. Three layers of offset PVC heat shrink are used to seal the silicone wire insulation to the PPE sleeve. I show a computer model cross-section of this

construction alongside a photo of the transmission line assembly in Fig. 4.22.

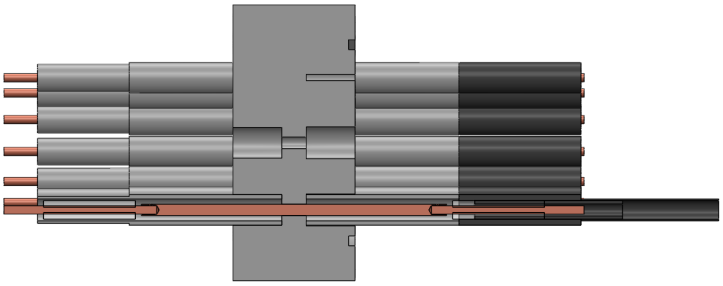

(a) CAD Model of vacuum feed through

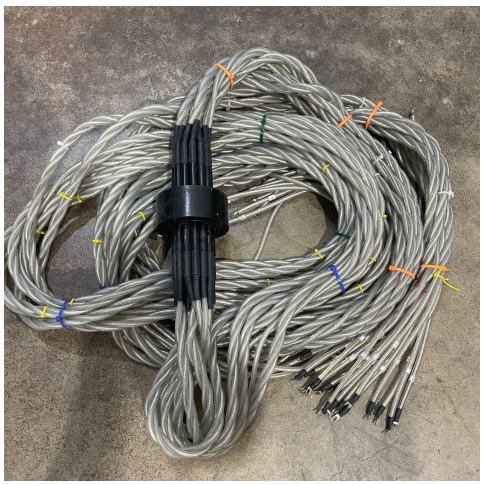

(b) Assembled transmission line

Figure 4.22: RMF transmission lines.

4.4.3 Performance

Moving forward to the RMFv3 thruster performance trends, I present in Fig. 4.23 and 4.24 the same plots as shown above for thrust, specific impulse, and efficiency. However, I have split up these plots into results for the pulsed operational mode and the continuous wave operational mode. These plots indicate the performance trends of the RMFv3 thruster across many operating conditions where parameters such as pulse length, power, duty cycle, flow rate, gas injection location, and magnetic bias field were varied. These varying operating conditions explain the variation in these plots at the same or similar specific energies.

The pulsed mode results exhibit a similar trend into the high specific energy end as for the v2 thruster which ran exclusively in pulsed mode (see Fig. 4.8). These plots show that all the performance metrics eventually show a negative trend with increasing specific energy. There may still be a steep increase near the low specific energy range, as was the case for the v2 thruster; however, this is difficult to identify in these plots. Ultimately, these results are very telling for the operation of these devices in pulsed mode, as the trend is not in line with what is seen for other inductive thrusters (see Sec. 3.2.3 and Ref. [71]). It is problematic for the scaling of these devices that the performance deteriorates as the energy per unit propellant is increased. This indicates that energy supply is mostly wasted as it is not going towards increasing the exhaust velocity of the propellant.

With that said, however, the continuous wave (CW) mode results show a completely

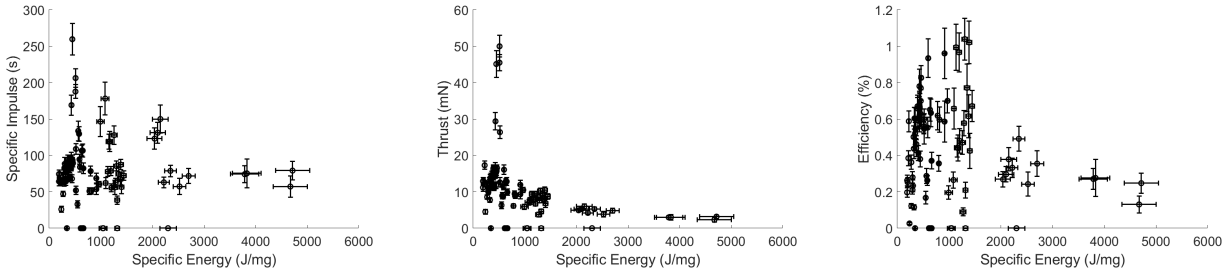

(a) I_{sp} (b) Thrust (c) Efficiency

Figure 4.23: RMFv3 pulsed mode performance parameters as a function of specific energy.

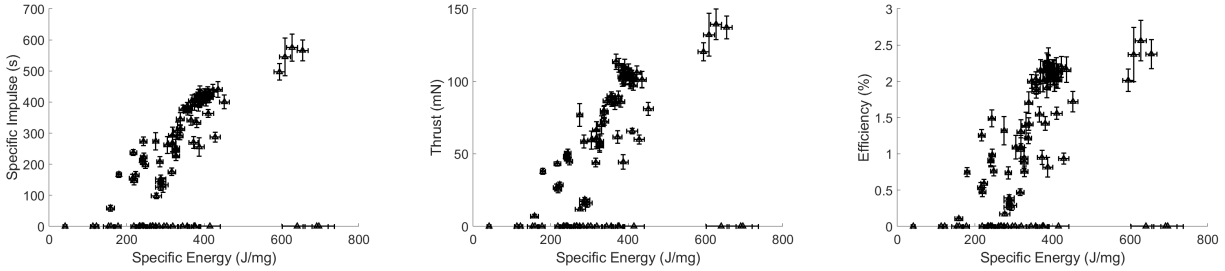

(a) I_{sp} (b) Thrust (c) Efficiency

Figure 4.24: RMFv3 continuous wave mode performance parameters as a function of specific energy.

different trend. In these plots, there is a strong correlation between the performance metrics and increasing specific energy. This is intriguing as this mode necessarily forgoes any I^2 thrust scaling and instead relies solely on the applied field for the Lorentz force (See Chapter 7). In this way, we should expect a CW mode RMF thruster to exhibit scaling similar to that of an applied field MPD thruster. However, if the applied field is increased in tandem with the driven current (which was largely the case for how we ran the experiment), the linear trend in these plots is expected behavior. This distinct change in performance scaling characteristics between pulsed and CW mode is what motivated the study presented in chapter 7 where I compare the component phenomenological efficiencies the RMFv3 thruster operating in both modes.

Interestingly, there are many null cases for the CW mode, where we measured zero thrust. These cases largely represent operating conditions where the applied field was dominant over the RMF field. This effectively quenches the azimuthal current drive, and in these cases, the thruster is unable to ignite.

To illustrate this effect, I show in Fig. 4.25 a plot of thruster efficiency in the CW mode as

a function of applied bias field strength. This is plotted for two different operating conditions, the first is a flow rate of 240 sccm xenon with an RMF strength of 13.6 G, and the second is for 257 sccm xenon and 20.5 G RMF. These plots show that there exists an optimum bias field for a given flow rate and RMF strength. This agrees with the theory presented in Sec. 3.2, Eq. 3.18 that the bias field acts as a opposing magnetizing force to the RMF and inhibits azimuthal current drive. The reason these curves have an maximum is that the radial component of the bias field is primarily responsible for increasing the Lorentz force thrust. This has the effect of increasing efficiency up to a point, then the electrons lose magnetization to the RMF and azimuthal current and efficiency begins to drop. However, Eq. 3.18 does not fully explain how swiftly the performance deteriorates, particularly in the 257 sccm case. Indeed, Eq. 3.18 predicts a smooth function of azimuthal current in regards to bias field strength. This rapid quenching of the RMF discharge is not fully understood and has been attributed to the interplay between flow rate, RMF strength, and ionization rate [78]. I discuss this further in Chapter 8 and present a theoretical model to explain its onset.

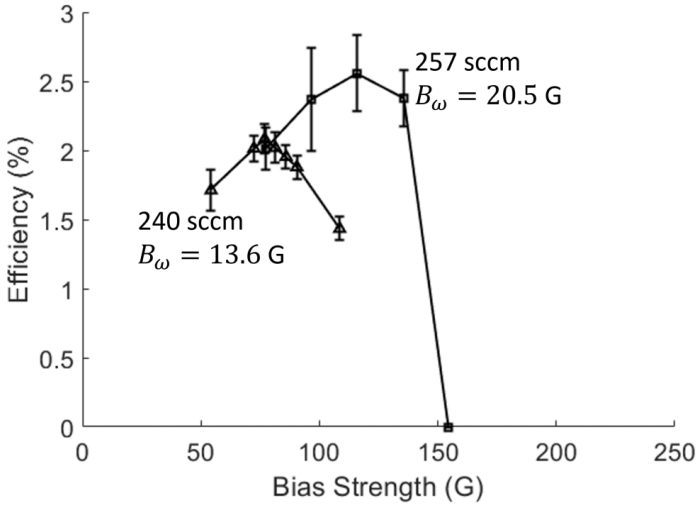

Figure 4.25: Continuous wave mode quenching effect. Reproduced from Ref. [78].

4.5 Summary

In this chapter, I described the details of the three RMF thruster prototypes developed at the University of Michigan. The development of these thrusters took place over five years and were initially inspired by the Electrodeless Lorentz Force Thruster (ELF) from MSNW.

The design iterations from the RMFv1 thruster through the RMFv3 thruster incorporated changes to the size and aspect ratio of the thrusters, their materials, the neutral injection schemes, RMF frequency, and importantly their power system architectures.

Table 4.1 summarizes key performance metrics for the three RMF thruster prototypes described earlier in this chapter. While these performance numbers may not be deemed impressive for high-performing electric propulsion systems, it is crucial to highlight the steady improvement between RMF generations. This performance trend culminates with a maximum thrust of 145 mN at a specific impulse of 600 s for the RMFv3 thruster. Although these figures are commendable for EP systems of the size of the RMFv3 thruster, it is noteworthy that the RMF consumes a substantial amount of power, resulting in a poor system efficiency of 2.8 %.

Table 4.1: Comparison of RMF Thruster Prototype Performance

Metric	RMFv1	RMFv2	RMFv3
Input Power	< 1 kW	< 4 kW	< 15 kW
RMF Frequency	20 kHz 125 kHz	420 kHz	413 kHz
Peak RMF Current	2 kA @ 20 kHz 400 A @ 125 kHz	1 kA	450 A pulsed 90 A CW
Coil Constant	0.06 G/A	0.06 G/A	0.13 G/A
Pulse Length	50 μ s	< 200 μs	< 30 s
Max duty cycle	1.5 %	3 %	100 %
Max Thrust	–	12.5 mN	145 mN
Max ISP	–	320 s	600 s
Max Efficiency	–	0.4 %	2.8 %

In this chapter I further presented performance results of the RMFv2 and RMFv3 thrusters as a function of specific energy. The negative trends observed for the v2 thruster and the v3 thruster in pulsed mode ultimately indicate that the energy transfer in the pulsed mode is not effective, and there's a fundamental difference in how the RMFv3 thruster operates in the continuous wave mode. Considering the known low overall efficiency of these thrusters, my goal is to measure discharge and plasma characteristics to clarify these performance trends and the overall efficiency. I aim to address these open questions in the next three chapters.

CHAPTER 5

Experimental Methods and Analysis Techniques

In this chapter, I describe the test equipment, diagnostic tools, and analysis methods utilized for the experimental results presented in Chapters 6 and 7. The majority of the experimental work in this thesis revolves around plasma diagnostic probing of the RMF version two and three thrusters to inform terms in the phenomenological efficiency model (See Chapter 3). These thrusters are tested under vacuum conditions and are typically operated in a pulsed mode, where a high amplitude RMF pulse produces discrete impulse "shots" several hundred times per second. The RMFv3 thruster, however, was also operated in a continuous (CW) mode where the RMF is applied continuously. The RMF systems on these thrusters are operated un-loaded in vacuum and loaded with plasma to characterize the power transfer. These terms: shot, pulsed, CW, plasma-loaded, vacuum-condition, ect., are referenced throughout this chapter.

I begin this chapter with a description of the vacuum test facility and infrastructure as well as a description and analysis procedures of the inverted pendulum thrust stand. While this work does not focus on direct thrust measurements for the RMF thrusters, I feel it is important to include here for completeness as I reference thrust measurements for comparison to the probe data.

The diagnostics used include a far-field guarded Faraday probe and retarding potential analyzer, near-field triple Langmuir probes, and current transformers to measure the waveforms through the RMF antennas. Typically, this suite would be accompanied by an E×B Wein filter to measure ion charge state. However, I have found that these measurements are very challenging to perform, as the thruster produces a very low signal-to-noise ratio for this diagnostic. For this reason, all of my analysis assumes singly charged ions unless otherwise stated. I provide some justification for this assumption in the following chapters. What follows in this chapter is the working principle of each diagnostic and what it measures, followed by a physical description, the data acquisition setup, and the data analysis techniques.

5.1 Test Facility

The experiments described here were conducted at the Alec Gallimore Large Vacuum Test Facility (LVTF) at the University of Michigan. This capsule-shaped vacuum chamber measures 6 m in diameter by 9 m long and is capable of pumping a maximum of 600 kL/s of xenon. For testing, we ran six of the PHPK TM1200i liquid-nitrogen-shrouded cryopumps with a combined rated pumping speed of 210 kL/s of xenon [92], and during thruster operation, the background pressure was typically on the order of 2×10^{-6} Torr-Xe. Pressure was monitored using a Stabil ion gauge 1 m radially from the thruster in the thruster's exit plane in accordance with best practices for electric propulsion testing [18]. The propellant used in this work was exclusively xenon, as the goals of the effort were to improve thruster performance, not necessarily improve thruster performance on alternative propellants. Gaseous xenon was fed to the thruster injectors and hollow cathode bore using two independent mass flow controllers. An Alicat scientific 50 sccm controller was used for the cathode bore, and an Alicat scientific 400 sccm controller was used for the neutral injector. These were then calibrated using a Bios Definer 220 flow calibration meter. Power to the RMF system was supplied by a Magna Power MT series 1000 V 150 A DC supply, and thruster power for efficiency measurements is taken as the DC reading from this supply. The bias magnets were powered using TDK Lambda GEN 40-19 DC supplies, the cathode keeper was run using a TDK Lambda GEN 300-5 DC supply, and the cathode-anode discharge was run using a TDK Lambda EMS 60-18 DC supply. The power input of these smaller supplies is not included in the efficiency analysis. The thrusters were placed on the chamber centerline approximately at the center of one hemispherical cap and fired at a chevroned graphite beam dump at the other end of the chamber. I show the base chamber setup schematically in Fig. 5.1.

5.2 Thrust Stand

The test articles were placed on an inverted pendulum thrust stand operating in displacement mode to directly measure the steady thrust generated during operation. In the continuous wave mode, this is straightforward; however, in the pulsed mode, the thruster fires at a sufficiently high pulse repetition rate as to not excite the natural frequency oscillation of the thrust stand. In our setup, this means running the thruster at a repetition rate $f_{\text{rep}} \gg 1$ Hz. The thrust stand incorporates a set of pivotal fixtures in addition to a set of tension springs to provide a restoring force to balance the weight of the thruster. These springs are sized to provide high sensitivity (low spring constant) while keeping the thruster balanced. Additionally, the power lines to the thruster must be draped through a "waterfall" to minimize

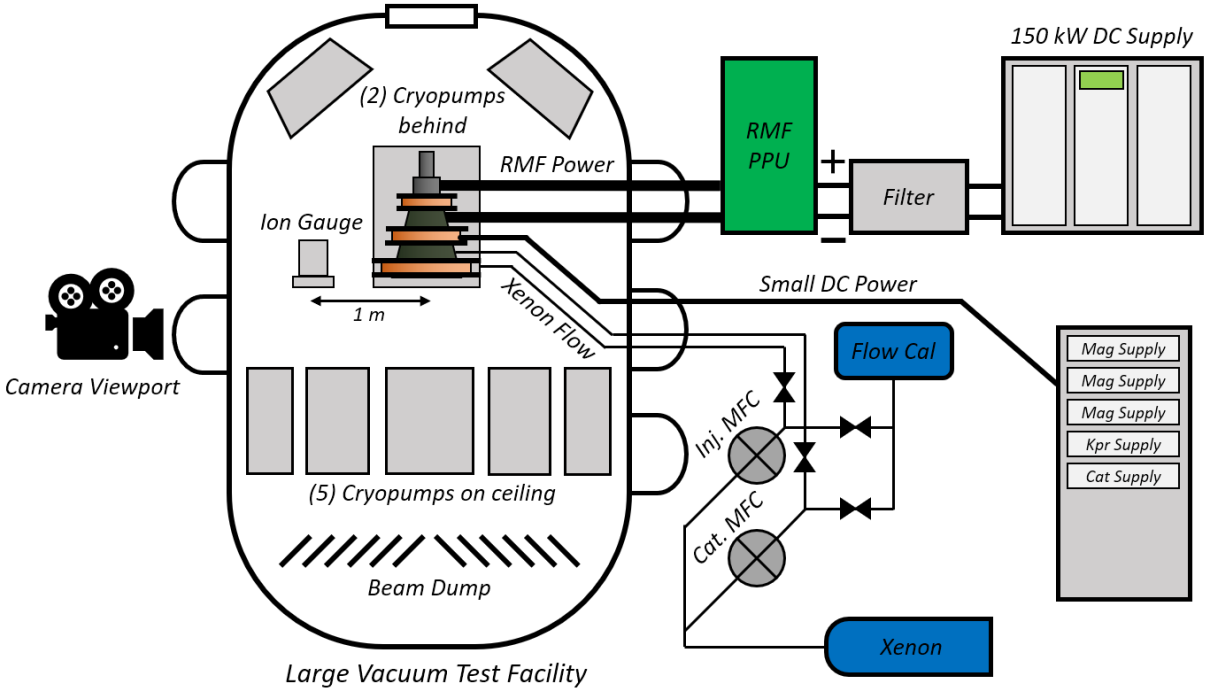

Figure 5.1: Schematic of base vacuum chamber setup showing locations of thruster, ion gauge, beam bump, power supplies, flow system, and cryopumps.

thermal expansion effects and frictional hysteresis.

The thrust stand uses an optical interferometer to measure the displacement of the thruster in response to an applied thrust force. Some thrust stands operate in "null mode" where a PID-tuned magnetic coil provides additional restoring force, such that the thruster does not physically displace during the thrust measurement. We are limited in operating the thrust stand in "displacement mode" where the restoring force is fully provided by the spring constant; this is due to electromagnetic interference from the RMF making a tuned magnetic coil infeasible. Additionally, the thrust stand incorporates an electrical fluid inclinometer to measure the tilt of the thruster platform. I show a photo of the thrust stand internals alongside a schematic in Figs. 5.2 and 5.3.

The thrust stand is calibrated in-situ in two steps. First, we perform a displacement versus inclination calibration where the platform is mechanically tilted with a fine-pitch lead screw. Second, we perform a displacement calibration against known masses applied sequentially to the platform, which captures the range of the anticipated thrust. During a thrust measurement, we record the uncontrolled inclination and displacement of the thruster platform. We then apply the inclination calibration to correct the displacement signal (typically

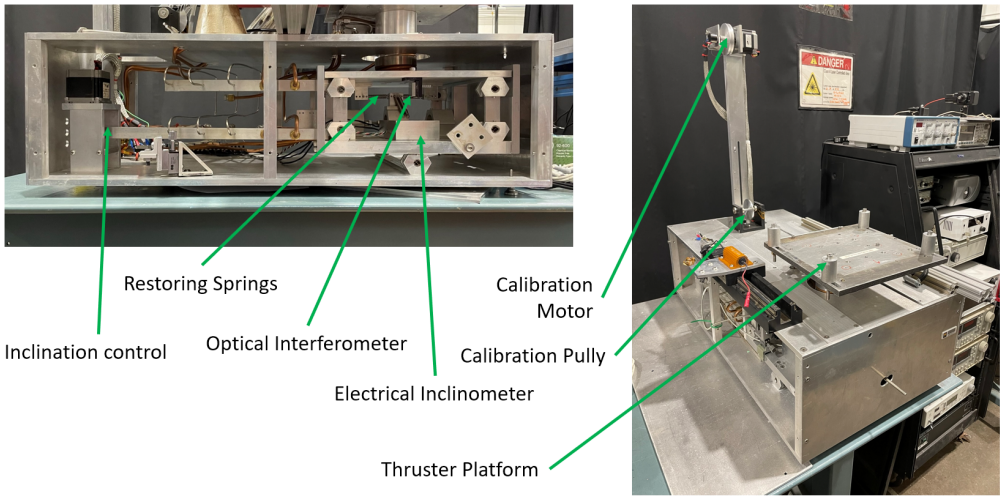

Figure 5.2: Photo of inverted pendulum thrust stand with major components labeled.

a small correction factor) and then apply the displacement calibration to convert displacement to thrust force. This process is presented graphically in Fig. 5.4. Further details on this procedure can be found in Ref. [82].

5.2.1 Measuring Steady-State Thrust

I present in Fig.5.5 an example of the measured force from a single thrust measurement. To generate this result, we continuously operate the cathode seed source with a constant propellant flow rate to the thruster and then apply the RMF for a total of ten seconds. We measure the change in thrust-stand displacement caused by the RMF system. We convert the displacement measurement into force using the thrust stand calibration. As seen in Fig. 5.5, there are typically large-scale oscillations in the measurement due to the under-damped nature of the thrust stand.

To determine thrust from this oscillatory measurement, we calculate an on-delta and an off-delta when the RMF was activated and deactivated, respectively. These deltas are determined by taking the average over a three-second window on either side of the RMF actuation. We use one standard error over this window to be the uncertainty of the force value. The length of the red bars in Fig. 5.5 indicates these averaging windows, and the upper and lower bars correspond to the range of the uncertainty in the mean value. Taking the average value of the two deltas (on and off) and combining their respective uncertainties in quadrature yields a steady thrust value and associated uncertainty for a single measurement. We then repeat several of these trials to capture the variability in the thrust measurement.

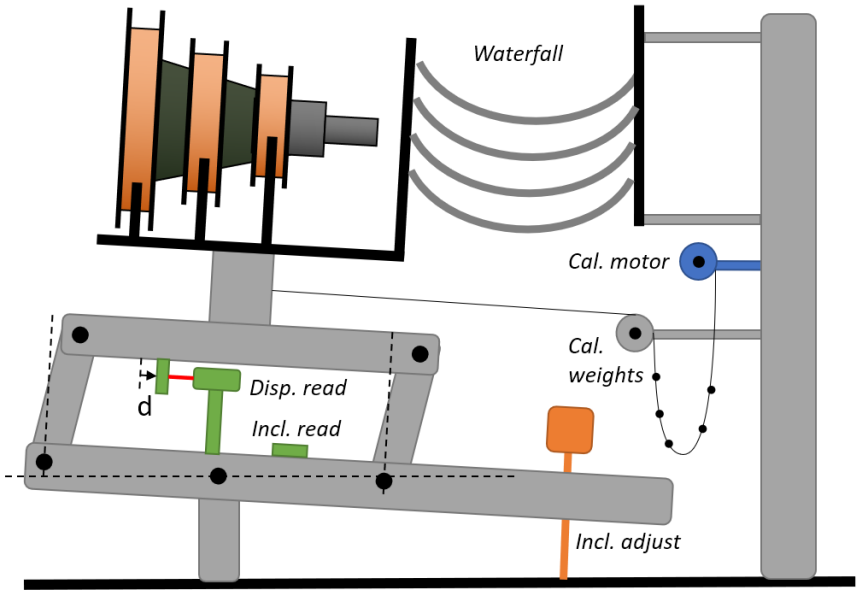

Figure 5.3: Schematic of inverted pendulum thrust stand.

The final thrust values reported in this work are the average of three or more trials. As shown in the figure, the uncertainty in the thrust measurements is on the order of 1 mN.

5.2.2 Conversion of Steady to Shot-to-Shot Performance Metrics

The above analysis is applicable in both continuous wave and pulsed modes. However, in the pulsed mode, the steady performance metrics (thrust, mass flow rate, and power) can be related to shot specific metrics (for an individual pulse) through the following equations:

$$J = \frac{T}{f_{\text{rep}}}, \tag{5.1}$$

$$M = \frac{\dot{m}}{f_{\text{rep}}}, \tag{5.2}$$

$$E_{\text{in}} = \frac{P_{\text{in}}}{f_{\text{rep}}}, \tag{5.3}$$

where f_{rep} is the commanded repetition rate of the pulses, T denotes the steady-state thrust measured experimentally over many pulses (> 1000), $\dot{m}$ is the constant mass flow rate fed to the thruster, and P_{in} is the average input power to the PPU. The first relationship is justified

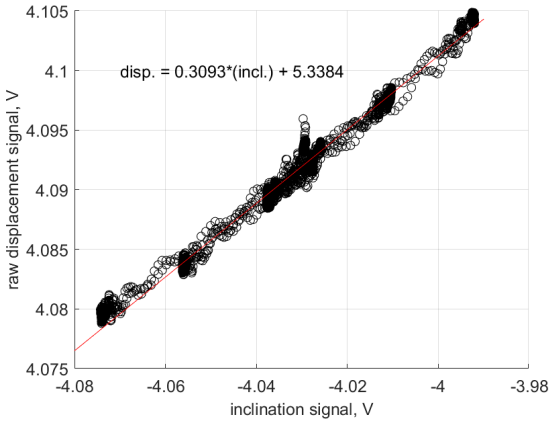

(a) Inclination calibration.

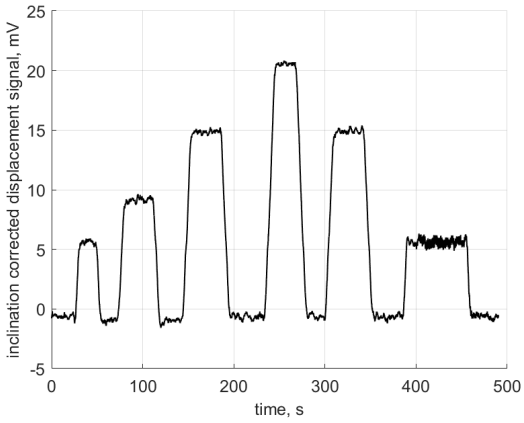

(b) Inclination corrected displacement signal curing calibration process.

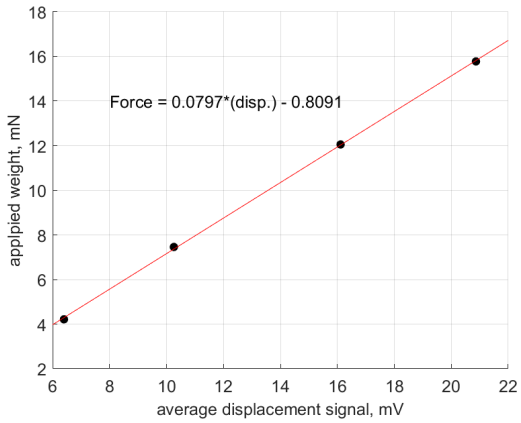

(c) Resulting force calibration curve

Figure 5.4: Inverted pendulum calibration procedure.

because the thruster was pulsed at a repetition rate much faster than the natural frequency of the thrust stand. The second equation stems from the fact that the repetition rates are commensurate with the neutral gas fill time, such that only marginal propellant is wasted between shots. The third relationship is based on the fact that although the PPU draws steady power due to passive filtering, power was only consumed by the thruster during the RMF pulse.

In addition to these per-shot quantities, I also remark that efficiency and specific impulse are informed from the steady-state measurements of thrust, power and flow rate:

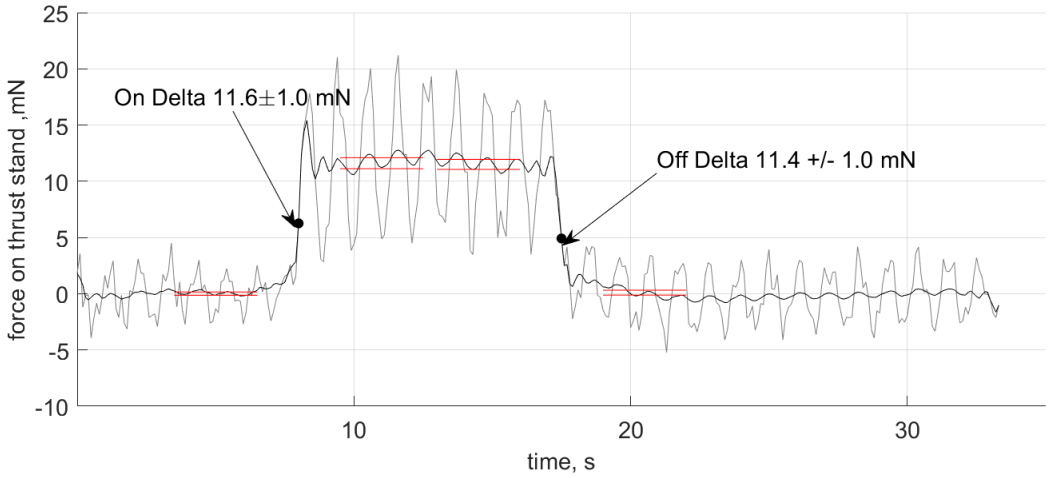

Figure 5.5: Example thrust measurement with raw thrust data (gray) and a moving average for comparison (black). The red bars indicate the averaging windows of the raw data employed for on/off measurements where the heights indicate the upper and lower values within uncertainty.

$$I_{\text{sp}} = \frac{T}{\dot{m} g_0} = \frac{J}{M g_0}, \tag{5.4}$$

$$\eta = \frac{T^2}{2\dot{m} P_{in}}, \tag{5.5}$$

where g_0 is the gravitational acceleration at Earth's surface. The uncertainty in efficiency and specific impulse are propagated forward from the uncertainty in thrust, mass flow rate, and power using standard quadrature rules.

5.3 Faraday Probe

A swept Faraday probe (FP) is employed to measure the far-field ion flux in the thruster plume. The probe is moved through the plasma region to obtain spatial profiles of ion current and is also used in the pulsed mode to measure the ion velocities from their time-of-flight from the thruster. The FP is effectively a planar Langmuir probe biased into ion saturation. The guard ring (biased to the same potential) ensures minimal ion sheath expansion occurs for the central collector, such that the ion current measured is reflective of the ion current density in the thruster beam.

5.3.1 Physical Description

The FP used in this work consisted of a 1.74 cm molybdenum collector and an annular 0.54 cm molybdenum guard ring with a 0.05 cm gap between them. Both the collector and guard were biased between -115 V to -60 V relative to facility ground to ensure that ion saturation was achieved. The need for such large negative potentials to repel electrons is documented in other RF thrusters [17] and is indirect evidence of some population of high-energy tail electrons in the beam. I show an image of the FP used in this work in Fig.5.6

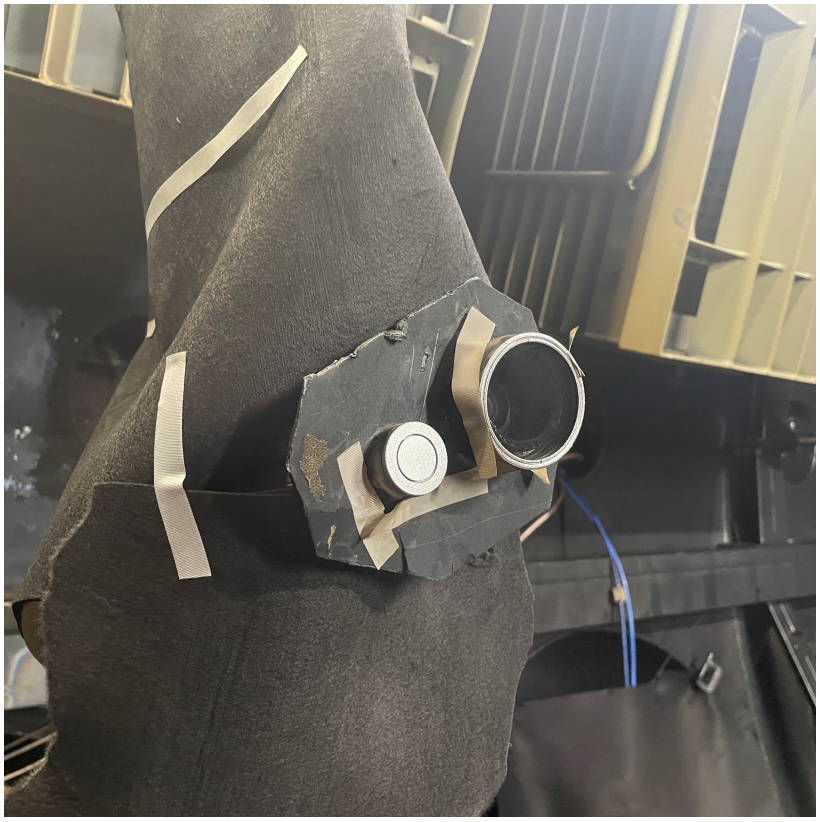

Figure 5.6: Image of Faraday probe used in experiment.

5.3.2 Measurement Setup

The far-field FP measurements were performed in a polar arc about the center of the thruster exit plane. This arc had a radius of 1.72 m (to avoid other diagnostics), and data were collected at roughly 5-degree increments from -90 to 90 degrees, with zero degrees corresponding to the thruster axis.

In the pulsed mode, the ion current is measured as the voltage drop across a known shunt resistance. The signal was passed through a 4^{th} order RC low-pass filter to attenuate noise

from the RMF. The corner frequency of this filter was 100 kHz and is the effective bandwidth of the measurement. The signal was sampled at 1 MHz using a 16-bit digital oscilloscope triggered off the RMF PPU controller. Because the RMF pulses provide a distinct time reference, I am able to overlay probe measurements at different locations to reconstruct a spatially and temporally resolved map of measurements. Specifically for the FP probe this means I can align the time traces of ion beam current at differing angles about the thruster using the start of RMF puling as a reference. This technique is used extensively in this work which I refer to as "time-aligning". For example, this can be also be used for voltage sweeps of Langmuir probes to create a time-voltage map of plasma characteristics. The uncertainty of the FP measurements is driven by the shot-to-shot variance of the pulses. Conversely, in the CW mode, the ion current is measured directly using a Keithley 6485 picoammeter, and the uncertainty comes from the difference of independent sweeps. I show in Fig. 5.7 the schematic of the acquisition setups for the FP.

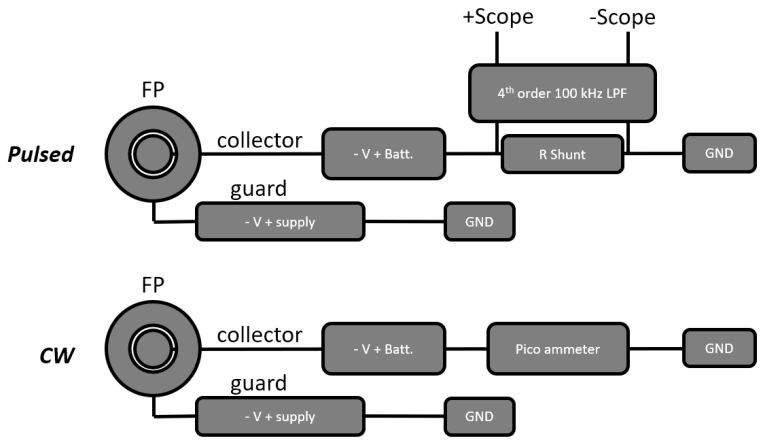

Figure 5.7: Faraday Probe measurement schematic for pulsed and CW modes.

5.3.3 Analysis Techniques

5.3.3.1 Beam Currents

The ion current density in the plume is related to the raw current measured with the Faraday probe by

$$j_{FP} = \frac{I_{FP}}{A_{FP} + \kappa_G} \kappa_{SEE}, \tag{5.6}$$

where I_{FP} is the raw signal, A_{FP} is the probe collector area, and κ_{SEE} and κ_G are, respec-

tively, secondary electron emission and geometric correction factors as presented in Ref. [10]. In our case, $\kappa_G = 0.0772$ cm^2, or 3.25% of our collector area, and $\kappa_{SEE} = 97.94\%$ for singly charged xenon striking molybdenum.

To determine the mass utilization of the thruster, we require a measurement of the total ion flux in the thruster beam. To measure the divergence efficiency, we also require a measurement of the axially directed component of this flux. I choose to keep these fluxes in terms of total and axial beam current for consistency with other works [41, 53, 89].

The total beam and axial beam currents are calculated from the FP current density measurement as

$$I_{\text{beam}} = 2\pi r^2 f_{rep} \int_0^{\pi/2} \int_0^{f_{rep}^{-1}} j_{FP}(t,\theta)\, dt \sin\theta\, d\theta, \tag{5.7}$$

$$I_{\text{axial}} = 2\pi r^2 f_{rep} \int_0^{\pi/2} \int_0^{f_{rep}^{-1}} j_{FP}(t,\theta)\, dt \cos\theta \sin\theta\, d\theta, \tag{5.8}$$

where r is the radial location from the thruster, θ is the polar angle to the thruster axis, and the time integral is performed over the pulse period f_{rep}^{-1}. I note here explicitly that the current density is a function of position and time. In the case of CW mode operation, however, j_{FP} is constant in time, and the time integral is unnecessary.

I can use these metrics to evaluate both the divergence and mass utilization efficiency. The divergence efficiency of the thruster is evaluated as

$$\eta_d = \left(\frac{I_{\text{axial}}}{I_{\text{beam}}}\right)^2 = \cos^2\Theta, \tag{5.9}$$

where Θ is a characteristic divergence angle. The ion mass flow from the thruster is then calculated as

$$\dot{m}i = \frac{m_i I_{\text{beam}}}{Ze}, \tag{5.10}$$

where m_i is the ion mass, 2.18×10^{-25} kg for xenon, e is the elementary charge, and Z is the effective ion charge, which again I assume to be 1. The mass utilization efficiency is then calculated as in Chapter 3

$$\eta_m = \frac{\dot{m}_i}{\dot{m}}, \tag{5.11}$$

where $\dot{m}$ is the neutral flow rate to the thruster, including the cathode flow.

5.3.3.2 Time-of-Flight Velocimetry

When operating a thruster in pulsed mode, I can leverage the persistent start of the RMF pulsing as a baseline to measure the velocity of the ions using their time-of-flight. This technique provides information on the energy of the ion beam using only the ion current density measurement from the FP. In this way, the ion force in the thruster beam can be written as

$$F_{beam} = \frac{2\pi r^2 m_i}{Ze} f_{rep} \int_0^{\pi/2} \int_0^{f_{rep}^{-1}} j_{FP}(t,\theta) v(t)\, dt \sin\theta\, d\theta, \tag{5.12}$$

where $v(t)$ is the velocity of the ion current reaching the probe at time t. I claim this velocity can be expressed as

$$v = \frac{r}{t - t_{iz}}, \tag{5.13}$$

where t_{iz} is an ionization time correction stemming from the fact that the RMF pulse begins before ionization and plasma acceleration. The bounds on this parameter range from $t_{iz} = 0 - 25$ μs, where the latter value corresponds to when density in the thruster reaches half its maximum (see Chapter 6, Sec 6.2.4). When this technique is used, the affected values are evaluated over this range of ionization times, and I report the resulting maximum and minimum values as the effective uncertainty bounds on the estimate with the nominal value coming from $t_{iz} = 12.5$ μs. I show graphically in Fig. 5.8 the time of flight for ions from Eq. 5.13 overlaid with FP beam current data.

Note, F_{beam} is not the directional thrust force but more like an ion beam pressure distributed over a downstream hemispherical surface. Using this term the plasma efficiency of the thruster can be written as

$$\eta_p = \frac{F_{\text{beam}}^2}{2\dot{m}_i P_p}, \tag{5.14}$$

where P_p is the power coupled into the plasma.

5.4 Current Transducers

To measure the current waveforms in the RMF antennas, I use a set of current transformers surrounding the conductors of each RMF phase. This measurement is important for RMF tuning—to ensure the PPU is driving at the thruster resonant frequency—and for the evaluation of coupling efficiency. The currents conducted through the center of each cur-

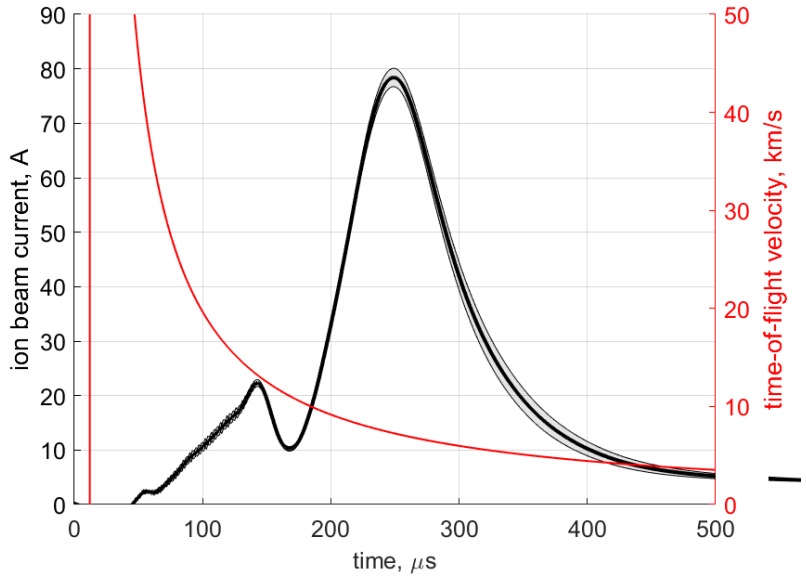

Figure 5.8: Ion velocimetry using Faraday probe time-of-flight. Black data is total beam current as a function of time, and the red curve is the corresponding ion speed for the current collected at that time.

rent transformer produce an EMF in the transformer coil, which drives a current through a calibrated terminating resistor. The voltage produced across this resistor is then directly proportional to the time-varying current conducted through the transformer.

5.4.1 Physical Description

In this study, I use a set of Pearson 110 wide band current monitors to measure these currents[1]. These coils have a -3 dB band between 1 Hz and 20 MHz and provide a consistent output (V/A) for frequencies in that band. These coils are placed as close to the RMF antennas as feasible to avoid picking up on any stray coupling or harmonics formed on the long power transmission lines. I show an image of two of these current transducers in Fig. 5.9.

5.4.2 Acquisition

The voltage output of the current monitors was passed through 10:1 compensated oscilloscope probes to reduce the output voltage. This signal was recorded using a 16-bit digital oscilloscope. I show in Fig. 5.10 the schematic of the acquisition setup for the current transducers.

[1]The three-phase setup includes one Pearson model 1025, which has a bandwidth of 160 Hz to 4 MHz. The 1025 was also connected directly to the oscilloscope for measurement.

Figure 5.9: Image of current transducers used in experiment.

5.4.3 Analysis

I use measurements of the RMF antenna currents to evaluate the energy transfer to the plasma. By comparing the amplitude of the currents relative to the DC input power under vacuum and plasma-loaded conditions, I can determine the effective additional resistive load caused by the plasma and, therefore, the power transferred to it. Some experimental data reflecting this process is presented throughout Chapter 4. This technique is similar to the one used by Weber in Ref. [95] and adapted for this work.

Under vacuum conditions, I assume that the entirety of the DC power supplied to the RMF PPU is consumed by effective parasitic resistances in the antenna circuits. I denote this as

$$P_{\text{in, vacuum}} = f_{rep} \int_0^{f_{rep}^{-1}} \left(\sum_{n=1}^{N_\phi} R_{c,n} I_n^2 \right) \, dt, \tag{5.15}$$

where N_ϕ is the number of phases, and $R_{c,n}$ and I_n are the parasitic resistance and current in phase n respectively. I further assume that $R_{c,n}$ is constant, which is acceptable if heating is minimal, and thus,

$$P_{\text{in, vacuum}} = f_{rep} R_c \int_0^{f_{rep}^{-1}} \left(\sum_{n=1}^{N_\phi} I_n^2 \right) \, dt, \tag{5.16}$$

where R_c is the effective vacuum resistance of the circuit. Under plasma-loaded conditions, the input power is now consumed by the circuit resistance and an effective plasma resistance, such that

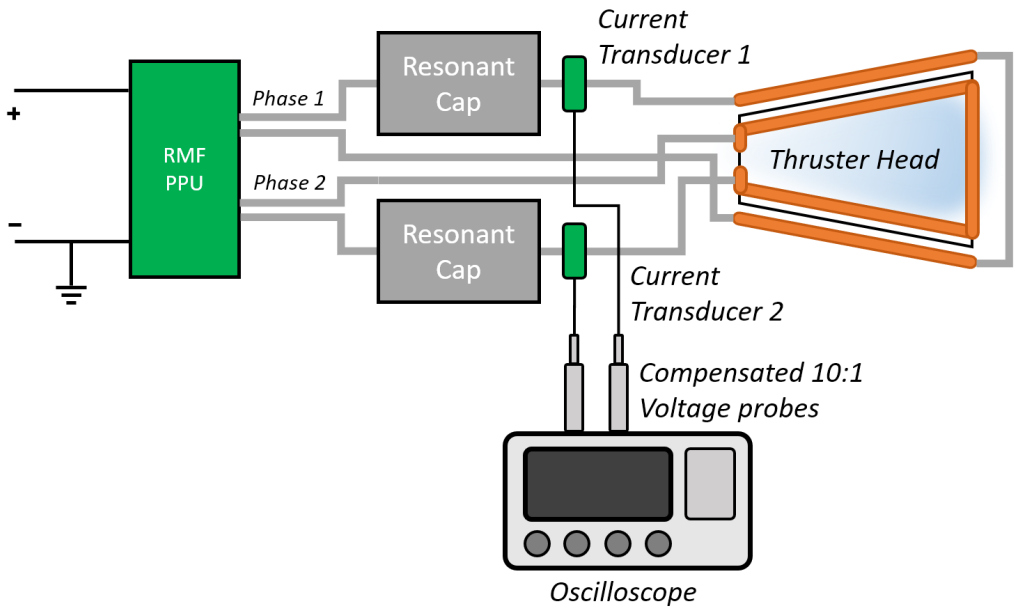

Figure 5.10: Current transducer measurement schematic showing location of probes in relation to RMF power system.

$$P_{\text{in, plasma}} = f_{rep}(R_c + R_p) \int_0^{f_{rep}^{-1}} \left(\sum_{n=1}^{N_\phi} I_n^2 \right) \, dt, \tag{5.17}$$

where R_p is the effective lumped plasma resistance shared across all phases. Following from this logic, the power deposited into the plasma is

$$P_{\text{p}} = f_{rep} R_p \int_0^{f_{rep}^{-1}} \left(\sum_{n=1}^{N_\phi} I_n^2 \right) \, dt, \tag{5.18}$$

and the coupling efficiency is calculated as

$$\eta_c = \frac{P_{\text{p}}}{P_{\text{in, plasma}}} = \frac{R_p}{R_p + R_c} = 1 - \frac{f_{rep} R_c \int_0^{f_{rep}^{-1}} \left(\sum_{n=1}^{N_\phi} I_n^2 \right) \, dt,}{P_{\text{in, plasma}}}. \tag{5.19}$$

In practice, I measure the total input power during thruster firing (vacuum or plasma loaded) and the associated RMF current waveforms and calculate an effective resistance

$$R_{\text{eff}} = \frac{P_{\text{in}}}{f_{rep} \int_0^{f_{rep}^{-1}} \left(\sum_{n=1}^{N_\phi} I_n^2 \right) \, dt,} \tag{5.20}$$

The circuit resistance, R_c, is inferred a priori by measuring the impedance of the system

during a pulse applied without plasma ($R_p = 0$) at a comparable power and operating condition (pulse rate, duty cycle, etc.). The plasma resistance is then calculated as $R_p = R_{\text{eff}} - R_c$. This assumes that the circuit impedance upstream of the plasma does not change between the vacuum and plasma-loaded shots, and the plasma is assumed to be the cause of any changes to the overall circuit impedance from the perspective of the power processing system. I report the uncertainty in coupling efficiency measurements from the standard deviation of three of more values for vacuum circuit resistance and three or more waveform and power measurements of the plasma.

5.5 Retarding Potential Analyzer

I use a retarding potential analyzer (RPA) to measure the ion velocity distribution function (IVDF) in the plume downstream of the thruster. The RPA operates effectively as an ion current collector with a high-pass ion energy filter, allowing only ions of sufficient energy to pass through the device and be collected. The RPA used in this work employs a set of four gridded apertures to achieve this functionality. As the plasma beam enters the RPA, it passes through these grids in sequence to the collector at the back of the device. The first grid is electrically floating and serves to attenuate the plasma density. The second grid is the primary electron selection grid, negatively biased to filter out electrons from the plasma. The third grid is the ion selection grid, biased positively with respect to ground, allowing only ions with sufficient energy to pass through. The final grid is a secondary electron suppression grid, also negatively biased negatively to return secondary electrons emitted from the collector. I show an image of the RPA used in this experiment in Fig. 5.11.

5.5.1 Physical Description and Acquisition Setup

The RPA used in this work has an aperture area of 6.45 cm^2 and consists of stainless steel grids with .276 mm mesh size at the following grid space spacings starting from the floating grid: .335, .173, .655, and .655 cm. The RPA is mounted on a translating motion stage downstream of the thruster behind a set of graphite panels. When the probe is in use, it is moved behind a 5 cm diameter aperture in the central graphite panel that is aligned to the centerline of the thruster. This way, the probe is shielded when not in use. I show images of this armored probe carrier in Fig. 5.12.

Measurements for the RPA fundamentally consists of a current-voltage sweep. The ion selection grid for the is applied using a 1000 V Kepco bipolar operational amplifier and measured using a GW Insteck GDM-8341 DMM. For pulsed mode measurements, the voltage

Figure 5.11: Image of retarding potential analyzer used in experiment.

is held constant, and current is passed through a high-accuracy 1 kΩ resistive shunt to ground. The voltage drop across this shunt is passed through the same LPF as used for the FP acquisition and recorded as a function of time with the digital oscilloscope at a 1 MHz sample rate. The selection grid voltage is then increased, and another current-time trace is recorded. This dataset is then time-aligned and rearranged into an I-V trace at each sample time starting at the trigger point set by the RMF PPU controller. In the CW mode, the steady current is recorded as a function of voltage with a Keithley 6485 picoammeter. For these measurements, the electron suppression grids were held at a constant -30 V, and the collector was held at -5 V, both relative to ground. I show in Fig. 5.13 the schematic of the acquisition setup for the RPA

5.5.2 Analysis

The RPA current as a function of voltage is given by

$$I(V) \propto \int_{qV}^{\infty} f(v) E dE, \tag{5.21}$$

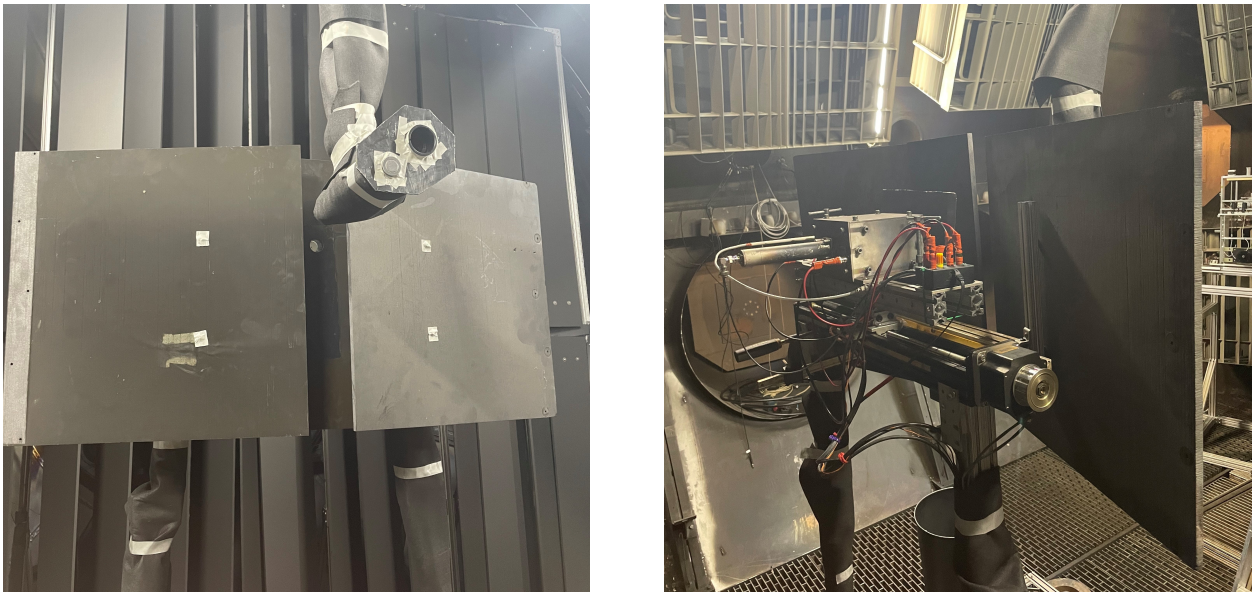

(a) Front view (b) Rear view

Figure 5.12: Images of armored probe carrier.

where V is the applied voltage, and $f(v)$ is the ion velocity distribution function (IVDF), and the substitution is made for $E = 1/2 m_i v^2$ [51]. Taking the derivative of this expression with respect to voltage reveals:

$$f\left(\sqrt{\frac{2qV}{m_i}}\right) \propto -\frac{dI}{dV}, \tag{5.22}$$

where f is the velocity distribution as a function of the retarding potential, and is therefore charge independent. In practice, a piecewise polynomial smoothing spline is fit to the RPA I-V sweep, and the analytical derivative of this function is taken to calculate f. This process avoids amplifying experimental noise through a numerical derivative.

The physically rigorous practice is to report an integrated mean value of the distribution. However, there are often low-energy peaks or tails associated with charge exchange or scattered populations that are not physically relevant to incorporate into the beam measurement. Therfore, beam ion energy is then reported as the peak, or most probable, value of the ion energy distribution. The most probable voltage is corrected for the plasma potential such that

$$V_{\text{beam}} = V_{mp} - V_p, \tag{5.23}$$

where V_{beam} is the beam voltage, V_{mp} is the most probable voltage from the IEDF, and V_p

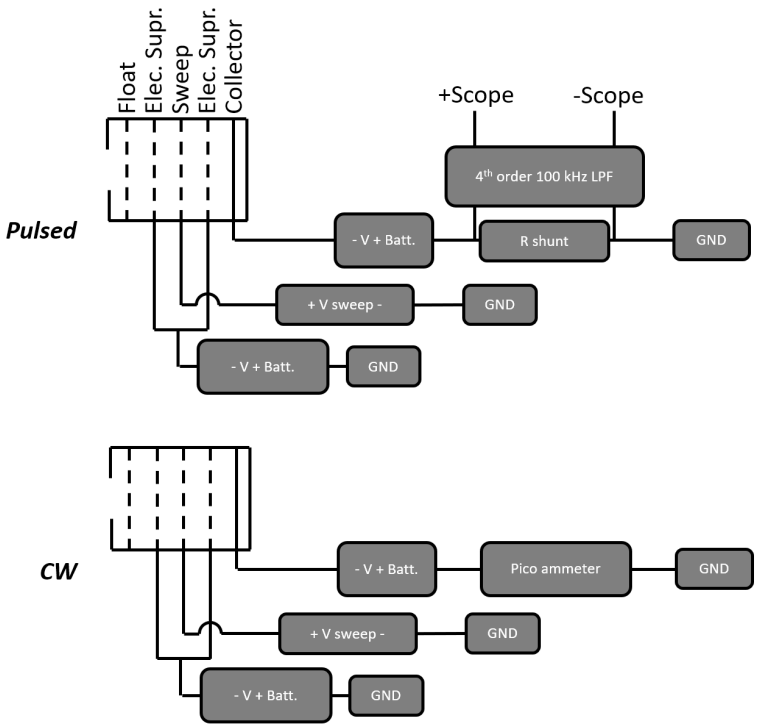

Figure 5.13: Retarding potential analyzer measurement schematic for pulsed and CW modes

is the plasma potential as measured by the far-field Langmuir probe (see following section). Note that for pulsed mode operation, $V_{\text{beam}}(t)$ is a function of time. Therefore, using the RPA data of ion retarding voltage, the plasma efficiency can be calculated as:

$$\eta_p = I_{\text{beam}} = \frac{f_{rep} \int_0^{f_{rep}^{-1}} V_{\text{beam}}(t) I_{\text{beam}}(t)\, dt}{P_p} \tag{5.24}$$

where $I_{\text{beam}}(t)$ is the spatially integrated beam current from the FP as a function of time.

5.6 Far-field Langmuir Probe

Because the ions experience RPA selection grid bias relative to the local plasma potential, the most probable voltage measured by the RPA must be corrected per Eq. 5.23. The plasma potential is measured using a cylindrical far-field (FF) Langmuir probe (LP) oriented along the beam axis, following LP best practices for electric propulsion [57]. If the voltage of the LP is lower than the plasma potential, the electron density (and therefore current) to the probe will be retarded, following a Boltzmann relation:

$$n = n_0 \exp\left(\frac{e(V_b - V_p)}{T_{eV}}\right), \tag{5.25}$$

where n_0 is the density far away from the probe, V_b is the probe bias, V_p is the plasma potential, and T_{eV} is the electron temperature in eV. For bias voltages larger than the plasma potential, the electron current will still increase due to sheath expansion; however, at a slower than exponential rate. This transition point ("knee") in the log current-voltage characteristic of the LP can be used to identify the plasma potential.

5.6.1 Physical Description and Acquisition Setup

The FF-LP is constructed of 0.4 mm tungsten wire, with a length of 2.67 mm. It has a transverse surface area of 6.7×10^{-6} m^2. The FF-LP is mounted along side the RPA on the translating motion stage downstream of the thruster which allows the two probes to measure the same position in the beam behind the orifice in the graphite panels. I show an image of the FF-LP used in this work in Fig. 5.14.

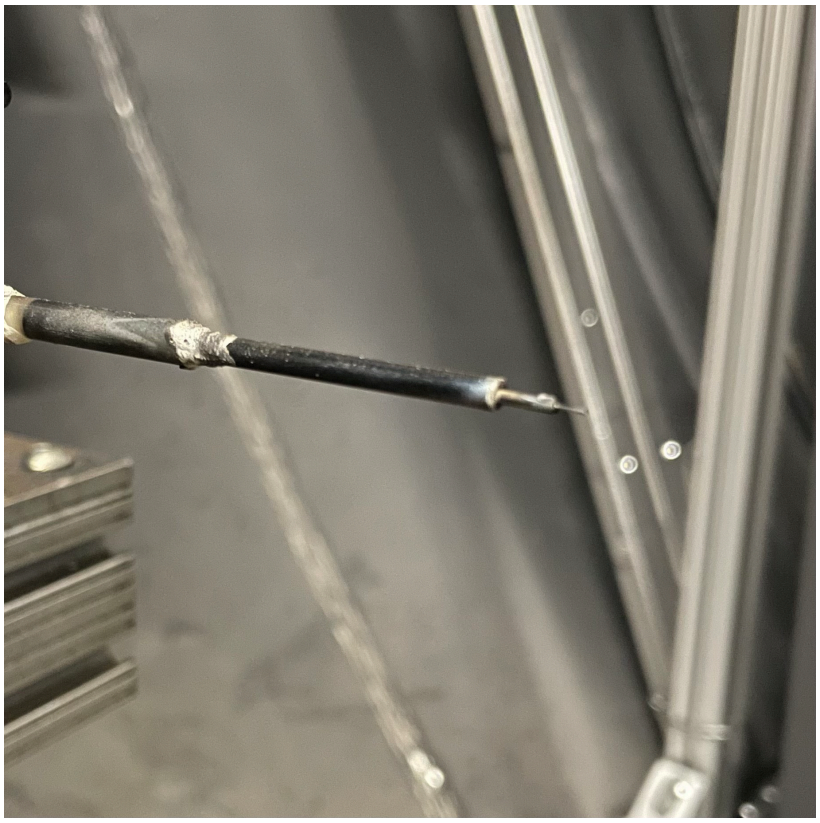

Figure 5.14: Image of far field Langmuir probe used in experiment.

Similar to the acquisition setup for the RPA, the current-voltage sweeps for the FF-LP

are perfromed using the 1000 V Kepco bipolar operational amplifier with the probe bias voltage measured using the GW Insteck DMM. Again, for pulsed measurements, the current is measured as the voltage drop across a 1 kΩ resistor the signal is passed through the LPF and recorded with the digital oscilloscope at a 1 MHz sample. Voltage is increased, and current as a function of time recorded again. These current traces are time-aligned to provide a I-V characteristic of the far-field plasma as a function of time. For the CW mode, the probe current was measured using the Keithley 6485 picoammeter. I show in Fig. 5.15 a schematic of the acquisition setups for the FF-LP.

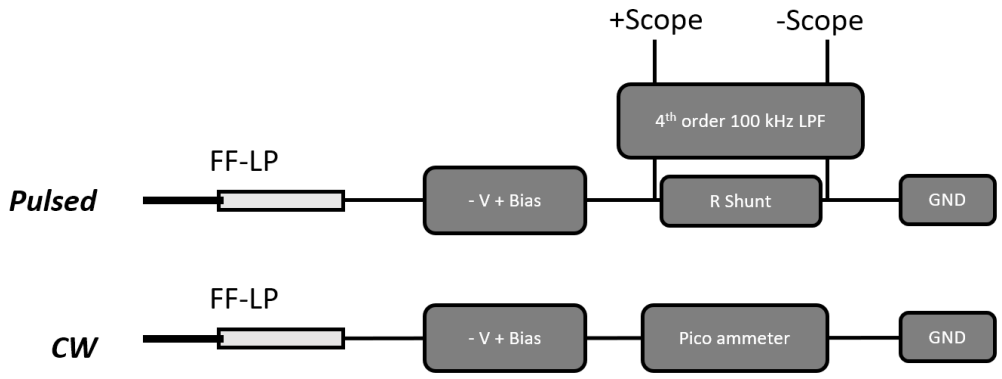

Figure 5.15: Far-field Langmuir probe measurement schematic for pulsed and CW modes.

5.6.2 Analysis

As mentioned, the plasma potential is determined by the FF-LP characteristic slowing from exponential in the electron retarding region to slower growth in the sheath expansion region. To locate this point using the natural log of electron current as a function of bias voltage I employ the "kneedle" algorithm [77]. This technique locates the point that maximizes the difference between normalized data and the line $y = x$. This technique is shown graphically in Fig. 5.16. I plot here the natural log of electron current on the left axis in black for a notional Langmuir probe trace. I then normalize this data over the range [0, 1], and take the difference to the normalized bias voltage (dashed line in Fig. 5.16). This normalized difference is plotted in red on the right axis, and the maximum of this curve is identified as the "knee" of the data and the plasma potential. For the data presented in this study, the error in plasma potential dominated the error in the RPA most probable voltage, and this error analysis is discussed in further detail alongside the results in Chapter 7.

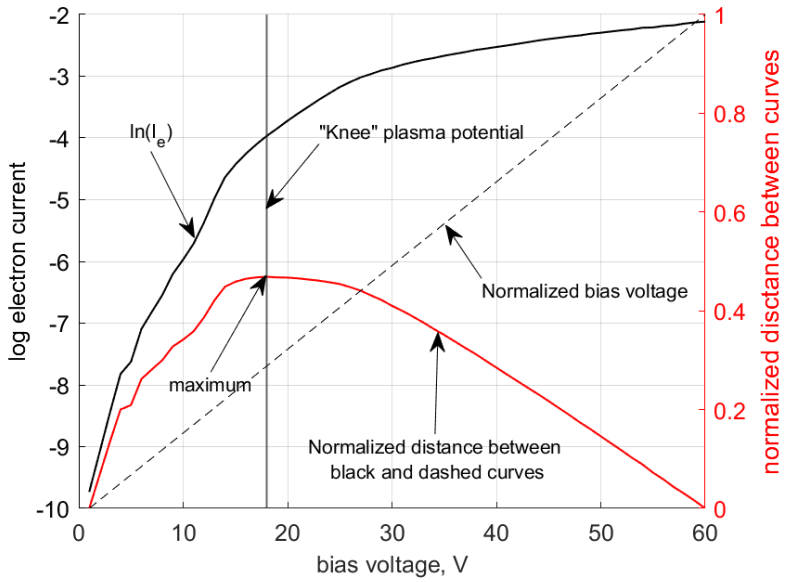

Figure 5.16: Plasma potential "knee" finding method using Kneedle algorithm.

5.7 Triple Langmuir Probe

In this work, a triple Langmuir probe (TLP) is utilized to measure plasma properties within the thruster. This probe offers the advantage of providing real-time measurements of electron density and temperature without requiring a voltage sweep, which can significantly increase data acquisition rate, especially when there are numerous experimental points to measure. However, a drawback of this approach is its reliance on the assumption that electrons follow a Maxwellian velocity distribution function. If high-energy tail electrons are present in the plasma, TLP measurements can exhibit errors of up to 50% [69]. Since the TLP provides limited information about the plasma, it becomes challenging to determine the presence of such electrons solely from the TLP measurements.

5.7.1 Physical Description and Operation

The TLP used in this work consists of three tungsten rods, each measuring 0.127 mm in diameter and 1.270 mm in length, with a 2 mm spacing between them. These dimensions are chosen with consideration to several effects. First, the electrode spacing must be small such that the probe can be considered to measure a single spatial point, but not too small such that the electrode sheaths overlap (distance larger must be than Debye length). Second, the collecting area must be large enough such to provide sufficient signal-to-noise ratio but not too large such that the current to the probe sufficiently impacts the beam currents. During

operation, one electrode is electrically floating, while the other two electrodes are biased to 28.8 V with respect to each other. The current between the biased probes is measured with a 10-turn coil around a 1 V/A Pearson coil paired with a 4th-order 100 kHz RC low-pass filter, and the voltage between the floating and positively biased electrodes is measured using a 50:1 floating differential probe. These signals are then recorded with an oscilloscope sampling at 1 MHz. I show this setup in Fig. 5.17.

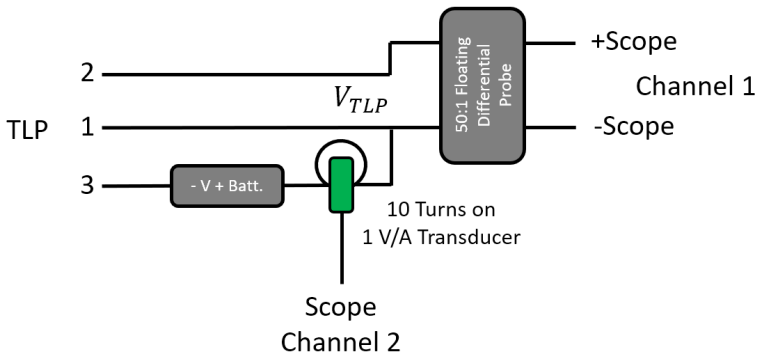

Figure 5.17: Triple Langmuir probe measurement schematic.

5.7.2 Acquisition setup

The TLP is mounted on a two-axis motion stage positioned in front of the thruster, allowing translation of the probe inside the thruster volume with the TLP aligned with the thruster axis. For each spatial location, 25 RMF pulses are recorded and subsequently averaged and smoothed to reduce measurement noise. I show in Fig. 5.18a an image of the TLP mounted next to a inductive b-dot probe (not relevant for this work) on the near-field motion stage. Additionally, Fig. 5.18 (b) shows the TLP performing measurements inside the thruster.

5.7.3 Analysis

To evaluate the expressions in Chapter 3, Section 3.4, information about the local plasma density, electron temperature, and neutral density is required. The TLP is employed to provide instantaneous measurements of electron temperature and density by effectively sampling three points on the full plasma I-V curve.

A typical TLP implementation, depicted in Figure 5.19, comprises three electrodes, each at a different potential. Probe 2 is allowed to electrically float, while a floating bias voltage (V_a) is enforced between probes 1 and 3. Using Kirchhoff's current law and the Boltzmann relation for electron current, equations for the current to each probe can be formulated:

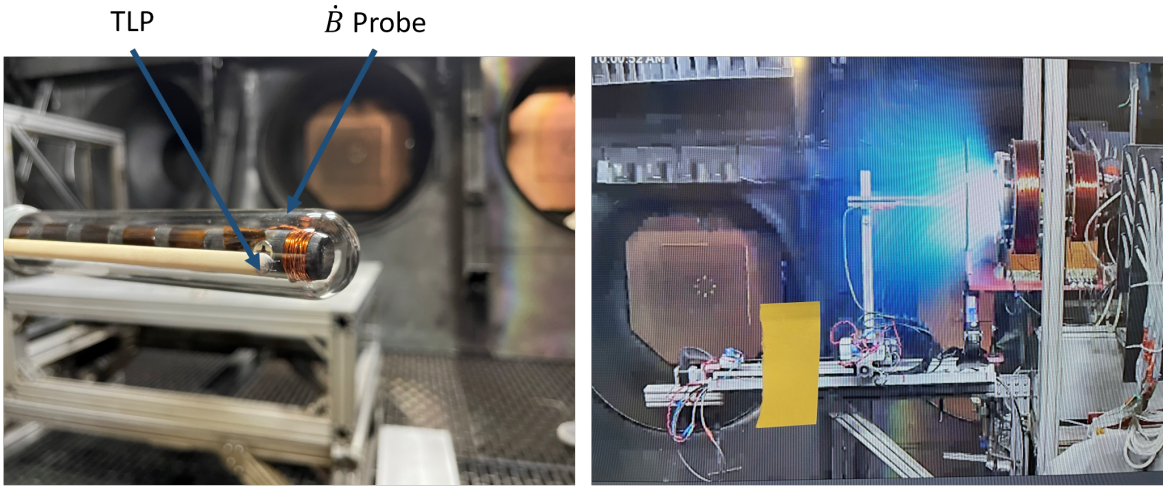

Figure 5.18: Images of TLP setup used in experiment. (a) Close up image of the triple Langmuir probe, and (b) image of the motion stages injecting probes into thruster during operation.

$$I_1 = I_{i1} - A_p j_e \exp\left(\frac{V_1}{T_{eV}}\right) = -I, \tag{5.26}$$

$$I_2 = I_{i2} - A_p j_e \exp\left(\frac{V_2}{T_{eV}}\right) = 0, \tag{5.27}$$

$$I_3 = I_{i3} - A_p j_e \exp\left(\frac{V_3}{T_{eV}}\right) = I, \tag{5.28}$$

where I_i is the ion current to each probe, A_p is the probe area, j_e is the electron saturation current density ($j_e = en\sqrt{eT_{ev}/2\pi m_e}$), and V_i is the potential of each probe. Following the derivation of Ref. [13], an implicit relation between the measured differential voltage $V_{TLP} = V_1 - V_2$ and the electron temperature can be derived as

$$1/2 = \frac{1 - \exp\left(-V_{TLP}/T_{eV}\right)}{1 - \exp\left(-V_a/T_{eV}\right)}. \tag{5.29}$$

This equation is presented graphically in Fig. 5.19(b). To calculate the plasma density as measured by the TLP, the shared term $A_p j_e$ is eliminated from the equations for the measured current carried by probes 1 and 3, resulting in

$$I_{TLP} = I_{i3}(V_3) - I_{i2}(V_2) \exp\left(\frac{V_{TLP} - V_a}{T_{eV}}\right). \tag{5.30}$$

For most Langmuir probe ion sheath models, the ion current contribution is expressed as the product of density, an electron temperature-dependent factor ($\gamma(T_{eV})$), and a probe voltage-dependent factor ($\beta(V)$). The electron density (n_e) can then be determined using the following expression:

$$n_e = \frac{\alpha I_{TLP}}{\gamma(T_{eV})} \left[\beta(V_3) - \beta(V_2) \exp\left(\frac{V_{TLP} - V_a}{T_{eV}} \right) \right]^{-1}. \tag{5.31}$$

Here, an ad hoc scaling factor (α) is introduced to account for the assumption that electrons follow a Maxwellian distribution, and that measurements from TLPs in non-equilibrium conditions can lead to significant errors [69]. In practice, if the density scaling factor is not included, the experimentally determined plasma power from the sum in Chapter 3, Eq. 3.39, exceeds the power measured as coupled into the plasma from the waveform measurements by more than twice. In the subsequent analysis, I adjust this parameter to ensure equal energy in both cases. Typically, the value of this scaling factor falls within an order of magnitude of unity.

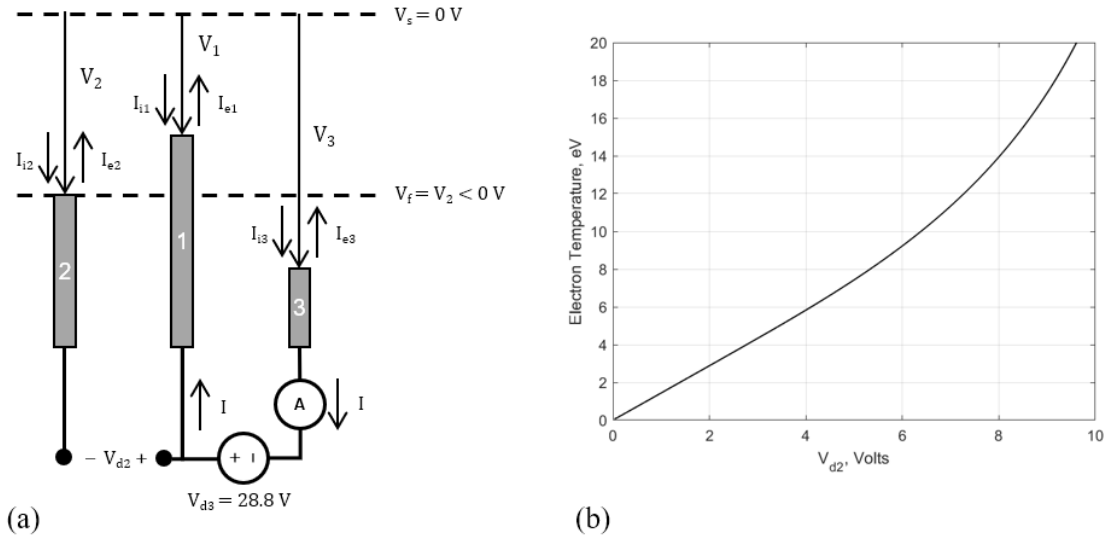

Figure 5.19: Triple Langmuir probe analysis diagrams. (a) TLP operation. (b) Function of measured voltage V_{d2} to electron temperature as described by Eq. 5.29.

Based on the geometry of the probe and the expected densities from prior measurements [29], I employ orbital motion-limited (OML) theory for the expansion of the ion sheath [57]. This is a result of the measured probe radius to Debye length ratio from the measurements

nearing or exceeding 50 [57]. In this framework, the OML parameters are defined as follows

$$\gamma_{OML} = \frac{eA_p}{\pi} \tag{5.32}$$

$$\beta_{OML}(V) = \sqrt{\frac{2e(-V)}{m_i}}. \tag{5.33}$$

where, A_p is the surface area of one electrode. Using this sheath expansion model, Eq. 5.31 becomes:

$$n_e = \alpha \frac{\pi I_{TLP}}{eA_p} \sqrt{\frac{m_i}{2e}} \left[\sqrt{V_a - V_{TLP} + \Phi} - \sqrt{\Phi} \exp\left(\frac{V_{TLP} - V_a}{T_{eV}} \right) \right]^{-1}, \tag{5.34}$$

where $\Phi = T_{eV}\sqrt{(2m_i)/(\pi m_e)}$ is the difference between floating voltage and plasma potential.

To characterize the uncertainty of these measurements, I show in Fig. 5.20 a selection of TLP data taken at one spatial measurement point. These figures show the traces recorded for a sequence of 25 RMF pulses in gray in addition to the average trace from these acquisitions overlaid in black. These results show that the RMF pulses are generally repeatable and stable with a spread of roughly 30 % of the peak signals. This uncertainly is largely driven by the RMF noise and more acquisitions would help to produce a cleaner average signal. However, this uncertainty is smaller that the uncertainty due to non-Maxwellian electron effects and therefore is not a dominant source of error.

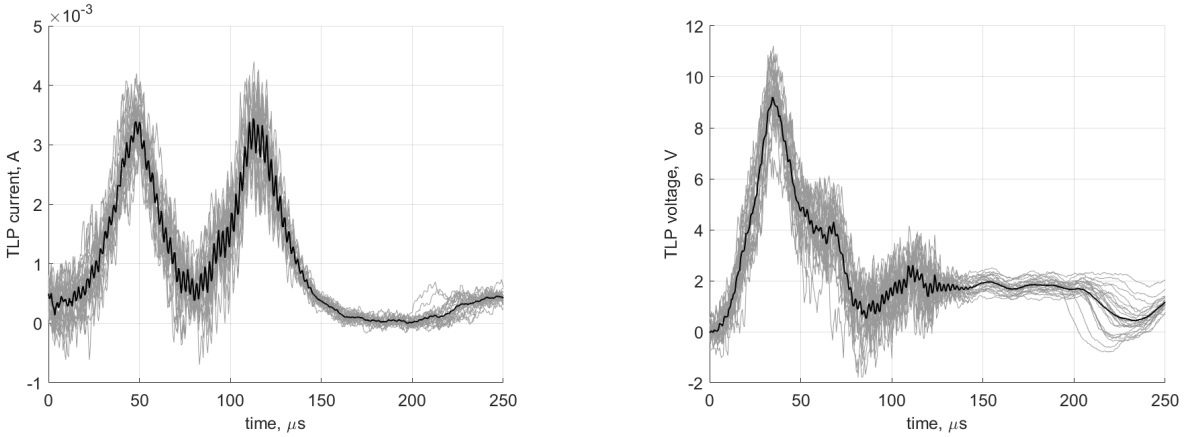

(a) Triple Langmuir probe current

(b) Triple Langmuir probe voltage

Figure 5.20: Triple Langmuir probe averaging analysis. Light gray represents acquisitions from 25 pulses and black is resulting average of that data. These measurements were performed at a fixed spatial location.

To estimate neutral density, I invoke continuity for the heavy species and assume negligible

convection on the time-scale of ionization, justified by the much longer transit time of neutrals compared to the characteristic ionization time-scale. After the time of peak ionization, I assume all neutrals are effectively converted to plasma. This assumption is supported in Chapter 6, Sec. 6.3.2.2, by the experimental observation that the mass utilization is of order unity when corrected for wasted gas between shots. I further assume that the plasma density is subsequently governed by convection only. This yields two relations between the neutral density and the plasma density:

$$\frac{\partial}{\partial t}\left(n_e + n_n\right) = 0 \text{ for } t \leq t_{pk} \tag{5.35}$$

$$\frac{\partial}{\partial t}\left(n_n\right) = 0 \text{ for } t > t_{pk}, \tag{5.36}$$

where t_{pk} is the time when I measure local peak plasma density. These expressions can be integrated to give an estimate for the neutral density at each spatial location:

$$n_n(t) = \begin{cases} n_e(t_{pk}) - n_e(t) & \text{for } t \leq t_{pk}, \\ 0 & \text{for } t > t_{pk}. \end{cases} \tag{5.37}$$

Using the local properties (n_e, n_n, and T_{eV}) at each measurement location, I can evaluate loss modes using the expressions in Chapter 3. The error in these measurements is primarily driven by the systematic uncertainty in the correction factor α, as density has an out-sized effect on the evaluation of the energy loss terms.

5.8 Summary

I began this chapter with an overview of the vacuum test facility and supporting infrastructure for this study. This was done to provide the reader with an understanding of the baseline tools used for thruster operation. Following this, I describe the suite of diagnostic tools used to measure properties of the ion beam, the plasma properties internal to the thruster, and the performance of the RMF power system. These diagnostics include a guarded Faraday probe, a set of current transducers, a retarding potential analyzer, and single and triple Langmuir probes. I explained the working principle of each of these diagnostics and the methods and equations used to measure each of the efficiency modes from Chapter 3. These diagnostics are employed in the following two chapters (6 and 7) to perform detailed studies of the RMF thruster prototypes to explain and characterize their performance.

CHAPTER 6

Measurements of Phenomenological Efficiency Modes of RMF Thrusters

In this chapter, I provide a comprehensive overview of experiments conducted on the PEPL RMFv2 thruster. The primary focus is on measuring the phenomenological efficiency modes—mass utilization, divergence efficiency, coupling efficiency, and plasma efficiency—as introduced in Chapter 3. To contextualize this research, I initially present a series of thrust and performance measurements conducted under various operating conditions of the RMFv2 thruster. These measurements reveal an optimal condition for the thruster, which becomes the focal point for the rest of the chapter.

Subsequently, I delve into detailed plasma diagnostic measurements performed on the thruster under this optimal condition and conduct a thorough evaluation of the efficiency breakdown. Following this analysis, I present measurements of the internal plasma properties of the thruster. Utilizing these measurements, I assess the contribution of internal loss modes to the plasma, aiming to assess the factors influencing the plasma efficiency of this device. The chapter concludes with an examination of the key drivers for these losses.

6.1 Experimental Setup

For this experiment, RMFv2 thruster was tested within the Alec Gallimore Large Vacuum Test Facility. Accompanying the thruster was a suite of diagnostic tools employed for measuring thruster performance and plasma properties. This suite includes the inverted pendulum thrust stand, antenna current transducers, the swept far-field Faraday probe, and a translated near-field triple Langmuir probe. Additional details about these diagnostics and their analysis are provided in Chapter 5.

For the thruster performance measurements presented in this chapter the flow rate is reported as the total flow through both the cathode and neutral injector mass flow controllers,

and the power is reported as the DC power supplied to the RMF PPU. The setup of these diagnostics within the vacuum facility for this experiment is illustrated in Fig. 6.1a.

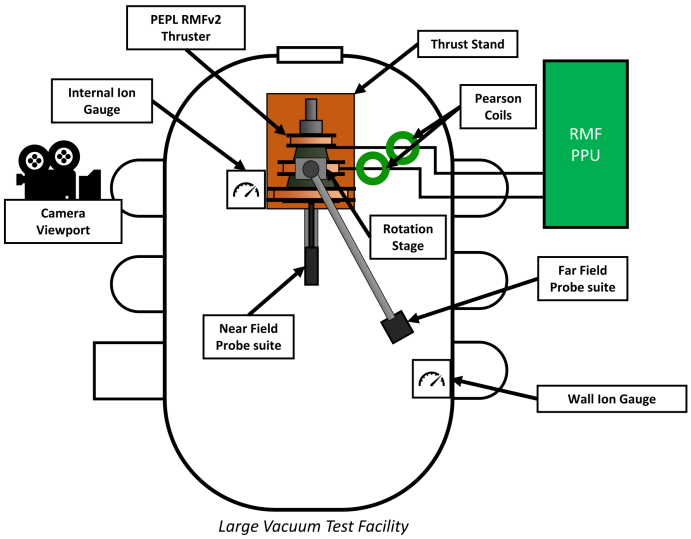

(a) Vacuum facility setup

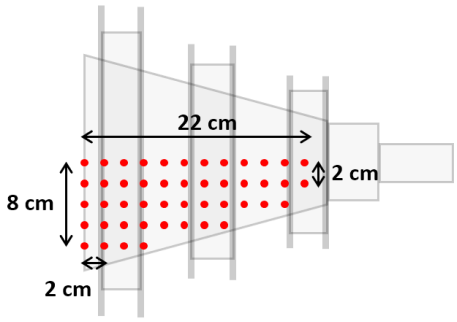

(b) TLP measurement locations

Figure 6.1: Setup for RMFv2 thruster experiment.

For the TLP measurements, a two-axis motion stage was utilized within the thruster near-field, enabling the translation of the probe on a horizontal plane aligned with the thruster axis. The measurements were conducted inside the thruster volume, covering an approximately 2 cm square grid that accounted for the taper of the thruster cone. The corresponding locations are illustrated in Fig. 6.1b.

6.2 Results

In this section, I present the experimental results of the RMF thruster performance and its internal plasma properties. I begin by reporting global performance measurements. Subsequently, I present the raw diagnostic data, including the RMF waveforms measured by the current transducers and figures of the Faraday probe-measured ion current density. Using these measurements, I calculate the four phenomenological efficiency values from the model presented in Chapter 3.

Following this, I present a raw data trace from the TLP and show time-resolved plots of plasma density and electron temperature inside the thruster. Using these measurements, I evaluate the spatial average of these properties over time, as well as an estimate for the evolution of average neutral density. Leveraging these measurements, I evaluate the con-

tributions to plasma losses—thermal, wall, ionization, and radiation—and present their magnitudes and relative fractions of the beam energy.

6.2.1 Global Performance

In Chapter 4, as part of the RMF thruster prototype description, I present global thruster performance trends. This data is displayed over the propellant-specific energy, which can be considered as power per flow rate and is measured in J/kg. In principle, higher specific energy should lead to higher thrust, specific impulse, and therefore efficiency. However, as indicated in Chapter 4, the trends in global performance for the RMFv2 thruster show an optimum in specific energy around 1000 J/mg.

Here, I aim to illustrate the source of this optimum by showcasing a set of specific performance measurements. These conditions involve varying the thruster flow rate from 2.7 mg/s to 5.4 mg/s xenon (30 - 60 sccm) at roughly constant power and RMF amplitude (1 kA peak, 2 kA pk-pk). This results in a range of specific energies from 770 J/mg for the high flow rate to 1,470 J/mg for the low flow rate. Apart from the flow rate, the thruster was operated at a standard set of conditions for the RMFv2 thruster, as shown in Table 6.1. I also include 10-second exposure images of the thruster operating at the three flow rates using the same camera aperture and settings in Fig. 6.2.

Table 6.1: RMFv2 Standard Operating Conditions

Parameter	Value
Total Flow Rate	$2.7 - 5.4\,\mathrm{mg/s}$
Bias Field	180
Pulse Length	125
RMF Amplitude	2.0
Rep Rate	$155 - 165\,\mathrm{Hz}$
Power	$4\,\mathrm{kW}$
Cathode-Anode Current	$18\,\mathrm{A}$
Cathode Flow Rate	$1.35\,\mathrm{mg/s}$

Figure 6.2 displays the beam plasma from the thruster diffusely extending downstream. This luminance pattern, observed under these operating conditions, is an indication of the time-averaged behavior over approximately 1500 pulses. While this image may not capture transient plasma behavior, previous high-speed imaging has revealed a distinct "D-shaped" plasma structure expelled from the thruster [80], with the time-integrated light intensity approximating this distinctive shape. The brightness of the plasma clearly increases with flow rate, extending from a downstream distance of 20 cm to 30 cm in line with the rising

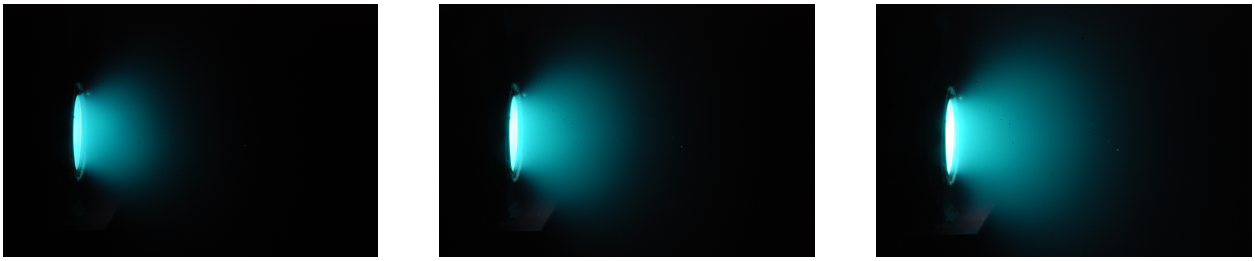

(a) 30 sccm flowrate (b) 45 sccm flowrate (c) 60 sccm flowrate

Figure 6.2: RMFv2 thruster firing under various operating conditions.

flow rate. Additionally, there is a noticeable increase in radial expansion from the upstream cone, which may correlate with a decrease in divergence efficiency.

Table 6.2: RMFv2 Performance Results

Flow rate Condition (mg/s Xe)	2.7		4.0		5.4	
Thrust (mN) and Impulse (μN-s)	7.91	49.4	11.6	74.9	11.7	7.07
Flow Rate (mg/s) and Mass (μg)	2.70	16.9	4.00	26.1	5.40	32.7
Power (W) and Energy (J)	3969	24.8	4066	26.2	4132	25.0
Thrust-to-Power (mN/kW)	1.99		2.85		2.83	
Specific Energy (J/mg)	1,470		1,000		766	
Specific Impulse (s)	299		292		220	
Efficiency (%)	0.29		0.41		0.31	

I present an overview of the RMF thruster's steady performance metrics for these operating conditions in Table 6.2. This includes thrust, mass flow rate, and delivered power. Additionally, equivalent per-shot values, including impulse, mass, and energy, are derived through a straightforward division by the pulse repetition rate, as discussed in Chapter 5. The table also features calculated specific energy (E_{in}/M), thrust-stand measured thruster efficiency (η) based on Eq.5.5, and specific impulse (I_{sp}) as per Eq.5.4.

The values in Table 6.2 are low compared to other state-of-the-art electric propulsion technologies like gridded ion and Hall thrusters. The efficiency and specific impulse are each one to two orders of magnitude smaller than typical for those devices. This behavior is consistent with other RMF thruster research efforts reported to date. For instance, Furukawa et al. estimated 7 mN of thrust for 3 kW RF power at 1.8 mg/s argon flow rate, yielding an efficiency of $\sim$0.5% and a specific impulse of 400 s [23]. These results were for substantially longer RMF pulse lengths (on the order of 100 ms), corresponding to a specific energy per shot of 1.67 J/μg. Weber, on the other hand, estimated for the ELF thruster a single-shot impulse of 338 μNs for 15.6 μg of nitrogen, yielding a specific impulse of 2,200 s [95].

While this specific impulse exceeds our reported values, this thruster was operated at a minimum of 10× the specific energy per shot (J/kg) of our system at roughly 10 J/μg. I note here that the actual total energy per shot (including losses in the driving circuit) was not reported in the previous work by Weber et al., which precludes a direct comparison with our measurement. With respect to efficiency, Weber in Ref. [95] reports a value of 8 %; however, this estimate did not include divergence losses, mass utilization, or coupling loss. Allowing for values consistent with our measured contributions (Sec. 6.2.5), this would bring the ELF efficiency to < 0.7 %, which ultimately is consistent with our measured efficiency. Furthermore, specifically allowing for divergence and mass utilization would also serve to lower their specific impulse measurements per Eq. 5.4. Radially directed energy would not contribute to thrust, and waste propellant between shots would increase measured mass flow to the thruster. Applying values for the RMFv2 for mass utilization and divergence would reduce the specific impulse to 1,050 s. This value remains higher than the RMFv2 specific impulse, however ELF was operated on nitrogen, as compared to the heavier xenon used here. To correct for this difference, I use the square root of the mass ratio between xenon and nitrogen, 0.33, which results in a corrected I_{sp} for the ELF thruster running on xenon of 345 s. This specific impulse is ultimately consistent with our measurements and the measurements of Furukawa in Ref. [23].

Despite the subtle trends in this data, I can identify both an increase in thrust with flow rate and a decrease in specific impulse. This suggests that the higher specific energy at lower flow rates imparts more energy to accelerate each ion, aligning with expectations. However, thrust does not increase in proportion with the flow rate, instead saturating between the 4.0 and 5.4 mg/s flow conditions. This indicates that there is a limit in the ability for the thruster to accelerate the propellant and that the increase in density from the higher flow rate permits the energy from the RMF to be absorbed through other means (see Sec. 6.2.6). Furthermore, while there is an increase in specific impulse at the high specific energy 2.7 mg/s case, it is marginal over the 4.0 mg/s case, but the reduction in mass flow down to 2.7 mg/s decreases the thrust precipitously. This makes sense as the force will be proportional to the azimuthal current density produced by the RMF, and as shown by Eq. 3.19, current density should scale with the mass flow supplied to the thruster.

Considering the interplay of these factors, the thruster exhibits an optimum efficiency at 4.0 mg/s. I now turn towards understanding the physical drivers behind these low performance metrics at this optimal condition. For instance, the low specific impulse may indicate either thermal acceleration dominance or low mass utilization, while the low efficiency could stem from losses attributed to the mechanisms identified in Chapter 3. Further exploration into the causes of these performance metrics is assessed in the subsequent sections.

6.2.2 Waveforms

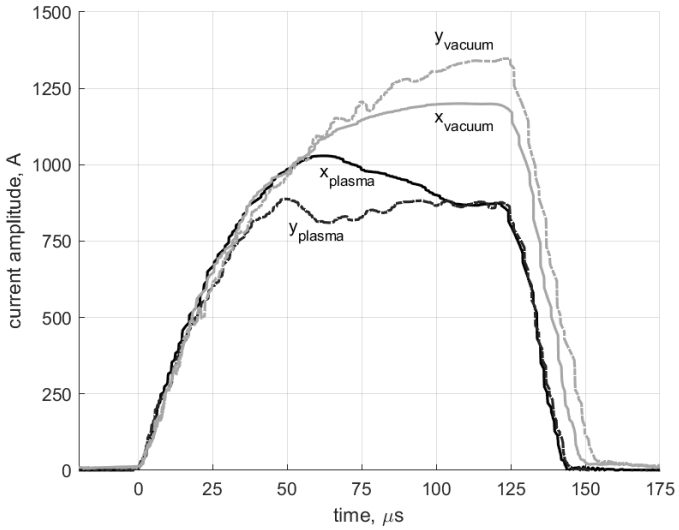

Figure 6.3: Antennas waveform envelopes for RMFv2 thruster. Dark lines are for plasma-loaded operation, and the light gray curves are for vacuum conditions. Labels 'x' and 'y' correspond to their respective antenna phase.

In Fig. 6.3, I present the envelopes of the high-frequency currents passing through the RMF antennas for a plasma-loaded and vacuum shot at the same DC input voltage of 235 V. For our RMF PPU operating at resonance, the ultimate value of the current amplitude in each case is determined by the effective resistance of the circuit. The disparity in amplitude between the two antenna sets (denoted X and Y) arises from differing stray inductance, leading to slightly off-resonance operation.

In both antennas, the higher peak currents in the unloaded vacuum case indicate an overall lower effective resistance in the resonant circuit. The vacuum shot exhibits a monotonic increase during the pulse to a value of 1250 A, and the amplitude rapidly decays after the end of the pulse at 125 μs. For the plasma-loaded case, the initial ramp-up is identical to the vacuum configuration. This can be explained by the fact that the low-density seed plasma does not present a significant load to the antennas. However, once the remaining propellant is ionized by the increasing RMF-driven current and begins to accelerate, the plasma load becomes significant, leading to non-monotonic behavior between 50 and 135 μs. The overall magnitude of the current in the plasma-loaded case reaches a maximum of $\sim$1000 A. The difference in the area under the two current envelopes (vacuum versus plasma) visually represents the energy coupled to the plasma in the plasma-loaded case.

Using Eq. 5.20, I measure an effective resistance for the plasma-loaded case of 282 $\pm$ 6

mΩ and an effective resistance of the unloaded vacuum case of 213 ± 1 mΩ. This yields a plasma resistance of 69 ± 6 mΩ. The uncertainty in these reported values is the standard deviation over three independent measurements.

6.2.3 Faraday Probe

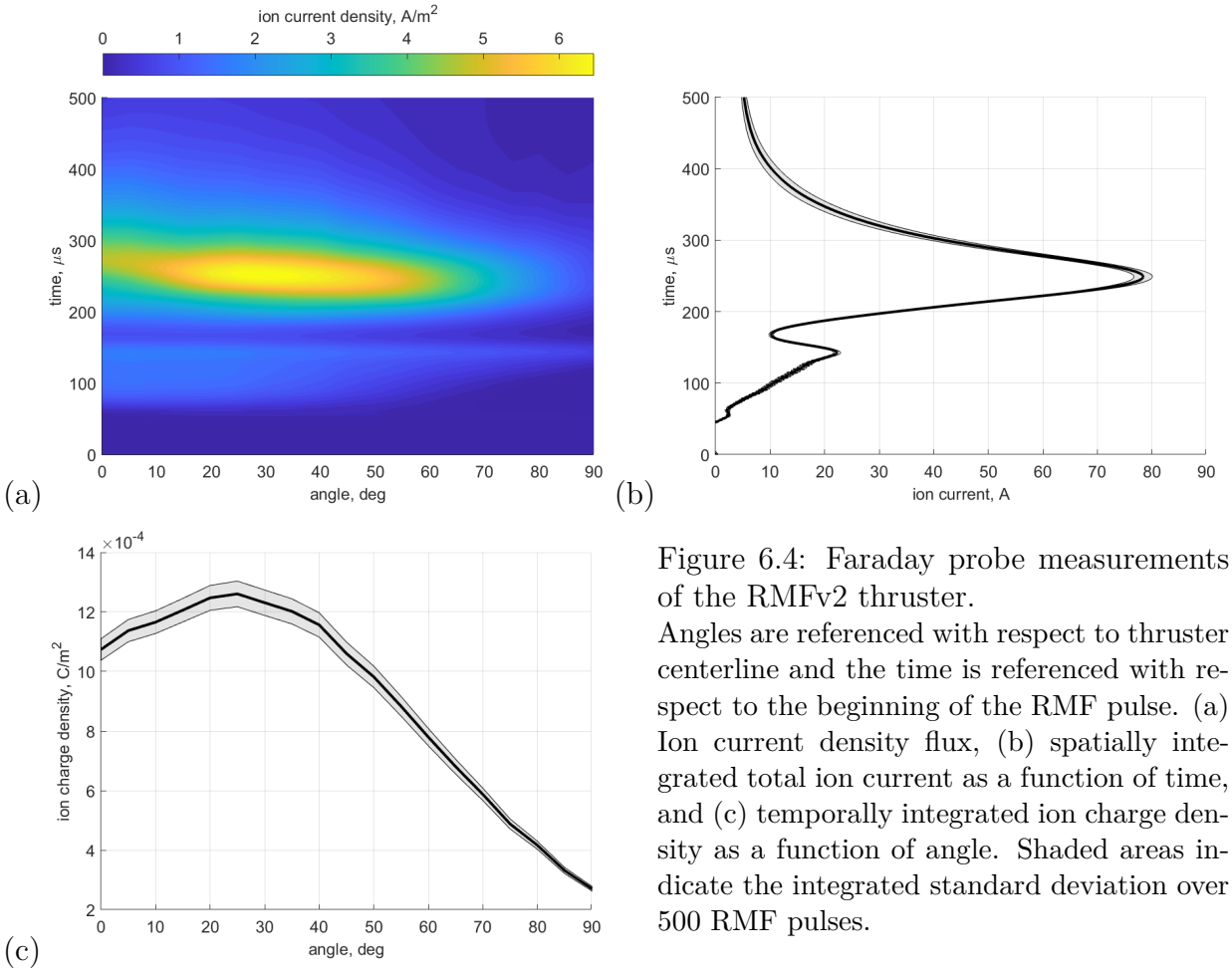

Figure 6.4: Faraday probe measurements of the RMFv2 thruster.
Angles are referenced with respect to thruster centerline and the time is referenced with respect to the beginning of the RMF pulse. (a) Ion current density flux, (b) spatially integrated total ion current as a function of time, and (c) temporally integrated ion charge density as a function of angle. Shaded areas indicate the integrated standard deviation over 500 RMF pulses.

In Fig.6.4, I present the measurements made with the FP of ion current density in the thruster plume. Specifically, Fig.6.4a shows the full dataset as a function of angle and time, where the angles are referenced with respect to the thruster centerline. Aspects of the plume acceleration can be further interrogated by integrating these results over space or time, which I show in Figs. 6.4b and 6.4c, respectively.

In Fig.6.4a, a dominant population of ions at 30 degrees with a time delay of ∼250 μs is evident, exhibited by the maximum in the plot. The peaked structure implies a toroidal plasmoid extending from the centerline out to 50 degrees. This result can be interpreted as a concentrated population of ions moving at an approximate speed of $u_e = 7$ km/s away

from the thruster (taking into account the ionization time, $t_{iz} = 12.5$ μs). The shape of this population can be attributed to the fact that the majority of RMF-induced current, and by extension Lorentz force acceleration, peaks between the thruster wall and centerline [82]. I remark that the apparent speed of the plasma torus does not directly map to specific impulse, e.g., $I_{sp} \neq u_e/g_0$. This disparity may be explained by large divergence as well as low mass utilization.

In Fig.6.4b, the ion beam current as a function of time is shown. In this form, the ion current exhibits a notable dispersion with a tail that extends beyond 500 μs. The results in Fig.6.4b suggest that although the bulk of the plasma is accelerated to the same speed, the RMF scheme results in a continuous spectrum of ion velocities. There may be a few factors driving this effect. For example, while the Lorentz force acts across the bulk of the thruster, ions at the back of the device will experience a longer exposure to this body force, thereby gaining more acceleration. The spatial distribution of ions subject to acceleration thus may result in a spectrum. Similarly, the spread may also be attributed to the influence of other forces in addition to the axial Lorentz force. For example, ions may be heated by compression from the radial component of the Lorentz force. Additionally, I note the existence of an early peak in current density between 75 - 150 μs, which is plausibly explained by the existence of faster, doubly-charged Xe^{2+}. I cannot explicitly confirm this, however, as I did not measure the ion charge state as a function of time in this work. For simplicity, in the remainder of this analysis, I neglect the contribution of any such secondary population. Given the low current density associated with this higher velocity population, I have found this simplification at most results in an error of 3 % from the reported values.

In Fig. 6.4c, the FP-measured current density integrated over time is shown. This results in a plot of charge density as a function of angle with respect to the thruster centerline. The large characteristic divergence of the RMF is evident from this plot, with substantial charge density extending out to an angle of 50 degrees. Furthermore, the dip in charge density on the centerline is consistent with our interpretation of a toroidal structure.

As figures of merit, I can use the data presented in Fig. 6.4 combined with Eqs. 5.7-5.12 from chapter 5 to determine key aggregate values for mass flow, ion current, and momentum transfer. To this end, I find the resulting steady ion mass flow rate, $\dot{m}_i = 3.11 \pm 0.01$ mg/s, the steady beam current, $I_{\text{beam}} = 2.29 \pm 0.01$ A, and the axial component of the beam current, $I_{\text{axial}} = 1.41 \pm 0.01$ A. Using the FP to perform ion velocimetry, and applying Eq. 5.12 from chapter 5, the beam force is $F_{\text{beam}} = 20.0 \pm 1.6$ mN, which, recall, acts as distributed ion beam pressure in the downstream hemisphere. Using these values results in a beam power of $P_{\text{beam}} = (F_{\text{beam}})^2/(2\dot{m}i) = 64 \pm 7$ W. Here, the errors stem from the propagation of the standard deviation of our 500 FP traces at each angular position and the uncertainty in the

ionization time delay, t_{iz} in Eq. 5.13 from chapter 5.

6.2.4 Triple Langmuir Probe

In this section, I present the results from the TLP measurements. I begin by showcasing an example measurement from the TLP. Subsequently, I display a chosen set of time-slices featuring spatially resolved internal plasma properties throughout the RMF pulse. Following this, I report the time-resolved spatially averaged plasma density, electron temperature, and an estimate for the neutral density. As discussed in Chapter 5, Section 5.7, these results were obtained by translating the TLP within the thruster between shot bursts, utilizing the repeatability of the shots to synchronize measurements.

6.2.4.1 Raw TLP Data

In Fig. 6.5, I present an example raw trace from the TLP. In this plot, V_{TLP} represents the differential measured voltage between electrodes 1 and 2, while I_{TLP} is the current passing through electrodes 1 and 3, as illustrated in Chapter 5, Fig. 5.19. An observable feature in the plot is the negative measured voltage V_{TLP} between 200 and 250 μs. This non-physical occurrence is likely a result of the probe becoming improperly biased once the plasma rarefies and ejects out of the thruster. Best practices for TLPs involve maintaining the bias voltage on the order of the electron temperature. However, this becomes challenging due to the large transients in plasma properties during the RMF pulse. Due to this persistent effect in the measurements, I limit the data presentation to the first 200 μs after the onset of the RMF. This choice is justified in Sec. 6.2.6, where Fig. 6.9 demonstrates that the loss mechanisms, which I seek to characterize, tend towards zero before the 200 μs cutoff as the plasma exits the device. Further discussion on this consideration is provided in Sec. 6.3.1.2.

6.2.4.2 Internal Plasma Properties

In Fig.6.6, I present spatially resolved plasma density and electron temperature for various times during thruster operation. These values were calculated using Eqs.5.29 and 5.34 from Chapter 5, using the instantaneous voltage and current, V_{TLP} and I_{TLP}, measured by the probe. The scaling factor employed in Eq. 5.34 for determining the density from the raw TLP trace is $\alpha = 0.637$.

Figure 6.6 reveals that the electron temperature peak is reached around 32 μs, with most of the hot electrons (around 12-15 eV) forming near the back of the thruster near the wall. This follows intuition, as that is the location where the RMF fields are the strongest and the least uniform due to the close proximity to the RMF antennas. Non-uniform fields

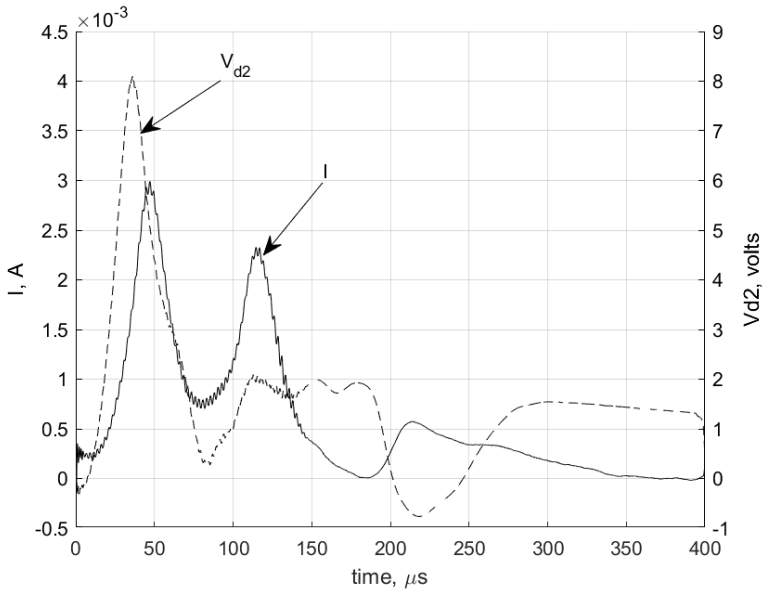

Figure 6.5: Example raw TLP trace.

would cause more randomized motion of the electrons and thus increased heating. For plasma density, peak values occur near 50 μs, notably after the electron temperatures peak. This is unsurprising given that the RMF ionization source couples energy into the free electrons which subsequently results in an ionization cascade. During this maximum, there is little spatial variation in plasma density across the entire thruster volume, ranging between $1 \times 10^{19}\text{m}^{-3}$ and $1 \times 10^{20}\text{m}^{-3}$. However, a slight off-center peak in plasma density exists, consistent with field-reversed-configuration (FRC) plasmoids [42]. Although interesting, the formation of FRCs is not a specific target for our thruster.

In Fig. 6.7, I show the spatially averaged properties of the plasma discharge from the TLP as a function of time. The results shown here are averaged by performing a numerical integral of the local plasma properties over the internal thruster volume in cylindrical coordinates. Additionally, I show the estimated volume-averaged neutral density from Eq.5.37. The uncertainty reported in these results is assumed to be a flat 50 % for both density and temperature. As discussed in Sec. 5.7, Langmuir probes and TLPs, in particular, are known to be inaccurate in non-equilibrium conditions up to our assumed degree of error, which is beyond what can be accounted for statistically [57, 69].

The mean plasma density begins to increase rapidly at the beginning of the RMF pulse and peaks at $1.9 \times 10^{19}\,\text{m}^{-3}$ after 50 μs. I take the time that the plasma density reaches half of this maximum (25 μs) as the upper bound on possible ionization delay times, t_{iz}, for the calculation of probe-measured beam force in Eq. 5.12. Following this peak, the plasma

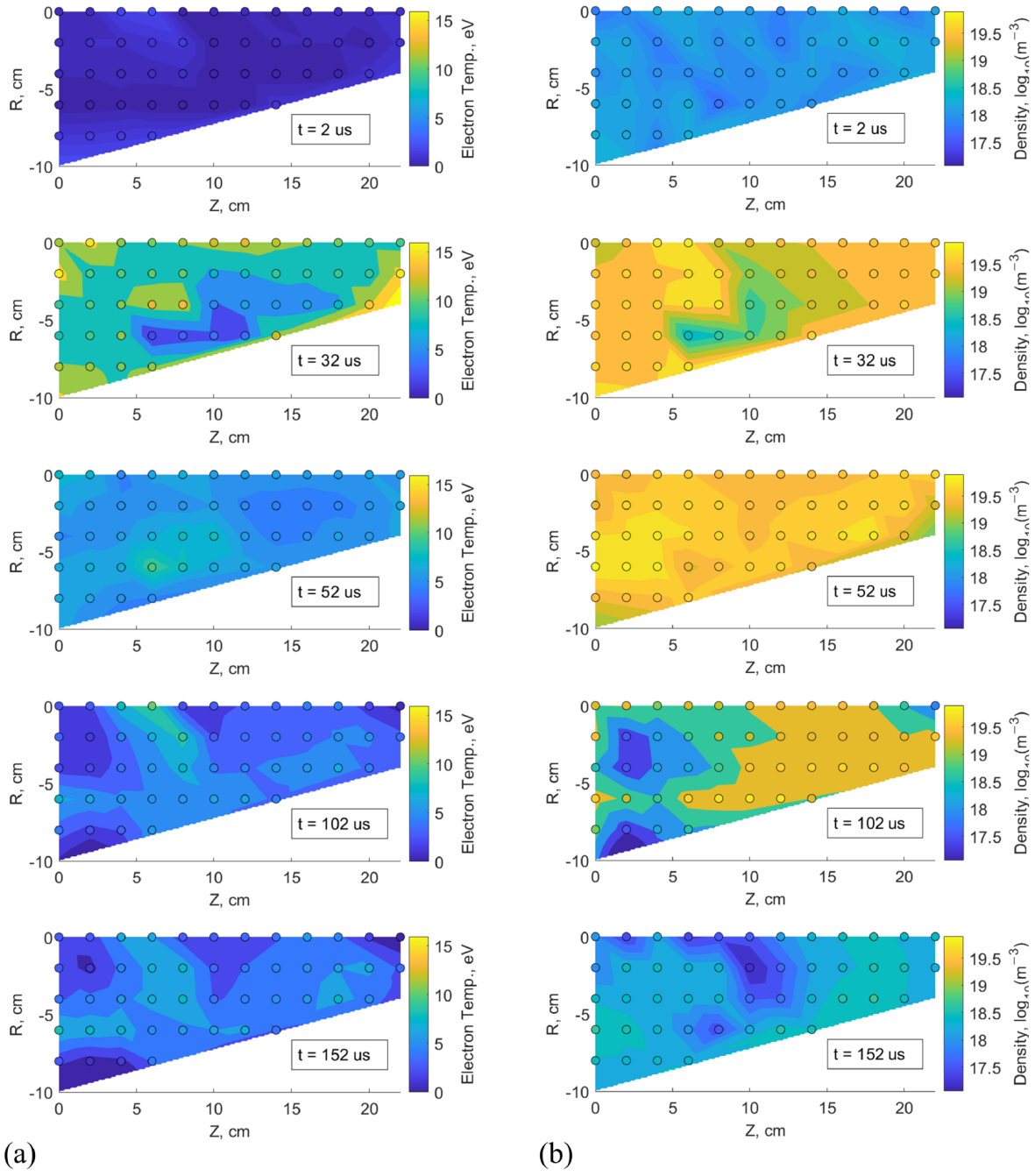

Figure 6.6: Spatially resolved plasma properties from triple Langmuir probe measurements. (a) Electron temperature in eV (b) Plasma density in $\log_{10}(m^{-3})$. The origin is located at the center point of the thruster exit plane with the thruster pointing left.

density decays for the duration of the plasma shot. This is a qualitative indication of the acceleration of the plasma out of the geometry.

The electron temperature, as shown in Fig.6.7, also increases with the RMF pulse du-

ration. Notably, the peak electron temperature is less than the first ionization energy of xenon (12.1 eV), indicating that the bulk of of the electrons do not have sufficient energy for ionization. This suggests the high rates of ionization observed are likely driven by a high-energy electron tail in the electron energy distribution. Relatedly, I suspect that there may be an even higher energy population contributing to the formation of doubly charged ions. Although I was not able to resolve such a population with the triple probing scheme, the fact that the Faraday probe needed to be biased to such high negative potentials (See Section 5.3) suggests indirectly that tail electrons may be present. The electron temperature profile leads the density by approximately 12 μs. The evolution of the average temperature with time profile likely can be explained by a balance between Ohmic heating from the RMF and energy sinks—such as ionization, wall loss, and radiation—that are linked to the evolving plasma density.

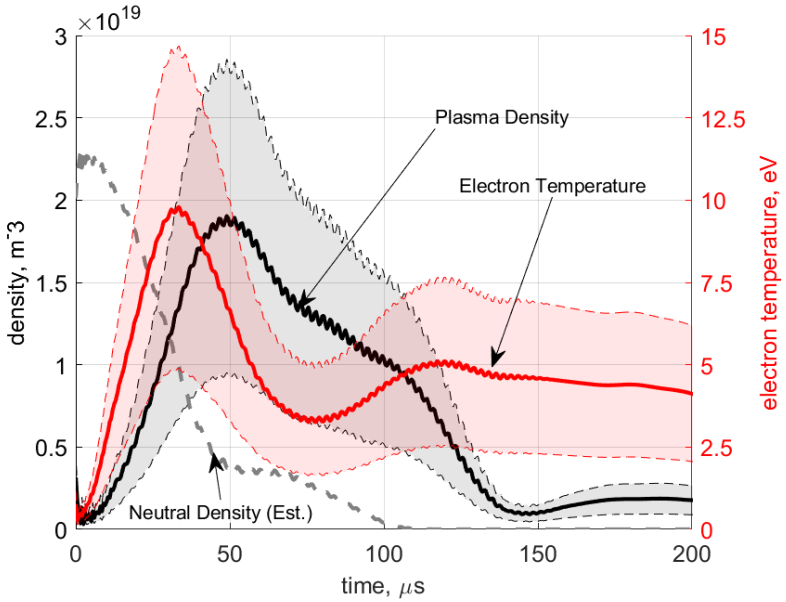

Figure 6.7: Spatially averaged internal plasma properties.

6.2.5 Efficiency Breakdown

I calculate efficiency terms defined in Section 3.3 using these plasma diagnostic results. I present these values in Fig. 6.8, where I also include, for comparison, the efficiency inferred from the thrust stand, η_{TS} (reproduced from Table 6.2), as well as the product of the terms inferred from probing, η_{probe}.

The divergence efficiency shown in this result by comparing the total beam current to the axially directed current following Eq. 5.9. This yielded 0.2% $\eta_d = 38.2 \pm 0.3\%$ with

a characteristic divergence angle of $\Theta \approx 52°$. This angle is consistent with the spatial distribution exhibited by Fig. 6.4c. I calculated the mass utilization following Eq. 5.11 from the measured steady ion mass flow rate and the neutral mass flow rate to arrive at a value of $\eta_m = 76.9 \pm 1.7\%$. Using the effective circuit resistances from the vacuum and plasma-loaded PPU, I determine a coupling efficiency of $\eta_c = 24.5 \pm 2.2\%$ via Eq. 5.19. Finally, with the beam power and plasma coupled energy, I calculated a plasma efficiency of $\eta_p = 6.4 \pm 1.0\%$ from Eq. 5.14. The product of these terms gives us a probe-measured efficiency of $\eta_{\text{probe}} = 0.46 \pm 0.09\%$.

Overall, the probe-measured efficiency agrees with the thrust stand efficiency within uncertainty, providing validation for these measurements. Furthermore, all of these terms are low when compared to equivalent terms in phenomenological efficiency analyses of more conventional electric propulsion systems like gridded ion and Hall thrusters. This is expected given that the overall performance of the RMF system is also lower.

While I discuss the physics impacting the magnitude of each efficiency mode in more detail in Sec. 6.3.2, I would like to briefly comment here on key trends. Specifically, the mass utilization is large relative to the other modes, indicating a high degree of conversion of neutral gas to plasma. The low divergence efficiency reflects the low collimation of the plume. The small coupling efficiency indicates 75% of the energy is parasitically consumed by the PPU and RMF antennas. Finally, the low plasma efficiency, a major driver for poor performance, suggests that 94% of the energy successfully coupled into the plasma by the RMF is not successfully converted to thrust and is wasted through other mechanisms.

6.2.6 Evaluation of Power Losses

I present in Fig. 6.9 the power losses over time from Eqs. 3.47, 3.44, and 3.51 in Chapter 3 for neutral excitation radiation, ion excitation radiation, ionization rate, and wall recombination loss. Note, in producing the results of this plot I did not perform the shot averaging integral in these equations and Fig. 6.9 shows the instantaneous power consumption for these mode over the course of a typical pulse.

Similar to the spatially averaged plasma properties values, Fig.6.9 shows a double-peak form for both radiative and wall losses across conditions. For radiative losses, the peaks occur at roughly 40 μs and 100 μs after the start of RMF pulsing, and for wall losses, these peaks occur near 30 μs and 80 μs. The earlier occurrence of wall losses is due to the increased dependence on electron temperature which leads the evolution of plasma density.

What becomes evident from these plots is that radiative and wall losses both contribute significantly to the low plasma efficiency, with these losses reaching peak powers of over 65

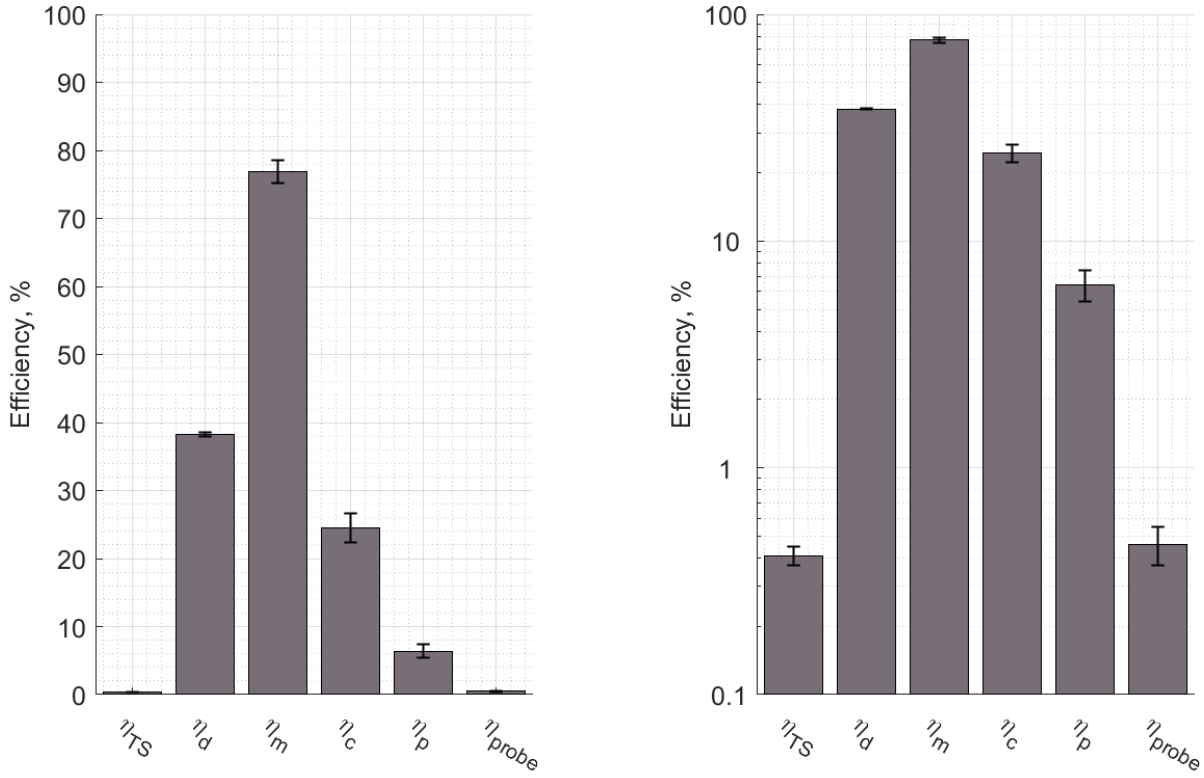

(a) linear scale

(b) log scale

Figure 6.8: Efficiency mode results for RMFv2.

kW. For reference, the RMF power over the 125 μs pulse is 210 kW. In total, radiative loss constitutes a larger energy loss per pulse due to the height of the second peak, which results from sustained plasma density in the latter half of the RMF pulse.

Integrating these losses over time, I show graphically in Fig. 6.10 the five channels of plasma power from Eq. 3.39. Alongside this, I show the fraction these loss modes exhibit relative to the beam power as a point of comparison following Eq. 3.40.

As can be seen, the beam power, representing the power successfully converted to thrust, is the second-lowest term. This is consistent with the observation that overall plasma efficiency is low. The second bar represents the thermal power of the ions. This is the smallest power mode but is significant relative to the impulsive power. The relatively high degree of thermal power may be explained either by variations in the magnitude of the accelerating force acting on the plasma—due to charge state or the radial dependence of axial Lorentz force—or by compressive work done by the radial component of the Lorentz force ($j_\theta \times B_z$). The ionization loss presented in Fig. 6.10 represents the power expended from the total rate of ionization

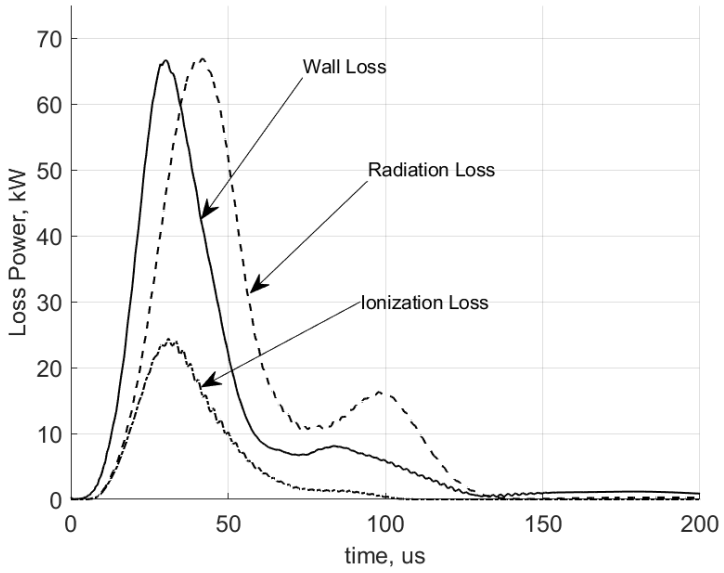

Figure 6.9: Time-resolved estimated power losses via energy channel in the RMv2 thruster.

collisions (from Eq. 3.44). This power is four times larger than the minimum "frozen flow" ionization cost based on the ejected ion mass ($P_{iz}^{\text{frozen flow}} = \varepsilon_{iz}\dot{m}_i/m_i$). This discrepancy might be attributed to high recombination rates that stem from the high plasma densities in the device. The wall loss as shown in Fig. 6.10 is over five times greater than the beam power. Thus, this also represents a substantial loss to plasma efficiency and likely can be explained by poor magnetic confinement of the electrons in addition to the substantial density displayed in the pulse. Finally, optical radiated power out of the thruster is the largest loss, constituting a loss of nearly sevenfold the beam power. As seen in Fig. 6.9, this radiation is primarily caused by the n_e^2 scaling of electron-ion excitation collisions, which dominate for the atypically large average plasma densities (compared to Hall or gridded thrusters, for example) exhibited during RMF pulsing. This idea of radiation losses being dominant for RMF thrusters has been indicated previously by Weber [95] and has also been suggested as an efficiency limiter for PIT thrusters by Polzin et al. [71].

In summary, I have shown that the performance of our RMF test article is consistent with previously reported experimental results, with an overall thrust efficiency of $0.41 \pm 0.4\%$ and a specific impulse of 292 s. Leveraging our phenomenological efficiency breakdown, I in turn have demonstrated that this poor performance can primarily be attributed to a low plasma efficiency, $\eta_p = 6.4 \pm 1.0\%$. This indicates that very little of the energy put into the plasma is converted to usable directed kinetic energy. Further examination into the energetic processes within the plasma revealed that the plasma loses energy during the

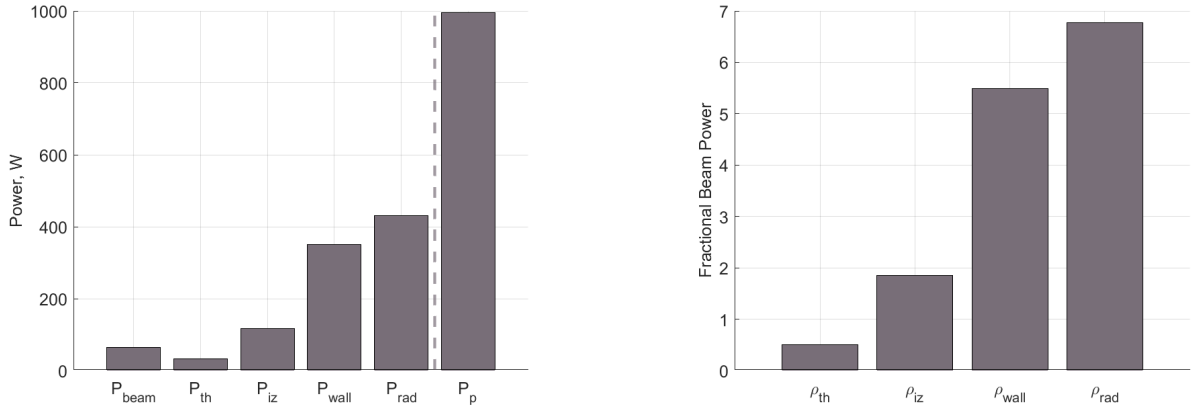

Figure 6.10: Plasma power loss channels, and power losses relative to the ion beam.

formation process primarily to excitation radiation and losses to the thruster walls. In the following section, I expand on the implications of these results and leverage our findings into possible strategies for improving performance.

6.3 Discussion

In this section, I discuss the limitations of our experimental methods and analysis. Additionally, I attempt to motivate physics-based explanations for the low performance of the RMF thruster. In turn, I suggest possible strategies, informed by these measurements, for increasing efficiency.

6.3.1 Measurement Considerations

6.3.1.1 Time-of-Flight

I address the validity of the key simplifying assumptions made in this study, starting with the time-of-flight velocimetry of the ion beam. As a first consideration, the ionization time delay, t_{iz}, introduces some ambiguity. In this work, I selected the upper bound of t_{iz} to correspond to the time when the measured plasma density reached half its peak value. This criterion is based on the interpretation that the plasma will not accelerate until reaching a critical density. Unfortunately, I was unable to directly measure the ion transit time due to the lack of direct velocity or energy information for the ion beam. I chose a sufficient range for t_{iz} to encompass the uncertainty of this assumption, and this error is reflected in the reported values. To enhance the accuracy of the ion speed measurement, future work could

involve a near-field trigger probe to establish a zero-drift-time reference or employ direct methods for ion velocimetry, such as laser-induced fluorescence.

6.3.1.2 TLP and Density

Secondly, as mentioned earlier, non-equilibrium electrons may introduce errors in TLP measurements. I estimate the relaxation time of fast electrons from the energy transfer collision frequency to be approximately 40 ns [75], which is much faster than the RMF pulse length, supporting our assumption of electron thermal equilibrium. However, electron drifts caused by the RMF may sustain a high-energy tail in the electron energy distribution. This could explain the need for a correction factor (Sec. 5.7) to yield physically plausible plasma densities, as TLPs tend to over-measure density and under-measure electron temperature in non-equilibrium conditions.

Additionally, for the calculation of plasma density, I employed OML theory based on the calculated ratios of probe radius to Debye length, following the best practices developed by Lobbia et al. [57]. While necessary, this single correction was over-constrained for the time-varying plasma, given the significant variation in the ratio of Debye length to probe radius over time, especially as the plasma cools and rarefies. Addressing this issue may involve increasing the probe radius and reducing the bias voltage to enable a thin sheath approximation and tune the bias closer to the electron temperature, respectively.

6.3.1.3 Loss Model

Lastly, in the analysis of plasma efficiency, when calculating the energy sub-terms, I made two major simplifications. First, I assumed the plasma freely streamed to the walls at the Bohm speed. However, the actual near-wall plasma in the thruster is subject to the applied magnetic field and fields arising from the RMF and azimuthally driven electron currents. This simplification likely results in an overestimate of the ion current to the walls, making the reported value for wall loss an upper bound. Second, our estimates of radiative loss do not incorporate a detailed collisional model for xenon. For simplicity, I represented the energetic loss due to the most prevalent excitation transitions for neutrals and singly charged ions. Similarly, Eq. 3.47 does not include any mechanism for photon absorption or collisional de-excitation, which can be important factors for total emitted radiation at or above our measured plasma densities [11]. Neglecting these effects may lead to an under-prediction of actual radiation losses, making our reported value a lower bound.

In practice, I included large yet physical error bounds to account for these effects. Even with these relatively large uncertainties considered, our overall conclusions remain

unchanged. For example, a key finding that holds outside of error bars is that radiation losses dominate the low plasma efficiency.

6.3.2 Efficiency Mode Discussion

6.3.2.1 Divergence Efficiency

The low divergence efficiency of the RMF thruster indicates inadequate collimation of the plume. This substantial divergence likely results from the sharply diverging magnetic bias field in this region [80] and the prevalence of thermally-produced isotopic thrust. It's noteworthy that electron cyclotron resonance (ECR) thrusters, utilizing a similar accelerating magnetic nozzle as an RMF thruster, exhibit a more tightly focused and axial beam in experiments, achieving divergence efficiencies between 85 % to 90 % [17]. This suggests potential for improving the divergence of our test article.

One possible method to enhance divergence is to strengthen the axial component of the bias field, to create a stronger compressive force when interacting with the driven azimuthal current. However, it's important to acknowledge that a more axial applied magnetic field may negatively impact Lorentz-force acceleration, as the radial component of the magnetic field would necessarily be reduced for a fixed field strength. Another potential outcome could be increased ion heating due to higher compression, leading to augmented divergence from randomized thermal motion. A thorough investigation into the optimal shape of the magnetic field such that the electron dynamics promote axial ion motion is necessary to better collimate the plasma to improve divergence efficiency.

6.3.2.2 Mass Utilization

The mass utilization efficiencies measured in this experiment do not constitute the critical loss factor for overall thruster performance. This stands in contrast to prior computational work [8], which suggested that mass utilization could significantly contribute to efficiency loss for RMF thrusters due to the interaction of a propagating ionization front with dense downstream neutrals. I hypothesize that the high mass utilization observed in this experiment results from the elevated plasma densities arising from the large amplitude current transients. This is further supported by the substantial power sink to ionization, as reflected in the rate of ionization estimated in Sec. 6.2.6.

It's worth noting that the mass utilization is not unity primarily due to wasted gas between shots. To illustrate, I can estimate the available neutral mass for a pulse using

$$M_{\text{fill}} = \frac{4\dot{m}L}{c_{th}}, \tag{6.1}$$

where L is the thruster length and c_{th} is the neutral thermal speed. In this work, this fill mass is 20.2 μg. Using this, I can calculate an pulse-wise mass flow rate

$$\dot{m}_{\text{pulse}} = f_{\text{rep}} M_{\text{fill}}, \tag{6.2}$$

which results in a value of 3.13 mg/s. In comparison to the FP-measured ion mass flow rate from Sec. 6.2.3, this indicates an effective mass utilization of 99.3 % for a given pulse. This implies that the thruster utilizes nearly all of the gas present when a shot is performed.

To increase mass utilization, one could, in principle, raise the pulse rate so that the fill time aligns with the pulse rate. For example, estimating a fill time for our test article as $t_{fill} = 4L/c_{th}$ suggests that the optimal pulse repetition frequency for our thruster is approximately 200 Hz (in contrast to the commanded rate of 155 Hz). Consequently, for a given thruster length, there might be an optimum pulse repetition frequency to maximize mass utilization without decreasing the mass per shot and, by extension, impulse. Although this dependency was not rigorously explored in this effort, it presents another potential strategy for marginally increasing thruster performance. However, it implies a certain power level to match the neutral fill times. This underscores an important distinction between RMF thrusters and PITs, where the coupling length (effective thruster length) is on the order of single centimeters. This analysis implies that the optimum pulse repetition rate for these thrusters is on the order of several kHz.

6.3.2.3 Coupling Efficiency

Our measured coupling efficiency values (approximately 25%) indicate that only a small fraction of the energy delivered from the power supply reaches the plasma. The primary sources of parasitic loss contributing to this inefficiency are the resistance in the antennas and the resistance in the driving elements from the PPU. To assess the contributions from antenna resistance, an estimate for the resistance of only the antennas can be made by assuming a 2× characteristic skin depth at 415 kHz, resulting in an estimated combined resistance for the two antennas of 21.6 mΩ. Comparing this antenna resistance to the measured plasma resistance (similar to Eq. 5.19, it is found that a significant portion of the power input to the antennas (76%) is coupled to the plasma. This indicates efficient power transfer to the plasma from the antennas and aligns with the calculated antenna-only coupling efficiency of the ELF thruster [95]. This suggests the overall coupling losses are dominated by the energy absorbed by the switching circuit of the PPU.

Potential strategies to mitigate coupling loss include increasing the load of the plasma or decreasing the resistance of the circuit. Addressing the first point, the startup process of pulsed operation leads to a substantial period with little plasma to absorb energy. Lengthening pulses of the RMF thruster could potentially enhance coupling efficiency by reducing startup losses for a given duty cycle. Additionally, increasing plasma density via a higher flow rate could raise the effective plasma load. However, gains in coupling efficiency from increased plasma density may be offset by the reduction in plasma efficiency resulting from higher plasma density. Notably, a lack of a uniform RMF field has been numerically shown to adversely affect plasma current drive in RMF plasma systems, suggesting that additional antenna phases could improve RMF thruster coupling by increasing RMF uniformity [42].

Regarding the second mitigation strategy, reducing the resistance in the PPU circuit can be achieved by lowering the overall current delivered through the RMF antennas. However, this reduction in current will also lead to decreased RMF penetration into the plasma column for a fixed electron density, resulting in a reduction in the driven azimuthal current and, consequently, Lorentz force. This effect may be mitigated by using multiple-turn antennas to increase the magnetic flux for a given current.

In practice, there are various approaches to address low coupling efficiency, but many involve trade-offs that impact other efficiency terms. While the test article was not optimized for maximizing coupling efficiency, these insights may prove valuable for enhancing coupling in future efforts.

6.3.2.4 Plasma Efficiency

As demonstrated in Sec.6.2.5, the dominant loss in the thruster is the plasma efficiency (Fig.6.8). Further analysis of the loss components to plasma efficiency (Fig.6.10) was conducted to gain insights into the plasma formation process. The general conclusion drawn from these results is that the primary loss processes in plasma efficiency are those scaling most with plasma density—linearly in the case of wall losses and quadratically for radiative losses. The prevalence of radiative loss, in particular, is attributed to the unusually high density in the RMF thruster. The peak density shown in Fig.6.7 is ten times higher than the peak plasma density in a 5-kW class Hall thruster operating at more than twice the propellant flow rate [33] and a hundred times higher than the density in a 5-kW class gridded ion thruster [16] at a similar flow rate. The two-order-of-magnitude increase in average densities in the RMF thruster results in 10,000 times more radiative loss due to quadratic scaling. The higher density in the RMF system, combined with the fact that peak densities in the RMF are spatially global over several centimeters—unlike the spatially localized peak densities over a few millimeters in Hall thrusters—explains why radiative excitation is a

comparatively larger loss for the RMF thruster.

This high ion density is largely a result of the pulsed ionization scheme as can be seen through the lens of Eq. 3.19. Restated here in terms of Maxwellian thermal speeds, this expression is

$$n = \frac{4\dot{m}}{m_i A c_{th}}, \tag{6.3}$$

where $\dot{m}$ is the mass flow rate, m_i is the particle/ion mass, A is the cross-sectional area, and c_{th} is the neutral thermal velocity. Quantitatively, for a mass flow rate of 4 mg/s, an area of 150 cm^2, and a neutral velocity of 200 m/s, the expected neutral density is approximately 2×10^{19} m^{-3}, closely matching the measured density. However, most of the neutral gas is injected upstream into the thruster, further increasing the density. In the RMF thruster, these slow neutrals are rapidly ionized by the RMF, leading to high ion densities, numerous excitation collisions, and substantial radiative losses. This ionization occurs on the order of tens of microseconds much faster than their residence time, $t_{residence} = L/v_{ex}$, where v_{ex} is the effective exhaust velocity of the propellant. Direct performance measurements of specific impulse indicate residence times for ions in the RMF thruster exceeding 100 microseconds [80], allowing ample time for ions to radiate energy. To address this issue, solutions to reduce density in these devices are sought to enhance plasma efficiency.

A simple geometric way to reduce the density while maintaining the mass bit per pulse would be to lengthen the thruster. Increasing the available volume for the neutral fill will allow a lower flow rate to achieve the same available propellant mass which directly reduces the density. If the thruster radius is unchanged, the coupling physics should be minimally effected, and the RMF antennas will have increased "contact" with the plasma slug. Another geometric solution is to implement a coaxial thruster configuration where the centerline flow is physically blocked. Any plasma that is formed along the thruster axis contributes to the radiative losses but contributes little to thrust because the Lorentz force scales like $F_{\text{Lorentz}} \propto en\omega r$, where ω is the RMF frequency, and r is the radial coordinate. Similar to the previous scheme, in this instance the total mass flow rate would be lowered to maintain the same density in the annular region, but the plasma density that previously existed on centerline would be eliminated. However for both of these schemes, there is a trade-off as they both increase the wall area, and therefore will increase the wall losses.

A straightforward geometric approach to reducing density while maintaining mass bit per pulse involves lengthening the thruster. By increasing the available volume for neutral fill, a lower flow rate can achieve the same available propellant mass, directly lowering density. If the thruster radius remains unchanged, coupling physics should be minimally affected, and

RMF antennas will have increased "contact" with the plasma. Another geometric solution is implementing a coaxial thruster configuration, where the centerline flow is physically blocked. Plasma formed along the thruster axis contributes to radiative losses but little to thrust due to the Lorentz force scaling like $F_{\text{Lorentz}} \propto en\omega r$, where ω is the RMF frequency, and r is the radial coordinate. Similar to the previous scheme, in this instance the total mass flow rate would be lowered to maintain the same density in the annular region, but the plasma density that previously existed on centerline would be eliminated. However for both of these schemes, there is a trade-off as they both increase the wall area, and therefore wall losses will increase.

Additionally, RMF thruster performance could be enhanced through operational changes. Some authors [95, 68] suggest switching to alternative propellants. While xenon is commonly used in electric propulsion due to its low ionization energy, argon, nitrogen, or molecular compounds like CO_2 or ammonia may be better choices for RMF, as shown by the PIT mk.V thruster achieving its highest efficiency with ammonia [68]. The reasoning is that, for these propellants, excitation and ionization collisions occur at a reduced rate, and molecules absorb energy into rotational and vibrational modes, which are potentially less detrimental to performance.

As another potential solution, we have recently explored operating the thruster in continuous wave (CW) mode instead of pulsed [82]. In CW mode, neutral gas buildup may be limited as propellant is continuously extracted in the ion beam at a velocity higher than the neutral thermal speed. Initial predictions from extrapolating plasma measurements from our RMF test article [82] suggest modest improvements in performance for a CW mode thruster. However, the advantages of CW mode are speculative, and further experimental efforts are required to evaluate these claims. A limitation of CW mode is the power processing; to maintain ionization, kA level currents through the RMF antennas are required, which is not achievable at steady state for our 5 kW-class thruster. Addressing this, pulse shaping techniques could be used, initiating ionization with a large current pulse and then slowly ramping down to a background level maintaining the discharge at a reduced amplitude, as theoretically investigated by Hugrass and Jones [43].

Despite techniques to reduce radiative and thermal losses, the energy analysis revealed by Fig. 6.10 suggests the thruster performance may still be low. This stems from the fact that the acceleration energy is less than the ionization energy—the minimal frozen flow loss with the device. Indeed, based on these values, the result may suggest that the maximum efficiency would be 30-40%. In practice, the reason for this upper bound bound likely can be attributed to poor acceleration in the thruster–suggesting that the Lorentz acceleration is low. To this point, experimental investigation into acceleration dynamics in the thruster [82]

reveals modest Lorentz force compared to thermal effects. This does not necessarily suggest an inherent limitation but underscores the need for further exploration, considering strategies to manipulate density, RMF power conditioning, and bias field geometry for enhanced acceleration.

6.4 Conclusions

In this study, I conducted experimental investigations to understand the historical low efficiencies observed in RMF thrusters. To this end, plasma diagnostic measurements were performed to assess the terms in the efficiency model from Chapter 3. Results indicated a divergence efficiency of $38.2 \pm 0.2\%$, mass utilization of $76.9 \pm 1.7\%$, coupling efficiency of $24.5 \pm 2.2\%$, and plasma efficiency of $6.4 \pm 1.0\%$. Combined, these values resulted in a probe-measured efficiency of $0.46 \pm 0.09\%$, closely aligning with the thrust stand measured efficiency of $0.41 \pm 0.04\%$.

While this efficiency measurement is consistent in order of magnitude with previous experimental studies of RMF thrusters (refer to Sec. 6.2.1), it falls markedly below the theoretical value of 85 % anticipated from earlier analytical studies [87]. A closer examination of this theoretical treatment revealed neglect of contributions from wall, recombination/ionization, and radiative losses. This work demonstrated that these factors can be dominant drivers of performance loss, particularly with the majority of energy lost as electromagnetic radiation due to excitation collisions in the plasma. The high plasma densities in the RMF pulse, exceeding 1×10^{19} m^{-3}, contribute significantly to these radiative losses. This suggests that the estimates for the actual theoretical upper bound in performance may need to be revisited.

Furthermore, I have discussed the physical drivers of each efficiency mode and leveraged our results to propose strategies to reduce their detrimental effects. A key conclusion is that the limitations of the current RMF thruster version stem from the high densities inherent to pulsed-mode thrusters. Indeed, RMF thrusters are a departure from more conventional pulsed inductive thrusters where the coupling between high amplitude, transiently-induced currents interacts with the high amplitude induced magnetic field to yield quadratic scaling with the applied current. The corresponding high thrust density in these devices presumably overcomes radiative and wall losses characteristic of high plasma density. By design, however, the RMF current drive scheme avoids high amplitude, transiently-induced currents to enable low voltage operation (see Chapter 2). This minimizes quadratic scaling with applied current in favor of an acceleration process depends on a linear interaction between the amplified current and background magnetic field [83]. As result, the high densities associated with pulsed operation serve only to adversely impact RMF thruster efficiency. This find-

ing would suggest that pulsed-mode RMF thrusters may be unable to achieve the efficiency levels competitive with state-of-the-art pulsed inductive and steady-state electric propulsion devices. This finding motivated the development of the RMFv3 thruster (as discussed in Chapter 4), and a key design change included facilitating operation in a continuous wave (CW) mode. This mode, in theory, allows the thruster to operate at lower internal densities to reduce wall and radiative losses and achieve higher efficiencies. In the following chapter, I investigate this method of operation and compare the performance and efficiency breakdown of CW mode relative to the typical pulsed mode operation for these thrusters.

CHAPTER 7

Pulsed vs Continuous-Wave Comparison of Operational Modes

7.1 Introduction

The experimentation with the RMFv2 thruster revealed that the pulsed operation of the device hindered its performance. The RMF proved ineffective at exhausting the high-density gas that accumulates between pulses, leading to significant collisional excitation radiation losses and diffusion losses to the thruster walls. A potential solution to this issue is to operate the thruster in continuous wave (CW) mode, where the RMF is applied at 100 % duty cycle, and plasma is continuously ejected from the device. This capability is potentially unique to RMF thrusters, as they can generate a steady azimuthal electron current and require less demanding circuitry than other inductive pulsed plasma thrusters.

In the CW framework, the RMF is applied to the plasma for substantially longer times than typical neutral particle transits (>1 s), ensuring no build-up of neutral density between pulses. In theory, this leads to higher mass throughput at lower densities, potentially resulting in higher average thrust, specific impulse, and increased efficiency for these devices. Prior to this work, improved performance under CW conditions had yet to be experimentally verified, but previous theoretical work suggests an efficiency increase of 2-3 times present performance is possible [79].

Leveraging the lessons learned from the RMFv2 thruster, we constructed the RMFv3 thruster to be capable of operating in both modes to test these claims. The goal of this chapter is to explore CW operation of RMF thrusters and compare efficiency to typical pulsed thruster operation. For this study I was unable to complete internal plasma property measurements of the RMFv3 thruster to make a direct internal loss mode comparisons. Instead, the experimental priority for this effort was to preform measurements using the far-field plasma diagnostic probes to evaluate the phenomenological efficiency breakdown for the two modes. To this end, this chapter is organized as follows: in Sec. 7.2, I describe

the pertinent physics that distinguishes CW from pulsed operation. In Sec. 7.3, I provide an overview of the experimental setup and describe the diagnostic probes employed in this study. In Sec. 7.4, I report both the global performance measurements for the two operational modes and the measurements from the diagnostic probes. Using these results, I evaluate the component efficiencies from the efficiency model from Chapter 3. In Sec. 7.5, I discuss these results to provide context for future thruster operation and design. Finally, in Sec. 7.6, I summarize this effort and orient the results in relation to previous findings.

7.2 Description of Pulsed and Continuous Wave Modes

In this study, we operate the thruster in two different modes to compare their performance. The first mode is the pulsed mode, involving short, high-amplitude applications of the RMF. This results in driving currents of approximately 500 A peak over pulse lengths around 100 μs. This mode offers two primary advantages. Firstly, it provides a higher RMF strength to drive the necessary azimuthal electron currents and ionize the propellant. Secondly, the time-varying azimuthal plasma current has the potential to generate opposing currents in the conductive structures of the engine. These opposing current loops repel each other and produce a thrust force which scales with the square of the driven plasma current as outlined in more detail in Sec. 2.2.3.

Table 7.1: Thruster Settings for CW and Pulsed Mode

Parameter	CW	Pulsed
Injector Mass Flow	257 sccm	257 sccm
Cathode Flow	15 sccm	15 sccm
RMF Power	10.3 ± 0.7 kW	10.5 ± 0.7 kW
RMF Frequency	415 kHz	415 kHz
Pulse Length	10 s	200 μs
Duty Cycle	100 %	7.8 %
Pulse Repetition Rate	-	390 Hz

The second mode under investigation is the CW mode, where the RMF is consistently applied to the plasma at 100 % duty cycle. With constant power, this necessarily leads to a lower RMF amplitude, around peak currents of 100 A in our case. Although CW mode loses the advantage of quadratic thrust scaling due to the relatively constant azimuthal currents in the plasma, it compensates by applying a consistent force to the plasma, resulting in higher average exit velocities. Additionally, the higher average velocity, through continuity, should produce a lower density plasma and reduce inelastic collisional losses. This is shown

in chapter 3 through the lens of Eq. 3.19 revealing that higher speed flows are less dense, and the loss modes in Sec. 3.4 scale with increasing density.

In Fig. 7.2, I present both a long exposure (1/400s) photo of the thruster operating in each mode and a single high-speed frame captured at a 50 kHz frame rate using a Photron SA5 fastcam. These images qualitatively depict the increase in plasma density between the two modes, with the pulsed mode photos exhibiting brighter plasma fluorescence. Notably, the high-speed photos reveal a distinct difference. Pulsed mode shows a large transient of plasma ejected as a mass from the thruster, a characteristic observed in high-speed photography of the RMFv2 thruster as well [82]. In contrast, the high-speed photo of CW mode displays a more diffuse glow towards the center of the thruster.

I present in Fig. 7.1 efficiency results for the pulsed and CW modes during initial performance exploration of operating conditions. These results are plotted over the injector flow rate and grouped into relevant performance parameters: pulse length for the pulsed mode, and RMF amplitude/power for the CW mode. The pulsed mode exploration revealed an optimum pulse length of 200 μs and performance increasing with flow up to 0.25 %. The CW mode plot shows increasing efficiency with flow up to 257 sccm flow rate, and reaches a maximum of over 2.5%. Notably, the 20.5 G RMF strength achieved the highest performance, but the heating at this power was a problem for extended diagnostic testing. Based on this exportation, I elected to perform this comparison study at an optimum operating condition for the CW mode based on the higher efficiency.

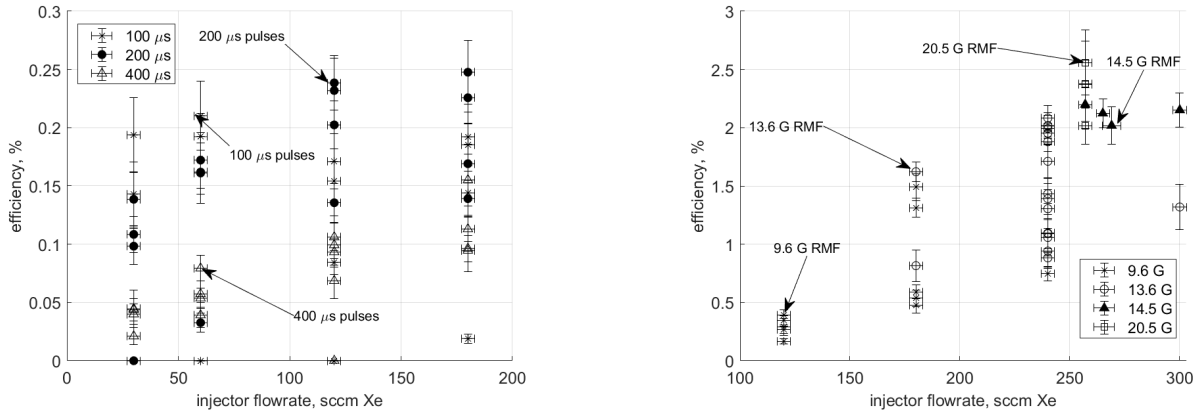

(a) Efficiency for pulsed mode exploration

(b) Efficiency for CW mode exploration

Figure 7.1: Thrust stand efficiency results RMFv3 operating condition exploration study.

Table 7.1 provides the thruster settings for the two operating modes, selected for performance comparison at approximately the same overall RMF power, bias magnetic field, and flow rate.

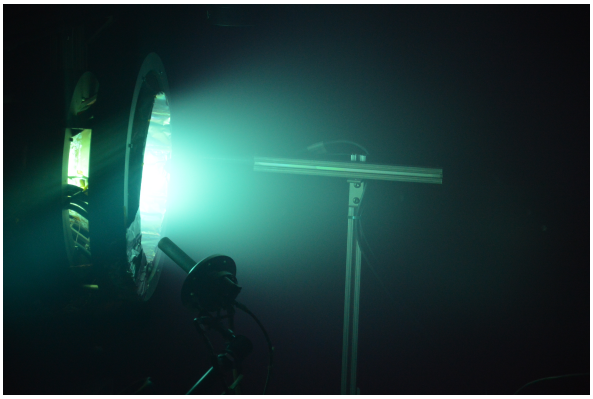

(a) 1/400s exposure of RMFv3 in CW mode

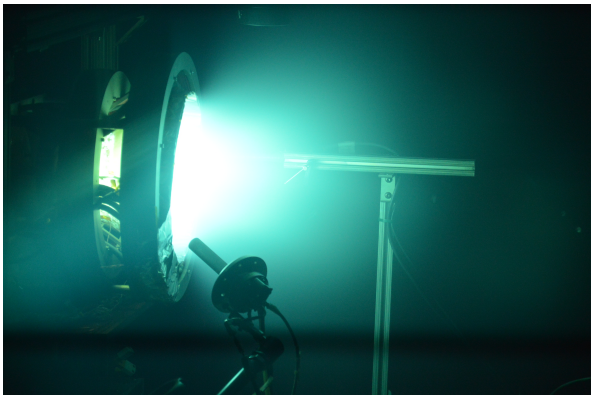

(b) 1/400s exposure of RMFv3 in Pulsed mode

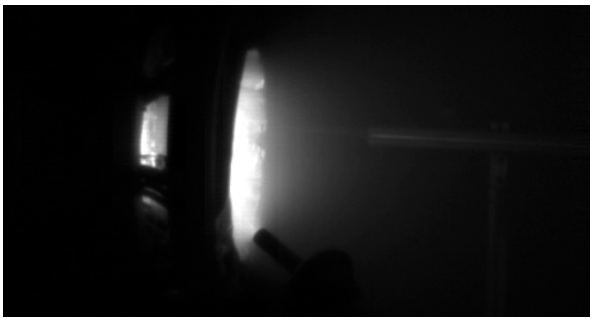

(c) 1/50ks exposure of RMFv3 in CW mode

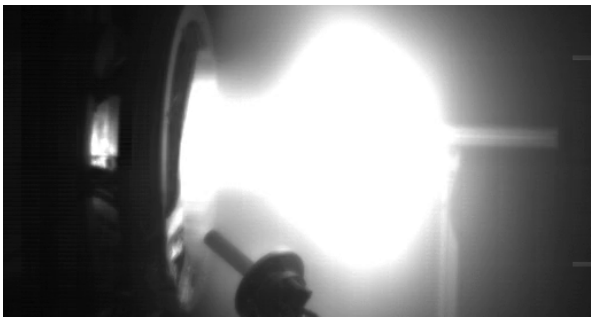

(d) 1/50ks exposure of RMFv3 in Pulsed mode

Figure 7.2: Pulsed and CW mode operational images for RMFv3 thruster.

7.3 Experimental Setup

In this study, I utilize a set of plasma and thruster diagnostics to investigate the plasma characteristics and performance of the RMF thruster in both the CW and pulsed modes. The diagnostic tools include several employed in the RMFv2 experiment, such as the inverted pendulum thrust stand, the RMF current transducers, and the swept far-field Faraday probe (FP). Additionally, I incorporate a far-field retarding potential analyzer (RPA) and Langmuir probe (FF-LP) positioned along the thruster centerline. This differs from the FP time-of-flight technique used for the RMFv2 thruster (see Sec. 6.2.3). The RPA is used here to capture the ion energies for both modes as time-of-flight velocimetry cannot be used for the CW mode as it is by definition not pulsed. Fig. 7.3 illustrates the locations of these tools within the vacuum facility.

The RMFv3 thruster is mounted on the inverted pendulum thrust stand, operated in displacement mode. For the new thruster design, the restoring springs had to be stiffened to support the additional weight of the resonant capacitor banks. Additionally, the calibration weights were increased to accommodate the new anticipated thrust range (0 - 200 mN). For

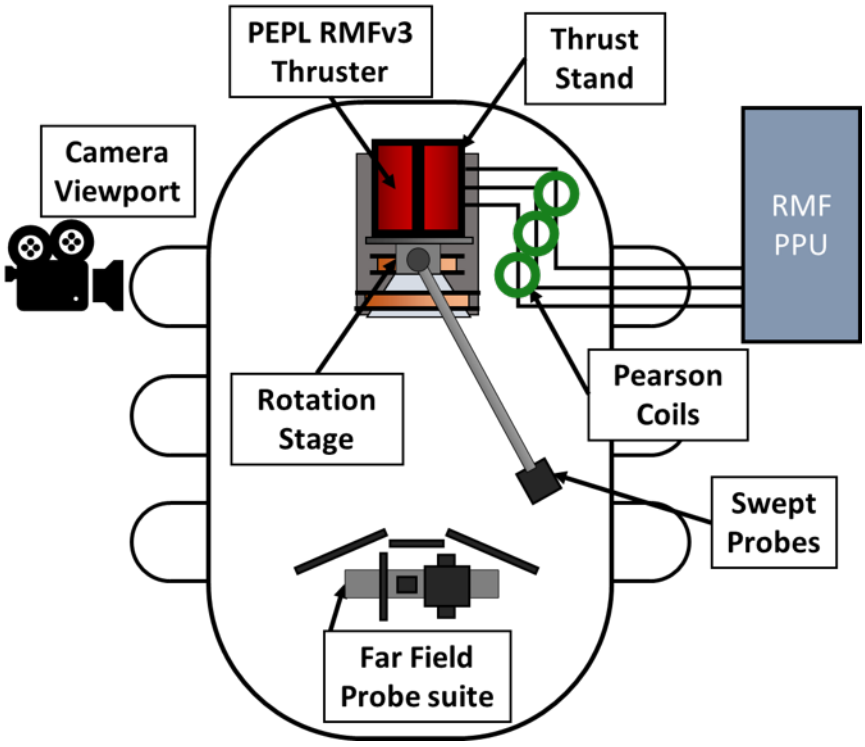

Figure 7.3: Experimental setup for the pulsed versus CW mode experiment.

reference I show a sample thrust measurement for the pulsed mode in Fig. 7.4.

Three wide-band current transducers are positioned around the conductors of each antenna phase, located behind the thruster and between the antenna and the resonant capacitor bank. These transducers measure the currents through each antenna for resonance tuning and the evaluation of coupling efficiency.

The FP measures the far-field ion flux throughout the plume. The probe is moved through the plasma beam to obtain spatial profiles of ion current density. It is swept through $\pm 90°$ with respect to the thruster centerline, and the rotation point is aligned with the center of the thruster exit plane. The probe is maintained at a constant 1.72 m radius from this point. In this study, -60 V relative to facility ground is sufficient to bias the collector and guard into ion saturation, compared to the -115 V required for the RMFv2 study.

The RPA measures the ion energy distribution in the plume downstream of the thruster. The ion selection grid is swept from 0 - 100 V with respect to ground to collect corresponding ion energies. The RPA is aligned to the thruster centerline at a distance of approximately 2 m from the thruster exit plane. Co-located with the RPA is the cylindrical FF-LP used to make measurements of the local plasma potential to correct the retarding voltages measured by the RPA. These diagnostics are discussed in greater detail in Chapter 5.

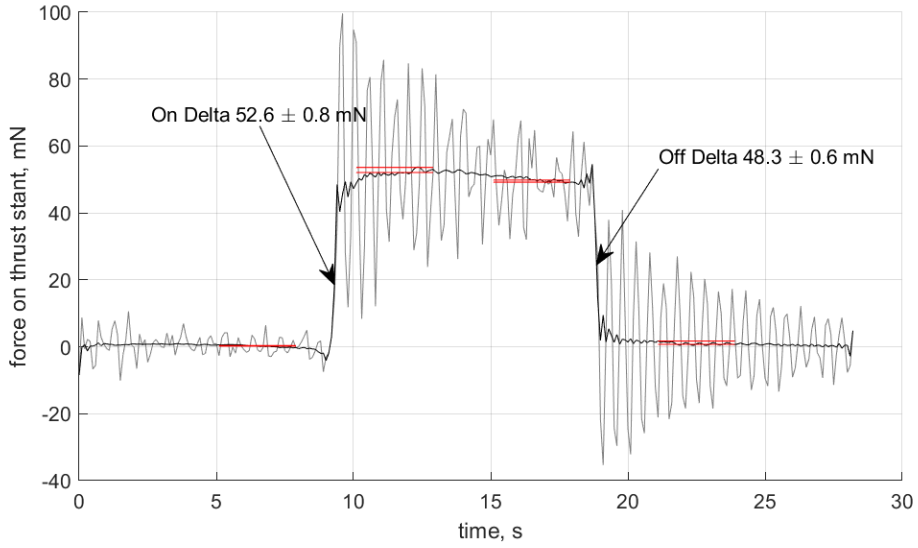

Figure 7.4: RMFv3 pulsed mode thrust measurement, with raw thrust data (gray) and a moving average for comparison (black). The red bars indicate the averaging windows of the raw data employed for on/off measurements where the heights indicate the upper and lower values within uncertainty

7.4 Results

In this section, I present the data from the diagnostic instruments for both the CW and pulsed mode operation of the RMF thruster. These collected data are analyzed and used to calculate the terms in the the phenomenological efficiency model described in chapter 3.

7.4.1 Global Performance

Table 7.2 presents the performance characteristics for both the pulsed and CW mode experimental conditions shown in Table 7.1. The thrust is measured using the thrust stand, and the uncertainty is derived from the spread of several independent measurements and calibrations. The mass flow rate is determined from the mass flow controllers, and the uncertainty is based on the magnitude of the calibration correction. The power is reported as the DC power supplied to the RMF power system, and the uncertainty arises from an assumed 5 % uncertainty in the voltage and current readings, as these are known to fluctuate during thruster operation.

From the table, it is evident that the CW mode exhibits significantly improved performance compared to the pulsed mode. With the same average flow rate and power, the CW mode generates over twice the thrust, resulting in an efficiency increase of over 450 %. This

Table 7.2: Global Performance Comparison Between Pulsed and Continuous Wave Mode Operation

	CW	PULSED
Thrust	$106 \pm 3\,\mathrm{mN}$	$49.7 \pm 1.4\,\mathrm{mN}$
Mass Flow Rate	$24.5 \pm 0.2\,\mathrm{mg/s}$	$24.5 \pm 0.2\,\mathrm{mg/s}$
Power	$10.3 \pm 0.7\,\mathrm{kW}$	$10.5 \pm 0.7\,\mathrm{kW}$
Thrust/Power	$10.31 \pm 0.06\,\mathrm{mN/kW}$	$4.73 \pm 0.03\,\mathrm{mN/kW}$
Specific Energy	$423 \pm 3\,\mathrm{J/mg}$	$429 \pm 3\,\mathrm{J/mg}$
Specific Impulse	$444 \pm 2\,\mathrm{s}$	$207 \pm 1\,\mathrm{s}$
Efficiency	$2.25 \pm 0.02\%$	$0.48 \pm 0.01\%$

increase not only meets but also exceeds the performance prediction for CW mode based on the extrapolation of the RMFv2 thruster data [79]. Furthermore, the pulsed mode operating condition exceeds the efficiency reported in Fig. 7.1. This is a result of a higher RMF power than what was used for that exploration study (10 kW vs 4 kW), where the power was increased through thruster pulse rate and duty cycle.

Examining the derived performance parameters reveals some key features. Notably, at equivalent specific energies, the CW mode produces over twice the specific impulse compared to the pulsed mode. However, this is likely driven by the wasted propellant between pulses and not influenced by the energy transfer of the system.

To make an estimate for the pulsed mode performance without this effect, I will artificially double the pulse repetition rate of the thruster, "in-post". By this I mean, I will double the thrust and double the power, such that the specific impulse matches the result of the CW mode. This assumes that each pulse is independent and produces a discrete impulse with some energy draw. The thruster operated this way, at a fictional pulse rate of 780 Hz, would addresses the specific impulse discrepancy to the CW mode. However, the lower thrust-to-power ratio in the pulsed mode under this modified condition makes it, at best, half as efficient as the CW mode, albeit at the expense of twice the power consumption, 20 kW. This clear indication suggests that additional thrust produced from self and structure-field interaction is not a significant effect as indeed the thrust to power is lower in the pulsed mode. In the following sections, I further assess the performance disparities between the two modes using the diagnostic probes.

7.4.2 Coupling Efficiency

Utilizing the Pearson coils to measure the currents through the RMF antennas, I can assess the coupling efficiency of the thruster. As previously stated, the coupling efficiency is defined

as the ratio of input power to power coupled into the plasma through the RMF system. The input power is measured as the product of the DC voltage and DC current supplied to the RMF PPU, as shown in Table 7.1 for the two modes.

The coupled plasma power can be evaluated by measuring an effective circuit resistance with and without the plasma present. The effective resistance for a given case is given by

$$R = \frac{P_{in}}{\sum_k \bar{I_k^2}}. \tag{7.1}$$

Here, the sum is taken over the number of phases (three in our case), P_{in} is the input DC power, and $\bar{I_k^2}$ is the time-averaged squared current through antenna phase k. This equation is analogous to the AC power deposited in an resistor $P = RI_{rms}^2$, where I_{rms} is the root-mean-squared current.

With the thruster unloaded, we find an effective vacuum resistance of $R_{CW,v} = 612 \pm 31$ mΩ for the CW mode and $R_{Pulsed,v} = 657 \pm 50$ mΩ for the pulsed mode using Eq. 5.20. These values are quite close to each other and within uncertainty, as expected, since the driving circuit hardware does not differ between modes, and the slight increase in resistance for the pulsed mode aligns with a current-dependent resistance increase for the IGBT semiconducting switches used in the PPU.

Repeating this process for the currents measured during thruster operation yields a plasma-loaded effective resistance of $R_{CW,p+v} = 1097 \pm 78$ mΩ for the CW mode and $R_{Pulsed,p+v} = 902 \pm 64$ mΩ for the pulsed mode. This results in a plasma resistance of $R_{CW,p} = 485 \pm 84$ mΩ for the CW mode, and $R_{Pulsed,p} = 245 \pm 81$ mΩ for the pulsed mode. These values are significantly higher than the 69 mΩ plasma resistance of the RMFv2 thruster, which can be attributed to the increased mass flow rate in the v3 thruster.

I can calculate the coupling efficiency according to Eq. 5.19, and using these values I arrive at a coupling efficiency of 44 ± 4 % for the CW mode and 27 ± 3 % for the pulsed mode. By definition, the power coupled to the plasma is then $P_p = \eta_c P_{in}$, resulting in an associated plasma-coupled power of 4.5 ± 0.5 kW and 2.9 ± 0.4 kW, for the CW and pulsed modes respectively.

These results demonstrate a notable increase in coupling efficiency for the CW mode, and the explanation becomes evident by examining the plasma-loaded waveforms of RMF current. In Fig. 7.5, I present the average envelopes of the RMF currents with plasma present for the CW and pulsed modes. In the CW mode, the current amplitude remains constant, indicating a consistent power transfer to the plasma. However, in the pulsed mode, the RMF current rises rapidly during the first 50 μs of the pulse, settles to a semi-steady value near 100 μs, and then slowly rises until the end of the pulse at 200 μs. This behavior indicates a

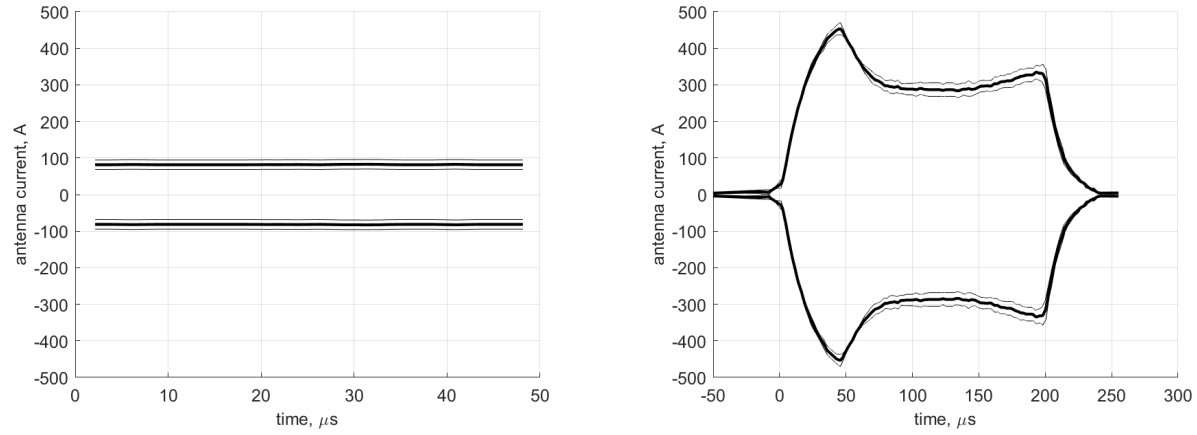

(a) (b)

Figure 7.5: Average RMFv3 current envelopes of the three RMF phases for (a) CW mode and (b) pulsed mode. Shaded areas represent the range of current amplitudes for the three RMF phases.

change in the effective circuit resistance over time.

In the first 50 μs, there is minimal loading as the plasma is ionizing, resulting in an effective resistance comparable to the vacuum case. Subsequently, the coupling increases as the plasma forms, and the current amplitude drops. During this time, the RMF forms the azimuthal plasma current, ejecting the plasma from the device. The slow rise at the end of the pulse is indicative of this plasma ejection. This initial startup time, where the plasma load is effectively nonexistent, leads to a repeating energy loss with every pulse, unlike the single initial transient for the CW mode. This effect explains the lower coupling efficiency in the pulsed mode.

7.4.3 Divergence and Mass Utilization

The FP measures the ion current density in the thruster plume. Using these measurements as a function of polar angle around the thruster, I can calculate both the divergence efficiency and the mass utilization of the thruster. In Fig. 7.6, I present the current density in the pulsed mode as a function of time in the thruster plume. This plot shares many characteristics with the ion current density plot of the RMFv2 thruster in Chapter 6. Again, the pulsed mode exhibits a large ion slug exiting the thruster with high current content, ranging out to an angle of 50 to 60 degrees. However, I'd like to note that the bulk of the ion population is moving notably slower than for the RMFv2 thruster, arriving at the probe 200 μs later. This results in an estimated ion speed of 4 km/s (using Eq. 5.13) compared to the estimated 7

km/s for the RMFv2 thruster. This is likely a result of the lower thruster specific energy for this experiment. Following, 3.22 is is expected that the exit velocity of the ions trends linearly with the specific energy, that is

$$u_{ex} =\propto \epsilon^*, \tag{7.2}$$

where ϵ^* is the specific energy. And indeed, the halved specific energy for the RMFv3 thruster results in roughly half the ion speed.

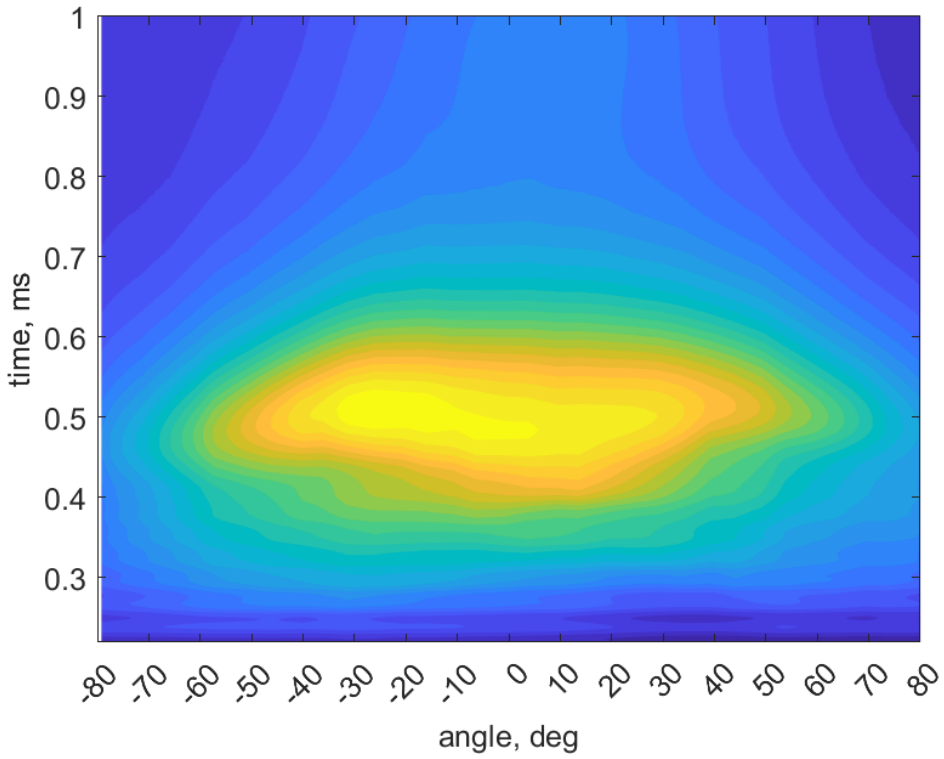

Figure 7.6: RMFv3 ion current in pulsed mode as a function of time.

In Fig. 7.7, I present the time-invariant ion current for both the pulsed and CW modes. This is directly measured for the CW mode and is the ion current density averaged over many pulses for the pulsed mode. The pulsed mode steady ion current is calculated as

$$j(\theta) = f_{rep} \int_0^{1/f_{rep}} j(\theta, t) dt, \tag{7.3}$$

where $j(\theta, t)$ is the ion current density as a function of time, t, and polar angle θ, and f_{rep} is the pulse repetition rate. In Fig. 7.7, the pulsed mode uncertainty (shaded area) is reported as a 95 % confidence interval from the standard deviation over 10 pulses, and the CW mode

uncertainty is reported as the maximum current difference measured between two FP sweeps.

Addressing these plots, we can observe that the CW mode results in a three times increase in centerline current density and a significantly more collimated beam. Notionally, the full-width-half-maximum for the CW is 45°, compared to 75° for the pulsed mode. To generate quantitative metrics, integration over a supposedly symmetric hemispherical surface is performed to calculate the total beam and axial beam currents according to Eq. 5.7 and 5.8 from Chapter 5. For the CW mode, the calculated total beam current is 17.6 ± 1.2 A, and the axial beam current is 12.4 ± 0.9 A. For the pulsed mode, the calculated total beam current is 13.3 ± 0.5 A, and the axial beam current is 7.7 ± 0.3 A.

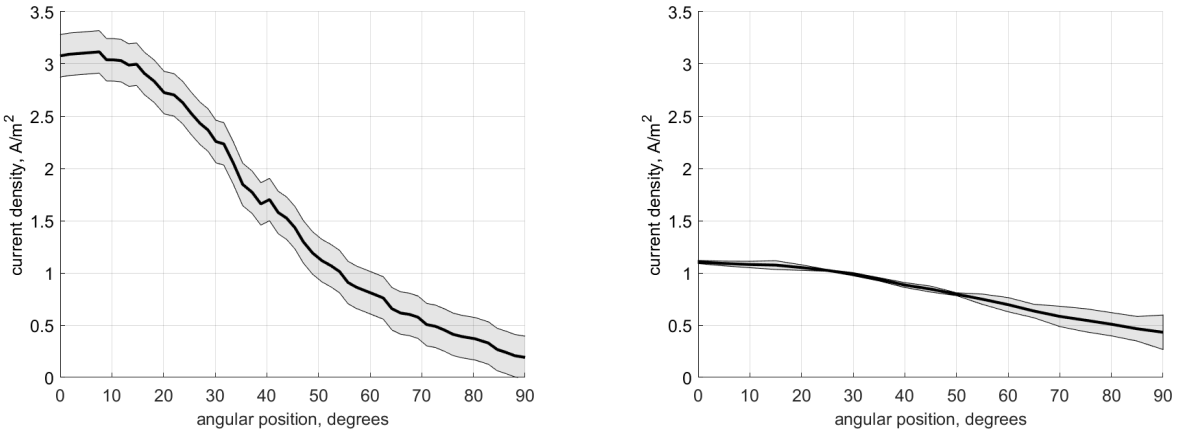

(a) (b)

Figure 7.7: Faraday probe measurements of ion current density in the v3 thruster far-field for (a) CW mode, and (b) pulsed mode.

In typical fashion, these two terms can be related to calculate the divergence efficiency as:

$$\eta_d = \frac{I_{\text{axial}}^2}{I_{\text{beam}}^2}. \tag{7.4}$$

This results in a divergence efficiency of 50 ± 7 % for the CW mode and 33 ± 3 % for the pulsed mode. This pulsed mode divergence is consistent with the divergence efficiency of the RMFv2 thruster, albeit slightly lower. The increased collimation measured for the CW mode may be attributed to two mechanisms related to the higher density plasma in the pulsed mode. First, the higher density in the pulsed mode will lead to larger thermal electron pressure forces in the plasma, likely resulting in the large measured divergence. Second, a higher plasma density will lead to larger azimuthal currents formed in the plasma, increasing the magnetic pressure central to the plasma, forcing it to expand once no longer confined by

the axial bias field. This is analogous to the self expanding force experienced by a loop of solid wire conducting large currents.

To calculate mass utilization rigorously, relative charge states for the collected ions are needed. Without such information, the assumption is again made that all ions are singly charged (consistent with Chapters 5 and 6). This is justified given that internal electron temperatures for RMF thrusters are typically low (∼10 eV) [30]. With this assumption, mass utilization can be calculated as

$$\eta_m = \frac{m_i I_b}{e\dot{m}}, \tag{7.5}$$

where, m_i is the ion mass, I_b is the total ion beam current, e is the elementary charge, and $\dot{m}$ is the neutral mass flow rate. This equation gives a mass utilization of 98 ± 8 % for the CW mode and 74 ± 5 % for the pulsed mode. This measurement again matches the pulsed mode performance of the RMFv2 thruster, with a significant increase up to near unity for the CW mode. This increase can be directly attributed to the higher duty cycle in the CW mode. I assume based on this result, roughly 25% of the propellant can leak out between shots in the pulsed mode. I expect, therefore, that the pulsed mode could also exhibit very high mass utilization when operated at pulse repetition rates commensurate with the neutral refill time of the thruster (See Chapter 6 Sec. 6.3.2.2). However, a higher duty cycle necessarily requires additional power to be supplied to the thruster. Alternatively, the adoption of fast pulsed gas injection valves may also address the low pulsed-mode mass utilization. Although, both of these techniques may be operationally prohibitive.

7.4.4 Plasma Efficiency

The evaluation of plasma efficiency requires measuring the bulk kinetic energy of the ion beam. To achieve this, I utilize a retarding potential analyzer positioned along the thruster centerline. This choice is made in lieu of using FP time-of-flight velocimetry (which I used for the RMFv2 thruster) for both modes, as the latter technique necessitates the thruster to be operated in pulsed mode.

The RPA assesses the retarding potential distribution of ions, effectively providing a charge-to-mass energy distribution. It is assumed that this distribution is uniform throughout the beam. This likely over estimates the total beam power as off axis ion are likely to be less energetic that the ones along centerline due to collisional scattering. However since the thruster beam is so diffuse (see FP results), it perhaps fair to say the ion energies are similarly isotropic.

Furthermore, it is crucial to note that the RPA measures ion energy with respect to

ground potential and does not consider the potential drop from the local plasma potential. To address this discrepancy, a cylindrical Langmuir probe is employed along the thruster beam to measure the plasma potential and correct the RPA measurements per the description given in Chapter 5. Below, I present the uncorrected raw measurements for the RPA, the plasma potential measurements from the Langmuir probe, and then assess the ion beam power and plasma efficiency for the two modes.

7.4.4.1 RPA

In Fig.7.8a, the measured retarding potential distribution for the CW mode is presented. The black line in Fig.7.8a illustrates the current measured by the RPA as a function of applied retarding voltage. The collected current encompasses all ions with energy higher than the applied voltage, thus allowing the determination of the ion energy distribution function given by

$$f(\varepsilon) \propto -\frac{dI_{RPA}}{dV}, \tag{7.6}$$

where I_{RPA} represents the collected current by the RPA, and V is the applied retarding voltage. The resulting normalized energy distribution function for the CW mode is plotted in red in Fig.7.8a. To mitigate the amplification of experimental noise through differentiation, I initially perform a piecewise spline fit to the RPA current data. The shaded areas in Fig.7.8a serve as a measure of the goodness of fit for this spline.

The CW ion energy distribution in Fig. 7.8a distinctly reveals two ion populations. The lower energy population is centered at 27 V, and I speculate this to be a result of charge exchange (CEX). The higher energy population, centered at 40 V, is likely associated with the main ion beam. Two reasons support the belief that the low energy population is a result of CEX. Firstly, the CEX cross-section is prevalent for xenon and is observed in many thruster experiments. Secondly, if this were instead the result of elastic scattering, a discrete peak would not be expected; rather, a gradual low energy tail extending from the main beam population would be anticipated.

To avoid incorporating the lower energy of the CEX ions, which are likely produced during the transit from the thruster to the RPA, I report the ion retarding voltage as the most probable voltage of this distribution, i.e. 40 V.

For the pulsed mode, the analysis becomes more intricate as ion energy becomes a function of time. Nevertheless, the same procedure outlined by Eq.7.6 can be applied to perform time-resolved ion current collection analysis by the RPA. The resulting normalized ion energy distribution function over time is presented in the color axis in Fig.7.8b, with the most

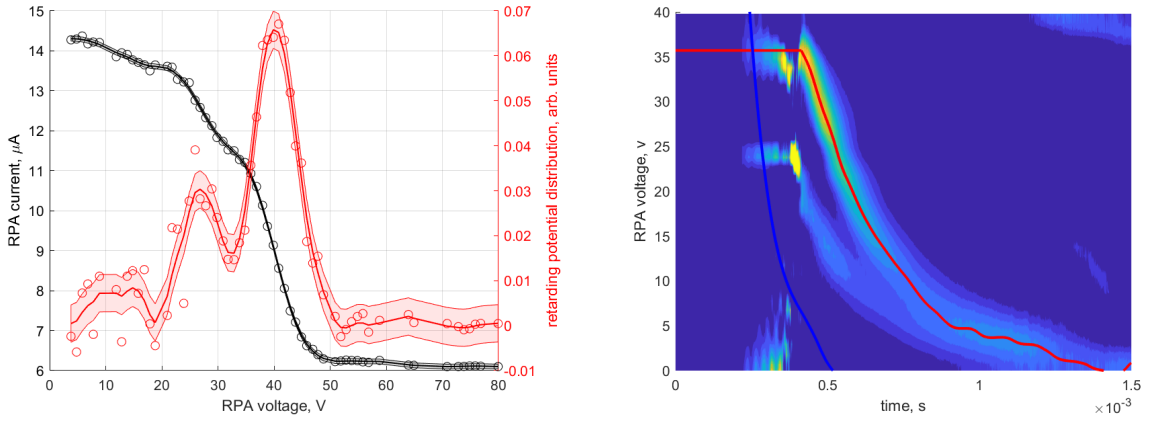

(a) (b)

Figure 7.8: RPA measurements on v3 thruster centerline for (a) CW mode, and (b) pulsed mode.

probable ion energy depicted as a red line. This plot reveals both the CEX population and the main beam population, which become more pronounced starting at 400 μs. Prior to this time, the plasma is sparse, and the normalized energy distributions are susceptible to stray noise. Because of this, I assume the ion energy is a constant before 450 μs and equivalent to the most probable voltage at this time once sufficient energy is present. This is a reasonable assumption for times after 250 μs as the IVDF shows peak content in this region. However, assuming this constant energy before 250 μs is purely for convenience and as can be seen later in Fig. 7.13 has little impact on the beam power measurements due to negligible ion beam current.

Both populations initially start at a high potential, 35 and 25 V, respectively, and then decay in energy towards 5 V by roughly 1 ms. This observation aligns with intuition, as the earliest ions to reach the probe will inherently possess the highest energy.

7.4.4.2 FF-LP

I now turn to the analysis of the far-field Langmuir probe (FF-LP) to determine the plasma potential correction for the RPA measurements. The FF-LP was positioned coincident with the location of the RPA along the thruster centerline via the translating motion stage described in Chapter 5. For this study, the FF-LP was swept ±60 V about ground to capture the plasma characteristic. In Fig. 7.9, a subset of this data for the CW mode is shown. This curve represents the average of three probe sweeps, and the shaded region denotes the standard deviation.

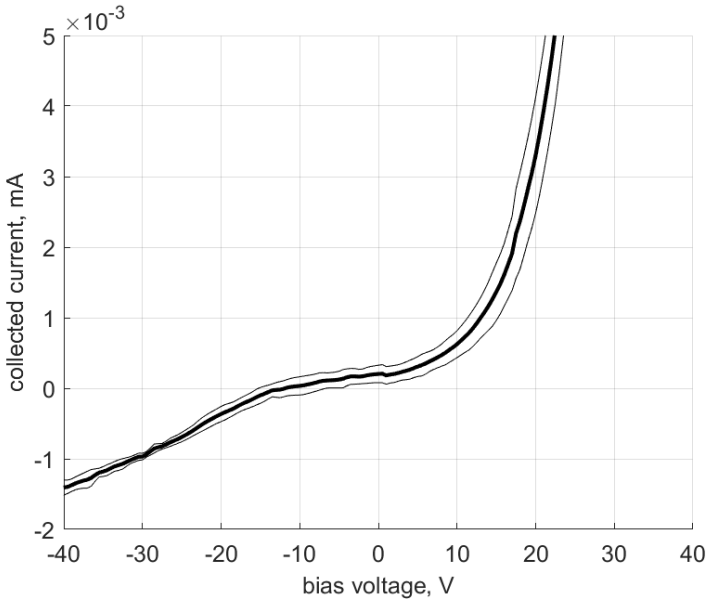

Figure 7.9: Far field Langmuir probe CW mode characteristic.

This LP characteristic exhibits some interesting behavior, making its analysis challenging. As the probe bias is lowered below the floating voltage ($V_f = -14V$) into ion saturation, the slope of the current exhibits an uncharacteristic steepening. Typical LP probe traces in stationary Maxwellian plasmas show much flatter ion saturation regions whose growth is governed by thermal sheath expansion. In this trace, the ion collection grows beyond what would be expected by typical sheath expansion.

This might be explained by the low-energy ion beam produced by the thruster. In typical EP plasmas, the small bias potentials applied to LPs are insignificant in deflecting high-energy beam ions. Consequently, aligning a cylindrical LP to be coaxial with the beam is normally sufficient to eliminate the effect of ion beam current. However, for the RMF thruster, the LP is capable of deflecting the beam ions into the probe at a higher rate than expected by thermal effects because the probe bias is on the order of the ion beam energy. This results in increased sheath expansion, as notionally illustrated in Fig. 7.10.

Given the low ion energies, it is expected that the beam ions will also impact the electron-collecting region of the FF-LP trace. To calculate the electron only contribution to current, I perform a least-squares linear fit to the ion region (specifically for V < 0) and subtract this contribution from the entire trace. In Fig. 7.11, the electron current is shown in red on the right axis, and the natural log of the electron current is presented in black on the left axis. As discussed in Chapter 5, at probe biases below the plasma potential, the electron current follows an exponential Boltzmann relation, while at biases above the plasma potential, the

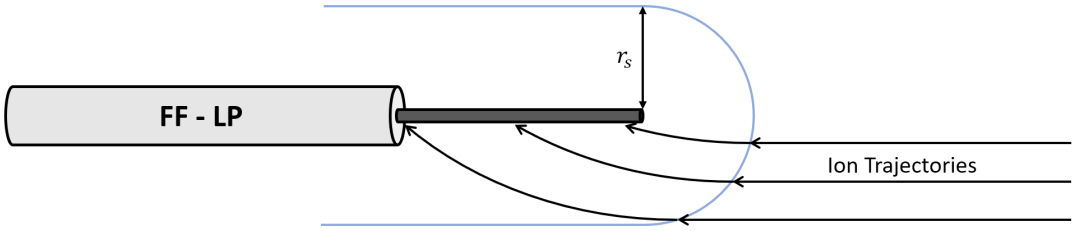

Figure 7.10: Notional low energy ion trajectories into negatively biased cylindrical Langmuir probe. r_s represents effective sheath radius.

electron current is governed by slower sheath expansion. Thus, the plasma potential can be identified as the "knee" in the electron current on a log plot.

In Fig. 7.11, the electron current characteristic exhibits two knees, one wide one at approximately at 40 V and one at 17 V. I speculate that the higher knee results from the ion beam current being fully reflected from the probe, altering the electron sheath, while the lower knee represents the true plasma potential. This aligns with the expectations from the RPA results, as the slow CEX population appears just above this lower potential.

To confirm this result, the inverse slope of the log electron current is used to calculate the electron temperature:

$$T_{eV} = \frac{\Delta V}{\Delta \ln(I_e)}, \tag{7.7}$$

where ΔV is the change in bias voltage, and $\Delta \ln(I_e)$ is the change in the log of the electron current. I plot in Fig. 7.11b a histogram for 100 linear fits to the natural log of elect current from Fig. 7.11a. Notably this includes the entire range past the "knee", and therefore fits of high (> 10 eV) electron temperatures can be seen. However, if I take the bottom of this distribution to be representative of the correct part of the trace, the electron temperature is approximately 5 eV.

By equating the electron and ion current at the floating voltage, the plasma potential can be calculated as:

$$V_p = T_{eV} \ln\left(\sqrt{\frac{m_i}{2\pi m_e}}\right) + V_f, \tag{7.8}$$

where V_f is the floating voltage. Using these measurements, a plasma potential of 12.4 V is obtained. Because these techniques differ and have their own inaccuracies, I average these values and report their difference as the uncertainty. This yields a plasma potential of 15 $\pm$ 5 V.

The same process is repeated for the pulsed mode data, which exhibits very similar effects.

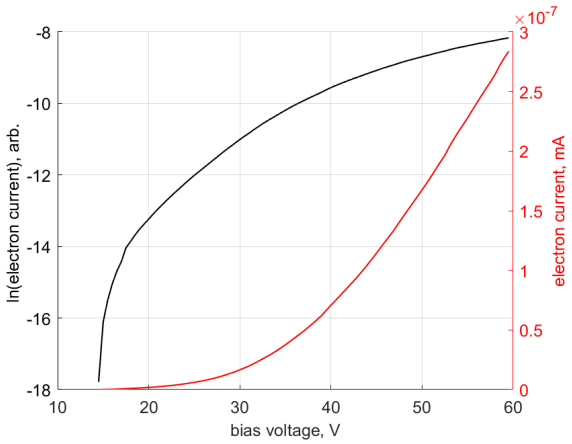

(a) Electron current (black) and natural log of electron current (red)

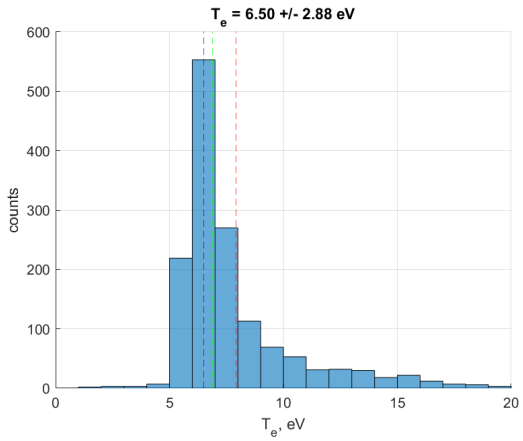

(b) Histogram of electron temperature fits to natural log of electron current

Figure 7.11: RMFv3 far field Langmuir probe results for the CW mode.

In Fig. 7.12a, the natural log of the electron current for several time-slices during the pulse is presented. This plot illustrates the knee potential drop from 60 V at 250 μs to 5 V at 1021 μs. Notably, the clear development of the ion beam knee at 555 μs corresponds to the moment when the bulk of the ion beam passes over the probe.

As the plasma potential appears to follow the lower end of the CEX population from the RPA, the reported plasma potential is 12 V less than the peak potential of the CEX population, with an uncertainty of 5 V informed by the CW LP analysis. This plasma potential is depicted as the blue line in Fig.7.8b, and the RPA data corrected for this plasma potential is shown in Fig.7.12b.

7.4.4.3 Beam Power

To calculate the power in the ion beam, the most probable ion energies from the RPA (corrected for plasma potential) are weighted with the total current density collected by the FP. For the CW mode, this is calculated as

$$P_{\text{beam}} = I_b(V_{\text{mp}} - V_p), \tag{7.9}$$

where V_{mp} is the most probable ion retarding voltage from the RPA. The resulting beam power for the CW mode is 440 $\pm$ 90 W. In the pulsed mode, this weighting needs to be performed as a function of time

$$P_{\text{beam}}(t) = I_b(t)[V_{\text{mp}}(t) - V_p(t)]. \tag{7.10}$$

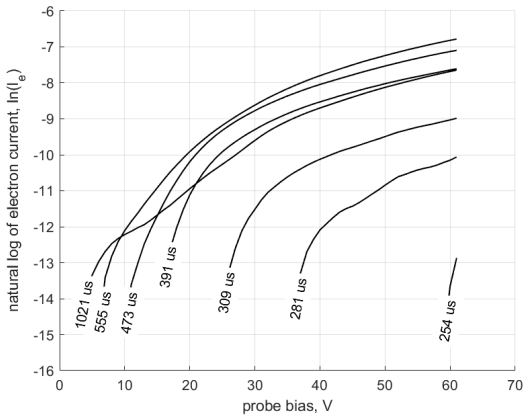

(a) Natural log of the electron current for various time in pulsed mode.

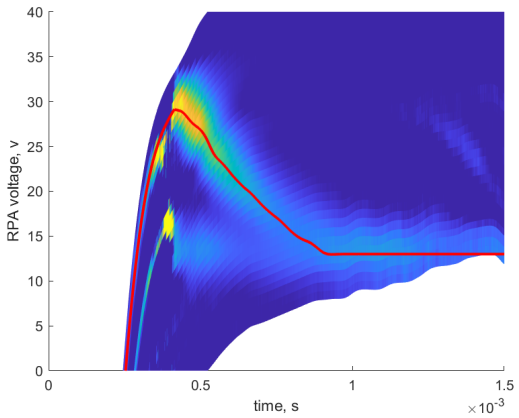

(b) Pulsed mode corrected RPA trace.

Figure 7.12: Pulsed mode RPA plasma potential correction.

This time-dependent beam power is shown in Fig. 7.13. The time-averaged beam power is then calculated as:

$$P_{\text{beam}} = f_{\text{rep}} \int_0^{1/f_{\text{rep}}} I_b(t)[V_{\text{mp}}(t) - V_p(t)]dt. \tag{7.11}$$

For the pulsed mode, the resulting ion beam power is 245±90 W. Finally, the plasma efficiency is calculated according to Eq. 5.24, resulting in 9.6 ± 2.3 % for the CW mode and 8.59 ± 3.34 % for the pulsed mode.

Although plasma efficiency remains the lowest component efficiency, there is an increase between the two operational modes. The reason for this can be seen through examination of the ion energy distribution functions in Fig.7.8. In the CW mode, the thruster consistently accelerates ions through a 25 V potential drop. In the pulsed mode, the fastest ions, arriving at the probe first, are accelerated to similar or slightly higher energies. However, much of the beam is significantly less energetic with a tail decaying over time. One might expect that the pulsed mode would result in higher acceleration of the ions for two reasons: first, the higher instantaneous power in the pulse mode provides more energy to accelerate them, and second, the transient plasma currents can couple energy into the flux conservers to drive additional radial magnetic field to accelerate the plasma (resulting in I^2 thrust scaling). However, these results suggest that the peak pulsed power is hampered by the increased plasma density in this mode. Indeed, the equivalent specific energies between the two modes results in equivalent peak acceleration. Furthermore, this equivalent accelerating potential indicates that the thruster in pulsed mode is not effectively capturing energy coupled into

the thruster structure, resulting in no enhanced accelerating force due to self and structure field effects.

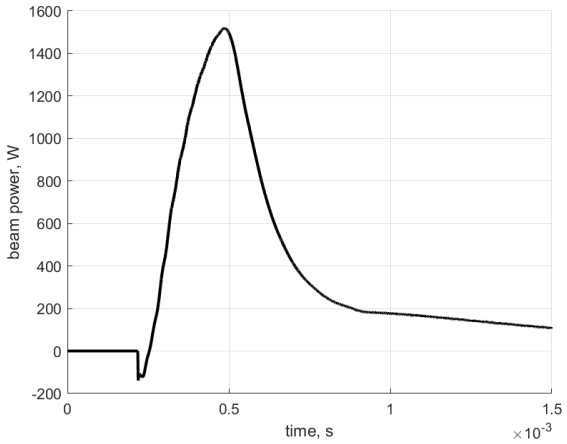

Figure 7.13: Ion beam power for the pulsed mode as a function of time as collected by the far-field diagnostic probes.

7.5 Discussion

I present the results shown above in a graphical format in Fig. 7.14(a). This chart illustrates an improvement in performance for the CW mode across all efficiency modes. Consequently, the overall probe-measured efficiency (per Eq. 3.34) is 0.58 ± 0.10 % for the pulsed mode and 2.07 ± 0.19 % for the CW mode. These probe-measured efficiencies align with the thrust-stand measured efficiency within uncertainty, as depicted for comparison in Fig. 7.14(b).

Notably, the pulsed mode operation presented here for the RMFv3 thruster did not perform any better than the pulsed mode operation of the RMFv2 thruster with an overall thrust stand measured efficiency of 0.48 ± 0.05% for the v3 thruster and 0.41 ± 0.04% for the v2 thruster. This can be seen through Fig.7.14(a) compared to Fig. 6.8 from Chapter 6. These two charts show very similar efficiency mode breakdowns for the two thrusters indicating that the underlying physics of the pulsed mode is largely the same for both. However at other operating conditions the v3 thruster was able to achieve a pulsed mode efficiency of up to 0.68 % which was a result of operating the thruster up to a pulse repetition rate of 500 Hz such that the higher efficiency is likely the result of improved mass utilization due to less wasted propellant between pulses. This result indicates that our design changes to the v3 thruster, apart from the adoption of CW mode, were largely unimpactful.

Turning now to the results for the pulsed vs CW mode study, Fig.7.14(a) shows that each

component efficiency mode increased for the CW mode over the pulsed mode. The largest relative mode increase was the coupling efficiency. This is a result of the continuous loading of the RMF antennas to the plasma in the CW mode. In the pulsed mode, the thruster has to re-ionize the propellant each cycle such that there is a substantial period where the RMF antennas are operating at high amplitude without any plasma load resulting in repeated losses. The mass utilization increases too in the CW mode up to 100 %. This is a direct result of the 100 % duty cycle in the CW mode such that there no propellant flow when the RMF is off as is the case for the pulsed mode. The rationale for the divergence efficiency increases in the CW mode over the pulsed mode is still not fully understood, but may be attributable to a higher component of Lorentz force relative to thermal pressure in the CW mode as the plasma density is reduced.

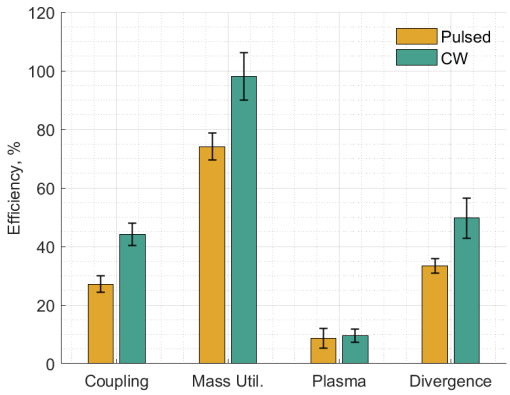

(a) Comparison of efficiency modes.

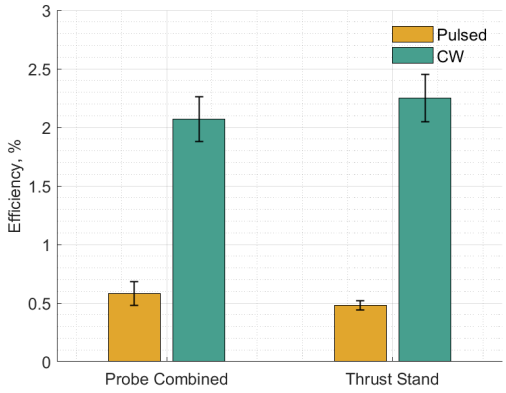

(b) Comparison of probe measured to thrust stand measured efficiency.

Figure 7.14: Phenomenological efficiency breakdowns for pulsed and CW mode.

Notably, the smallest improvement in terms of relative increase comes from plasma efficiency. It is important to note that the CW combined probe result underestimates the thrust stand-measured efficiency, while the pulse probe result overestimates it. This discrepancy is likely due to the high relative uncertainty in the plasma efficiency measurement and is attributed to the difficulty with the plasma potential correction for the RPA. As a result, using the thrust stand efficiency to infer the plasma efficiency (other modes remain as probe measured) reveals an increase from 7.4 % in the pulsed mode to 10.43 % in the CW mode. This is a notable improvement and agrees with the intuition that plasma efficiency should increase with lower collisional losses due to a reduction in density.

However, this plasma efficiency results still supports the interpretation presented in Chapter 6 that the RMF drive scheme cannot effectively directly couple to the plasma, as is the

case for theta-pinch and PIT thrusters. These more directly coupled thruster architectures have axially oriented coils which can self-accelerate the plasma as they both drive the azimuthal plasma current and provide the accelerating magnetic field for the Lorentz force. As a result, increasing peak powers in these systems increases plasma acceleration. However, for the RMF thruster, the transverse coils do not self accelerate the plasma which implies that the system is insensitive to how the power is applied. For instance, our results show that the higher instantaneous power in pulsed mode does not result in a higher force on the plasma. This distinction can be seen through the lens of Eqs. 2.4 and 2.5.

One might expect the plasma efficiency to be significantly higher in the CW mode, given the lower density, resulting in fewer energetic losses and more beam energy. However, plasma efficiency remains the largest loss mode for the thruster in CW mode, as evidenced by the results shown in Fig. 7.8. The low acceleration potentials measured are insufficient to evacuate the plasma from the thruster before it loses energy through collisional processes, such as interaction with the thruster wall. Although lower density may reduce radiative losses, wall losses can still be substantial, as predicted by Sercel in Ref. [79]. In this way, the RMF thruster in CW mode is similar to a Hall thruster operating at very low voltages, which would similarly not efficiently produce an energetic ion beam.

To achieve high plasma efficiency at this power and flow rate, the thruster would need to generate a potential drop for the ions an order of magnitude larger, ranging from 200 to 300 V (See Chapter 8). A straightforward approach to enhance this metric would be to increase the radial component of the applied magnetic field. However, experimental observations indicate that increasing the strength of the applied magnetic field leads to a sharp decline in performance above a critical value [78]. Specifically, in the CW mode, the thruster may fail to ignite if the applied magnetic field is too strong.

This phenomenon can be interpreted through Eq. 3.15 from Chapter 3, restated here as

$$\bar{u_\theta} = \frac{\omega r}{1 + 2\left(B_0^2 + \zeta^2\right)/B_\omega^2} \tag{7.12}$$

where ω is the RMF frequency, r is the radius, B_0^2 is the amplitude of the static magnetic field, ζ is an electron collision parameter, and B_ω is the RMF strength. The denominator in this expression indicates that as the applied magnetic field increases, the electron fluid becomes more magnetized to that field and has a diminished response to the RMF. This ultimately results in a substantial reduction in azimuthal current drive and, consequently, reduced thruster performance.

To address this issue, the RMF strength must be increased proportionally to the radial bias field. This is particularly important for the CW mode, where the current amplitude is

already reduced. The most effective method to enhance the RMF strength is likely to use additional antenna turns or ferromagnetic cores. Although this may increase antenna inductance and consequently voltage, it may be tolerable due to the overall lower currents relative to the pulsed mode. Additionally, the axial component of the applied magnetic field may be less critical for plasma confinement in the CW mode compared to the pulsed mode. In the pulsed mode, the axial field is necessary to compress the plasma and maintain confinement. However, with a reduction in plasma density in the CW mode, there is less internal magnetic pressure from the plasma to counteract. In this case, it may be beneficial to utilize the entire applied magnetic field—which impedes current drive regardless of direction—in the radial direction, where it can work to accelerate the ions. These adjustments may lead to a significant departure from the single-turn air-core antennas and conical magnetic-nozzle shape of ELF heritage [95]. Indeed, CW mode RMF thrusters may evolve towards shorter coaxial configurations, allowing the RMF and radial bias field to be maximized simultaneously.

7.6 Conclusion

In this chapter, I conducted an evaluation of the performance of an RMF thruster operating in pulsed and continuous wave modes. The pulsed mode involves the application of a high-amplitude RMF for 200 μs at a 7.8 % duty cycle, while the CW mode consists of sustained RMF application at approximately one quarter of the amplitude used in the pulsed mode. When considering the same power, flow rate, and applied magnetic field, I observed a substantial improvement in thruster efficiency for the CW mode, exceeding 4.5 times that of the pulsed mode.

To explain this finding, I performed measurements of phenomenological efficiency modes, including coupling efficiency, divergence efficiency, mass utilization, and plasma efficiency. On average, I found that the CW mode enhances all of these metrics by a multiplicative factor of 140 %. Notably, the plasma efficiency in the pulsed mode is lower than for the CW mode, suggesting that high-amplitude pulses do not result in higher average beam power. This supports the hypothesis that RMF thrusters operating in pulsed mode are inherently inefficient. In pulsed mode, the high plasma density, stemming from the dense pre-pulse neutrals, does not contribute to increased plasma acceleration since RMF thrusters cannot directly apply force to the plasma through their antenna currents, unlike other inductive pulsed plasma thrusters. Instead, the dense plasma leads to enhanced collisional losses within the thruster, resulting in inefficient operation.

Despite the improvements achieved in the CW mode, the overall efficiency of RMF thrusters remains below the state-of-the-art for electric propulsion, at approximately 2.2 %

jet efficiency (inclusive of power supply losses). A specific design focus on this operational regime may offer additional performance enhancements, especially considering that the thruster, and particularly the power system, was designed to operate in both modes for this study. I posit that enhancing the RMF strength and applied magnetic field in the CW mode represents a promising avenue for improving the performance of RMF thrusters, as this mode fully embraces the unique continuous directed current drive of RMF coupling.

CHAPTER 8

RMF Performance Model and Theoretical Maximum Efficiency

8.1 Introduction

Based on the findings presented in the previous chapter, there is compelling evidence that the continuous wave (CW) method of operation for RMF thrusters will consistently outperform the pulsed mode. This superiority arises as a result of the indirect coupling between the antenna and the accelerating Lorentz force in RMF thrusters. For RMF thrusters, high energy pulses lose comparably more energy through inelastic collisional processes than other IPPTs because the high densities inherent to pulsed mode (See Sec. 6.4) are not compensated for by an increase in the Lorentz (and therefore jet power) from the primary coil magnetic fields.

Despite the improved performance in the CW mode, the overall system efficiency remained below 3 %, falling considerably short of competitive benchmarks for electric propulsion systems. However, considering the CW mode as the prospective direction for RMF thrusters, I aim to explain and predict the operation of thrusters in this mode. This chapter is dedicated to formulating a model for RMF thruster efficiency, with two primary objectives: firstly, to evaluate the potential of RMF thrusters for achieving high performance, and secondly, to identify parameters that could enhance their efficiency.

The chapter begins with an analysis of the bias field strength within the thruster. This static field primarily facilitates the Lorentz force acceleration of the plasma. However, as detailed in Chapter 3, an increase in the bias field hinders the magnetization of electrons to the RMF and reduces azimuthal electron current. Consequently, an optimal field strength exists to maximize thrust in relation to the RMF strength. This optimum point establishes a connection between RMF strength, RMF frequency, bias field, and the accelerating force.

In the subsequent section, I leverage this ideal operating point to develop a one-dimensional model for thruster plasma efficiency, coupling efficiency, and mass utilization.

Towards the end of the chapter, I provide a summary of key insights derived from the model and propose viable strategies to enhance RMF thruster performance.

8.2 Summary of Major Assumptions

To produce the results for this chapter I make several simplifying assumptions. In this section, I enumerate each of the primary ones and explain my justification for making them.

8.2.1 RMF Current Drive Assumptions

The model presented below is based on the RMF current drive model presented in Chapter 3, to review the assumptions made in the derivation of that model include:

1. Infinitely long plasma cylinder such that the RMF drives electric field gradients in the axial direction only—simplification of thruster geometry.
2. Pressure forces neglected in electron Ohms law—pressure forces should be a small contribution relative to the "cold" Lorentz force in the CW mode.
3. Ion motion neglected in electron Ohms law—ion motion will be slow on the relevant time scales.
4. Neutral collisions will be neglected in electron Ohms law—simplification, but in practice will contribute to increased electron resistivity.
5. Axial electron currents are in-phase with the RMF—justified by Ref. [42].
6. High frequency variation in azimuthal electron drift is ignored in favor of the period average drift—justified by addressing only low frequency thruster behavior.
7. Ampere's law is not solved for and the magnetic field fully penetrates the plasma—justified by adherence to the modified skin depth expression in Eq. 3.17.

The major two assumptions here that differ between this work and the work of Sercel in Ref. [78] is the lack of electron pressure forces and the assumption of in-phase axial electron currents. The choice to ignore pressure stems from my focus on the CW mode where pressure forces are less important, while Sercel focused on pulsed mode where pressure is relevant but only contributes to ∼10% of the thrust force [78]. I include the assumption that the axial electron currents are in-phase with the RMF as an important factor to show that the azimuthal component of the RMF does not appear as a drag term to the azimuthal electron drift. Without this assumption, it is difficult to see this result clearly.

8.2.2 Performance Model Assumptions

For the performance model in the latter part of this chapter I also make the following assumptions:

1. Drag force to the RMF is only provided by the radial bias field—justified in the limit that the RMF and radial bias field are strong.
2. 1D flow—generally justified by thruster geometry, albeit the geometry of the v3 thruster is stretching this assumption.
3. Ions and electrons move as a bulk fluid in the axial direction—justified by quasi-neutrality.
4. Plasma is fully ionized by the RMF—justified by mass utilization results from Chapters 6 and 7.
5. The RMF and bias field are constant over the thruster length—done for simplicity.
6. The electron temperature is constant inside the thruster volume—informed by internal diagnostics from chapter 6, however this is likely non physical.

These assumptions permit me to form a simple analytical model for the performance of RMF thrusters operating in CW mode. In the following sections, I explain the impact of bias field strength of current drive to obtain optimum performance and how that set-point translates into the efficiency modes of of the thruster.

8.3 Optimum Bias Field Strength

Recalling the model from Chapter 3 for RMF current drive considering plasma resistivity and the counter magnetization of the bias field, the equation for the average azimuthal electron motion is given by

$$u_\theta = \frac{2}{3}\frac{\omega R}{1+2\left(B_0^2+\zeta^2\right)/B_\omega^2}, \tag{8.1}$$

where the average is taken over the thruster cross-sectional area. In this equation, ω represents the RMF frequency, R is the thruster radius, B_0 is the bias field strength, $\zeta = m_e\nu/e$ stands for a collisional resistivity/drag factor, and B_ω represents the RMF strength.

I can express an static Ohm's law for electrons, repurposed from Eq. 3.7 as

$$0 = -en_e\left(\vec{E} + \vec{u} \times \vec{B}\right) - \nabla p_e - m_e n_e \nu_{ei}(\vec{u} - \vec{u_i}). \tag{8.2}$$

I assume as stated above that there is no pressure component, and that the electrons and ions move as a bulk fluid in the axial direction. Under these assumptions and the influence of the RMF and bias field the static axial component of this equation is

$$E_{z,0} = u_\theta B_{r,0}, \tag{8.3}$$

where $E_{z,0}$ is the ambipolar electric field responsible for ion acceleration, and $B_{r,0}$ is the radial component of the bias field. This expression functions as a static force balance underlying the high-frequency Ohm's law relation described in Chapter 3. Substituting u_θ into this expression gives:

$$E_{z,0} = \frac{2/3\omega R B_{r,0}}{1 + \frac{2}{B_\omega^2}\left(B_{r,0}^2 + B_{z,0}^2 + \zeta^2\right)}. \tag{8.4}$$

Interestingly, this expression exhibits a non-monotonic behavior concerning the applied radial bias field and reaches a maximum at

$$B_{r,0}^* = \sqrt{B_\omega^2/2 + B_{z,0}^2 + \zeta^2}. \tag{8.5}$$

This optimal radial field, $B_{r,0}^*$, yields a maximum electric field of

$$E_{z,0}^* = \frac{\omega R}{3\sqrt{2}} \frac{B_w^2}{\sqrt{2\zeta^2 + 2B_{z,0}^2 + B_\omega^2}}. \tag{8.6}$$

Moreover, in the limit where resistivity and axial bias field are small relative to the RMF strength, the maximum achievable electric field is

$$E_{z,0}^* = \frac{\omega R}{3\sqrt{2}} B_\omega. \tag{8.7}$$

Note, this electric field is consistent with an E×B drift corresponding to the azimuthal electron motion driven by the RMF. This is consistent with the analysis of Blevin and Thonemann from Ref. [7] within a scaling factor.

In Fig. 8.1, I present normalized curves of $E_{z,0}$ as a function of $B_{r,0}$ for various values of $Z^2 = (B_{z,0}^2 + \zeta^2)/B_\omega^2$. This plot indicates that increasing the applied radial field increases the Lorentz force, thus increasing the ambipolar field, $E_{z,0}$, up to an optimum point. Past this point, the electrons become preferentially biased to the applied radial field and are no longer entrained to the RMF. This results in a decreasing ambipolar field at high $B_{r,0}$. This

trend can also be seen through Eq. 8.4 as the numerator scales linearly with $B_{r,0}$ and the denominator scales with $B_{r,0}^2$.

The figure further illustrates that increasing the non-accelerating drag terms Z has the effect of reducing the maximum achievable accelerating field and shifting its location towards higher applied radial fields. Additionally, the plot clearly indicates that the applied radial field should be approximately on the order of the RMF strength. It emphasizes that the real degrees of freedom to enhance the accelerating force are thruster size, RMF strength, and RMF frequency.

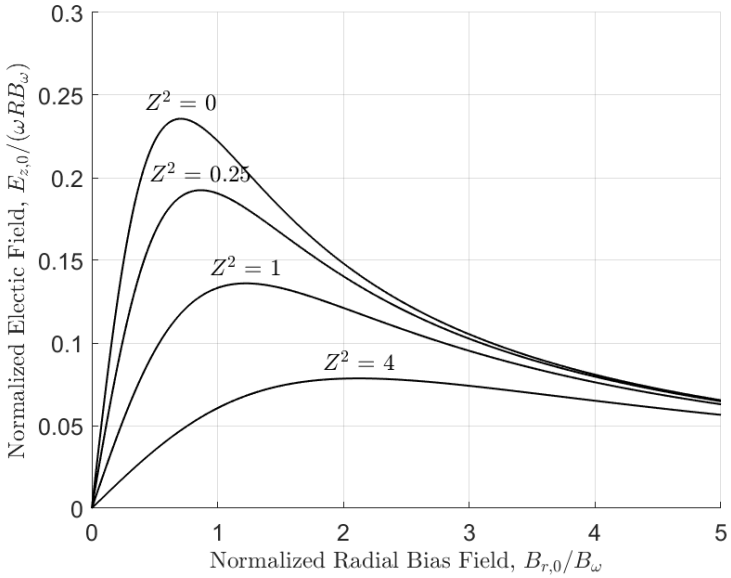

Figure 8.1: Normalized model for average ion accelerating electric field.

8.4 Thruster Performance Model

In this section, I leverage the RMF current drive model and the ion acceleration to synthesize a comprehensive analytical performance model. The primary objective of this model is to describe and predict the efficiency scaling modes observed and measured in the preceding chapters of this work. I confine this analysis to RMF thrusters operating in the continuous-wave (CW) mode for two main reasons. Firstly, the CW mode facilitates easier analysis as the plasma is generally not time-varying. Secondly, based on the findings in Chapter 7, the CW mode for RMF thrusters appears to be the most promising path towards achieving competitive RMF thruster performance. Additionally, in this model, I adopt the restrictive assumption that the thruster behaves one-dimensionally, resembling a tube or channel flow.

I show the dimensions and notional solution of this model in Fig. 8.2

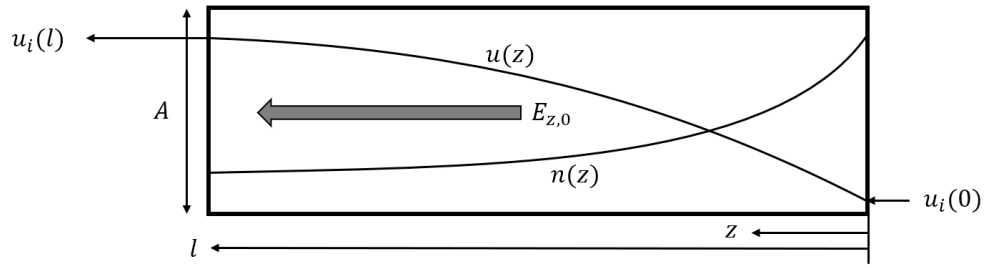

Figure 8.2: 1D model geometry showing axial dimension, z, thruster length and area, l, and A, the plasma density and speed, n and u, and the constant applied electric field from the RMF Lorentz force, $E_{z,0}$.

Utilizing this model towards the end of the section, I present a hypothesis explaining why the experimental results in the CW mode exhibit a clear quenching effect, to the extent of extinguishing the plasma, as the bias field strength is increased. This effect is presented and discussed in Chapter 4, Sec. 4.4.3.

8.4.1 Plasma Efficiency

I initiate this analysis by focusing on the most critical mode for RMF thrusters: the plasma efficiency. I begin with the general expression for the electric field that accelerates the ions:

$$E_{z,0} = u_\theta B_{r,0}. \tag{8.8}$$

Assuming that this field is uniform over some region of length l where RMF and bias field are constant, I can utilize the conservation of energy for the ions to derive an expression for the ion velocity in the thruster as a function of position:

$$u_i(z) = \sqrt{\frac{2q_i E_{z,0} z}{m_i} + u_i^2(0)}, \tag{8.9}$$

where z is the axial position from the rear of the thruster, m_i is the ion mass, and q_i is the ion charge. We will make the simplifying assumption that $q_i = e$. For this expression, I take $u_i(0) = \sqrt{8kT_i/(\pi m_i)}$ as the neutral thermal speed entering the thruster. Assuming, for now, that the RMF fully ionizes the propellant (supported by the experimental measurements in Chapters 6 and 5) and invoking mass continuity, I arrive at an expression for plasma density as

$$n(z) = \frac{\dot{m}}{m_i u_i(z) A}, \tag{8.10}$$

where $\dot{m}$ is the mass flow rate through the thruster, and A is the cross-sectional area. With these two expressions in Eq. 8.10 and 8.8, I can estimate terms for the power flow in the thruster. Most importantly, the beam power is

$$P_{\text{beam}} = \frac{e\dot{m}}{m} E_{z,0} l, \tag{8.11}$$

where I have ignored the small initial thermal velocity. Next, I also include the loss modes, which include ionization and thermal loss, excitation radiation loss, and collisional wall loss. The ionization and thermal loss can be thought of as the "frozen flow" energy convected out of the thruster by the ions and electrons. This is written as:

$$P_{\text{frozen}} = \frac{e\dot{m}}{m} \left(\varepsilon_{iz} + \frac{3}{2} T_e \right), \tag{8.12}$$

where ε_{iz} is the ionization energy in eV carried by the ions, and $\frac{3}{2}T_e$ is the mean thermal energy carried by the electrons. For simplicity, I assume that all thermal energy is not recoverable and the thrust is produced entirely by the "cold" u_θ-driven Lorentz force consistent with Chapter 3. Fundamentally, this loss mode is unavoidable as ionization is required for any plasma thruster to operate, and sufficient electron temperature is necessary to achieve it. This mode puts an upper bound on thruster performance based primarily on the ionization energy of the propellant.

Continuing, I can write an expression for the excitation collision loss for neutrals and ions

$$P_{\text{rad}} = \int_V e n^2 \langle \sigma_{ex} v_e \rangle \varepsilon_{ex} dV, \tag{8.13}$$

where $\langle \sigma_{ex} v_e \rangle (T_e)$ is the Maxwellian-averaged excitation cross-section, and ε_{ex} is the excitation energy, and the integral is taken over the thruster volume. Note, that under my assumption of 100 % mass utilization the radiative power is driven exclusively by ion excitation reactions, and thus scales as n^2 while neutral excitation is neglected. I can rewrite this integral as

$$P_{\text{rad}} = Ae \langle \sigma_{ex} v_e \rangle \varepsilon_{ex} \int_0^l n(z)^2 dz \tag{8.14}$$

where I assume that the electron temperature is constant in the RMF region of the thruster. Solving this integral for the functional form of ion density (Eq. 8.10) yields:

$$P_{\text{rad}} = \frac{\dot{m}^2}{m_i A} \frac{e\langle \sigma_{ex} v_e \rangle \varepsilon_{ex}}{2 q_i E_{z,0}} \ln\left(1 + \frac{\pi q_i E_{z,0} l}{4 k_b T_i}\right) \tag{8.15}$$

In practice, the exit energies of the ions are significantly higher than their incident thermal energies, even for poorly performing thrusters. In light of this fact, I will disregard the ln term as it is a weakly varying function and treat it as a constant factor with an order of magnitude of 10. This reduces Eq. 8.15 to

$$P_{\text{rad}} = 5 \frac{\dot{m}^2}{m_i A} \frac{e\langle \sigma_{ex} v_e \rangle \varepsilon_{ex}}{q_i E_{z,0}}. \tag{8.16}$$

Lastly, I can express the wall loss as

$$P_{\text{wall}} = \int_{A_{\text{wall}}} 0.6 n \sqrt{\frac{eT_e}{m_i}} e \left(\frac{5}{2} T_e + 2\Phi\right) dA_{\text{wall}}, \tag{8.17}$$

where the integral is performed over the wall area A_{wall}, T_e represents the electron temperature in electron volts, and Φ denotes the potential drop through the wall sheath, which is a function of the ion mass and electron temperature [57, 32]. I will approximate this integral as

$$P_{\text{wall}} = 2\pi R 0.6 \sqrt{\frac{eT_e}{m_i}} e \left(\frac{5}{2} T_e + 2\Phi\right) \int_0^l n(z) dz, \tag{8.18}$$

where I again assume a constant electron temperature in the thruster and use an average wall radius R. Note, this expression is also valid for reasonably proportioned conical (and truncated conical) thrusters where the axial length is greater than or equal to the thruster radius ($l \geq R$). I again replace the density using Eq. 8.10, and upon solving the integral, I arrive at

$$P_{\text{wall}} = 2\pi R 0.6 \frac{\dot{m}}{m_i A} \sqrt{\frac{eT_e}{m_i}} e \left(\frac{5}{2} T_e + 2\Phi\right) \frac{m_i}{q_i E_{z,0}} \left(\sqrt{u_i^2(0) + \frac{2 q_i E_{z,0} l}{m_i}} - u_i(0)\right). \tag{8.19}$$

Once again, assuming exhaust velocity is much larger than inlet thermal speed, $u_i(0)$, this expression is simplified to

$$P_{\text{wall}} = 3.77 \frac{Rl}{A} \frac{\dot{m}}{m_i} \sqrt{\frac{2eT_e}{q_i E_{z,0} l}} e \left(\frac{5}{2} T_e + 2\Phi\right). \tag{8.20}$$

With these expressions, I can formulate a comprehensive expression for the total power flow into the plasma:

$$P_{\mathrm{p}} = P_{\mathrm{beam}} + P_{\mathrm{frozen}} + P_{\mathrm{rad}} + P_{\mathrm{wall}}. \tag{8.21}$$

Which can be expanded into:

$$P_{\mathrm{p}} = \frac{\dot{m}}{m_i} q_i E_{z,0} l \left[1 + \frac{E_{\mathrm{frozen}}}{q_i E_{z,0} l} + E_{\mathrm{wall}} \frac{Rl}{A} \sqrt{\frac{eT_e}{q_i^3 E_{z,0}^3 l^3}} + 5 \frac{\dot{m} l}{A} \frac{e \langle \sigma_{ex} v_e \rangle \varepsilon_{ex}}{q_i^2 E_{z,0}^2 l^2} \right]. \tag{8.22}$$

In this form, I can derive an expression for the plasma efficiency of the thruster similar to Eq. 3.40:

$$\eta_p = \frac{P_{\mathrm{beam}}}{P_{\mathrm{p}}} = \frac{1}{1 + \frac{E_{\mathrm{frozen}}}{q_i E_{z,0} l} + E_{\mathrm{wall}} \frac{Rl}{A} \sqrt{\frac{eT_e}{q_i^3 E_{z,0}^3 l^3}} + 5 \frac{\dot{m} l}{A} \frac{e \langle \sigma_{ex} v_e \rangle \varepsilon_{ex}}{q_i^2 E_{z,0}^2 l^2}}. \tag{8.23}$$

From this expression, it is evident that the plasma efficiency should increase with an increasing electric field. This makes intuitive sense, as increasing the accelerating potential both enhances the jet power and reduces the average propellant density, thus minimizing losses. This effect underscores the critical importance of operating an RMF thruster at the optimum $B_{r,0}^*$ to maximize the accelerating electric field. However, a large caveat to this is the assumption that electron temperature is independent of electric field. The large azimuthal drifts that result from operation at the optimum electric field $E_{z,0}^*$ likely corresponds to increased Ohmic heating and higher electron temperatures. I expand on this effect further in Sec. 8.4.4.

In Fig 8.3, I plot η_p from Eq. 8.23 as a function of the electric field, along with the relative loss terms (the non unity additive terms in the denominator of Eq. 8.23). The chosen free parameters are set to mimic v3 thruster operation, including an electron temperature of 15 eV, an average radius of 10 cm ($A = 2\pi R^2$), a length of 15 cm, and a mass flow rate of 25 mg/s of xenon. The figure indicates that plasma efficiency is highly sensitive to the electric field below approximately 2000 V/m, then gradually tapers off to near unity around 10 kV/m. This suggests that, for a competitively efficient thruster overall, the electric field needs to be somewhat greater than 6000 V/m. Eq. 8.4 further demonstrates that achieving this requires an increase in RMF frequency, thruster radius, or RMF field strength.

Examining the relative losses, it is observed that as the electric field increases, the radiative loss ρ_{rad} becomes the least significant most rapidly, followed by the frozen flow loss ρ_{fz}, and then the wall loss ρ_{wall}. This trend aligns with intuition from other plasma thruster systems where radiative loss is typically neglected, and wall loss dominates.

For the RMFv3 thruster's peak performance, the accelerating field was approximately 345 V/m. This value is derived from the bias magnetic field of 40 G, the RMF frequency of 413

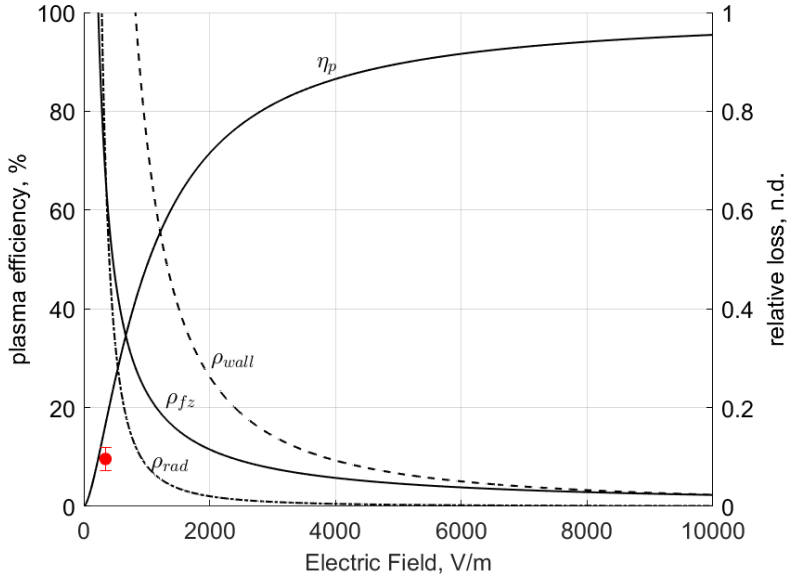

Figure 8.3: Plasma efficiency scaling from 1D model. Experimental measurement of plasma efficiency shown in red.

kHz, and the knowledge from Eq. 8.1 that the azimuthal electron velocity, $u_\theta = 1/2\omega r$, for the optimum $B_{r,0} = B^*_{r,0}$ (as also measured experimentally by Sercel [78]). With this value of $E_{z,0}$ in our simple model, the predicted plasma efficiency is 16.6 %, notably close to the experimentally measured value of 9.6 ± 2.3 % for this operating condition.

8.4.2 Coupling Efficiency

Continuing the derivation of this analytical efficiency model, I can utilize the expressions generated for the power into the plasma to derive an expression for the effective resistance of the plasma. By definition, this plasma resistance is given by

$$R_\mathrm{p} = \frac{2P_\mathrm{p}}{I_\omega^2}, \tag{8.24}$$

where I_ω is the peak current through the RMF coils. It is important to clarify here that R_P is not related to the azimuthal plasma current (e.g. I_θ, J_θ, or u_θ), but is the effective plasma resistance as seen by the RMF antennas. This is reflective of the approach presented in Chapter 5 for the calculation of coupling efficiency. Furthermore, this expression makes no attempt to quantify the small-scale processes that contribute to plasma resistivity, and instead takes an overarching view of how power is deposited into the plasma. This differs from the approach of Little et al. [55] who characterize the plasma resistivity as it pertains

to the driven azimuthal plasma currents for PITs. One caveat to this statement is that P_p is a function of electron temperature through the loss processes presented in the prior section, and it is indeed through the electron temperature that the electron dynamics and resistivity relate to this lumped plasma resistance, R_p. This relation is discussed further in Sec. 8.4.4.

The current through the coils is related to the RMF magnetic field via a general expression of the form

$$B_\omega = f(R,l)\mu N I_\omega = \alpha I_\omega. \tag{8.25}$$

Here, $f(r,l)$ is a geometric factor in units of m^{-1} that is generally a function of the thruster radius and length, μ is the effective magnetic permeability of the magnetic circuit taking into account ferromagnetic materials, and N is the number of coil turns in the RMF antenna. Grouping the leading terms in Eq. 8.25, I define a coil constant $\alpha = f\mu N$, which describes the RMF strength for a given current. Substituting Eq. 8.25 into the expression for plasma resistance, I arrive at the following expression:

$$R_\mathrm{p} = \frac{2\alpha^2 \frac{\dot{m}}{m_i}}{B_\omega^2}\left[q_i E_{z,0} l + E_\mathrm{frozen} + E_\mathrm{wall}\frac{Rl}{A}\sqrt{\frac{eT_e}{q_i E_{z,0} l}} + 5\frac{\dot{m} l}{A}\frac{e\langle\sigma_{ex} v_e\rangle\varepsilon_{ex}}{q_i E_{z,0} l}\right]. \tag{8.26}$$

Next, I replace the electric field with the maximum $E^*_{z,0}$, assuming the radial bias field is set optimally. Using Eq. 8.7, this results in

$$R_\mathrm{p} = \frac{(\alpha\omega R)^2 \frac{\dot{m}}{m_i}}{9{E^*_{z,0}}^2}\left[q_i E^*_{z,0} l + E_\mathrm{frozen} + E_\mathrm{wall}\frac{Rl}{A}\sqrt{\frac{eT_e}{q_i E^*_{z,0} l}} + 5\frac{\dot{m} l}{A}\frac{e\langle\sigma_{ex} v_e\rangle\varepsilon_{ex}}{q_i E^*_{z,0} l}\right] \tag{8.27}$$

Some trends of this expression become clear in the limit of high accelerating electric field. In this limit, Eq. 8.27 reduces to

$$R_\mathrm{p} = \frac{1}{9}\frac{(\alpha\omega R)^2 l}{E^*_{z,0}}\frac{q_i \dot{m}}{m_i}. \tag{8.28}$$

This equation reveals that increasing the optimum electric field (recall this is directly proportional to B_ω) has the effect of decreasing the plasma load on the RMF. This is a direct result of the plasma power P_p scaling linearly with the RMF strength, while the power deposited in the circuit scales as the square of the RMF strength ($B_\omega \propto I_\omega$).

In Fig. 8.4, I show the predicted plasma resistance by the model in Eq. 8.27 as a function of $E^*_{z,0}$ for several values of α. The remaining free parameters are chosen the same as for Fig. 8.3. Note that $\alpha = 0.13$ G/A reflects the coil constant for the RMFv3 thruster as measured

by a DC Gauss meter (see Sec. 4.4.1.5).

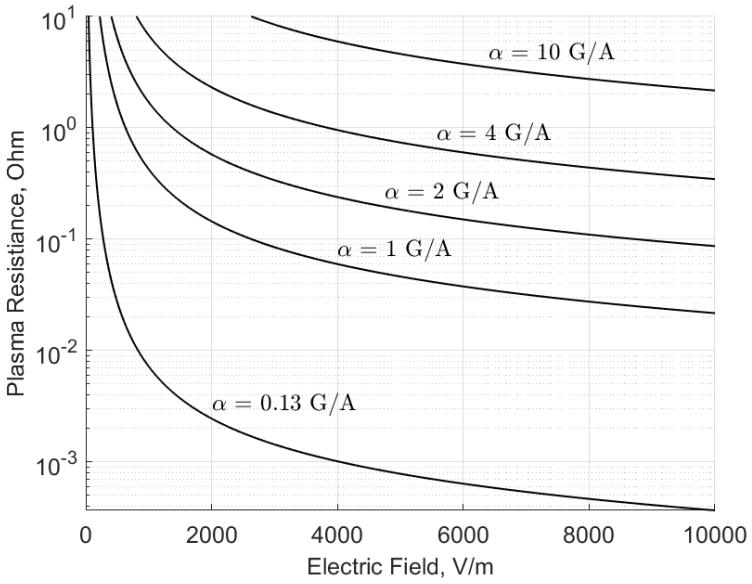

Figure 8.4: Plasma resistance from 1D model.

Now, I can use Eq. 8.27 for R_p to formulate a formula for the coupling efficiency of the RMF power system:

$$\eta_\mathrm{c} = \frac{R_\mathrm{p}}{R_\mathrm{p} + R_\mathrm{c}} = \frac{1}{1 + \frac{R_\mathrm{c}}{R_\mathrm{p}}}, \tag{8.29}$$

where R_c is a constant circuit resistance, typically on the order of a few hundred milli-ohms. Substituting the reduced expression for R_p from Eq. 8.28 yields:

$$\eta_\mathrm{c} = \frac{1}{1 + \frac{9E^*_{z,0} m_i R_\mathrm{c}}{(\alpha\omega R)^2 q_i l \dot{m}}}. \tag{8.30}$$

This expression reveals that increasing the accelerating electric field will negatively impact coupling efficiency. This is a result of the plasma load increasing linearly with the electric field (B_ω), while the circuit losses increase quadratically. This is in contrast to other IPPT systems where the Lorentz force scales quadratically with the time-varying magnetic field (I^2 thrust scaling), and coupling efficiency is largely independent of field strength and is primarily driven by other factors such as propellant density and antenna geometry [72, 68]. For the RMF system, these factors are also at play, and I can identify several strategies to improve coupling efficiency for RMF thrusters:

1. Reducing unloaded circuit resistance R_c to the lowest possible value; this is intuitive

to reduce circuit losses.

2. Increasing the load of the propellant, achieved through higher particle flow rates $\dot{m}/m_i$ or higher charge ions q_i.

3. Increasing the RMF frequency ω and thruster radius. This allows for additional plasma load by increasing the Lorentz force.

4. Potentially most importantly, increasing the coil constant α, as this reduces RMF antenna current without limiting B_ω. This involves higher μ materials such as ferrite, increasing the number of antenna turns N, or improving the geometric factor f.

In Fig. 8.5, I plot the coupling efficiency using the full plasma resistance model from Eq. 8.27 as a function of $E^*_{z,0}$ for several values of α. The free parameters are the same as in Fig. 8.3 and 8.4, with the addition of the circuit resistance, $R_\mathrm{c} = 600$ mΩ, a value informed by the CW RMFv3 experiment.

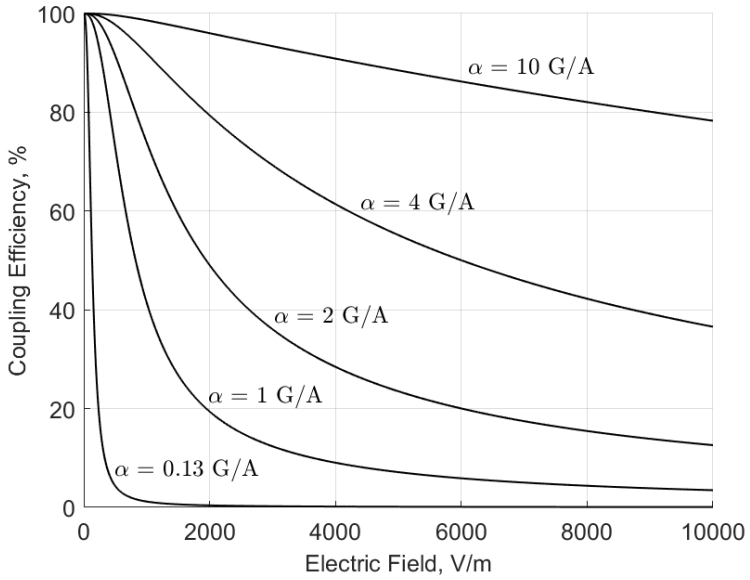

Figure 8.5: Coupling efficiency scaling for 1D model.

This model does not show the same level of agreement with the experiment as the plasma efficiency model in Eq. 8.23. This curve predicts a coupling efficiency of 10 % for the optimum v3 CW case, compared to the experimental value of 44 %. Due to the steep gradient along the $\alpha = 0.13$ G/A line, a 50 % error in the accelerating field would be needed to make the model match the experiment. While this error is notable, this simple model does predict in the right order of magnitude.

Looking at the curves in Fig. 8.5, reveals the sensitivity to the coil constant α. This parameter increasing one to two orders of magnitude—achievable with higher turns and magnetic materials—has a dramatic effect on the coupling efficiency, particularly at the upper end of the accelerating electric field. To fully appreciate this result, I can combine the coupling efficiency expression with the plasma efficiency to obtain a combined power efficiency for the thruster:

$$\eta_{\mathrm{p}}\eta_{\mathrm{c}} = \frac{P_{\mathrm{beam}}}{P_{\mathrm{p}} + \frac{1}{2}R_c I_\omega^2} = \frac{1}{\frac{1}{\eta_{\mathrm{p}}} + \frac{1}{2}\frac{R_c I_\omega^2}{q_i \frac{\dot{m}}{m_i} E_{z,0}^* l}}. \tag{8.31}$$

By reducing this expression, using Eq. 8.25 to replace I_ω, I arrive at

$$\eta_{\mathrm{p}}\eta_{\mathrm{c}} = \frac{1}{\frac{1}{\eta_{\mathrm{p}}} + 9\frac{E_{z,0}^* m_i R_c}{(\alpha\omega R)^2 q_i l \dot{m}}}. \tag{8.32}$$

Notably, this function is not monotonic in the applied RMF field. The reciprocal of η_{p} decreases to unity with increasing electric field (as η_{p} also tends towards unity), and the second term in the denominator (the coupling term) increases linearly with electric field strength. Expanding terms for $1/\eta_{\mathrm{p}}$ gives

$$\eta_{\mathrm{p}}\eta_{\mathrm{c}} = \frac{1}{1 + \rho_{\mathrm{frozen}} + \rho_{\mathrm{wall}} + \rho_{\mathrm{rad}} + 9\frac{E_{z,0}^* m_i R_c}{(\alpha\omega R)^2 q_i l \dot{m}}}. \tag{8.33}$$

I plot this expression in the same manner as I do for Fig .8.5 in Fig 8.6. These curves show plainly that without taking into account the coupling efficiency, increasing the electric field or RMF amplitude does not result in overall increased performance. As electric field in increased, low coupling efficiency dominates and overall efficiency decreases. Physically, the optimum condition that arises from Eq. 8.33 is a result of the plasma efficiency increasing as a result of increased Lorentz force due to higher field strengths while coupling efficiency decreases as larger stronger fields results in enhanced circuit losses.

To identity this optimum point, I return to Fig. 8.3. From this plot it becomes evident that wall loss is the most dominant mechanism within the relevant range of applied electric fields for our facsimile of RMFv3 thruster operation. Recognizing this, we can exclude the non-wall loss modes in Eq. 8.33, which reduces to

$$\eta_{\mathrm{p}}\eta_{\mathrm{c}} = \frac{1}{1 + E_{\mathrm{wall}}\frac{Rl}{A}\sqrt{\frac{eT_e}{q_i^3 E_{z,0}^3 l^3}} + 9\frac{E_{z,0}^* m_i R_c}{(\alpha\omega R)^2 q_i l \dot{m}}}. \tag{8.34}$$

Using this equation, I can identify the maximum power efficiency, which occurs at

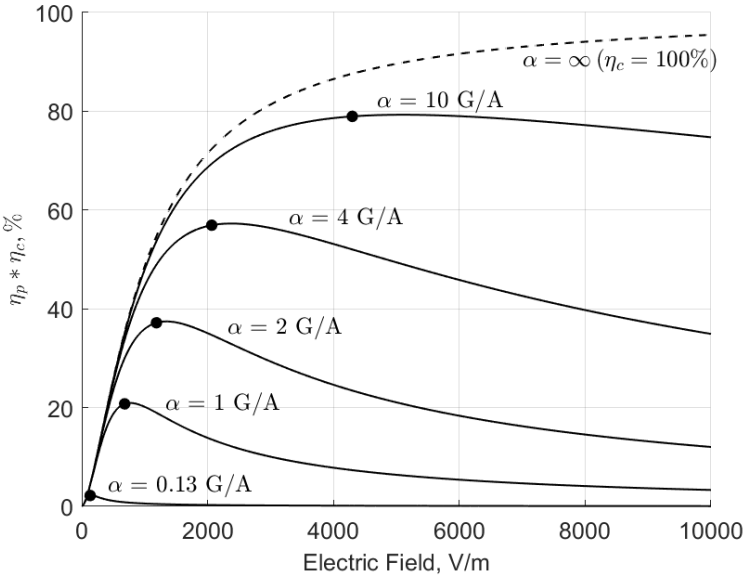

Figure 8.6: Combined efficiency scaling for plasma efficiency and coupling efficiency.

$$E_{z,0}^{**} = \left(\frac{1}{6\pi} \frac{E_{\text{wall}} R \sqrt{T_e} l (\alpha\omega)^2 \dot{m}}{R_c m_i} \right)^{2/5} \tag{8.35}$$

I plot these maximum values as filled circles in Fig. 8.6. Under the assumption of dominant wall loss, there exists good agreement for the maximum of these curves.

8.4.3 Mass Utilization Efficiency

I can formulate an expression for mass utilization by balancing the volumetric ionization rate with the beam particle flow rate. The expression I derive is consistent with the assumption in Eq. 8.10 as it represents a step function where mass utilization is either 100 % or 0 %. In this analysis, I do not include internal recombination (either collisional or via diffusion to the wall) in this analysis, as this effect results in a reduction in plasma density but does not constitute a mass loss for the system. The volumetric ionization rate can be written as

$$\dot{N}_{iz} = A \int_0^\infty n_n(z) n(z) \langle \sigma_{iz} v_e \rangle dz, \tag{8.36}$$

where A is the thruster area, $\langle \sigma_{iz} v_e \rangle$ is the Maxwellian-averaged ionization rate coefficient, and $n_n(z)$ is the neutral density. I can again make the assumption of constant electron temperature to solve this integral:

$$\dot{N}_{iz} = A\langle\sigma_{iz}v_e\rangle \int_0^l n_n(z)n(z)dz. \tag{8.37}$$

I now claim that the neutral density decays exponentially as a function of axial distance as a result of ionization:

$$n_n(z) = n_0 \exp\left(\frac{-z}{l_{iz}}\right), \tag{8.38}$$

where n_0 is the initial density at $z = 0$, and l_{iz} is a ionization path length. This is consistent with the assumption of unity mass utilization if $l_{iz} \ll L$. Furthermore, from particle continuity, I claim that the plasma density now follows as

$$n(z) = \frac{\dot{n} - n_n(z)u_0}{u(z)}, \tag{8.39}$$

where $\dot{n} = \dot{m}/(m_i A)$. Note this is a slight alteration to Eq. 8.10, but again this should not alter the results above if ionization length is relatively short. Using these expressions for density in Eq. 8.37 reveals

$$\dot{N}_{iz} = A\langle\sigma_{iz}v_e\rangle\dot{n}n_0\sqrt{\frac{\pi m_i l_{iz}}{4qE_{z,0}}}(\sqrt{2}-1). \tag{8.40}$$

This ion production rate necessarily must be less than the exit mass flow rate of ions from the thruster, which for unity mass utilization is $\dot{n}A$. Using this I can form an inequality for the ion production rate as

$$\dot{N}_{iz} \geq \dot{n}A. \tag{8.41}$$

To reduce this expression I claim that ionization length can be written as

$$l_{iz} = \frac{\gamma u_0}{n_0\langle\sigma_{iz}v_e\rangle}, \tag{8.42}$$

where γ is a scaling factor. Substituting this into Eq. 8.40 and then Eq. 8.41 and multiplying both sides by the thruster length l yields

$$\gamma\frac{\pi}{4}\left(\sqrt{2}-1\right)^2 m_i\dot{n}l\langle\sigma_{iz}v_e\rangle \geq qE_{z,0}l. \tag{8.43}$$

I now substitute back the expression for mass flow relative to $\dot{n}$ to arrive at

$$\gamma\frac{\pi}{4}\left(\sqrt{2}-1\right)^2 \dot{m}\frac{l}{A}\langle\sigma_{iz}v_e\rangle \geq qE_{z,0}l. \tag{8.44}$$

This equation is essentially a limit to the exhaust velocity of the ions as a function of the thruster aspect ratio l/A, the mass flow rate, and the propellant selection and electron temperature, $\langle \sigma_{iz} v_e \rangle (T_e)$. I can now substitute in the expression for exit ion velocity and express that in terms of specific impulse

$$u_i(l) = \sqrt{\frac{2q_i E_{z,0} l}{m_i}} = I_{sp} g_0, \tag{8.45}$$

where I_{sp} is the specific impulse, and g_0 is Earth's gravitational acceleration. Note this expression is again only valid when mass utilization is 100 %. Substituting specific impulse from this expression into Eq. 8.44 gives

$$I_{sp} \leq \frac{1}{g_0} \sqrt{0.26 \gamma \frac{\dot{m}}{m_i} \frac{l}{A} \langle \sigma_{iz} v_e \rangle}. \tag{8.46}$$

This expression is powerful, as specific impulse is the driving feature of electric propulsion, and as this expression contains so few parameters. A similar limitation on specific impulse is also suggested by Hara et al. in Ref. [37]. In Fig. 8.7, I present several specific impulse curves for xenon and the RMFv3 thruster geometry as functions of mass flow rate, considering various values of electron temperature. These curves are plotted using $\gamma = 5$ which is purely ad hoc and reflects an ionization length of 1 cm which is roughly the correct order of magnitude. The relationship between ionization rate coefficient and Maxwellian electron temperature can be found in Ref. [32].

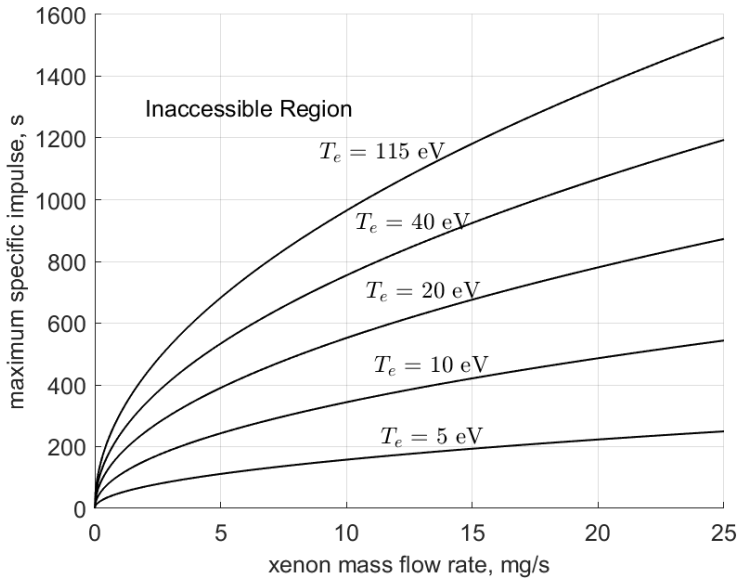

Figure 8.7: Maximum theoretical specific impulse from 1D model.

These curves demonstrate that specific impulse and, consequently, performance can be significantly limited when the electron temperature is low or when the length-to-area ratio is very low as is the case for all our RMF thruster prototypes. Based on this model, the wide thruster exit area of the RMFv3 limits the specific impulse for the flow rates plotted here to below 1600 s, which is only possible for very high electron temperatures. In this work, I have shown that the electron temperature in RMF thrusters is not particularly high (See chapter 6), as can be the case for Hall thrusters. In light of that, Eq. 8.46 may be the explanation for the quenching effect seen in the CW mode operation of the RMFv3 thruster. It might be the case that we were attempting to operate the thruster at a specific impulse larger than this maximum. If that were the case, the ionization rate would not be able to keep up with the flux of particles out of the device, and the plasma would extinguish. Furthermore, the mass flow rate dependency in Eq. 8.46 may explain why the thruster was able to increase specific impulse at higher mass flow rates. The largest 1D specific impulse we were able to achieve was approximately 850 s at 25 mg/s. This agrees with the model for an electron temperature of rougly 20 eV.

This cut-off will affect the overall efficiency of the system, and in Fig. 8.8, I plot the location of this cut-off for 15 eV electrons. The filled circles in this plot indicate the accelerating field location where the mass utilization is expected to go to zero. Note, the effect of including mass utilization in Fig. 8.8 does not change the overall shape of the curves from Fig. 8.6. The mass utilization cut-off, as seen in Fig. 8.7, is sensitive to electron temperature; in general, the electron temperature is likely to increase with increasing electric and magnetic fields, as more energy is put into the system in these cases and Ohmic heating is likely to increase due to higher electron drift speeds. The exact function of electron temperature in response to the electric field is difficult to determine due to sensitivity in electron heat flux, resistivity, and the potential for wave-driven effects. However, a functional form of electron temperature would serve to locate accessible and inaccessible regions of this plot where we would expect the plasma to extinguish.

8.4.4 Ohmic Heating

Many of the aforementioned expressions are functions of electron temperature. In this analysis, I have assumed a constant electron temperature within the thruster volume. This assumption appears reasonable given the density and collisionality within the thruster, supported by the experimental measurements presented in Chapter 6.

An analytical model of the specific electron temperature is beyond the scope of this study as the resistivity within the plasma is not well characterized under the influence of

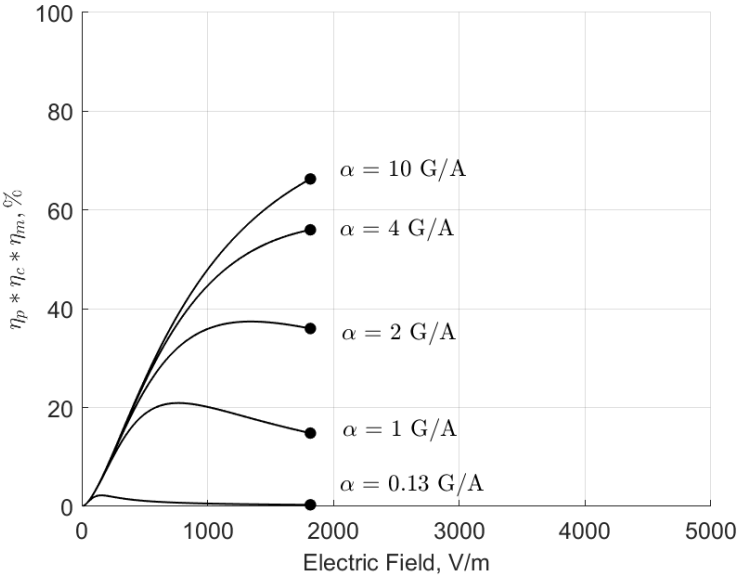

Figure 8.8: Combined efficiency scaling including mass utilization limits.

the RMF. As a result, a full electron energy equation to ascertain the electron temperature does not provide meaningful results with this model using a classically modeled plasma collision frequency and resistivity. However, to understand the driving factors on the electron temperature, it is important to characterize the heating mechanism from the RMF. Here, I provide an expression for Ohmic heating resulting from RMF application to elucidate the scaling and factors influencing it.

The Ohmic heating of the electrons can be expressed as

$$P_{\text{heat}} = \int_V E \cdot J_e \, dV, \tag{8.47}$$

where E is the electric field, and J_e is the electron current. I consider this term to be primarily driven by the time-varying axial electric field and electron currents induced by the RMF. Here, I neglect the steady electric field term as this is likely to be small component to the overall heating. Subsequently, I simplify Eq. 8.47 as follows

$$P_{\text{heat}} = \int_V E_z J_{e,z} dV, \tag{8.48}$$

where E_z is the axial electric field produced by the RMF, and $J_{e,z}$ are axial electron currents. It is important to recall that E_z is directly derived from Faraday's law in the RMF:

$$E_z = \omega r B_\omega cos(\omega t - \theta). \tag{8.49}$$

Returning to Ohm's law, I can express the axial electron velocity from the RMF as

$$u_z = \frac{u_\theta B_r - E_z}{\zeta}, \tag{8.50}$$

where again I have explicitly stated the collision term as $\zeta = \frac{m_e \nu_{ei}}{e}$ for clarity. It is worth noting that in the formulation of the axial electron velocity, I have neglected the radial electron velocity, a departure from the derivation of u_θ. Assuming that the heating is predominantly driven by high-frequency motion, I restrict the radial magnetic field to include only the RMF. This simplification reduces Eq. 8.50 to

$$u_z = \frac{u_\theta - \omega r}{\zeta} B_\omega cos(\omega t - \theta). \tag{8.51}$$

Using this I can write axial current density as

$$J_z = en\frac{\omega r - u_\theta}{\zeta} B_\omega cos(\omega t - \theta). \tag{8.52}$$

The Ohmic heating power can then be written as

$$P_{\text{heat}} = \int_0^l \int_0^{2\pi} \int_0^R en\omega r \frac{\omega r - u_\theta}{\zeta} B_\omega^2 cos^2(\omega t - \theta) r dr d\theta dz. \tag{8.53}$$

This expression simplifies to

$$P_{\text{heat}} = \frac{\pi e^2 \omega B_\omega^2}{m_e} \int_0^R r^2(\omega r - u_\theta) dr \int_0^l \frac{n}{\nu_{ei}} dz \tag{8.54}$$

At this point, it is identified that $\nu_{ei} \propto n$, making the z integrand essentially a constant typically dependent on $T_e^{-3/2}$. Additionally, the steady azimuthal electron current derived in Chapter 3 can be substituted, restated here as

$$u_\theta = \frac{\omega r}{1 + 2\left(B_0^2 + \zeta^2\right)/B_\omega^2}. \tag{8.55}$$

With these substitutions, the Ohmic heating power becomes:

$$P_{\text{heat}} = \frac{\pi e^2 \omega^2 B_\omega^2 l R^4}{4 m_e} \frac{n}{\nu_{ei}} \left(1 - \frac{1}{1 + 2\left(B_0^2 + \zeta^2\right)/B_\omega^2}\right) \tag{8.56}$$

Notably, for optimum $B_{r,0} = B_{r,0}^*$, the parenthetical term goes to 1/2, simplifying the steady azimuthal electron current to $u_\theta^* = 1/2\omega r$. This results in a simplified expression for the heating power:

$$P_{\text{heat}} = \frac{\pi l (e\omega B_\omega R^2)^2}{8 m_e} \frac{n}{\nu_{ei}}. \tag{8.57}$$

From this expression, we can identify that both the RMF frequency and magnitude represent significant factors for electron heating, as they scale quadratically. This implies that for higher electron temperatures—which increases ionization rate and eases specific impulse limitations—it is advisable to maximize both these parameters. This becomes particularly important for alternative propellants that exhibit higher ionization energies and smaller ionization cross-sections. However, note that increasing the Ohmic heating term from Eq. 8.57 will eventually show diminishing returns to performance. This is a result of heating power eventually surpassing what is needed for the requisite ionization power and instead contributing to additional losses. Little et al. showed through a similar model for PIT performance that the ratio of Ohmic heating power to ionization power ($P_{\text{heat}}/P_{\text{iz}}$ here) is best kept at a factor of roughly 1.5 for satisfactory mass utilization efficiency [55].

Furthermore, in Eq. 8.57 the collision frequency ν_{ei} is responsible for the resistivity that results in electron heating which, as mentioned above, typically scales inversely with electron temperature. This parameter is the link between the electron energy equation—through the electron temperature—to the loss processes that influence the plasma efficiency and coupling efficiency as in the sections above. As this model exists, a classical description of the electron collision frequency does not yield physically plausible results for the electron temperature if a full electron energy equation is written. This is a large caveat to this work and needs to be closed for a complete description of the thruster plasma. Indeed, this may need to be informed by additional experimental measurements of internal plasma properties such as is the case with calibrated anomalous resistivity for Hall thrusters [59].

8.5 Summary

In summary, the RMF efficiency model outlined above highlights several key factors crucial for optimizing the performance of continuous wave mode RMF thrusters. To increase the plasma efficiency of the thruster, requires a significant increase in the Lorentz force / accelerating electric field. Presently we are operating at points near 300 V/m which results in the 20 - 30 V retarding potential seen in the probe data from Chapter 7. The model presented above tells us that we need to be operating an order of magnitude higher in accelerating potential up to 3000 V/m in order to achieve high efficiency in this mode. Given optimum tuned bias field, the parameters we have at out disposal to increase E_z are RMF frequency and strength, ω and B_ω respectfully, and the thruster radius R. While I do not expressly

identify trends in the divergence efficiency, it is likely that increasing the accelerating force will improve divergence efficiency, just as hall thrusters operating at higher voltages are mode collimated [1, 3].

The coupling efficiency model shows us that blindly increasing the force will have a substantial negative impact on the coupling efficiency. This is because an increase in B_ω for example will also increase the power of the system, and what the model shows is that the plasma load from the thruster does not scale as fast as the parasitic power lost to resistive elements in the circuit. This means that an increase in coil constant is required to increase both the coupling and plasma efficiency. For good performance an increase in 1-2 orders of magnitude in coil constant is required. This is a substantial departure from the single or double turn air-core RMF antennas that have been implemented thus far.

Furthermore, the model for mass utilization indicates a discharge cut-off where the convective plasma ejection rate exceeds the ionization rate within the thruster. This is a particularly significant problem for RMF thrusters, as the electrons move in the same directions as the ions, as opposed to hall thrusters where the retrograde electron current can sustain the discharge. This model through the ionization rate coefficient shows us that attaining high electron temperature through increased Ohmic heating is vital to avoid this quenching effect. The primary knobs here are increased ω and B_ω, and R. However, while thruster radius can improve the heating it also increases the area and the accelerating force, potentially hindering mass utilization due to reduced plasma density for a given flow rate. Additionally, increasing electron temperature will also increase the inelastic losses to the thruster walls, through radiated power, and frozen flow losses and the balance these effects for efficient thruster operation is worthy of additional study.

The model implies that large-diameter thrusters with high RMF field and frequency are imperative for competitive performance. These findings suggest that RMF thrusters in CW mode, in principle, can achieve high efficiency upwards of 65 %. However, achieving this potential requires a significant departure from traditional construction methods, calling for very high-frequency antenna currents, possibly up to several megahertz, and significantly higher coil constants.

CHAPTER 9

Discussion and Conclusion

9.1 Summary of Findings

Throughout this document, I investigate and explain the low efficiency of rotating magnetic field (RMF) thrusters. This electric propulsion technology, studied intermittently over several decades, shows some promise in addressing future in-space propulsion needs. However, the efforts so far have only been passably successful, and RMF thruster prototypes have demonstrated sub-par performance.

This work begins in Chapter 1 with an overview of electric propulsion and its benefits over chemical propulsion by divorcing the power source from the propellant flow to achieve rocket exhaust velocities unattainable by chemical sources. In this chapter, I discuss the outstanding needs in electric propulsion and how a class of inductive pulsed plasma thrusters is suited to address these issues.

In Chapter 2, I provide background information on the operation of both pulsed plasma thrusters and how inductive pulsed plasma thrusters differ but exhibit similar scaling. Building on this necessary context, I describe how the RMF thruster operates and differs from these other devices. Following this, I provide a literature review on RMF thruster research, outlining key outstanding questions for this technology. The remainder of this document attempts to answer these questions.

In Chapter 3, I present the theory of how an RMF thruster converts electrical energy into propulsive jet power. This includes a description of the azimuthal electron current dive produced by the rotating field and a derivation of an efficiency model for the RMF thruster that includes the effects of individual phenomena that can hinder performance. This model is referenced frequently in the latter chapters as a framework to interpret the performance of the RMF thruster.

Chapter 4 describes the details of three RMF thruster prototypes built throughout this effort. These thrusters ranged from version 1 constructed in 2019 to the version 3 thruster

built in 2023. This chapter explains some of the design considerations for these devices, particularly pertaining to deviations in form and function between thruster generations. It also presents a set of performance comparisons between the prototypes, ultimately resulting in the RMFv3 thruster achieving 145 mN of thrust at 600 s specific impulse with an efficiency of 2.8 %.

In Chapter 5, I describe the experimental facilities, diagnostics, and methods used to characterize the efficiency modes described in Chapter 3. The diagnostics include an inverted pendulum thrust stand for direct performance measurements, a Faraday probe to measure the ion current density distribution, a set of current transducers to monitor the antenna currents, a retarding potential analyzer to measure the ion energy distribution, and a set of Langmuir probes to evaluate internal thruster plasma properties.

These introductory chapters set up the bulk of the experimental and analytical work contained in the latter three chapters of this thesis. In Chapter 6, I present measurements of the efficiency modes for the RMFv2 thruster. Through this effort, I find that the low efficiency of the RMF thruster is dominated by poor plasma efficiency, which relates to the conversion of power coupled to the plasma into kinetic ion beam power. While other efficiency modes show room for improvement, the plasma efficiency constitutes over a 90% energy loss within the thruster. In light of this, I estimate the energy contributions to this loss using the internal Langmuir probes to evaluate the internal thruster plasma properties. From this, much of the energy is found to be lost through excitation radiation collisions, with a smaller yet important contribution from wall contact loss. These losses result from high plasma density (1×10^{19} m) that appears to be characteristic of pulsed RMF thruster operation, indicating that pulsed mode RMF thrusters may be unable to achieve competitive efficiency.

The results from Chapter 6 directly inform the experiment conducted on the RMFv3 thruster detailed in Chapter 7. This thruster was designed, in large part, to explore the difference in operation between pulsed and continuous wave (CW) mode, where the RMF is run at 100% duty cycle. This was done to confirm whether CW mode is just as effective at accelerating the plasma, as the duty cycle increase will increase specific impulse and thus lower the average plasma density. The measurements confirm this theory, and we found the RMFv3 thruster produced roughly double the thrust and specific impulse when operated in CW mode compared to a similar operating condition in pulsed mode. Furthermore, the efficiency breakdown shows all metrics improving by around 50 % in the CW mode. Thus, steady RMF application improves overall thruster efficiency by nearly 400 %.

In light of this result, I explore CW mode operation further in Chapter 8. Here, I present an analytical model for the performance of an RMF thruster operating in CW mode. This

model uses expressions for the internal energy modes for the thruster derived in Chapter 3, with an expression for the electric potential the RMF is able to produce to accelerate the ions. The accelerating potential is maximized with an optimum ratio between the applied bias field strength and the strength of the RMF. Using this model, I am able to reproduce the efficiency of the RMFv3 thruster operating in CW mode with reasonable accuracy. Using the model, I predict RMF thruster efficiency can reach up to 65%. However, this requires a substantial departure from the way RMF thrusters presently are built and operated, calling for higher RMF frequencies and RMF antennas that are able to produce much stronger fields with less current.

9.2 Contributions to the Field

In this work, I set out to answer several open questions regarding the operation of RMF thrusters. These questions stem from the poor efficiency and thrust performance of this technology shown across research groups. Because of this, my overarching goal is to distinguish between unknown limiting physical mechanisms driving their operation and ineffective engineering implementations. My specific contributions towards this goal have been:

1. **Identified major drivers for efficiency loss in RMF thrusters:** I used a suite of plasma probes to populate an efficiency model for the RMFv2 and RMFv3 thruster prototypes. This model revealed that the poor performance of these thrusters is driven by low conversion of coupled plasma power to ion beam energy, where the vast majority of the power is lost through inelastic collisional processes. The largest portion of the energy leaves the thruster as photonic radiation from electronic excitation collisions, and another large fraction is lost through contact with the thruster walls.

2. **Leveraged physical insights to guide designs for improved thruster performance:** The large collisional losses in RMF thrusters were found to be a direct result of the high neutral density that builds up between pulses in the thruster. These neutrals are able to be rapidly ionized by the RMF, but because the RMF antenna does not directly push against the plasma, they have a long residence time within the thruster. To overcome this, we constructed the RMFv3 thruster, which was able to operate in continuous wave mode and avoid this neutral build-up. As a result, the RMFv3 thruster showed significant improvement in thrust, specific impulse, and efficiency in the CW mode. This trend was further assessed and validated using plasma diagnostic tools.

3. **Inferred maximum theoretical performance in light of these efficiency losses using experimental measurements and first-principles analysis:** Using the insights gained through the RMFv2 and RMFv3 thruster experiments, I derived an analytical performance model for RMF thrusters operating in CW mode. This model takes into account many of the limiting performance considerations uncovered during the RMFv3 thruster test. Furthermore, it predicts the maximum efficiency for the RMFv3 thruster within a factor of two. I identify that the critical parameter to increase for performance is the ion accelerating electric field. However, this is limited by the mass utilization of the thruster and also cannot be done without also improving the coil constant (in terms of Gauss-per-ampere) of the RMF antennas. Using the model, I conjecture that RMF thrusters can achieve an efficiency upwards of 65%.

9.3 Future Work

Despite the progress made in comprehending RMF thrusters' physical mechanisms, their performance remains far from competitive. There exists a substantial opportunity for advancing the technology to address its existing limitations. Based on the findings presented here, I propose exploring several avenues of research to build upon these results.

9.3.1 Improvement of CW RMF Thrusters

In this work, a meaningful result was the development of the CW mode RMF thruster. This mode for RMF thrusters has not been explored elsewhere, and we have demonstrated that it outperforms pulsed mode operation for RMF thrusters. However, the performance of the CW system is still lacking. This is largely a result of the low RMF strengths produced. As shown in Chapter 8 and confirmed by work done by Sercel [78], for increased efficiency, the RMF should be at least an order of magnitude stronger (>100 G). This is to ensure strong magnetization of the electrons to the RMF while permitting a strong bias field to accelerate the plasma. This could be achieved by increasing the current through the RMF coils; however, this will increase the ohmic losses in the circuit faster than the power put into the ion beam. This necessarily means that the RMF antennas need to consist of more turns. This increases the field strength while keeping the coil current low. A drawback of this approach is that it will also increase the required coil driving voltage. For an inductor, the peak AC driving voltage is

$$V_\omega = \omega N A_\mathrm{m} B_\omega, \tag{9.1}$$

where ω is the frequency, N is the number of turns, A_{m} is the cross-section of produced field, and B_{ω} is the magnetic field amplitude. This equation is universally enforced as a direct result of Faraday's law. As a result, other inductive IPPTs may become more attractive, if higher voltages are indeed also required for RMF thrusters. These pulsed systems still can suffer from mass utilization and/or require the use of pulsed valves. However, leveraging the findings from RMF CW mode operation may be a path forward. One could imagine a CW mode pulsed inductive thruster or theta pinch thruster that exhibits high beam power (as the coil couples directly to the plasma) and high mass utilization as a result of sustained operation. This route my indeed be a suitable path forward for inductive propulsion concepts.

Part of the challenge of RMF thrusters is the intricacy of their power systems. While coupling efficiency was not found to be the lowest efficiency mode for these thrusters, it still represents a substantial power loss to the overall system. These losses are not always accounted for in radiofrequency thruster research, but it is critical to advance power systems in step with the thruster technology. An RMF power system must be carefully designed for a given plasma load to achieve high performance. One limiting factor of the RMFv3 thruster, for instance, was that the power system was designed to operate both in pulsed and CW mode, which resulted in inefficiencies for both. A direct result being that the thruster could only operate for 10 to 30 seconds in CW mode before the antennas overheated. Future CW mode RMF thrusters likely require bespoke power systems that are carefully designed to match the thruster and plasma load. Philosophically, the RMF power system is as much a part of the thruster technology as any other part of the device—a distinct departure from how the power systems of other electric propulsion devices are regarded.

9.3.2 Thruster Modeling

The RMF performance model presented here offers an updated perspective on the operational limitations of RMF thrusters in the new CW mode of operation. However, it is important to note that the model, despite its predictive intent, has certain gaps that require additional analysis.

In particular, the model requires a priori knowledge of the electron temperature in the thruster to evaluate the rates of collisional processes. The RMF is ultimately responsible for the heating of the electrons, and its efficacy plays a crucial role in addressing both the losses and the ionization of the propellant. The analytical model presented here is not suited to address this aspect, and to improve the model would require self-consistently solving for the electron temperature. However, deriving a complete heat equation for electrons may not be entirely accurate, as the current model is based on a fluid approach. The interaction of

RMF waves with electrons is likely a significant factor in heating, and careful consideration of the electron heat flux may be crucial for plasma cooling and isotropy. To address this, a kinetic approach or empirical measurements from thruster experiments may be necessary. Thus, this may resemble the challenges faced in solving the anomalous electron transport problem in hall thrusters.

With improved RMF models, the analysis here could be expanded to consider various factors such as the thruster and antenna geometries, the relationship between the force of acceleration, wall losses, and thruster radius. Currently, a comprehensive understanding of these aspects is lacking for CW mode RMF thrusters. In summary, while the performance model provides valuable insights, its reliance on a priori empirical data and the need for a more nuanced understanding of various factors underscore the importance of continued work in this direction.

9.3.3 Alternative Propellants

This study focused exclusively on the operation of RMF thrusters using xenon as a propellant. It's noteworthy that RMF thrusters, along with inductive propulsion in general, are designed with a particular interest towards alternative propellants, especially molecular gases. Indeed, the PIT mkIV achieved its best performance on ammonia, a complex molecule that is theorized to favorably reduce radiation losses.

We have previously investigated and analyzed the RMFv2 thruster running on CO_2—as an alternative to toxic ammonia—with the hopes of similarly improving performance by reducing radiation [28]. However, the thruster demonstrated mediocre performance. I attribute the outcome of this test to suboptimal nature of the RMF thruster at that point in time. Achieving satisfactory performance with alternative gases critically requires maximizing mass utilization, which, in turn, requires high electron temperatures. This is because alternative propellants have smaller ion cross sections and higher ionization energies than xenon—hence why xenon is a good EP propellant. Our RMF thrusters have exhibited relatively low Maxwellian electron temperatures compared to similarly powered Hall thrusters. However, there is evidence that high-energy electron tails are produced in these devices which aids in the demonstrated high mass utilization. Further investigation into the electron heating mechanism of RMF thrusters, and a characterization of their internal electron energy distribution function is thus warranted.

In light of these findings, there is also compelling need for future studies to characterize the performance of RMF thrusters operating on alternative propellants. This research direction becomes particularly significant if advancements in RMF thruster technology can enhance

its performance when using xenon. Exploring alternative propellants aligns with the broader objective of improving mass utilization and electron temperatures, contributing to the overall development of RMF thruster technology.

9.4 Concluding Remarks

In conclusion, this document presents a comprehensive investigation into the efficiency challenges faced by RMF thrusters, a technology with potential significance as a future in-space propulsion system. These findings shed light on both the underlying physics driving RMF thruster operation and the engineering considerations essential for their optimization.

Through experimentation and analysis, I have identified key factors contributing to the low efficiency of RMF thrusters, notably emphasizing the significant energy losses associated with collisional processes resulting in a poor plasma efficiency. As a result, I conjecture that pulsed mode RMF thrusters are not capable of achieving competitive performance. The lack of direct coupling between the plasma and the RMF coils results in high density plasmas in the pulse mode that exacerbate both excitation radiation and wall losses.

Our development and successful testing of a CW mode RMF thruster offers a promising avenue for improving performance. However, this requires a significant evolution to how RMF thrusters are currently built. If my performance predictions for CW mode RMF thrusters are accurate and they are able to achieve efficiencies above 65 %, they may be a promising candidate for future in-space propulsion. A thruster such as this would be a competitor to high current density Hall thrusters and high power applied field MPD thrusters, with the advantage of not necessitating high current cathodes.

The contributions made in this work include an advancement in the scientific understanding of RMF thrusters. In particular, I have evaluated the loss mechanisms present in current RMF thrusters and found paths to improve their performance. Beyond this identification of issues, I have provided actionable insights for future research and development efforts. Proposals for enhancing CW mode RMF thrusters, optimizing power systems, refining performance modeling, and exploring alternative propellants represent pivotal areas for continued research. By addressing these challenges and leveraging the insights gleaned from this work, RMF thruster technology may be able to overcome present limitations and advance in-space propulsion capabilities.

BIBLIOGRAPHY

[1] Yassir Azziz, Manuel Martinez-Sanchez, and James Szabo. Effect of discharge voltage on plume divergence of a high specific impulse hall thruster. In *41st AIAA/ASME/SAE/ASEE Joint Propulsion Conference & Exhibit*, page 4403, 2005.

[2] S.I. Babic and C. Akyel. Magnetic force calculation between thin coaxial circular coils in air. *IEEE Transactions on Magnetics*, 44:445–452, 4 2008.

[3] Matthew Baird, Thomas Kerber, Ron McGee-Sinclair, and Kristina Lemmer. Plume divergence and discharge oscillations of an accessible low-power hall effect thruster. *Applied Sciences*, 11(4):1973, 2021.

[4] Laszlo Balogh. Fundamentals of mosfet and igbt gate driver circuits. *Texas Instruments–Application report*, 2017.

[5] Archit Bapat, Pramod B Salunkhe, and Aakash V Patil. Hall-effect thrusters for deep-space missions: A review. *IEEE Transactions on Plasma Science*, 50(2):189–202, 2022.

[6] Robert E Biggs. *Space Shuttle Main Engine: The first twenty years and beyond*, volume 29. American Astronautical Society, 2008.

[7] H. A. Blevin and P. C. Thonemann. Plasma confinement using an alternating magnetic field. *Nuclear Fusion Supplement, Part 1*, page 55, 1962.

[8] Jeremiah Brackbill, Jean Luc Cambier, Natalia E. Gimelshein, and Sergey F. Gimelshein. Numerical analysis of neutral entrainment effect on field-reversed configuration thruster efficiency. *Journal of Propulsion and Power*, 30:1450–1458, 2014.

[9] John Brophy, Charles Garner, Barry Nakazono, Mike Marcucci, Mike Henry, and Don Noon. The ion propulsion system for dawn. In *39th AIAA/ASME/SAE/ASEE Joint Propulsion Conference and Exhibit*, page 4542, 2003.

[10] Daniel L. Brown, Mitchell L. R. Walker, James Szabo, Wensheng Huang, and John E. Foster. Recommended practice for use of faraday probes in electric propulsion testing. *Journal of Propulsion and Power*, 33:582–613, 2017.

[11] Murat¸ Celik. *Experimental and Computational Studies of Electric Thruster Plasma Radiation Emission*. PhD thesis, Massachusetts Institute of Technology, 2007.

[12] Francis F Chen. *Introduction to plasma physics and controlled fusion*. Springer, 1984.

[13] Sin Li Chen and T. Sekiguchi. Instantaneous direct-display system of plasma parameters by means of triple probe. *Journal of Applied Physics*, 36:2363–2375, 1965.

[14] Edgar Choueiri. Scaling of thrust in self-field magnetoplasmadynamic thrusters. *Journal of Propulsion and Power*, 14(5):744–753, 1998.

[15] Simone Ciaralli. *A study of the lifetime of miniaturized ablative pulsed plasma thrusters*. PhD thesis, University of Southampton, 2014.

[16] M H Corbett. In-situ measurements of discharge plasma characteristics during thrust operation of the t6 gridded ion thruster. In *31st International Electric Propulsion Conference*, 2009.

[17] S. Correyero, J. Jarrige, D. Packan, and E. Ahedo. Plasma beam characterization along the magnetic nozzle of an ecr thruster. *Plasma Sources Science and Technology*, 28, 9 2019.

[18] John W. Dankanich, Mitchell L. R. Walker, Michael W. Swiatek, and John T. Yim. Recommended practice for pressure measurement and calculation of effective pumping speed in electric propulsion testing. *Journal of Propulsion and Power*, 33:668–680, 2016.

[19] The Economist. How rare-gas supply adapted to russia's war. *The Economist Newspaper*, 2023.

[20] John Foster and Anil Bansal. Beyond inert gases: The promise of plasma cathodes. In *The American Physical Society Gaseous Electronics Conference*, 2023.

[21] Takeru Furukawa, K. Shimura, D. Kuwahara, and S. Shinohara. Verification of azimuthal current generation employing a rotating magnetic field plasma acceleration method in an open magnetic field configuration. *Physics of Plasmas*, 26, 2019.

[22] Takeru Furukawa, S. Shinohara, and D. Kuwahara. Electrodeless plasma propulsion with electromagnetic acceleration effect by using rotating magnetic field current drive method. *AIAA Propulsion and Energy 2020 Forum*, pages 1–11, 2020.

[23] Takeru Furukawa, K. Takizawa, K. Yano, D. Kuwahara, and S. Shinohara. Spatial measurement in rotating magnetic field plasma acceleration method by using two-dimensional scanning instrument and thrust stand. *Review of Scientific Instruments*, 89, 4 2018.

[24] Christopher Galea, Stephanie Thomas, Michael Paluszek, and Samuel Cohen. The princeton field-reversed configuration for compact nuclear fusion power plants. *Journal of Fusion Energy*, 42(1):4, 2023.

[25] H E Gallagher. Poisoning of lab6 cathodes. *Journal of Applied Physics*, 40:44–51, 2 1969.

[26] Marcel P Georgin, Michael S McDonald, and John W Brooks. Theory of rf plasma cathodes and supporting experiments for electric propulsion applications. In *AIAA SCITECH 2023 Forum*, page 0844, 2023.

[27] Tate Gill. The electron merry-go-round. Youtube, 2022. https://www.youtube.com/watch?v=pRrrnMv4ejM.

[28] Tate Gill, Christopher L Sercel, and Benjamin Jorns. Simulations of alternative propellants for inductive pulsed plasma thrusters. In *AIAA SCITECH 2023 Forum*, page 0451, 2023.

[29] Tate Gill, Christopher L. Sercel, Joshua M. Woods, and Benjamin A. Jorns. Experimental characterization of efficiency modes in a rotating magnetic field thruster. In *AIAA SCITECH 2022 Forum*, page 2191, 2022.

[30] Tate M Gill, Christopher L Sercel, and Benjamin A Jorns. Experimental investigation into efficiency loss in rotating magnetic field thrusters. *Plasma Sources Science and Technology*, 33(1):015006, 2024.

[31] James Gilland. Mission impacts of in-situ propellant usage for electric propulsion vehicles. In *41st AIAA/ASME/SAE/ASEE Joint Propulsion Conference & Exhibit*, page 4267, 2005.

[32] Dan M. Goebel and Ira Katz. *Fundamentals of Electric Propulsion: Ion and Hall Thrusters*. Jet Propulsion Laboratory, California Institute of Technology, 2008.

[33] James Haas and Alec Gallimore. An investigation of internal ion number density and electron temperature profiles in a laboratory-model hall thruster. In *36th AIAA/ASME/SAE/ASEE joint propulsion conference and exhibit*, page 3422, 2000.

[34] Yukap Hahn. Electron-ion recombination processes-an overview. *Reports on Progress in Physics*, 60(7):691, 1997.

[35] Scott J. Hall. *Characterization of a 100-kW Class Nested-Channel Hall Thruster*. PhD thesis, University of Michigan, 2017.

[36] Ashley K Hallock, Adam K Martin, Kurt A Polzin, Adam C Kimberlin, and Richard H Eskridge. Single-and repetitive-pulse conical theta-pinch inductive pulsed plasma thruster performance. *IEEE Transactions on Plasma Science*, 43(1):433–443, 2015.

[37] Kentaro Hara, Michael J Sekerak, Iain D Boyd, and Alec D Gallimore. Perturbation analysis of ionization oscillations in hall effect thrusters. *Physics of Plasmas*, 21(12), 2014.

[38] Makoto Hayashi. Determination of electron-xenon total excitationcross-sections, from threshold to 100 ev, fromexperimental values of townsend's α. *J. Phys. D: Appl. Phys*, 16:581–589, 1983.

[39] Daniel A Herman, Timothy Gray, Ian Johnson, Sarah Hussein, and Taylor Winkelmann. Development and qualification status of the electric propulsion systems for the nasa ppe mission and gateway program. In *37th International Electric Propulsion Conference*, 2022.

[40] Carrie S Hill. *Translation Studies on an Annular Field Reversed Configuration Deivce for Space Propulsion*. PhD thesis, Michigan Technological University, 2012.

[41] Richard R. Hofer and Alec D. Gallimore. High-specific impulse hall thrusters, part 2: Efficiency analysis. *Journal of Propulsion and Power*, 22(4):732–740, 2006.

[42] Waheed N. Hugrass. Cylindrical plasma equilibria maintained by means of a rotating magnetic field. *Journal of Plasma Physics*, 28(2):369–378, 1982.

[43] Waheed N. Hugrass. Existence of non-unique steady state solutions to the rmf current drive equations. *Australian Journal of Physics*, 38(2):157–169, 1985.

[44] Waheed N. Hugrass. Influence of the spatial harmonics on the rotating magnetic field current drive. *Australian Journal of Physics*, 39(4):513–527, 1986.

[45] Robert G Jahn. *Physics of electric propulsion*. Dover Publications, 2006.

[46] Robert S. Jankovsky, Sergey Tverdokhlebov, and David Manzella. High power hall thrusters. In *35th Joint Propulsion Conference and Exhibit*, 1999.

[47] Ieuan R. Jones and Waheed N. Hugrass. Steady-state solutions for the penetration of a rotating magnetic field into a plasma column. *Journal of Plasma Physics*, 26:441–453, 1981.

[48] David E Kirtley, John T Slough, Michael Pfaff, and Chris Pihl. Steady operation of an electromagnetic plasmoid thruster. In *Joint Army Navy NASA AirForce Conference*, 2011.

[49] Syri Koelfgen, Richard Eskridge, Mike Lee, Adam Martin, Clark Hawk, and Peter Fimognari. Magnetic and langmuir probe measurements on the plasmoid thruster experiment (ptx). In *40th AIAA/ASME/SAE/ASEE Joint Propulsion Conference and Exhibit*, 2004.

[50] Justin Koo, EM Sousa, and R Martin. High fidelity modeling of field reversed configuration (frc) thrusters. Technical report, Tech. Rep. AFRL-RQ-ED-TR-2017-0002, Air Force Research Laboratory (AFMC), 2017.

[51] Shu T Lai and Catherine Miller. Retarding potential analyzer: Principles, designs, and space applications. *AIP Advances*, 10(9), 2020.

[52] Kyun Ho Lee and Sang Ryool Lee. Comparative study of lunar mission requirements and onboard propulsion system performance. *Progress in Aerospace Sciences*, 47(6):480–493, 2011.

[53] Raymond Liang and Alec D. Gallimore. Far-field plume measurements of a nested-channel hall-effect thruster. In *49th AIAA Aerospace Sciences Meeting including the New Horizons Forum and Aerospace Exposition*, page 1016, 2011.

[54] Jesse A. Linnell and Alec D. Gallimore. Efficiency analysis of a hall thruster operating with krypton and xenon. *Journal of Propulsion and Power*, 22(6):1402–1418, 2006.

[55] Justin M Little, Gordon I McCulloh, and Cameron Marsh. Ionization and current sheet formation in inductive pulsed plasma thrusters. *Journal of Applied Physics*, 132(9), 2022.

[56] Xixuan Liu, Xinfeng Sun, Ning Guo, and Xiaodong Wen. Plume performance of electrodeless plasmoid electromagnetic propulsion. *IEEE Transactions on Plasma Science*, 50(7):2138–2146, 2022.

[57] Robert B. Lobbia and Brian E. Beal. Recommended practice for use of langmuir probes in electric propulsion testing. *Journal of Propulsion and Power*, 33(3):566–581, 2017.

[58] L Marks, K Clark, W Von Jaskowsky, and R Jahn. Mpd thruster erosion measurements. In *16th International Electric Propulsion Conference*, page 1884, 1982.

[59] Thomas A Marks and Benjamin A Jorns. Challenges with the self-consistent implementation of closure models for anomalous electron transport in fluid simulations of hall thrusters. *Plasma Sources Science and Technology*, 32(4):045016, 2023.

[60] Adam K Martin, Kurt A Polzin, Francis M Curran, Roger M Myers, and Mitchell A Rodriguez. A technology maturation plan for the development of nuclear electric propulsion. In *Joint Army-Navy-NASA-Air Force (JANNAF) Meeting*, 2022.

[61] Ioannis G Mikellides, Ira Katz, Richard R Hofer, and Dan M Goebel. Magnetic shielding of a laboratory hall thruster. i. theory and validation. *Journal of Applied Physics*, 115(4), 2014.

[62] Pavlos G. Mikellides and James K. Villarreal. High energy pulsed inductive thruster modeling operating with ammonia propellant. *Journal of Applied Physics*, 102, 2007.

[63] Kenneth E Miller, James Prager, Alex Henson, Kyle McEleney, Joshua Woods, Christopher Sercel, Tate Gill, Eric Viges, and Benjamin Jorns. Continuously-operating repetitively-pulsed rmf-frc thruster and power system. In *IEEE International Conference on Plasma Science*. IEEE, 2021.

[64] Ned Mohan, Tore Undeland, and William Robbins. *Power Electronics: Converters, Applications, and Design*. Wiley, 2002.

[65] National Academies of Sciences Engineering and Medicine. *Space nuclear propulsion for human mars exploration*. 2021.

[66] David Y Oh, Steve Collins, Tracy Drain, William Hart, Travis Imken, Kristina Larson, Danielle Marsh, Dhack Muthulingam, John Steven Snyder, Denis Trofimov, et al. Development of the psyche mission for nasa's discovery program. In *36th International Electric Propulsion Conference*, page 192, 2019.

[67] JE Polk, W Von Jaskowsky, AJ Kelley, and RG Jahn. Measurement of mpd thruster erosion using surface layer activation. *Journal of Propulsion and Power*, 3(1):33–38, 1987.

[68] Kurt A. Polzin. Comprehensive review of planar pulsed inductive plasma thruster research and technology. *Journal of Propulsion and Power*, 27(3):513–531, 2011.

[69] Kurt A Polzin, Emma Blumhagen, Alicia C Sherrod, and Trevor M Moeller. Behavior of triple langmuir probes in non-equilibrium plasmas. *AIAA Propulsion and Energy Forum*, 2019.

[70] Kurt A Polzin, Ashley K Hallock, Kamesh Sankaran, and Justin M Little. *Circuit Modeling of Inductively-coupled Pulsed Accelerators*. CRC Press, 2022.

[71] Kurt A Polzin, Adam K Martin, Richard H Eskridge, A C Kimberlin, B M Addona, A P Devineni, N R Dugal-Whitehead, and Ashley K Hallock. Summary of the 2012 inductive pulsed plasma thruster development and testing program. Technical report, NASA-Marshall Space Flight Center, Huntsville, AL, 2013. No. NASA/TP-2013-217488.

[72] Kurt A. Polzin, Adam K. Martin, Justin Little, Curtis Promislow, Benjamin A. Jorns, and Joshua M. Woods. State-of-the-art and advancement paths for inductive pulsed plasma thrusters. *Aerospace*, 7(8):105, 2020.

[73] Space Propulsion and Advanced Concepts Engineering Laboratory. High-pulse-rate pulsed inductive thruster (hiper-pit), 2024. https://www.uwspacelab.com/research.

[74] Douglas Rapp. High energy-density liquid rocket fuel performance. In *26th Joint Propulsion Conference*, page 90, 1968.

[75] A. S. Richardson. *2019 NRL plasma formulary*. Naval Research Laboratory, 2019.

[76] Joshua L. Rovey, Christopher T. Lyne, Alex J. Mundahl, Nicolas Rasmont, Matthew S. Glascock, Mitchell J. Wainwright, and Steven P. Berg. Review of multimode space propulsion. *Progress in Aerospace Sciences*, 118:100627, 2020.

[77] Ville Satopaa, Jeannie Albrecht, David Irwin, and Barath Raghavan. Finding a" kneedle" in a haystack: Detecting knee points in system behavior. In *2011 31st international conference on distributed computing systems workshops*, pages 166–171. IEEE, 2011.

[78] Christopher Sercel. *Characterization of Performance and Current Drive Mechanism for the Rotating Magnetic Field Thruster*. PhD thesis, University of Michigan, 2023.

[79] Christopher L. Sercel, Tate Gill, and Benjamin Jorns. Performance predictions for cw-mode operation of an rmf thruster. In *AIAA SCITECH 2023 Forum*. American Institute of Aeronautics and Astronautics, 2023.

[80] Christopher L. Sercel, Tate Gill, Joshua M. Woods, and Benjamin Jorns. Performance measurements of a 5 kw-class rotating magnetic field thruster. In *AIAA Propulsion and Energy 2021 Forum*. American Institute of Aeronautics and Astronautics, 2021.

[81] Christopher L Sercel, Tate M Gill, and Benjamin A Jorns. Inductive probe measurements during plasmoid acceleration in an rmf thruster. In *37th International Electric Propulsion Conference*, 2022.

[82] Christopher L Sercel, Tate M Gill, and Benjamin A Jorns. Inductive probe measurements in a rotating magnetic field thruster. *Plasma Sources Science and Technology*, 32(10):105017, 2023.

[83] Christopher L. Sercel, Joshua M. Woods, Tate M. Gill, and Benjamin A. Jorns. Impact of flux conservers on performance of inductively driven pulsed plasmoid thrusters. In *AIAA Propulsion and Energy 2020 Forum*. American Institute of Aeronautics and Astronautics, 2020.

[84] Christopher L. Sercel, Joshua M. Woods, Tate M. Gill, Eric Viges, Ricardo G. Van Zanten, and Benjamin A. Jorns. Design of a 30-kw rmf-frc thruster. In *36th International Electric Propulsion Conference*, page 4911, 2018.

[85] Shunjiro Shinohara, Hiroyuki Nishida, Takao Tanikawa, Tohru Hada, Ikkoh Funaki, and Konstantin P Shamrai. Development of electrodeless plasma thrusters with high-density helicon plasma sources. *IEEE Transactions on Plasma Science*, 42(5):1245–1254, 2014.

[86] John Slough, George Votroubek, and Chris Pihl. Creation of a high-temperature plasma through merging and compression of supersonic field reversed configuration plasmoids. *Nuclear Fusion*, 51(5):053008, 2011.

[87] John T. Slough, David E. Kirtley, and Thomas E. Weber. Pulsed plasmoid propulsion: The elf thruster. In *31st International Electric Propulsion Conference*, page 265, 2009.

[88] William D Stevenson et al. *Elements of power system analysis*, volume 4. Mcgraw-hill New York, 1982.

[89] Leanne L Su, Alexander R Vazsonyi, and Benjamin Jorns. Performance of a 9-kw magnetically-shielded hall thruster with krypton. In *AIAA Propulsion and Energy 2020 Forum*, page 3617, 2020.

[90] Y. Sun, I. Levchenko, J. W.M. Lim, L. Xu, S. Huang, Z. Zhang, F. Thio, G. C. Potrivitu, M. W.A.B. Rohaizat, O. Cherkun, C. S. Chan, O. Baranov, K. Bazaka, and S. Xu. Miniaturized rotating magnetic field-driven plasma system: Proof-of-concept experiments. *Plasma Sources Science and Technology*, 30(6), 2021.

[91] Infineon Technologies. Igbts – insulated gate bipolar transistors, 2024. https://www.infineon.com/cms/en/product/power/igbt/.

[92] PHPK Technologies. Cryopump tm1200i, 2024. https://www.phpk.com/wp-content/uploads/2019/09/TM1200i-10B.pdf.

[93] Jamie Waldock, David E. Kirtley, and John T. Slough. Electromagnetic optimization of frc-based pulsed plasma thrusters. In *33rd International Electric Propulsion Conference*, page 376, 2013.

[94] Yang Wang, Yan Fei Wang, Xi Ming Zhu, Oleg Zatsarinny, and Klaus Bartschat. A xenon collisional-radiative model applicable to electric propulsion devices: I. calculations of electron-impact cross sections for xenon ions by the dirac b-spline r-matrix method. *Plasma Sources Science and Technology*, 28(10), 2019.

[95] Thomas E Weber. *The Electrodeless Lorentz Force Thruster Experiment*. PhD thesis, University of Washington, 2010.

[96] Joshua Woods. *Performance of a Rotating Magnetic Field Thruster*. PhD thesis, University of Michigan, 2022.

[97] Joshua M. Woods, Christopher L. Sercel, Tate M. Gill, and Benjamin A. Jorns. Performance measurements of a rotating magnetic field thruster. In *AIAA Propulsion and Energy 2020 Forum*, 2020.

[98] Joshua M. Woods, Christopher L. Sercel, Tate M. Gill, Eric Viges, and Benjamin A. Jorns. Data-driven approach to modeling and development of a 30 kw field-reversed configuration thruster. In *36th International Electric Propulsion Conference*, pages IEPC–2019–717, 2019.

[99] Space X. Starlink technology, 2024. https://www.starlink.com/technology.

[100] JK Ziemer and EY Choueiri. Scaling laws for electromagnetic pulsed plasma thrusters. *Plasma Sources Science and Technology*, 10(3):395, 2001.